

UCSF

UC San Francisco Electronic Theses and Dissertations

Title

Translation regulation by autophagy and nutrient stress

Permalink

<https://escholarship.org/uc/item/59h0f8gw>

Author

Goldsmith, Juliet Eve

Publication Date

2018

Peer reviewed|Thesis/dissertation

Translation regulation by autophagy and nutrient stress

by

Juliet Goldsmith

DISSERTATION

Submitted in partial satisfaction of the requirements for the degree of

DOCTOR OF PHILOSOPHY

in

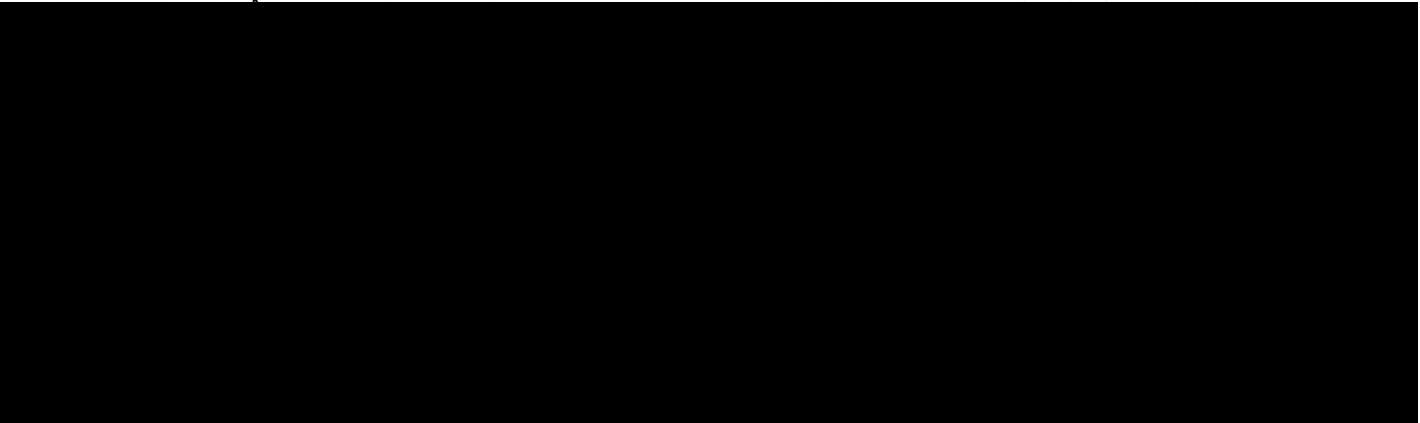
Biomedical Sciences

in the

GRADUATE DIVISION

of the

UNIVERSITY OF CALIFORNIA, SAN FRANCISCO



Committee in Charge

Copyright 2018
by
Juliet Goldsmith

Acknowledgements

Many people say that pursuing a graduate degree is a way of avoiding a real job. Of course, the people who manage to achieve a doctorate are incredibly passionate about their research, which perhaps can be confused by outsiders as all fun and no work. Although you can still get a student discount at a lot of places, the years spent as a graduate student definitely count as a “real job” as this is the entry level position on the path to becoming a principle investigator, equivalent to the CEO of a start-up to use Bay Area terminology. I would also argue this job has unique challenges because of the singularity of the project, long and sometimes unpredictable hours, pressure to advance your career through high impact publications and presentations, and the constant processing of data in the back of your head outside of lab. While the success or failure of a thesis research project lies with the graduate student, it is impossible to accomplish (especially with ones mental health intact) without an incredible amount of support from those around you. I would like to take this opportunity to thank the people who have made this thesis possible.

First, I would like to thank those who have helped me shape my project to where it is today. My thesis committee, Davide Ruggero, Kevan Shokat, and Rushika Perera, have been tremendously helpful during meetings and one-on-one, providing insight, ideas, constructive criticism, advice on career plans, and general support. In addition to their outpouring of wisdom, I am thankful to all of my committee members for the time they took to write me letters of recommendation. I learned a lot of techniques from Craig Stumpf from the Ruggero Lab, especially relevant was help troubleshooting the ribosome profiling experiments. I had amazing help from Saurabh Asthana, Adam

Olshen and Barry Taylor in analyzing my ribosome profiling data. And recently, I have had amazing guidance from Stephen Floor who fortuitously is a recent faculty hire at UCSF and expert in translation regulation and eIF4A1, which became an important part of my thesis research.

I would like to thank my thesis advisor, Jay, who has been the most supportive mentor throughout the past years. Jay managed to be guiding while letting me take projects in entirely new directions. Even when it felt like nothing was working, Jay was never frustrated (or at least never showed it) and remained constantly encouraging, but also pragmatic. Jay taught me about the science of autophagy, how to write a successful grant, how to put a paper together, and how to present and communicate research to those outside of the lab. He provided me the opportunities to present my research at conferences, both near and far, which has been incredibly helpful for my career. I admire how Jay runs his lab, and I am sure I will take some of his tricks with me when I start my own lab in the future.

One of the things that most impresses me about Jay is how he manages to recruit the best people to his lab. My colleagues over the years have been the smartest, kindest, most helpful and encouraging people I have ever worked with, and I am so happy that I can consider them my close friends as well. They have taught me so many lab techniques, have been sounding boards for crazy experiment ideas and are contagious in their excitement for science. Hanna was the one who recruited me to the Debnath lab, and she was right. Spending time outside of lab with Candia, Lyndsay, Hanna, Tim, Drew, Jen, Ari and Teresa, getting coffee, watching baseball or march madness, skiing in Tahoe, eating amazing food, or just going to Yancy's on a Friday

afternoon, has been a relief from the stresses of research. The people in the Debnath lab have made the time I spent here fun and happy.

I also received a tremendous amount of support from outside of lab. Rory, our cat who is very spoiled and very well photographed, has been a source of joy and comfort for the past three years. I made amazing, close friends in graduate school that I am sure I will keep forever. Samira, I can't wait for our kids to be friends. I have to thank my best friend Sarah, who moved to San Francisco for me (or a great job opportunity, but I like to think I was the main draw) and who listened to me complain, supported me by many girl's days and dumplings, and became my favorite exercise (and toast) buddy. My parents were hugely supportive, and although I know they don't completely understand everything that I worked on or went through, they have made such an effort to be involved – even keeping crib notes handy to tell their friends what I have been working on.

Mostly, I have to thank my amazing husband Matthew. He knows all of the time he has patiently waited for me in lab, listened to me complain, and hugged me when I completely lost it, but I don't think he can possibly understand how much this has meant to me. It's a cliché, but he is my rock. Matthew, I am so lucky that you continue to support me every day.

Translation regulation by autophagy and nutrient stress

by Juliet Goldsmith

Abstract

Protein translation is necessary for cell function, but it is an incredibly energy demanding process, and is therefore tightly regulated by the metabolic state of the cell. There are a plethora of translation control mechanisms that are only recently being elucidated. My thesis research has investigated how perturbing the metabolic state of the cell, both subtly via autophagy inhibition and with a sledge-hammer of acute amino acid starvation, impacts translation rates on both a global and mRNA by mRNA basis. Overall, I found that these stresses do not repress translation as expected, indicating the identification of novel mechanisms of protein translation regulation.

The majority of my thesis focused on the role of autophagy in regulating protein translation. Autophagy, a cellular sorting, degradation and recycling system, is crucial for the survival of cells under stress and has been demonstrated to play a role in the progression of many human diseases, including cancer and neurodegeneration. By promoting protein degradation, autophagy is proposed to maintain amino acid pools to sustain protein synthesis during metabolic stress. I utilized ribosome profiling to delineate the effects of acute genetic ablation of autophagy on protein translational control. Instead of shaping overall global rates of cap dependent translation, autophagy supports the translation of specific mRNAs, most notably targets involved in cell cycle control and DNA damage repair, by modulating the availability of RNA binding proteins

to interact with mRNAs. Specifically, by enabling the protein translation of the DNA damage repair protein BRCA2, autophagy is functionally required to attenuate DNA damage as well as promote cell survival in response to PARP inhibition. This helps to explain the reported increased DNA damage in autophagy deficient cells, and is an important consideration for autophagy inhibitors as adjuvant chemotherapies, which are being tested now.

I have also uncovered a novel mechanism of protein translation regulation following acute amino acid starvation. Although mTORC1 signaling indicates repressed translation, ³⁵S-methionine incorporation rates more than double following amino acid withdrawal. This increase in translation rates can be prevented by addition of leucine, although the molecular mechanisms controlling this novel process remain to be identified.

Table of contents

Chapter 1	Introduction	1
References	for Introduction	28
Chapter 2	Ribosome profiling reveals specific translational control downstream of the autophagy pathway mediated by RNA binding protein availability	37
References	for Chapter 2	97
Chapter 3	Autophagy regulates the translation of some metabolic genes and immune response genes	100
References	for Chapter 3	118
Chapter 4	Acute starvation induced translation	119
References	for Chapter 4	155
Chapter 5	Autophagy and cancer metabolism	158
References	for Chapter 5	178
Chapter 6	Concluding remarks	183
Appendix A	NBR1 enables autophagy-dependent	186
References	for Appendix A	199
Appendix B	Antitumor adaptive immunity remains intact following inhibition of autophagy and antimalarial treatment	207
References	for Appendix B	220

List of Tables

Chapter 2

Table 1	List of top 30 significant changes assessed by ribosome profiling	69
----------------	---	----

Chapter 4

Table 1	Comparison chart of various acute starvation media	144
Table 2	List of top 30 significantly enriched ribosome occupancies in starved versus fed conditions	145
Table 3	Gene ontology of mRNAs with significantly enriched ribosome occupancy during starvation	146
Table 4	List of top 30 significantly decreased ribosome occupancies in starved versus fed conditions	147
Table 5	Gene ontology of mRNAs with significantly decreased ribosome occupancy during starvation	148

List of Figures

Chapter 1

Figure 1	Overview of mammalian translation initiation	23
Figure 2	Overview of the autophagy trafficking process	25
Figure 3	Chaperone mediated autophagy	26
Figure 4	AMPK and MTORC1 as metabolic regulators of autophagy	27

Chapter 2

Figure 1	Minimal effects of Atg12 genetic deletion on global translation, intracellular amino acid levels, and mTORC1 signaling	57
Figure 2	Ribosome profiling reveals that autophagy supports the translation of proteins required for DNA damage response and cell cycle control	59
Figure 3	Reduced BRCA2 protein translation in autophagy deficient cells	61
Figure 4	The 5'UTR of <i>Brca2</i> determines translational sensitivity to autophagy due to RNA binding protein interactions	63
Figure 5	Decreased BRCA2 levels in Atg12 deleted cells results in increased DNA damage and centrosome abnormalities	65
Figure 6	Atg12 deletion <i>in vivo</i> leads to reduced BRCA2 and increased DNA damage	67
Figure S1	Analysis of Atg deletion in mouse embryonic fibroblasts (related to Figure 1)	70
Figure S2	Ribosome profiling quality control metrics (related to Figure 2)	72
Figure S3	<i>Brca2</i> translation is impaired in autophagy deficient cells	74
Figure S4	The 5'UTR of <i>Brca2</i> determines its translational response to autophagy (related to Figure 4)	75
Figure S5	Autophagy inhibition causes increased DNA damage independent of ROS, and sensitizes cells to PARP inhibitors (related to Figure 5)	78

Chapter 3

Figure 1	mRNAs that had significantly enriched for ribosomes during autophagy inhibition group loosely to genes involved in metabolism	109
-----------------	---	-----

and growth response

Figure 2	Autophagy deleted cells are sensitive to cell cycle inhibitors, not sensitive to CPT inhibitors, under fed conditions	111
Figure 3	The RNA binding protein RBM4 shows striking relocalization in starvation, autophagy deletion	112
Figure 4	Atg12 knockout T-cells have impaired proliferation following stimulation, possibly higher translation rates	114

Chapter 4

Figure 1	Acute starvation induced translation is rapid and sustained in a variety of cell types	135
Figure 2	Canonical markers of translation indicate that protein translation should be attenuated in acute starvation conditions	137
Figure 3	Protein turnover, calcium, glucose, serum, vitamins and non-essential amino acids, do not prevent ASIT	139
Figure 4	L-leucine prevents ASIT	141
Figure 5	Experiments to confirm increased translation rates are inconclusive	143

Chapter 5

Figure 1	Tumor suppressive roles for autophagy in cancer	176
Figure 2	Tumor-promoting roles for autophagy in cancer	177

Appendix A

Figure 1	Impaired migration rate and increased FA size in autophagy deficient cells	189
Figure 2	Autophagy promotes FA turnover in migrating cells	190
Figure 3	Autophagy inhibition results in enhanced cell spreading	191
Figure 4	Autophagosomes associate with dynamic FAs during disassembly	192
Figure 5	NBR1 facilitates cell migration and FA turnover	193
Figure 6	NBR1-mediated selective autophagy promotes FA disassembly	194
Figure S1	Autophagy enables migration of multiple cell types	201

Figure S2	Autophagosomes localize to FAs	202
Figure S3	Regulation of migration and FAs by the autophagy cargo receptor NBR1	203
Figure S4	NBR1 knockdown leads to enhanced cell spreading	204
Figure S5	NBR1 interacts with FA proteins and promotes FA disassembly	205

Appendix B

Figure 1	Genetic models of autophagy deficiency in mouse melanoma and mammary cancers	210
Figure 2	T cell infiltration is unchanged in autophagy-deficient mouse tumors	211
Figure 3	T cell functional status is unchanged in autophagy-deficient mouse tumors	212
Figure 4	Transgenic OT-1 cell activation is unchanged in autophagy-deficient OVA-expressing tumors	214
Figure 5	Dox-treated autophagy-deficient tumors elicit equivalent T cell responses despite altered secretion of immunomodulatory factors	216
Figure 6	Antimalarial-treated tumors exhibit equivalent T cell responses	218
Figure S1	Validation of autophagy deficiency in B16 melanoma and 4T1	222
Figure S2	Representative dot plots of T cell functional markers	223
Figure S3	T cell suppression and activation potential are unchanged in autophagy-deficient mouse tumors	224
Figure S4	Validation of autophagy deficiency in B78-OVA mouse melanoma	226
Figure S5	Autophagy deficient cells are more sensitive to doxorubicin treatment	228

Chapter 1

Introduction

Content in the following chapter includes text modified from:

Autophagy and cancer metabolism by Juliet Goldsmith, Beth Levine and Jayanta Debnath, published in *Methods in Enzymology* in 2014 (PubMed PMID: 24862259).

Contributions: I was primarily responsible for writing the content in the first draft of this manuscript. Jay Debnath supervised this project and Beth Levine provided critical comments. We all edited and revised subsequent drafts.

The complement of proteins in a cell determines what the cell can do – whether that is migrate, activate an inflammatory response, divide or simply survive. What proteins are present in the cell is determined by 1) what proteins are being translated and 2) what proteins are degraded. While transcriptional changes can lead to protein changes on the order of hours, translational regulation can alter which proteins are being produced on the order of minutes, provided the mRNAs are already in the cell. Therefore translational control allows for rapid building of novel proteins to affect proteome homeostasis. Throughout this thesis, I focus on the regulation of protein translation under the stresses of autophagy inhibition and acute starvation. Both were previously assumed to dampen all protein translation, yet we have found evidence to support the contrary.

In this introduction, I outline the mechanisms and key regulators of protein translation and autophagy, and what was currently known about the effect of one on the other.

1. Overview of translation machinery

Eukaryotic protein translation can be divided into three major steps: 1) initiation; 2) elongation; and 3) termination. This section provides a brief overview of the key factors required for each step in mammalian protein translation. There are many excellent reviews that are more comprehensive, and I refer to them throughout each section.

1.1 Initiation

The eIF2 ternary complex is formed by the heterotrimer of eIF2 α , eIF2 β , and eIF2 γ , tRNA charged with methionine and GTP. The GTP in the ternary complex is loaded by the guanine nucleotide exchange factor eIF2B, which exchanges GDP for GTP for each reforming of the ternary complex (Figure 1a). Once the ternary complex is formed, it binds to the 40S ribosomal subunit to form the 43S pre-initiation complex (Figure 1b). It is thought that the pre-initiation complex assembly is stimulated by the initiation factors eIF1, which sits at the E site of the 40S subunit, eIF1A, which sits at the A site of the 40S subunit, and eIF3 which orients around the E side of the 40S subunit. The eIF4F complex, consisting of eukaryotic initiation factors eIF4E, eIF4A, and eIF4G, along with eIF4B are recruited to the m⁷-GTP cap at the distal 5' end of the mRNA and loaded by the hydrolysis of ATP. The eIF4F complex then begins to unwind the secondary structure of the mRNA 5'UTR by helicase activity of eIF4A. The 43S pre-initiation complex and eIF4F bound to the mRNA then interact to form the 48S complex, which begins scanning the 5'UTR for the start codon (Figure 1d, e). When the scanning 48S complex carrying the met-tRNA pairs with the start codon (often an AUG), eIF5 – a GTP activating protein – is recruited and induces eIF2 to hydrolyze its bound GTP, releasing eIF2-GDP from the 48S complex and allowing for the recruitment of the 60S ribosomal subunit and eIF5B-GTP, which displaces eIF2-GDP, eIF5, eIF3, and eIF1 (Figure 1f). When eIF5B hydrolyzes GTP, eIF5B and eIF1A are released and the 80S ribosome is fully assembled and ready for translation elongation¹ (Figure 1g).

1.2 Elongation

Elongation is the most rapid step in translation. The accuracy and efficiency depends greatly on the tRNA amino acid pool, the secondary and tertiary structure of the mRNA, and co-translational protein folding²⁻⁴. Most of elongation relies on the catalytic activity of the ribosome, matching the codon to the tRNA, and fusing the new amino acid onto the peptide chain⁵. There are two elongation factors in eukaryotes, eEF1A and eEF2, which are involved in bringing the aminoacyl-tRNA to the ribosome, and moving the peptidyl-tRNA to the next ribosomal site as the reaction progresses. eEF1A consists of two subunits, α which mediates the entry of charged aminoacyl-tRNAs into the A site of the ribosome and β which acts as a GEF to catalyze the release of GDP from α . eEF1B is the exchange factor that facilitates the cycling of GDP to GTP for eEF1A to be recycled for the next round. Peptide bond formation tilts the tRNAs in the A and P sites towards the P and E sites and eEF2 catalyzes the translocation of the tRNA and mRNA down the ribosome at the end of each round of polypeptide elongation upon the hydrolysis of GTP and release of GDP.

Additionally, hypusinated eIF5A, which depends on the presence of spermidine in the cell, has also been shown to be important for elongation by stimulating the reactivity of the peptidyl-tRNA in the P site with the aminoacyl-tRNA in the A site.

1.3 Termination

When the ribosome encounters a stop codon, the eukaryotic release factor eRF1, which is a tRNA shaped protein that recognizes the termination codons with high affinity, and eRF3, which interacts with the C-terminal end of eRF1 and facilitates the release of the polypeptide from the ribosome with GTP hydrolysis⁶.

2. Regulating translation

The process of translation is very tightly regulated, acting on key proteins throughout the entire process, and along the entire length of the mRNA. This section is by no means a fully comprehensive overview of all of the regulation pathways for translation. Instead, I hope to address some of the major known regulatory pathways and mechanisms that will be alluded to throughout this thesis.

2.1 Signaling pathways down stream of metabolic stimuli

One of the major regulators of protein translation is the availability of energy and amino acids in the cell. Therefore, many nutrient and energy sensing regulatory pathways converge to integrate signals and modulate protein translation. It is thought that many of these pathways converge on mTOR, which is nicknamed the master regulator of protein translation. Of the two mTOR complexes, complex 1 is most well understood, and I will focus on its regulation and role in protein translation. mTOR complex 1 (mTORC1) is a homodimer with five main components: Raptor, mLST8, PRAS40, Deptor, and mTOR. mTORC1 regulates the translational machinery as a whole, but ribosome profiling analysis has shown a preferential regulation of 5'TOP motif mRNAs by mTORC1^{7,8}. mTORC1 phosphorylates S6K and 4EBP1. When 4EBP is dephosphorylated, it binds and sequesters eIF4E, preventing the assembly of the initiation complex. Phosphorylation by mTORC1 on four sites prevents 4EBP from interacting with eIF4E, and allows for cap-dependent translation to proceed. Phosphorylation of S6K by mTORC1 activates its kinase activity, and promotes the phosphorylation of S6, eEF2K and PDCD4. While it is unclear what function phosphorylation of S6 plays in translation, the phosphorylation of eEF2K and PDCD4

are inhibitory and relieve the translational repression that those two proteins play on eEF2 and eIF4A respectively⁹.

Upstream, mTORC1 is regulated by the availability of growth factors, energy and amino acids. For example, activation of IRS1 leads to the kinase cascade of activation through PDK1 and AKT, resulting in the relief of inhibition of mTORC1 by TSC2 phosphorylation. Energy levels can be sensed by AMPK, which can directly phosphorylate and activate TSC2 when the AMP:ATP ratio is high. Amino acid signaling to mTORC1 is a more complex process than the other energy signaling pathways, and it has only in the past ten years that the major regulatory mechanisms have been described. In times of plenty of amino acids, mTORC1 is recruited to the lysosome, which maintains an internal pool of amino acids through lysosomal degradation of proteins and transporters at the membrane surface. The Rag complex Regulator at the lysosomal membrane is activated when there are plenty of amino acids, which recruits mTORC1 to the lysosome surface, bringing mTORC1 into close proximity with its activator Rheb, which maintained in a GTP bound state around the lysosomes. Rheb is necessary for the activation of mTORC1 by all upstream signals, and therefore it is thought that amino acid availability is therefore the limiting factor for all mTORC1 activation¹⁰⁻¹³.

Another key regulator of protein translation that is regulated by the metabolic state of the cell is eIF2 α . When eIF2 α is phosphorylated at serine 51, its affinity for eIF2B is greatly increased so that it is sequestered away from the ternary complex formation and cannot contribute to translation initiation. Phosphorylation of eIF2 α has other significant downstream impacts, regulating stress responses, apoptosis and NF κ B

signaling by promoting the translation of ATF4 and repressing the translation of IKB α ¹⁴–¹⁶. eIF2 α can be phosphorylated by four different kinases in response to different stresses. GCN2 is one of the kinases that phosphorylates eIF2 α in response to amino acid starvation. GCN2 is activated upon the binding of uncharged cognate tRNAs, so that when there is even a single amino acid depletion, GCN2 is activated^{17,18}. Additionally, it is thought that mTORC1 phosphorylates GCN2 on a repressive site, so that when there is an abundance of nutrients sensed by mTORC1, GCN2 is repressed. Other kinases that phosphorylate eIF2 α are PERK, PKR and HRI in response to ER stress, dsRNA and oxidative or heavy metal stress respectively. eIF4E has been demonstrated to be phosphorylated under starvation and stress conditions as well, although the impact that this phosphorylation has on translation is unclear^{19–21}.

2.2 cap versus IRES dependent translation, isoforms of initiation factors

Translation initiation can occur using non-canonical initiation factors and proteins, and these types of initiation may preferentially promote the translation of certain mRNAs over others. Translation initiated at internal ribosome entry sites (IRES) does not require an m⁷GTP cap or many of the same initiation factors. Rather, only eIF3, eIF2 and IRES transactivating factors (ITAFs) are thought to be recruited to specific IRES motifs and recruit the ribosome, although what factors are required seems to depend on the IRES motif. It is thought that IRES-mediated translation occurs when cap-dependent translation initiation is prevented, freeing up ribosomes and initiation factors for IRES mediated initiation²². There are only a few rigorously validated cellular IRES motifs, although there are many putative motifs as well, and the sequences can differ dramatically. Whether the sequence or structure dictates the ability for the motifs to

promote ribosome binding will be able to be identified once more motifs have been validated.

Furthermore, there are multiple isoforms of initiation factors that have unique functions. For example, there are three isoforms of eIF4A: eIF4A1, eIF4A2, and eIF4A3. While all share approximately 90% sequence identity, eIF4A3 has a completely different localization and function in the cell, and while eIF4A1 and eIF4A2 can compensate for each other *in vitro*, they appear to have distinct roles *in vivo*²³. eIF4G1 and eIF4G3 seem to be able to functionally compensate for each other, but eIF4G2 promotes distinct mRNA translation^{24,25}. There are many other similar proteins to eIF4G that can alternately impact protein translation. Three isoforms of eIF4E exist. eIF4E1 is tumor promoting²⁶, eIF4E2 is activated during hypoxia²⁷ and its upregulation can be tumor promoting²⁸, yet eIF4E3 acts as a tumor suppressor²⁹. Additionally, phosphorylation of eIF4E seems to direct distinct programs of translational control, which impacts cancer progression^{20,30}.

2.3 Ribosome specificity

Another layer of control on translation is dependent on the pool of ribosomes available. Specialized ribosomes comprised of different and unique sets of ribosomal subunits may also direct which mRNA transcripts are translated in space and time^{31,32}. For example RPL38 containing ribosomes regulate HOX mRNA translation³³. The specific levels of control are only now being elucidated.

2.4 5'UTR structure, modifications (m⁶A) and RNA binding proteins

The sequence and structure of the 5'UTR of mRNAs can have a dramatic impact on their translation efficiency³⁴. Multiple start codons can lead to stalling or truncated and unproductive proteins, for example in the case of ATF4 translation. A 5'UTR that has a low folding energy (ie a high amount of secondary structure) relies more on the action of eIF4A, and therefore is dependent on the availability of the helicase for translation initiation^{35–38}. Addition of the modification m⁶A on the 5'UTR by a m⁶A methyltransferase like METTL3 can promote cap independent translation^{39,40}, or direct specific responses such as regulating the translation of DNA repair genes in response to UV damage⁴¹, or promoting the heat shock response⁴². Lastly, RNA binding motifs within the 5'UTR sequence can lead to the binding RNA binding proteins (RBPs), of which there are many in the cell⁴³. RBPs can promote or inhibit translation, as well as regulate mRNA stability, splicing, and localization^{44,45}. For example, Musashi-1 (MSI1) has been shown to translationally repress p21 and NUMB in kidney cells⁴⁶, but can promote the translation of Dnmt and GLD2 in *Xenopus* oocytes – whether these functions are maintained in mammalian cells is unknown^{47,48}. Another RBP, RBM4, is activated during arsenite stress and hypoxic stress to repress cap-dependent translation and promote IRES mediated translation in an *in vitro* assay^{27,49}, while under normal conditions it is involved in alternative splicing⁵⁰.

2.5 Elongation factors

eEF2 can be phosphorylated in mammalian cells by the protein kinase eEF2K, which impairs translation by preventing eEF2 from binding to the ribosome. The requirement of eIF5A function on the post-translational modification of hypusine means

that mammalian cells are dependent on the availability of spermidine for efficient translation.

2.6 3'UTR, miRNA and polyA tails

The mRNA when initiating translation is thought to form a lariat structure, where the polyA tail is brought into close proximity to the cap. polyA binding protein (PABP) interacts with eIF4G and eIF4E and has been demonstrated to enhance translation initiation, and in some cases has been shown to be essential. Because of the significant enhancement that PABP can play in the translation initiation of some mRNAs, any RNA binding proteins that associates with the 3'UTR and disrupts PABP binding or lariat formation, can decrease translation initiation rates or re-initiation rates following one round of translation. Another mechanism of translational control around the 3'UTR are the binding of miRNAs, which can lead to the suppression of the mRNA translation, whereas binding of miRNAs to the 5'UTR often preferentially leads to mRNA degradation⁵¹⁻⁵³.

3. Overview of the autophagy machinery

The process of macroautophagy occurs in a series of distinct steps: 1) initiation of the isolation membrane; 2) nucleation; 3) elongation of the double-membrane structure to form the autophagosome; and 4) fusion to the lysosome to form an autolysosome, in which the contents are degraded (Figure 2). Studies in yeast have revealed over 30 autophagy-related genes (ATGs) involved in the autophagic trafficking process, many of whose mammalian orthologues have also been identified⁵⁴. This

section provides an overview of the key molecular complexes that comprise the autophagy machinery in mammalian cells – more detailed reviews can be found elsewhere ^{55–57}.

3.1. Initiation and the ULK complex

In mammals, autophagosome initiation requires the ULK complex, which consists of ULK1/2 (orthologous to yeast Atg1) associated with ATG13, FIP200 and ATG101 ⁵⁸ (Figure 2A). At least three different ULK proteins are involved in different aspects of autophagy, among which ULK1 and ULK2 bear highest similarity to yeast Atg1. Under nutrient rich conditions, the ULK complex interacts with MTORC1 and remains inactivated by MTORC1-mediated phosphorylation. However, upon nutrient deprivation, MTORC1 dissociates from the complex resulting in the dephosphorylation of inhibitory sites and concomitant autophosphorylation of activating sites in ULK1 and 2 ⁵⁹. The kinase activation of ULK1 and 2 then leads to the phosphorylation and activation of ATG13 and FIP200 ⁶⁰. The active complex then initiates nucleation by interaction with the Beclin 1/ATG14/VPS34 complex.

3.2. Nucleation and Beclin 1/ATG14/VPS34 complex

The formation of autophagosomes requires the activity of the class III phosphatidylinositol 3-kinase (PI3K) VPS34, which is essential for phosphatidylinositol 3-phosphate (PI3P) production during the early stages of phagophore nucleation. VPS34 forms a complex with the yeast Atg6 orthologue Beclin 1, ATG14L, and VPS15/PIK3R4 (p150) ^{61,62}. Various binding partners of Beclin 1 have been identified (Figure 2B), including UVRAG ^{62,63}, ATG14L/Barkor ^{61,64}, and AMBRA1 ⁶⁵, all of which positively regulate Beclin 1 activity. Notably, ATG14L plays a critical role in specifying the site of

the VPS34 complex relocation and therefore phagophore nucleation⁶⁴. UVRAG also interacts with SH3GLB1/Bif-1 (an N-BAR domain protein), which potentially leads to phagophore membrane curvature, and expedites autophagosome-lysosome fusion^{66,67}. In addition to these positive regulators, other Beclin 1-interacting partners, including BCL-2, BCL-xL, Rubicon (RUN domain and cysteine-rich domain containing, Beclin 1-interacting protein), AKT, and EGFR are negative regulators of the Beclin 1/VPS34 autophagy-promoting complex^{61,64,68–70}. Overall, these studies indicate that multiple class III PI3K complexes exist concurrently within the cell, suggesting that these proteins can exquisitely tune the level of autophagy. Notably, several proteins in this complex have tumor-suppressive or anti-proliferative effects, which are discussed in detail below.

3.3. Elongation and the ATG12/ATG8 conjugation systems

The elongation of the phagophore membrane requires two ubiquitin-like conjugation systems. In the first, ATG7 and ATG10 (E1 and E2-like enzymes respectively) conjugate ATG12 to ATG5. The ATG5-ATG12 complex binds ATG16 and forms a large multimeric complex called the ATG16L complex, which is essential for the elongation of the nascent phagophore (Figure 2C). The second conjugation system involves cleavage of the ubiquitin-like molecule, ATG8, by the protease ATG4 to expose a C-terminal glycine residue required for subsequent activation and conjugation reactions. Several mammalian orthologues of yeast Atg8 have been identified, of which the best characterized is microtubule associated protein 1 light chain 3 (MAP1LC3A or LC3)⁷¹. Atg4 also has 4 mammalian isoforms, although the specificities are not yet known^{72,73}. Ultimately, LC3 is conjugated to the lipid phosphatidylethanolamine (PE)

via ATG7 and E2-like ATG3 and is subsequently recruited to both the outer and inner surfaces of the autophagosomal membrane (Figure 2C). LC3 and other Atg8 family members can mediate membrane tethering and hemifusion, which may be important in fusion of the ends of the phagophore membrane into a closed autophagosome ⁷⁴.

In addition, LC3 is an important mediator for selectively targeting cargo for autophagic degradation. Several ubiquitin-binding proteins have been identified as cargo receptors for autophagy substrates ⁷⁵, including p62/SQSTM1 ⁷⁶, NBR1 ⁷⁷, NDP52 ⁷⁸, and OPTN ⁷⁹. These cargo receptors contain a well-conserved linear amino acid motif called the LIR (LC3-interacting region) that is necessary for specific targeting to the autophagosome. Interestingly, the LIR consensus sequence has been identified in a number of proteins, suggesting that the repertoire of LC3-interacting proteins acting as cargo receptors for selective autophagy may be expansive. In support of this, a large-scale proteomic study demonstrated that the mammalian ATG8 family has 67 high confidence interactions with other cellular proteins ⁸⁰.

3.4. Fusion

After an autophagosome forms, it fuses with the endosome or lysosome where the engulfed components may be recycled. Autophagosomes travel along microtubules, pushed by dynein motor proteins, to lysosomes. Fusion requires ESCRT, SNAREs – specifically syntaxin 17 ⁸¹ -- , VPS family proteins, and RAB7. Fusion to the lysosome is the last step in the degradation of the intra-compartmental components, and impaired lysosome function prevents complete autophagic flux. Hence, lysosomotropic agents such as hydroxychloroquine (HCQ) are used experimentally to inhibit autophagy. These lysosomal inhibitors are proposed to impair autophagosome maturation and flux by

altering the pH of the lysosome; nonetheless, it is important to recognize that these compounds impact a broad array of processes other than autophagy.

3.5. Chaperone-Mediated Autophagy (CMA)

Although this review principally focuses on macroautophagy, it is important to recognize that multiple routes of autophagic degradation exist, including microautophagy, and chaperone-mediated autophagy (CMA)⁸². CMA warrants special attention because of its emerging role in cancer^{83–85}. CMA is a highly selective form of autophagy in which specific proteins are targeted to the lysosome via their interaction with a cytosolic chaperone protein– HSC70– that recognizes and binds to a specific pentapeptide motif – the KFERQ sequence. This interaction leads to binding to the lysosome via a variant of the lysosome-associated membrane protein type 2A (LAMP2A), and after some unfolding, the targeted protein is directly delivered into the lysosome for degradation (Figure 3)^{86–88}. Interestingly, CMA can be induced in mammalian cells when macroautophagy is inhibited and vice versa, indicating that a switch in one type of autophagy can compensate for deficiency in the other^{89,90}.

4. Metabolic stimuli regulating autophagy

Metabolic stresses often occur in solid tumors and the tumor microenvironment – rapidly multiplying tumor cells and tumors that have yet to initiate angiogenic programs often cannot maintain nutrient supply and quickly become hypoxic. To forestall senescence or death, tumor cells metabolically reprogram and engage autophagy to survive in the hostile tumor microenvironment^{91,92}. Metabolites, oxygen concentration

and oncogenes all regulate initiation of autophagosome formation, and the regulation of autophagy is finely balanced by integration of all these signals (Figure 4). In this section, we provide an overview of the regulation of autophagy by specific metabolites and metabolic stressors in tumor cells, focusing on cancer-relevant pathways.

4.1. Nutrient starvation

Autophagy is strongly induced in response to nutrient starvation, which is primarily controlled by mammalian target of rapamycin (MTOR). MTOR was initially identified as a key negative regulator of autophagy in yeast and has been confirmed to function as a major regulator of mammalian autophagy⁹³. MTOR acts as a master sensor of metabolic state; signals from growth factors, amino acids, oxidative stress and DNA damage alter MTOR interactions with binding partners, thereby regulating MTOR activity. Active MTORC1 under nutrient conditions modulates rates of translation, lipid synthesis, mitochondrial proliferation, and phosphorylates ULK1/2 and ATG13 to block autophagy. Under nutrient deprivation, ATG13 and ULK1/2 are dephosphorylated by an unknown phosphatase, leading to autophagosome formation^{60,94–96}.

4.2. Glucose

As noted by Otto Warburg in 1924, cancer cells preferentially utilize glycolysis over oxidative phosphorylation as a source of energy in aerobic conditions. Glycolysis is thought to provide a growth advantage by maintaining intracellular pools of metabolites for anabolism⁹⁷. Therefore, cancer cells are more sensitive to low levels of glucose than non-transformed cells. Low glucose levels induce autophagy in a wide variety of mammalian cell types, and this regulation appears to be partially dependent on the activation of AMPK⁹⁸. AMPK is activated by a high ratio of AMP to ATP⁹³. Under

conditions of low intracellular energy, activated AMPK induces autophagy both by phosphorylating ULK1, resulting in its activation, as well as by inhibiting MTORC1 via phosphorylation of Raptor^{99,100}. During glucose deprivation, AMPK-dependent Beclin 1 phosphorylation activates the pro-autophagy Beclin 1/VPS34 complex¹⁰¹. However, the balance of nutrient availability is crucial for autophagy induction, especially since autophagy is an ATP-consuming process. Under starvation conditions, the addition of glucose (up to a threshold) promotes autophagy via a p38 MAPK-dependent pathway¹⁰².

4.3. Amino acids

Autophagy is inhibited in an MTORC1-dependent manner based on levels of amino acids in the cytoplasm. Amino acids activate Rag GTPases, which promote translocation of MTORC1 to the lysosomal surface, resulting in MTORC1 activation and inhibition of autophagy via ULK1/2. Intra-lysosomal amino acid levels also regulate MTORC1 activity in a vacuolar ATPase-dependent manner, which may function as a means of feedback inhibition of the autophagic process¹¹⁻¹³. Amino acid levels also alter the signalling of the RAS/RAF1/ERK1/2 pathway, which regulates autophagy induction. High amino acid levels inhibit activation of RAF1, which prevents ERK1/2 dependent phosphorylation of Gα interacting protein, resulting in decreased stimulus-induced autophagy in HT-29 intestinal cells¹⁰³⁻¹⁰⁵. Specific amino acids also have distinct effects on autophagy inhibition. Leucine has the strongest inhibitory effect on autophagy. Leucyl t-RNA synthetase, an intracellular leucine sensor, binds to and regulates RagGTP interaction with MTORC1, leading to autophagy inhibition¹⁰⁶.

4.4. Glutamine

When glucose levels are low, cells commonly shift to glutaminolysis to maintain TCA cycle ATP and NADPH production. Ammonia produced during glutaminolysis increases autophagic flux by an MTORC1-independent pathway^{107,108}. Moreover, leucine levels regulate glutamate dehydrogenase (GLUD1) activity which promotes autophagy by inhibiting MTORC1 activity and modulating ROS levels¹⁰⁹. Accordingly, the production of ammonia by GLUD1-mediated oxidative deamination of glutamate to α -ketoglutarate may also regulate autophagy in a similar fashion to ammonia generated from glutaminolysis; however this intriguing hypothesis requires further testing. Moreover, it is important to recognize that glutaminolysis may not always promote autophagy. Indeed, glutamine and leucine together have been reported to activate MTORC1 and therefore inhibit autophagy in a glutaminolysis-dependent manner¹¹⁰, indicating that the regulation of autophagy by glutamine is sensitive to metabolic context. Glutamine depletion was reported to decrease mRNA levels of *Atg5* in wild-type MEFs, supporting the finding that glutaminolysis may promote autophagy¹¹¹.

4.5. Lipids and free fatty acids

In cancer cells, the impact of altered lipid metabolism on autophagy regulation is not as well-defined as that of glucose and glutamine metabolism. Fatty acid synthesis is generally restricted to specific tissues, but is often upregulated in cancers¹¹². Palmitate, the simplest and most abundant fatty acid and the product in fatty acid synthesis, stimulates autophagy in muscle, liver, neurons and pancreatic cells. Palmitate-induced autophagy is mediated by JNK1 activity and PKC activity, and is independent of MTOR,^{113–115}. However, the induction of autophagy may not increase autophagic flux in

pancreatic cells ¹¹⁶, although there is conflicting data about the turnover of long-lived proteins. Further experiments, such as using GFP and mCherry tagged LC3, will clarify this point. Additionally, the autophagic response to fatty acids may be highly tissue specific. In hepatocytes, palmitate was found to promote apoptosis instead of autophagy, while oleate – the most abundant mono-unsaturated fatty acid – was found to promote autophagy via increasing ROS levels ¹¹⁷. The synthetic fatty acid 2-hydroxyoleic acid induced ER stress and autophagy in glioma cell lines but not a control fibroblast cell line, and resulted in glioma cell differentiation ^{118,119}. How 2-hydroxyoleic acid induces ER stress remains unknown. However, it has been shown that excess lipid storage in non-adipose tissue can cause endoplasmic reticulum (ER) stress, which increases autophagy via MTOR, JNK, and increased transcription of autophagy genes ^{120–123}.

4.6. Hypoxia and reactive oxygen species

Hypoxia and reactive oxygen species (ROS), often found in the poorly-vascularised tumor microenvironment, have been shown to increase autophagic flux via several mechanisms. Most directly, reactive oxygen species inhibit ATG4 autophagosome turnover activity, allowing for maintenance of lipidated LC3 necessary for autophagosome formation ¹²⁴. Autophagy is upregulated during hypoxia via hypoxia inducible factor 1 α (HIF1 α) induction of BNIP3 and BNIP3L, which bind to Beclin 1 to promote autophagy ¹²⁵. AMPK promotes autophagy independently of HIF in response to severe hypoxia. While BNIP3-regulated autophagy protects cells from death, AMPK-induced autophagy promotes cell death, pointing to the influence of cellular context on the outcome of autophagy ¹²⁶.

ROS-mediated damage also likely controls autophagy. ROS damages DNA, proteins, and organelles¹²⁷ and accumulated damage and subsequent metabolic stress activate autophagic programs. In addition to starvation, JNK-mediated autophagy induction is often associated with oxidative stress^{128,129}. Stress-activated JNK results in phosphorylation of BCL-2, an anti-apoptotic protein that binds to and inhibits Beclin 1⁶⁸ causing the release of Beclin 1 and autophagy induction¹³⁰. In another indirect mechanism, low oxygen concentrations leads to acidification of the environment, and autophagy is upregulated in response to low pH independent of oxygen concentration¹³¹.

5. Interplay of translation and autophagy

How autophagy can regulate protein translation is an area of active interest. Both protein translation and autophagy are tightly regulated by the metabolic state of the cell, in particular the availability of amino acids. Because protein translation is a highly energy demanding anabolic process and autophagy is a catabolic process, in times of low nutrients protein translation is dampened and autophagic flux is enhanced, both through the regulation of mTOR. It was therefore thought that autophagy could support translation in times of nutrient stress. In support of this hypothesis, in yeast during nitrogen starvation autophagy is required to maintain protein translation¹³². Studies in yeast have also shown that under starvation, autophagy specific to ribosomes termed ribophagy is induced to help promote cell survival^{133,134}. While there are eukaryotic orthologs to the yeast ribophagy genes, evidence of ribophagy in mammalian cells is circumstantial. Furthermore, the autophagy adaptor protein p62, which is degraded

during high autophagic flux, has been shown to be a positive regulator for Rag-dependent activation of mTORC1, indicating that autophagy may indirectly impact protein translation through this mechanism as well¹³⁵.

The molecular links between autophagy and translation of specific mRNAs in the cell are being elucidated and strengthened. One study showed that HIF1 α translation in starvation is dependent on a putative IRES in the 5'UTR of *Hif1 α* and induced macroautophagy, as demonstrated by the dependence on AMPK and p38 signaling, Atg5, and a functioning lysosome¹³⁶. How autophagy directly contributes to this translation is unknown. In Chapter 2, I elucidate some of the mechanisms for how we believe autophagy can regulate the translation of certain mRNAs, although we did not identify HIF1 α as an autophagy-responsive mRNA in our studies.

On the other hand, how autophagy is regulated by translational control has been identified of late, essentially the flip side to the research I present in Chapter 2. The eIF2 α /ATF4 translational stress response upregulates the transcription of many essential autophagy genes in response to leucine starvation¹²³. Furthermore, downstream of eIF2 α phosphorylation, particularly in response to ER stress, eEF2K is activated and induces autophagy¹³⁷. HuD, an RBP, binds to the 3'UTR of Atg5 and promotes translation in pancreatic cells¹³⁸. A recent study found that the translation of Atg3 is controlled by the availability of eIF5A¹³⁹. Another group demonstrated that loss of RACK1 from the ribosomes induces autophagy by increasing Bcl-XL which interacts with Beclin-1 and induces autophagy in a non-canonical manner, although RACK1 loss has also been shown to impair autophagy in a translation independent manner^{140–142}.

Conclusion

These two processes, protein translation and autophagy, regulate the cellular proteome and can rapidly remodel it in response to a variety of stresses. In this thesis, I examine how autophagy and metabolic stress impact protein translation. Chapters 2 and 3 focus on the role that autophagy plays in regulating protein translation under both basal and starvation conditions. In Chapter 2, I present the culmination of the majority of my thesis research: the text for the manuscript submitted and in revision at Developmental Cell. I found that autophagy impacts the translation of specific mRNAs that promote cell cycle control and DNA damage repair. In Chapter 3, I briefly expand upon some additional preliminary findings resulting from the ribosome profiling detailed in Chapter 2, and link these findings to other research from the Debnath lab that is published or in press. Chapter 4 presents novel findings on translational control during acute starvation that is independent of autophagy or mTORC1/2. This chapter chronicles a new translation phenomenon we termed acute starvation induced translation (ASIT), although the mechanisms and significance remain unknown. The results from Chapters 2-4, while not directly tested in cancer models, may have implications for cancer research and therapy as discussed in their respective discussions. Chapter 5 is taken from a review I wrote that is focused on cancer metabolism and how autophagy can support it. In Chapter 6: concluding remarks, I summarize the key findings and attempt to place them in the context of current literature.

Figure 1

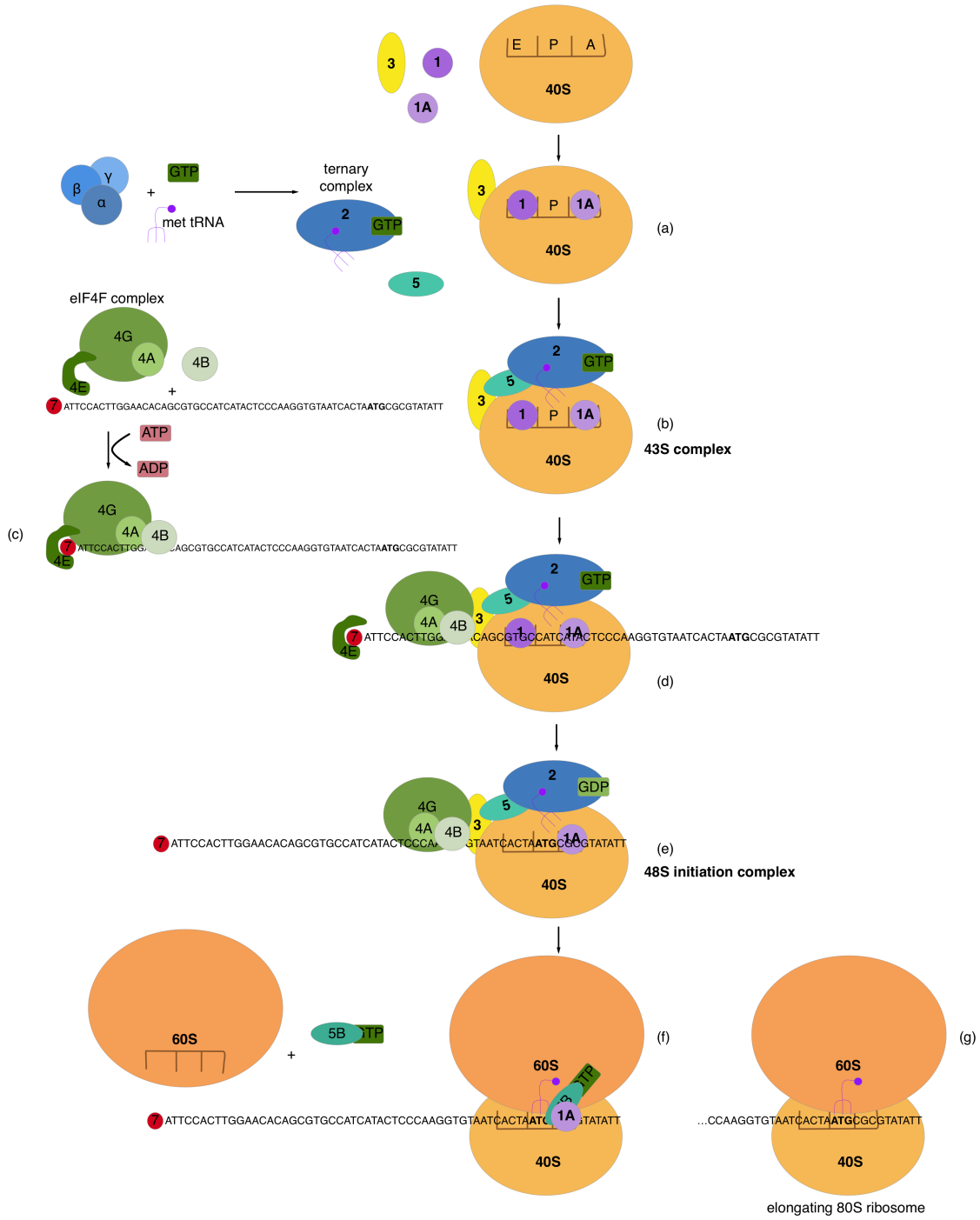


Figure 1: Overview of mammalian translation initiation

Eukaryotic translation initiation is a complex process involving many proteins and complexes. First, a 40S ribosome subunit, with eIF1 and eIF1A in the E and A sites respectively and eIF3 associated (a), interacts with the eIF2 ternary complex to form the 43S preinitiation complex (b). Contemporaneously, the eIF4F complex consisting of eIF4G, eIF4E and eIF4A, interacts with eIF4B at the m⁷-GTP cap of mRNA (c). Then, eIF4F bound to mRNA interacts with the preinitiation complex to attach it to the mRNA 5'UTR (d). The bound 43S subunit scans the mRNA, using the associated helicase activity of eIF4A to unwind secondary structure, until it reaches the initiation codon, at which point the met-tRNA in the ternary complex recognizes the start codon, the scanning complex switches to a "closed" conformation, and eIF1 is displaced, which allows eIF5-mediated hydrolysis of eIF2-bound GTP (e). This is called the 48S initiation complex. Now, the 60S ribosome subunit is recruited, along with eIF5B bound to GTP, which displaces eIF1, eIF2, eIF5, and eIF3 (f). The GTP bound to eIF5B is hydrolysed and eIF5B and eIF1A are released leaving an elongation competent 80S ribosome (g).

Figure 2

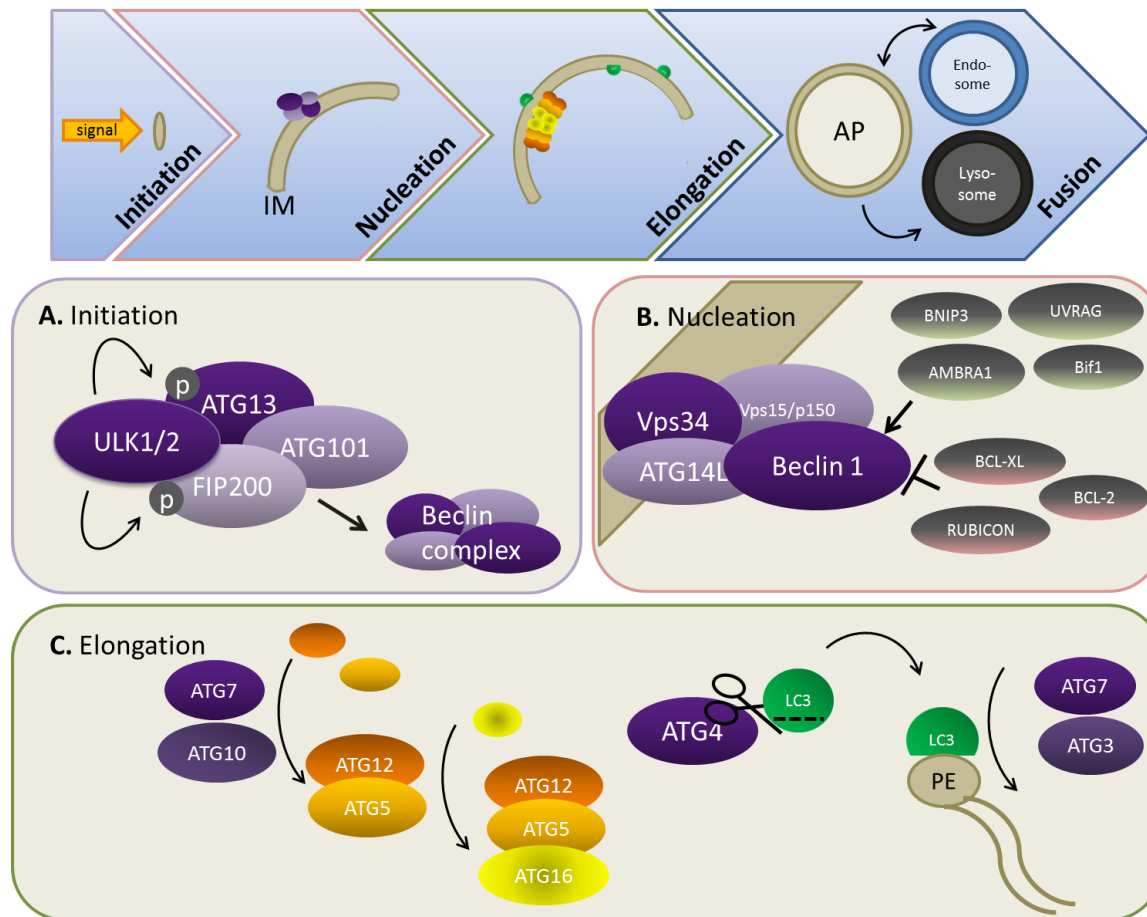


Figure 2: Overview of the autophagy trafficking process

The process of macroautophagy occurs in a series of distinct steps: 1) initiation of the isolation membrane (IM); 2) nucleation; 3) elongation of the double-membrane structure to form the autophagosome (AP); and 4) fusion to endosomes and lysosomes ultimately results in the formation of an autolysosome, in which the contents are degraded. **(A)** Initiation is mediated by the ULK complex. Activation of ULK kinase activity leads to the phosphorylation of FIP200 and ATG13, and initiates nucleation via interaction with the Beclin 1 complex. **(B)** The Beclin 1/VPS34/ATG14/PIK3R4 (p150) complex interacts with multiple interacting partners that positively and negatively regulate Beclin 1/VPS34 lipid kinase activity, resulting in fine-tuning of autophagosome nucleation. **(C)** Elongation requires two ubiquitin-like conjugation pathways that form the ATG12-ATG5/ATG16 complex and phosphatidylethanolamine (PE)-conjugated LC3.

Figure 3

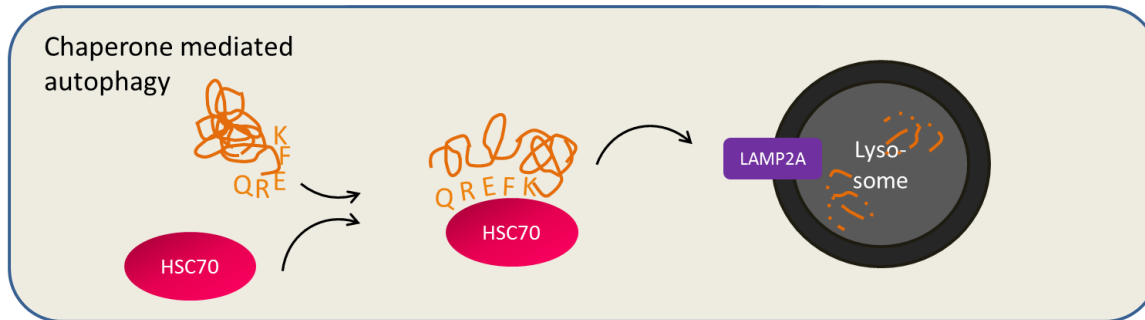


Figure 3: Chaperone mediated autophagy

Chaperone mediated autophagy is an additional route by which proteins are degraded in the lysosome. HSC70 binds to proteins with a KFERQ pentapeptide motif, assists in protein unfolding, and delivers the targeted protein directly to the lysosome for degradation via interaction with lysosome-associated membrane protein type 2A (LAMP2A).

Figure 4

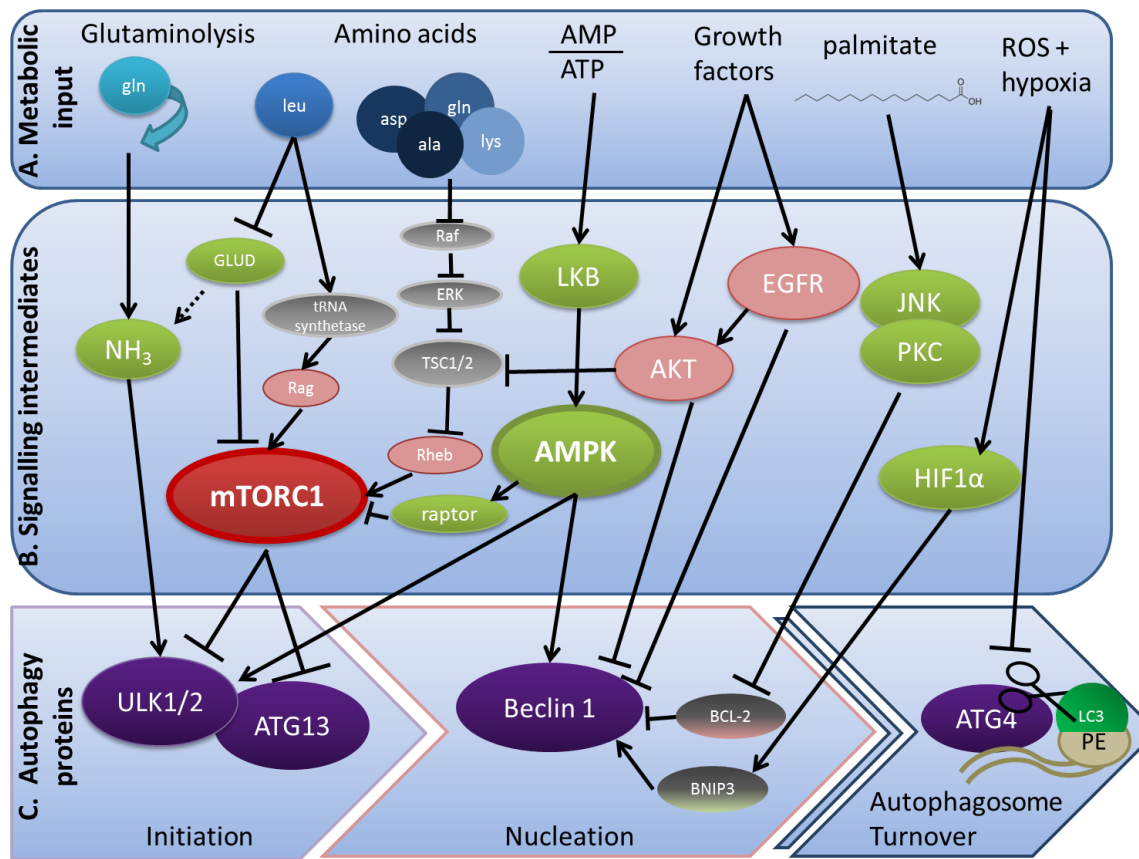


Figure 4: AMPK and MTORC1 as metabolic regulators of autophagy

The control of autophagosome formation and turnover is tightly controlled by many upstream metabolic stimuli. Metabolic input (**A**), such as concentrations of ammonia, general and specific amino acid levels, ATP to ADP ratio and signals of growth and stress such as growth factors, reactive oxygen species, and palmitate, signal to initiate autophagosome formation and inhibit turnover either through signalling intermediates (**B**) or by directly inhibiting or activating key autophagy-related proteins (**C**). AMPK1 and MTOR are principle signalling integrators and modulators of autophagy – they sense glucose and amino acid levels and act on ULK1/2, ATG13 and Beclin 1 to inhibit autophagy in times of plenty, and promote autophagy under energy lean circumstances.

References

1. Jackson, R. J., Hellen, C. U. T. & Pestova, T. V. The mechanism of eukaryotic translation initiation and principles of its regulation. *Nat. Rev. Mol. Cell Biol.* **11**, 113–127 (2010).
2. Gingold, H. & Pilpel, Y. Determinants of translation efficiency and accuracy. *Mol. Syst. Biol.* **7**, 1–13 (2011).
3. Yu, C. H. *et al.* Codon Usage Influences the Local Rate of Translation Elongation to Regulate Co-translational Protein Folding. *Mol. Cell* **59**, 744–754 (2015).
4. Spencer, P. S., Siller, E., Anderson, J. F. & Barral, J. M. Silent substitutions predictably alter translation elongation rates and protein folding efficiencies. *J Mol Biol* **422**, 328–335 (2012).
5. Beringer, M. & Rodnina, M. V. The Ribosomal Peptidyl Transferase. *Mol. Cell* **26**, 311–321 (2007).
6. Dever, T. E. & Green, R. The elongation, termination, and recycling phases of translation in eukaryotes. *Cold Spring Harb. Perspect. Biol.* **4**, 1–16 (2012).
7. Thoreen, C. C. *et al.* A unifying model for mTORC1-mediated regulation of mRNA translation. *Nature* **485**, 109–113 (2012).
8. Hsieh, A. C. *et al.* The translational landscape of mTOR signalling steers cancer initiation and metastasis. *Nature* **485**, 55–61 (2012).
9. Sengupta, S., Peterson, T. R. & Sabatini, D. M. Regulation of the mTOR complex 1 pathway by nutrients, growth factors, and stress. *Mol. Cell* **40**, 310–322 (2010).
10. Settembre, C. *et al.* A lysosome-to-nucleus signalling mechanism senses and regulates the lysosome via mTOR and TFEB. *EMBO J.* **31**, 1095–1108 (2012).
11. Zoncu, R. *et al.* mTORC1 senses lysosomal amino acids through an inside-out mechanism that requires the vacuolar H⁽⁺⁾-ATPase. *Science (80-.).* **334**, 678–683 (2011).
12. Sancak, Y. *et al.* The Rag GTPases bind raptor and mediate amino acid signaling to mTORC1. *Science (80-.).* **320**, 1496–501 (2008).
13. Sancak, Y. *et al.* Ragulator-Rag complex targets mTORC1 to the lysosomal surface and is necessary for its activation by amino acids. *Cell* **141**, 290–303 (2010).
14. Wek, R. C., Jiang, H.-Y. & Anthony, T. G. Coping with stress: eIF2 kinases and translational control. *Biochem. Soc. Trans.* **34**, 7 (2006).
15. Harding, H. P. *et al.* Regulated translation initiation controls stress-induced gene expression in mammalian cells. *Mol. Cell* **6**, 1099–1108 (2000).
16. Deng, J., Lu, P. & Zhang, Y. Translational repression mediates activation of nuclear factor kappa B by phosphorylated translation initiation factor 2. ... *Cell. Biol.* **24**, 10161–10168 (2004).
17. Wek, S. A., Zhu, S. & Wek, R. C. The histidyl-tRNA synthetase-related sequence

- in the eIF-2 alpha protein kinase GCN2 interacts with tRNA and is required for activation in response to starvation for different amino acids. *Mol. Cell. Biol.* **15**, 4497–506 (1995).
18. Zhang, P. *et al.* The GCN2 eIF2alpha Kinase Is Required for Adaptation to Amino Acid Deprivation in Mice. *Mol. Cell. Biol.* **22**, 6681–6688 (2002).
 19. Scheper, G. C. & Proud, C. G. Does phosphorylation of the cap-binding protein eIF4E play a role in translation initiation? *Eur. J. Biochem.* **269**, 5350–5359 (2002).
 20. Robichaud, N. *et al.* Phosphorylation of eIF4E promotes EMT and metastasis via translational control of SNAIL and MMP-3. *Oncogene* 1–11 (2014). doi:10.1038/onc.2014.146
 21. Stead, R. L. & Proud, C. G. Rapamycin enhances eIF4E phosphorylation by activating MAP kinase-interacting kinase 2a (Mnk2a). *FEBS Lett.* **587**, 2623–8 (2013).
 22. Komar, A. a. & Hatzoglou, M. Cellular IRES-mediated translation: The war of ITAFs in pathophysiological states. *Cell Cycle* **10**, 229–240 (2011).
 23. Lu, W.-T., Wilczynska, A., Smith, E. & Bushell, M. The diverse roles of the eIF4A family: you are the company you keep. *Biochem. Soc. Trans.* **42**, 166–172 (2014).
 24. Shatsky, I. N., Dmitriev, S. E., Andreev, D. E. & Terenin, I. M. Transcriptome-wide studies uncover the diversity of modes of mRNA recruitment to eukaryotic ribosomes. *Crit. Rev. Biochem. Mol. Biol.* **49**, 164–77 (2014).
 25. Kaiser, C. *et al.* Activation of cap-independent translation by variant eukaryotic initiation factor 4G in vivo. *RNA* **14**, 2170–2182 (2008).
 26. Ruggero, D. *et al.* The translation factor eIF-4E promotes tumor formation and cooperates with c-Myc in lymphomagenesis. *Nat. Med.* **10**, 484–6 (2004).
 27. Uniacke, J. *et al.* An oxygen-regulated switch in the protein synthesis machinery. *Nature* **486**, 126–9 (2012).
 28. Uniacke, J., Perera, J. K., Lachance, G., Francisco, C. B. & Lee, S. Cancer cells exploit eIF4E2-directed synthesis of hypoxia response proteins to drive tumor progression. *Cancer Res.* **74**, 1379–1389 (2014).
 29. Osborne, M. J. *et al.* eIF4E3 acts as a tumor suppressor by utilizing an atypical mode of methyl-7-guanosine cap recognition. *Proc. Natl. Acad. Sci. U. S. A.* **110**, 3877–82 (2013).
 30. Furic, L. *et al.* eIF4E phosphorylation promotes tumorigenesis and is associated with prostate cancer progression. *Proc. Natl. Acad. Sci. U. S. A.* **107**, 14134–9 (2010).
 31. Xue, S. & Barna, M. Cis-regulatory RNA elements that regulate specialized ribosome activity. *RNA Biol.* **12**, 1083–7 (2015).
 32. Genuth, N. R. & Barna, M. The Discovery of Ribosome Heterogeneity and Its Implications for Gene Regulation and Organismal Life. *Mol. Cell* **71**, 364–374

- (2018).
33. Xue, S. *et al.* RNA regulons in Hox 5'UTRs confer ribosome specificity to gene regulation. *Nature* **2**, 33–38 (2015).
 34. Leppek, K., Das, R. & Barna, M. Functional 5' UTR mRNA structures in eukaryotic translation regulation and how to find them. *Nat. Rev. Mol. Cell Biol.* **19**, 158–174 (2017).
 35. Svitkin, Y. *et al.* The requirement for eukaryotic initiation factor 4A (eIF4A) in translation is in direct proportion to *RNA* 382–394 (2001).
 36. Gandin, V. *et al.* NanoCAGE reveals 5' UTR features that define specific modes of translation of functionally related MTOR-sensitive mRNAs. *Genome Res.* **26**, 636–648 (2016).
 37. Iwasaki, S., Floor, S. N. & Ingolia, N. T. Rocaglates convert DEAD-box protein eIF4A into a sequence-selective translational repressor. *Nature* **534**, 558–561 (2016).
 38. Ringnér, M. & Krogh, M. Folding free energies of 5'-UTRs impact post-transcriptional regulation on a genomic scale in yeast. *PLoS Comput. Biol.* **1**, 0585–0592 (2005).
 39. Meyer, K. D. & Jaffrey, S. R. The dynamic epitranscriptome: N6-methyladenosine and gene expression control. *Nat Rev Mol Cell Biol* **15**, 313–326 (2014).
 40. Meyer, K. D. *et al.* 5' UTR m6A Promotes Cap-Independent Translation. *Cell* 1–12 (2015). doi:10.1038/cr.2014.162
 41. Xiang, Y. *et al.* RNA m6A methylation regulates the ultraviolet-induced DNA damage response. *Nat. Publ. Gr.* **543**, 573–576 (2017).
 42. Zhou, J. *et al.* Dynamic m6A mRNA methylation directs translational control of heat shock response. (2015). doi:10.1038/nature15377
 43. Castello, A. *et al.* Insights into RNA biology from an atlas of mammalian mRNA-binding proteins. *Cell* **149**, 1393–406 (2012).
 44. Glisovic, T., Bachorik, J. L., Yong, J. & Dreyfuss, G. RNA-binding proteins and post-transcriptional gene regulation. **582**, 1977–1986 (2008).
 45. Jung, H., Gkogkas, C. G., Sonenberg, N. & Holt, C. E. Remote Control of Gene Function by Local Translation. *Cell* **157**, 26–40 (2014).
 46. Jadhav, S. *et al.* RNA-binding Protein Musashi Homologue 1 Regulates Kidney Fibrosis by Translational Inhibition of p21 and Numb mRNA. *J. Biol. Chem.* **291**, 14085–14094 (2016).
 47. Rutledge, C. E. *et al.* Efficient translation of Dnmt1 requires cytoplasmic polyadenylation and musashi binding elements. *PLoS One* **9**, (2014).
 48. Cragle, C. & MacNicol, A. M. Musashi protein-directed translational activation of target mRNAs is mediated by the poly(A) polymerase, germ line development defective-2. *J. Biol. Chem.* **289**, 14239–14251 (2014).

49. Lin, J., Hsu, M. & Tarn, W. Cell stress modulates the function of splicing regulatory protein RBM4 in translation control. **104**, 1–6 (2007).
50. Markus, M. A., Yang, Y. H. J. & Morris, B. J. Transcriptome-wide targets of alternative splicing by RBM4 and possible role in cancer. *Genomics* **107**, 138–144 (2016).
51. Valencia-Sanchez, M. A., Liu, J., Hannon, G. J. & Parker, R. Control of translation and mRNA degradation by miRNAs and siRNAs. *Genes Dev.* **20**, 515–524 (2006).
52. Stroynowska-Czerwinska, A., Fiszer, A. & Krzyzosiak, W. J. The panorama of miRNA-mediated mechanisms in mammalian cells. *Cell. Mol. Life Sci.* **71**, 2253–2270 (2014).
53. Fabian, M. R., Sonenberg, N. & Filipowicz, W. Regulation of mRNA Translation and Stability by microRNAs. *Annu. Rev. Biochem.* **79**, 351–379 (2010).
54. Nakatogawa, H., Suzuki, K., Kamada, Y. & Ohsumi, Y. Dynamics and diversity in autophagy mechanisms: lessons from yeast. *Nat. Rev. Mol. Cell Biol.* **10**, 458–67 (2009).
55. Yang, Z. & Klionsky, D. Mammalian autophagy: core molecular machinery and signaling regulation. *Curr. Opin. Cell Biol.* **22**, 124–131 (2010).
56. Klionsky, D. An overview of autophagy: Morphology, mechanism and regulation. *Antioxid. Redox Signal.* 1–39 (2013). doi:10.1089/ars.2013.5371
57. Klionsky, D. & Emr, S. Autophagy as a regulated pathway of cellular degradation. *Science (80-.)*. **290**, 1717–1721 (2000).
58. Mizushima, N. The role of the Atg1/ULK1 complex in autophagy regulation. *Curr. Opin. Cell Biol.* **22**, 132–9 (2010).
59. Chan, E. Y. mTORC1 phosphorylates the ULK1-mAtg13-FIP200 autophagy regulatory complex. *Sci. Signal.* **2**, pe51 (2009).
60. Jung, C. H. *et al.* ULK-Atg13-FIP200 Complexes Mediate mTOR Signaling to the Autophagy Machinery. *Mol. Biol. Cell* **20**, 1992–2003 (2009).
61. Zhong, Y. *et al.* Distinct regulation of autophagic activity by Atg14L and Rubicon associated with Beclin 1-phosphatidylinositol-3-kinase complex. *Nat. Cell Biol.* **11**, 468–76 (2009).
62. Itakura, E., Kishi, C., Inoue, K. & Mizushima, N. Beclin 1 Forms Two Distinct Phosphatidylinositol 3-Kinase Complexes with Mammalian Atg14 and UVRAG. *Mol. Biol. Cell* **19**, 5360–5372 (2008).
63. Liang, C. *et al.* Autophagic and tumour suppressor activity of a novel Beclin1-binding protein UVRAG. *Nat. Cell Biol.* **8**, 688–99 (2006).
64. Matsunaga, K. *et al.* Two Beclin 1-binding proteins, Atg14L and Rubicon, reciprocally regulate autophagy at different stages. *Nat. Cell Biol.* **11**, 385–96 (2009).
65. Fimia, G. M. *et al.* Ambra1 regulates autophagy and development of the nervous

- system. *Nature* **447**, 1121–5 (2007).
66. Liang, C. *et al.* Beclin1-binding UVRAG targets the class C Vps complex to coordinate autophagosome maturation and endocytic trafficking. *Nat. Cell Biol.* **10**, 776–87 (2008).
 67. Takahashi, Y. *et al.* Bif-1 interacts with Beclin 1 through UVRAG and regulates autophagy and tumorigenesis. *Nat. Cell Biol.* **9**, 1142–51 (2007).
 68. Pattingre, S. *et al.* Bcl-2 antiapoptotic proteins inhibit Beclin 1-dependent autophagy. *Cell* **122**, 927–39 (2005).
 69. Wang, R. C. *et al.* Akt-mediated regulation of autophagy and tumorigenesis through Beclin 1 phosphorylation. *Science (80-.)*. **338**, 956–9 (2012).
 70. Wei, Y. *et al.* EGFR-Mediated Beclin 1 Phosphorylation in Autophagy Suppression , Tumor Progression , and Tumor Chemoresistance. *Cell* **154**, 1–16 (2013).
 71. Weidberg, H., Shpilka, T., Shvets, E., Shinder, V. & Elazar, Z. LC3 and GATE-16/GABARAP subfamilies are both essential yet act differently in autophagosome biogenesis. *EMBO* **29**, 1792–1802 (2010).
 72. Li, M. *et al.* Kinetics comparisons of mammalian Atg4 homologues indicate selective preferences toward diverse Atg8 substrates. *J. Biol. Chem.* **286**, 7327–38 (2011).
 73. Shpilka, T., Weidberg, H., Pietrokovski, S. & Elazar, Z. Atg8: an autophagy-related ubiquitin-like protein family. *Genome Biol.* **12**, 226 (2011).
 74. Weidberg, H. *et al.* LC3 and GATE-16 N termini mediate membrane fusion processes required for autophagosome biogenesis. *Dev. Cell* **20**, 444–54 (2011).
 75. Johansen, T. & Lamark, T. Selective autophagy mediated by autophagic adapter proteins. *Autophagy* **7**, 279–296 (2011).
 76. Bjørkøy, G. *et al.* p62/SQSTM1 forms protein aggregates degraded by autophagy and has a protective effect on huntingtin-induced cell death. *J. Cell Biol.* **171**, 603–14 (2005).
 77. Kirkin, V. *et al.* A role for NBR1 in autophagosomal degradation of ubiquitinated substrates. *Mol. Cell* **33**, 505–16 (2009).
 78. Thurston, T. L. M., Ryzhakov, G., Bloor, S., von Muhlinen, N. & Randow, F. The TBK1 adaptor and autophagy receptor NDP52 restricts the proliferation of ubiquitin-coated bacteria. *Nat. Immunol.* **10**, 1215–21 (2009).
 79. Wild, P. *et al.* Phosphorylation of the autophagy receptor optineurin restricts Salmonella growth. *Science* **333**, 228–33 (2011).
 80. Berhends, C., Sowa, M. E., Gygi, S. P. & Harper, J. W. Network organization of the human autophagy system. *Nature* **466**, 68–76 (2010).
 81. Itakura, E., Kishi-Itakura, C. & Mizushima, N. The hairpin-type tail-anchored SNARE syntaxin 17 targets to autophagosomes for fusion with endosomes/lysosomes. *Cell* **151**, 1256–69 (2012).

82. Mizushima, N. Autophagy: process and function. *Genes Dev.* **21**, 2861–73 (2007).
83. Kon, M. *et al.* Chaperone-mediated autophagy is required for tumor growth. *Sci. Transl. Med.* **3**, 109ra117 (2011).
84. Lv, L. *et al.* Acetylation targets the M2 isoform of pyruvate kinase for degradation through chaperone-mediated autophagy and promotes tumor growth. *Mol. Cell* **42**, 719–30 (2011).
85. Vakifahmetoglu-Norberg, H. *et al.* Chaperone-mediated autophagy degrades mutant p53. *Genes Dev.* **27**, 1718–30 (2013).
86. Cuervo, A. M., Terleckyh, S. R., Dice, J. F. & Knecht, E. Selective binding and uptake of ribonuclease A and glyceraldehyde-3-phosphate dehydrogenase by isolated rat liver lysosomes. *J. Biol. Chem.* **269**, 26374–26380 (1994).
87. Koga, H., Martinez-vicente, M., Macian, F., Verkhusha, V. V & Cuervo, A. M. A photoconvertible fluorescent reporter to track chaperone-mediated autophagy. *Nat. Commun.* **2**, (2011).
88. Dice, J. F., Chiang, H., Spencer, E. P. & Backer, J. M. Regulation of Catabolism of Microinjected Ribonuclease A. *J. Biol. Chem.* **261**, 6853–6859 (1986).
89. Massey, A. C., Kaushik, S., Sovak, G., Kiffin, R. & Cuervo, A. M. Consequences of the selective blockage of chaperone-mediated autophagy. *Proc. Natl. Acad. Sci. U. S. A.* **103**, 5805–10 (2006).
90. Wang, Y. *et al.* Loss of macroautophagy promotes or prevents fibroblast apoptosis depending on the death stimulus. *J. Biol. Chem.* **283**, 4766–77 (2008).
91. DeBerardinis, R. J., Lum, J. J., Hatzivassiliou, G. & Thompson, C. B. The biology of cancer: metabolic reprogramming fuels cell growth and proliferation. *Cell Metab.* **7**, 11–20 (2008).
92. Lozy, F. & Karantza, V. Autophagy and cancer cell metabolism. *Semin. Cell Dev. Biol.* **23**, 395–401 (2012).
93. Kroemer, G., Mariño, G. & Levine, B. Autophagy and the integrated stress response. *Mol. Cell* **40**, 280–93 (2010).
94. Neufeld, T. TOR-dependent control of autophagy: biting the hand that feeds. *Curr. Opin. Cell Biol.* **22**, 157–168 (2010).
95. Jung, C. H., Ro, S.-H., Cao, J., Otto, N. M. & Kim, D.-H. mTOR regulation of autophagy. *FEBS Lett.* **584**, 1287–95 (2010).
96. Zoncu, R., Efeyan, A. & Sabatini, D. M. mTOR: from growth signal integration to cancer, diabetes and ageing. *Nat. Rev. Mol. Cell Biol.* **12**, 21–35 (2011).
97. Vander Heiden, M. G., Cantley, L. C. & Thompson, C. B. Understanding the Warburg effect: the metabolic requirements of cell proliferation. *Science (80-)*. **324**, 1029–33 (2009).
98. Williams, T., Forsberg, L. J., Viollet, B. & Brenman, J. E. Basal autophagy induction without AMP-activated protein kinase under low glucose conditions. *Autophagy* **5**, 1155–65 (2009).

99. Kim, J., Kundu, M., Viollet, B. & Guan, K.-L. AMPK and mTOR regulate autophagy through direct phosphorylation of Ulk1. *Nat. Cell Biol.* **13**, 132–41 (2011).
100. Mihaylova, M. M. & Shaw, R. J. The AMPK signalling pathway coordinates cell growth, autophagy and metabolism. *Nat. Cell Biol.* **13**, 1016–23 (2011).
101. Kim, J. *et al.* Differential regulation of distinct Vps34 complexes by AMPK in nutrient stress and autophagy. *Cell* **152**, 290–303 (2013).
102. Moruno-Manchón, J. F., Pérez-Jiménez, E. & Knecht, E. Glucose induces autophagy under starvation conditions by a p38 MAPK-dependent pathway. *Biochem. J.* **449**, 497–506 (2013).
103. Gozuacik, D. & Kimchi, A. Autophagy as a cell death and tumor suppressor mechanism. *Oncogene* **23**, 2891–906 (2004).
104. Pattingre, S., Bauvy, C. & Codogno, P. Amino acids interfere with the ERK1/2-dependent control of macroautophagy by controlling the activation of Raf-1 in human colon cancer HT-29 cells. *J. Biol. Chem.* **278**, 16667–74 (2003).
105. Ogier-Denis, E., Pattingre, S., El Benna, J. & Codogno, P. Erk1/2-dependent phosphorylation of Galpha-interacting protein stimulates its GTPase accelerating activity and autophagy in human colon cancer cells. *J. Biol. Chem.* **275**, 39090–5 (2000).
106. Han, J. M. *et al.* Leucyl-tRNA synthetase is an intracellular leucine sensor for the mTORC1-signaling pathway. *Cell* **149**, 410–24 (2012).
107. Eng, C. H., Yu, K., Lucas, J., White, E. & Abraham, R. T. Ammonia derived from glutaminolysis is a diffusible regulator of autophagy. *Sci. Signal.* **3**, ra31 (2010).
108. Cheong, H., Lindsten, T. & Thompson, C. B. Autophagy and Ammonia. *Autophagy* **8**, 122–123 (2012).
109. Lorin, S. *et al.* Glutamate dehydrogenase contributes to leucine sensing in the regulation of autophagy. *Autophagy* **9**, 850–60 (2013).
110. Durán, R. V *et al.* Glutaminolysis activates Rag-mTORC1 signaling. *Mol. Cell* **47**, 349–58 (2012).
111. Lin, T. *et al.* Resetting glutamine-dependent metabolism and oxygen consumption Autophagy. *Autophagy* **8**, 1477–1493 (2012).
112. Santos, C. R. & Schulze, A. Lipid metabolism in cancer. *FEBS J.* **279**, 2610–23 (2012).
113. Tan, S. H. *et al.* Induction of autophagy by palmitic acid via protein kinase C-mediated signaling pathway independent of mTOR (mammalian target of rapamycin). *J. Biol. Chem.* **287**, 14364–76 (2012).
114. Martino, L. *et al.* Palmitate activates autophagy in INS-1E β -cells and in isolated rat and human pancreatic islets. *PLoS One* **7**, e36188 (2012).
115. Komiya, K. *et al.* Free fatty acids stimulate autophagy in pancreatic β -cells via JNK pathway. *Biochem. Biophys. Res. Commun.* **401**, 561–7 (2010).

116. Las, G., Serada, S. B., Wikstrom, J. D., Twig, G. & Shirihai, O. S. Fatty acids suppress autophagic turnover in β -cells. *J. Biol. Chem.* **286**, 42534–44 (2011).
117. Mei, S. *et al.* Differential roles of unsaturated and saturated fatty acids on autophagy and apoptosis in hepatocytes. *JPET* **339**, 487–498 (2011).
118. Marcilla-Etxenike, A. *et al.* 2-Hydroxyoleic acid induces ER stress and autophagy in various human glioma cell lines. *PLoS One* **7**, e48235 (2012).
119. Terés, S. *et al.* 2-Hydroxyoleate, a nontoxic membrane binding anticancer drug, induces glioma cell differentiation and autophagy. *Proc. Natl. Acad. Sci. U. S. A.* **109**, 8489–94 (2012).
120. Tomohiro, Y. & Klionsky, D. J. Endoplasmic reticulum stress: a new pathway to induce autophagy. *Autophagy* **3**, 160–162 (2007).
121. Qin, L., Wang, Z., Tao, L. & Wang, Y. ER stress negatively regulates AKT/TSC/mTOR pathway to enhance autophagy. *Autophagy* **6**, 239–47 (2010).
122. Ogata, M. *et al.* Autophagy is activated for cell survival after endoplasmic reticulum stress. *Mol. Cell. Biol.* **26**, 9220–31 (2006).
123. B'chir, W. *et al.* The eIF2 α /ATF4 pathway is essential for stress-induced autophagy gene expression. *Nucleic Acids Res.* **41**, 7683–99 (2013).
124. Scherz-Shouval, R. *et al.* Reactive oxygen species are essential for autophagy and specifically regulate the activity of Atg4. *EMBO J.* **26**, 1749–60 (2007).
125. Bellot, G. *et al.* Hypoxia-induced autophagy is mediated through hypoxia-inducible factor induction of BNIP3 and BNIP3L via their BH3 domains. *Mol. Cell. Biol.* **29**, 2570–81 (2009).
126. Papandreou, I., Lim, a L., Laderoute, K. & Denko, N. C. Hypoxia signals autophagy in tumor cells via AMPK activity, independent of HIF-1, BNIP3, and BNIP3L. *Cell Death Differ.* **15**, 1572–81 (2008).
127. Wellen, K. E. & Thompson, C. B. Cellular metabolic stress: considering how cells respond to nutrient excess. *Mol. Cell* **40**, 323–32 (2010).
128. Eisenberg-Lerner, A. & Kimchi, A. DAP kinase regulates JNK signaling by binding and activating protein kinase D under oxidative stress. *Cell Death Differ.* **14**, 1908–15 (2007).
129. Kang, R., Zeh, H. J., Lotze, M. T. & Tang, D. The Beclin 1 network regulates autophagy and apoptosis. *Cell Death Differ.* **18**, 571–80 (2011).
130. Wei, Y., Pattingre, S., Sinha, S., Bassik, M. & Levine, B. JNK1-mediated phosphorylation of Bcl-2 regulates starvation-induced autophagy. *Mol. Cell* **30**, 678–88 (2008).
131. Wojtkowiak, J. W. *et al.* Chronic autophagy is a cellular adaptation to tumor acidic pH microenvironments. *Cancer Res.* **72**, 3938–47 (2012).
132. Onodera, J. & Ohsumi, Y. Autophagy is required for maintenance of amino acid levels and protein synthesis under nitrogen starvation. *J. Biol. Chem.* **280**, 31582–6 (2005).

133. Kraft, C., Deplazes, A., Sohrmann, M. & Peter, M. Mature ribosomes are selectively degraded upon starvation by an autophagy pathway requiring the Ubp3p/Bre5p ubiquitin protease. *Nat. Cell Biol.* **10**, 602–10 (2008).
134. Beau, I., Esclatine, A. & Codogno, P. Lost to translation: when autophagy targets mature ribosomes. *Trends Cell Biol.* **18**, 311–4 (2008).
135. Duran, A. *et al.* Article p62 Is a Key Regulator of Nutrient Sensing in the mTORC1 Pathway. *Mol. Cell* **44**, 134–146 (2011).
136. Wu, C., Huang, D. & Lin, W. Beclin-1-independent autophagy positively regulates internal ribosomal entry site-dependent translation of hypoxia-inducible factor 1 α under nutrient deprivation. *Oncotarget* **5**, (2014).
137. Py, B. F., Boyce, M. & Yuan, J. A critical role of eEF-2K in mediating autophagy in response to multiple cellular stress. *Autophagy* **5**, 393–396 (2009).
138. Kim, C. *et al.* The RNA-binding Protein HuD Regulates Autophagosome Formation in Pancreatic β Cells by Promoting Autophagy-related Gene 5 Expression *. **289**, 112–121 (2014).
139. Lubas, M. *et al.* eIF 5 A is required for autophagy by mediating ATG 3 translation. 1–17 (2018). doi:10.15252/embr.201846072
140. Kim, H. D., Kong, E., Kim, Y., Chang, J. & Kim, J. RACK1 depletion in the ribosome induces selective translation for non-canonical autophagy. **8**, e2800-10 (2017).
141. Erbil, S. *et al.* RACK1 Is an Interaction Partner of ATG5 and a Novel Regulator of Autophagy *. *J. Biol. Chem.* **291**, 16753–16765 (2016).
142. Zhao, Y., Wang, Q., Qiu, G. & Zhang, W. J. RACK1 Promotes Autophagy by Enhancing the Atg14L-Beclin 1-Vps34-Vps15 Complex Formation upon Phosphorylation by AMPK Article RACK1 Promotes Autophagy by Enhancing the Atg14L-Beclin 1-Vps34-Vps15 Complex Formation upon Phosphorylation by AMPK. *CellReports* **13**, 1407–1417 (2015).

Chapter 2

Ribosome profiling reveals specific translational control downstream of the autophagy pathway mediated by RNA-binding protein availability

This chapter is a manuscript currently in revision.

Contributions: I performed the experiments, analyzed and visualized the data, and wrote the initial drafts with the following contributions: Conceptualization, Juliet Goldsmith and Jayanta Debnath; Writing – Review and Editing, Jayanta Debnath, Timothy Marsh, Saurabh Asthana and Adam Olshen; Software for the ribosome profiling analysis (Babel), Saurabh Asthana and Adam Olshen; Resources, Timothy Marsh and Deepthisri Suresh provided tissue lysate from Atg12^{ff} and Atg12^{KO} mice, Andrew M Leidal provided plasmids for overexpression of myc-tagged LC3 family members, Adam Olshen and Saurabh Asthana assisted with ribosome profiling analysis; Funding Acquisition, Jayanta Debnath, Adam Olshen; Supervision, Jayanta Debnath.

Summary

By promoting protein degradation, autophagy is proposed to maintain amino acid pools to sustain protein synthesis during metabolic stress. To date, the impact of the autophagy pathway on the protein translational landscape in mammalian cells remains unclear. Here, we utilize ribosome profiling to delineate the effects of acute genetic ablation of autophagy on protein translational control. Instead of shaping overall global rates of cap dependent translation, autophagy supports the translation of specific mRNAs, most notably targets involved in cell cycle control and DNA damage repair, by modulating the availability of RNA binding proteins, such as MSI1 and eIF4A1, to interact with mRNAs. Specifically, by enabling the protein translation of the DNA damage repair protein BRCA2, autophagy is functionally required to attenuate DNA damage as well as promote cell survival in response to PARP inhibition. Overall, our findings illuminate new roles for autophagy in mammalian cell fate by directing the protein translational landscape.

Introduction

Autophagy, a cellular recycling system that degrades proteins and organelles by delivery to the lysosome, promotes cell survival and fitness in response to metabolic and oxidative stress¹. At the same time, protein translation is tightly regulated by the metabolic state of the cell. The Rag complex senses lysosomal amino acid levels and signals through mTORC1 to regulate cap dependent protein translation^{2,3}. Upon amino acid starvation, reduced mTOR signaling attenuates global cap-dependent protein translation, while concurrently inducing autophagy^{4,5}. Accordingly, in starving cells and tissues, autophagy-mediated recycling of amino acids is proposed to sustain residual translation of proteins, in particular those necessary for survival and metabolic adaptation during starvation or stress. In support, studies in *Saccharomyces cerevisiae* demonstrate autophagy is crucial to maintain protein translation during nitrogen starvation⁶. However, in mammalian cells, it remains unclear whether autophagy similarly impacts protein translation, either in nutrient replete or starvation conditions.

Here, we utilize ribosome profiling to dissect how the autophagy pathway impacts the translational landscape, both at baseline and in response to starvation. We uncover a more nuanced role for autophagy than modulating overall protein translation rates in mammalian cells. Abolishing autophagy does not globally suppress cap-dependent or IRES-dependent translation during nutrient stress. Instead, autophagy regulates specific translational programs involved in DNA repair, centrosome clustering and cell cycle control. Furthermore, the reduced translation of these targets is not associated with the impaired recycling of amino acids; rather, autophagy supports a specific subset of the transcriptome via modulating availability of RNA binding proteins, such as MSI1 and

eIF4A1. Our studies also more specifically demonstrate that autophagy enables the translation of the DNA damage repair gene *Brca2*, resulting in diminished levels of BRCA2 and increased DNA damage in autophagy deficient cells, which can be rescued upon ectopically enforcing BRCA2 expression. We propose that autophagy is required for the efficient translation of proteins necessary for DNA damage repair and cell cycle fidelity.

Results

Acute autophagy deletion minimally impacts intracellular amino acid levels and global translation rates

Atg12 is an essential autophagy gene required for the elongation of the double membrane structure during autophagosome formation^{7,8}. To limit the effects of long-term adaption due to the lack of autophagy in mammalian cells, we created a cell culture model for rapid and efficient *Atg12* deletion. SV40 large T antigen immortalized mouse embryonic fibroblasts (MEF) homozygous for *Atg12* floxed alleles⁹, and heterozygous for the Cre^{ER} allele driven from the ubiquitous Cag promoter (*Atg12^{ff}; Cag-Cre^{ER}*), were treated with 4-hydroxytamoxifen (4OHT), resulting in ablation of *Atg12* and robust autophagy inhibition. Within 2d, the null allele was detectable by PCR (Figure S1A), and after 5d, no detectable *Atg12* protein was found by immunoblotting. Lipidation and lysosomal turnover of LC3 (LC3-II) was profoundly attenuated in *Atg12^{KO}* cells, resulting in the accumulation of the autophagy cargo receptor, p62/SQSTM1 (Figure S1B). For subsequent studies, we analyzed *Atg12^{KO}* cells at 5d following 4OHT treatment.

First, we assessed the effect of autophagy loss on overall global protein translation, using a ^{35}S methionine incorporation assay. Cells were starved for 2h in Hanks Buffered Saline Solution (HBSS), a serum free, amino acid free saline solution containing glucose. This brief starvation period induces autophagy but precedes major transcriptional changes associated with starvation¹⁰ (Figure S1C). We found no differences in ^{35}S methionine incorporation in Atg12^{KO} cells compared to control (Atg12^{ff}) cells, in either fed or starved conditions (Figure 1A, B). Similar results were observed in a broader array of immortalized MEFs lacking various autophagy regulators, including Atg12 , Atg5 , Atg7 or Atg3 (Figure S1D) as well as in primary MEFs lacking Atg12 (Figure S1E). Hence, the genetic loss of autophagy does not acutely impact *de novo* protein synthesis in mammalian cells.

In parallel, we measured whether Atg12 deletion impacts intracellular free amino acid levels, and found minimal differences between Atg12^{ff} and Atg12^{KO} MEFs in both nutrient-rich conditions and following HBSS starvation for up to 2h (Figure 1C). Only two amino acids, glutamine and glycine, were decreased in Atg12^{KO} cells compared to controls grown in nutrient-rich full media conditions (Figure S1F, G), and upon starvation, the only amino acid lost more rapidly in Atg12^{KO} cells was glutamic acid (Figure S1H). Notably, Atg12^{KO} cells exhibited increased levels of oxoproline during starvation (Figure S1I), suggesting low glutamine levels may be due to reduced extracellular glutamine uptake through the gamma-glutamyl cycle. Interestingly, essential amino acids, including the branched chain amino acids (leucine, isoleucine and valine), serine and threonine all exhibited higher measured levels in Atg12^{KO} cells compared to controls at baseline (Figure S1J-N). Although arginine is not discernible by

this technique, hydroxylamine levels were higher at baseline in the Atg12^{KO} starved cells, suggesting arginine metabolism in the autophagy deleted cells may be enhanced (Figure S1O). Although autophagy is proposed to sustain *de novo* protein translation by recycling amino acids, these results indicate that intracellular levels of most amino acids remain intact in autophagy deficient cells following short-term nutrient starvation.

Next, we investigated the effects of autophagy inhibition on mTORC1, which regulates the translation of mRNAs containing TOP motifs including translational machinery¹¹, and is considered a master regulator of cell growth and protein translation¹². Downstream markers of mTORC1 activation, phosphorylation of 4EBP1 at Ser65 and ribosomal protein S6 at Ser240 and 244, demonstrated that mTORC1 activity was robustly inhibited following HBSS starvation. No significant differences in mTORC1 activity between autophagy competent and deficient cells were observed, either in fed or starved conditions (Figure 1D-F), and no differences in the rates of mTORC1 signaling pathway attenuation were detected over 24h of starvation¹³ (Figure 1H).

The availability of translation initiation factors or variant isoforms can regulate the rate of translation and impact which mRNAs are translated¹⁴⁻¹⁶. Initiation factor 2-alpha (eIF2 α) phosphorylation, which represses cap-dependent global translation¹⁷, was slightly increased (Figure 1D, G). However, there was no difference in the ratio of IRES-dependent to cap-dependent translation between Atg12^{ff} and Atg12^{KO} cells using well-characterized viral IRES motifs from cricket paralysis virus (CrPV) (Figure 1I) and Hepatitis C virus (HCV) (Figure S1P). Additionally, we found no changes between Atg12^{ff} and Atg12^{KO} cells in the binding of the inhibitory factor 4E binding protein (4EBP1) to the m⁷GTP cap (Figure 1J), nor cap interaction abilities of key initiation

factors eIF4E, eIF4G1, or their variants eIF4E2 or eIF4G2, using an m⁷GTP cap-pulldown assay (Figure 1K). Overall, these results indicate that the genetic loss of autophagy in both nutrient replete and short-term starvation conditions does not impact mTORC1 signaling or global protein translation.

Ribosome profiling of autophagy deficient cells reveals translational regulation of specific mRNA transcripts

To more thoroughly understand the role of autophagy on protein translation, we employed ribosome profiling (RP), a sensitive and unbiased technique to identify the changes in the rate of translation of all expressed mRNAs in the context of autophagy deficiency¹⁸. Briefly, translating ribosomes are fixed onto mRNAs by treatment with cycloheximide such that ribosome protected footprints (RPFs) can be isolated, amplified, deep-sequenced, mapped to the transcriptome and normalized to total mRNA levels. Analysis of the sequenced reads was performed using Babel¹⁹.

Atg12^{ff} and Atg12^{KO} cells were compared to each other in full media conditions and after 2h HBSS starvation. Verifying experimental quality and reproducibility between replicates, we found generally equal and low levels of contaminating rRNA reads, RPF versus mRNA count plots were similar, and found a statistically significant correlation (Pearson's) of both the raw values of RNA and RPF counts and the calculated p-values (Figure S2A-C). Substantiating that autophagy does not globally impact protein synthesis, minimal changes in the numbers of RPF counts per mRNA were found between Atg12^{ff} and Atg12^{KO} cells, while RPF counts in starved versus fed Atg12^{ff} cells decreased over all biological replicates (Figure 2A-C). Instead, Atg12

regulated ribosome occupancy on a small subset of mRNAs, both positively and negatively. Analysis of the fold change of RPF counts vs. fold change of mRNA counts per gene revealed general changes in the transcriptional and translational landscape (Figure 2D-F). Statistical significance was assessed at the gene level using Babel; Supplementary Table 1 lists the 30 most significant genes from each comparison.

We functionally grouped genes into two cohorts from significant ribosome occupancy changes between Atg12^{ff} and Atg12^{KO} cells in both fed and starved conditions: those exhibiting increased ribosome occupancy in Atg12^{KO} compared to Atg12^{ff} (Figure 2G), and those exhibiting reduced ribosome occupancy in Atg12^{KO} cell compared to Atg12^{ff} (Figure 2H). Among the cohort of targets exhibiting reduced ribosome occupancy in Atg12^{KO} cells, gene ontology (GO) analysis corroborated significant enrichment of genes involved in cell cycle control and chromosome organization (Figure S2D). In contrast, no significant differences in biological processes were evident in the cohort displaying increased ribosome occupancy in Atg12^{KO} cells.

These translational changes correlated with slowed cell cycle progression. Atg12^{KO} cells exhibited slower growth rates compared to the Atg12^{ff} cells in full media (Figure 2I) and a significantly decreased percentage of cells in G1 in an unsynchronized population (Figure 2J). Compared to controls, both Atg12^{KO} MEFs and MEFs subject to acute pharmacological autophagy inhibition using Spautin-1, chloroquine or the Uik1 inhibitor SBI-0206965, exhibited a higher percentage of phospho-Histone H3 (pH3) positive cells (Figure 2K-M, S2F) and higher pH3 protein levels (Figure 2N, O), consistent with increased time in mitosis. Upon synchronizing cells with a double thymidine block, and monitoring time through various stages of the cell cycle by

propidium iodide staining following release, Atg12^{KO} cells progressed more slowly through S-phase and G2/M than Atg12^{ff} cells (Figure 2P). We postulate that translation of cell cycle control mRNAs may represent an important consequence of enhanced autophagic flux observed during early mitosis and S phase²⁰.

Autophagy promotes the translation of BRCA2

In addition to targets involved in cell cycle control, several genes with significantly lower ribosome occupancy in Atg12^{KO} cells regulated DNA damage, a process previously linked to autophagy²¹. We focused on the function of autophagy to enable the translation of *Brca2*, a statistically significant hit in our RP analysis. BRCA2, commonly deleted in heritable breast cancer, functions in DNA double strand break repair and centrosome clustering. Atg12^{KO} cells exhibited reduced BRCA2 protein levels compared to controls in both fed and starved conditions (Figure 3A, B). Corroborating that reduced levels of BRCA2 arose from defective autophagy, not a unique, non-autophagic function of Atg12, we observed lower steady state BRCA2 protein levels in Atg5 deleted and Atg7 depleted MEFs (Figure 3C, D). In addition, CRISPR engineered HEK293T cells lacking Atg7, Atg14, and Atg12 exhibited lower steady state BRCA2 protein levels (Figure 3E, F), indicating that autophagy dependent control of BRCA2 is not limited to fibroblasts.

We next assessed if these lower BRCA2 steady state protein levels were due to reduced translation. We found no significance differences between Atg12^{ff} and Atg12^{KO} MEFs in either *Brca2* mRNA levels (Figure 3G) or in BRCA2 protein stability or turnover following cycloheximide treatment (Figure 3H, I), which did not impact autophagic flux

(Figure S3A). Consistent with decreased ribosome occupancy on *Brca2* in autophagy deficient cells, a decreased proportion of *Brca2* mRNA was present in a high polysome fraction (fraction 9) in Atg12^{KO} HEK293T cells compared to control (Figure S3B). Furthermore, we labeled newly synthesized protein in cells with azidohomoalanine (AHA), a methionine analog that can be conjugated to biotin, and pulled down BRCA2 to monitor the rate of label incorporation. We observed impaired label incorporation in the Atg12^{KO} cells compared to the scramble control cells (Figure 3J-K). Overall, these results demonstrate efficient *Brca2* translation requires an intact autophagy pathway.

Autophagy modulates the availability of RNA binding proteins to bind to the 5'UTR of *Brca2*

The untranslated regions (UTRs) of mRNAs function as important regulators of translational efficiency; 5'UTRs can contain upstream open reading frames and motifs to interact with various RNA binding proteins (RBPs), while the 3'UTR RBP binding and miRNA motifs²².

We interrogated whether the *Brca2* 5' and 3' UTRs mediated translational control downstream of autophagy. A green fluorescent protein (GFP) reporter was transiently overexpressed in the Atg12^{ff} or Atg12^{KO} MEFs alone or flanked by the 5' UTR or 3'UTR of *Brca2*, individually and in combination. GFP protein levels were decreased in the presence of the 5'UTR of *Brca2*, but not the 3'UTR, in Atg12^{KO} compared to Atg12^{ff} cells, despite equivalent *Gfp* expression (Figure 4A, Figure S4A). Moreover, utilizing nano-luciferase reporters to quantitatively measure the effects of *Brca2* UTRs, we observed significantly decreased luciferase activity in the Atg12^{KO} MEFs compared to

Atg12^{ff} when the 5'UTR of *Brca2* preceded luciferase (Figure 4B). Hence, the 5'UTR of *Brca2* contains the region that mediates autophagy dependent translation of the mRNA.

We observed that the 5'UTRs of the cohort of targets exhibiting lower RP occupancy in Atg12^{KO} cells had significantly lower folding energies compared to the 5'UTRs of a random sampling of mouse genes (Figure S4B). To adjust for length of the UTRs, the minimum free energy (MFE) within the 5'UTRs was predicted by RNALfold²³; significant differences were detected between the two groups (Figure 4C, S4C, D). These results indicate that mRNAs whose translation efficiency is enhanced in autophagy competent cells possess above average 5'UTR secondary structure complexity. Indeed, *Irf7*, another hit from our ribosome profiling screen also showed lower protein levels in Atg12^{KO} cells, and was notable for a complex 5'UTR secondary structure^{24,25} (Figure S4E).

The secondary structure of the 5'UTR can slow, or prevent, translation via diverse molecular mechanisms²⁶. Since mRNAs with complex secondary structures rely upon RNA helicases to facilitate the loading and reading of ribosomes^{27,28}, we investigated whether the helicase eIF4A1, part of the eIF4F complex that recruits ribosomes to mRNA, was altered in Atg12^{KO} cells. Although the total protein levels of eIF4A1 were unchanged in Atg12^{KO} cells (Figure S4F), cap-pulldown assays demonstrated reduced interaction between the translational initiation helicase eIF4A1 and the m⁷GTP cap in Atg12^{KO} cells (Figure 4D, E), suggesting the sequestration of eIF4A1 away from mRNAs in autophagy deficient cells. RNA immuno-precipitation confirmed decreased interaction between endogenous eIF4A1 and *Brca2* mRNA in Atg12^{KO} versus Atg12^{ff} cells (Figure 4F, S4G), as well as *Irf7* and *Trp53* (Figure S4H, I).

To further understand eIF4A1 sequestration, we tested the interaction between eIF4A1 and known autophagy cargo receptors (ACRs), mediators of selective autophagy that accumulate upon autophagy inhibition. We observed increased co-localization of eIF4A1 within puncta of the ACR p62/SQSTM1 in autophagy deficient cells (Figure 7G, H) and immunoprecipitation studies indicated that endogenous eIF4A1 interacts with endogenous p62/SQSTM1 in Atg12^{KO} but not Atg12^{ff} cells (Figure 4I). In contrast, autophagy deficiency did not enhance the interaction of eIF4A1 with NBR1, a similar ACR (Figure 4H, I). The interaction between p62/SQSTM1 and eIF4A1 did not require RNA, but we cannot rule out the necessity of other proteins to bridge the interaction (Figure S4J). p62/SQSTM1 depletion rescued the ability of eIF4A1 to interact with the cap, and overexpression of a mutant p62/SQSTM1 that cannot be degraded by autophagy (p62 Δ LIR) reduced eIF4A1 binding to the cap (Figure 4J, K, S4K). Notably, p62/SQSTM1 has been previously implicated in the sequestration of the E3 ligase KEAP1 away from its target substrate NRF2 in autophagy deficient cells²⁹. Based on our results, we propose a similar model in which the accumulated p62/SQSTM1 in Atg12^{KO} cells sequesters eIF4A1 away from the translation initiation complex. While p62/SQSTM1 knockdown was not sufficient to restore BRCA2 or IRF7 protein levels in Atg12^{KO} cells (Figure S4L, M), it was able to enhance eIF4A1 binding to *Hnnpc*, whose translation is dependent on eIF4A1³⁰ (Figure S4N). Interestingly, although eIF4A1 interaction with the cap is reduced in Atg12^{KO} cells, the overlap between autophagy sensitive mRNAs and mRNAs sensitive to eIF4A1 inhibition is minor (Figure S6O), suggesting eIF4A1 availability is not the only determinant of autophagy dependent translation.

The 5'UTR of *Brca2* contains two predicted binding sites for the RBP MSI1, which has been demonstrated to repress translation of *p21* and *Numb*³¹. We therefore assayed MSI1 binding to *Brca2* by RNA immunoprecipitation and observed increased MSI1 associated with *Brca2* in the Atg12^{KO} cells (Figure 4L). Atg12^{KO} MEFs in both fed and starved conditions demonstrated a modest accumulation of MSI1 (Figure 4M). MSI1 possesses 4 putative LC3 interacting domains (LIRs)³² and MSI1 interacted with LC3B, GABARAP, GABARAPL1, and GABARAPL2 (Figure 4N), suggesting that MSI1 is selectively targeted by autophagy. To further define how MSI1 accumulation affected *Brca2* translation, we shRNA depleted MSI1 in Atg12^{ff} and Atg12^{KO} MEFs, and measured the levels of BRCA2. While MSI1 knockdown alone seemed to decreased BRCA2 levels, Atg12 deletion did not further lower BRCA2 levels (Figure S4P-R). Therefore, we postulate that *Brca2* translation downstream of autophagy involves the coordinate regulation of multiple RNA binding proteins that interact with the 5'UTR of *Brca2*.

Decreased BRCA2 results in DNA damage accumulation and centrosome defects in autophagy deficient cells

We next dissected the functional consequences of reduced BRCA2 translation in autophagy deficient cells. BRCA2 deficient cells are impaired in homologous recombination and accumulate DNA damage³³. Accordingly, we observed increased levels of DNA damage in Atg12^{KO} MEFs (independent of Cre), evidenced by increased levels of γ H2AX, a marker of double strand DNA damage, by immunofluorescence and immunoblotting, as well as increased puncta double positive for γ H2AX and 53BP1 by

immunofluorescence (Figure 5A-B, D, S5A). Similar increases in γ H2AX were observed in Atg5^{KO} MEFs and autophagy-deficient 293T cells (Figure S5B).

Previous work showing increased DNA damage in autophagy deficient mammalian cells³⁴ attributes this to reactive oxygen species (ROS) produced from defective mitochondria³⁵. However, no significant differences were observed between Atg12^{ff} and Atg12^{KO} cells in ROS levels, mitochondrial mass or membrane potential (Figure 5C, Figure S5C). Importantly, treatment with the ROS scavenger N-acetyl cysteine had minimal effects on γ H2AX levels in Atg12^{KO} cells, whereas enforced overexpression of the human *Brca2* cDNA decreased the levels of γ H2AX in Atg12^{KO} cells (Figure 5D) and in Atg deleted HEK293T cells (Figure S5D). Overall, these results indicate that the impaired translation of *Brca2* exacerbates DNA damage in autophagy-deficient cells.

We next treated Atg12^{KO} cells with the Poly ADP-ribose polymerase (PARP) inhibitors rucaparib, olaparib, and BMN to assess if reduced BRCA2 protein levels conferred sensitivity to inhibition of single strand DNA damage repair, as previously observed in the context of BRCA2 genetic deficiency^{36,37}. Indeed, Atg12^{KO} cells exhibited increased sensitivity to PARP inhibitors, evidenced by increased γ H2AX and cleaved caspase 3 levels (Figure 5E, Figure S5G), as well as impaired colony replating efficiency following PARP inhibitor treatment (Figure 5F).

BRCA2 contributes to clustering of mother and daughter centrosomes following duplication³⁸. We observed similar impairments in centrosome clustering in Atg12^{KO} cells. The distance between the two centrosomes in non-mitotic cells was increased (Figure 5G, H) and there was a significant increase in percentage of cells with more

than two centrosomes in Atg12^{KO} cells compared to wild type controls (Figure 5G, I). These defects in centrosome organization may exacerbate DNA damage and slow cell cycle progression in Atg12^{KO} cells³⁹. In addition to *Brca2*, our ribosome profiling analysis identified additional targets involved in centrosome function, such as *Haus3* and *Cntln*, that exhibited reduced ribosome occupancy in Atg12^{KO} cells, suggesting that autophagy-dependent translation of multiple mRNAs may functionally contribute to centrosome organization.

Reduced BRCA2 protein levels and increased DNA damage upon acute autophagy deletion *in vivo*

We assessed the effects of autophagy ablation on BRCA2 protein levels *in vivo* following systemic acute genetic deletion of *Atg12* in adult mice. At 6 weeks of age, *Atg12^{ff} CagCre^{ER}* mice were subject to treatment with tamoxifen or vehicle control for five consecutive days (Figure 6A)⁴⁰. Loss of Atg12 correlated with accumulation of the autophagy substrate p62/SQSTM1 and the absence of LC3-II at 2 weeks following tamoxifen administration (Figure 6B). Atg12^{KO} animals survived for 10 weeks following the acute loss of autophagy. Similar to acute systemic genetic deletion of Atg7 in adult mice⁴¹, systemically deleted Atg12 mice were smaller and failed to gain weight following deletion (Figure 6C, D). Immunoblotting revealed decreased BRCA2 protein levels in the kidney and cerebral cortex of Atg12^{KO} mice compared to autophagy competent Atg12^{ff} controls (Figure 6E, F). This correlated with increased levels of DNA damage, evidenced by a two-fold increase in γ H2AX positive nuclei in the kidney, cerebral cortex,

and small intestine of Atg12^{KO} mice (Figure 6G, H). These *in vivo* findings are consistent with our *in vitro* results that an autophagy pathway supports the production of BRCA2.

Discussion

Using ribosome profiling, we have uncovered that autophagy regulates the translation of specific proteins in mammalian cells. Strikingly, our results show important differences in the starvation response between mammalian cells and *Saccharomyces cerevisiae*, which rely heavily on autophagy to maintain amino acid availability and protein synthesis during starvation^{6,42}. In contrast, global protein synthesis and the availability of intracellular amino acids remains largely intact in mammalian cells following acute autophagy ablation, including cells undergoing short term starvation, suggesting that other proteolytic pathways, such as direct delivery of ER and plasma membrane components to the lysosome^{43,44}, likely compensate to maintain amino acid levels in response to stress.

Importantly, we demonstrate that basal autophagy enables the efficient translation of the DNA damage repair protein BRCA2. As a result, when autophagy is inhibited, increases in DNA damage and centrosome defects are observed. We propose that autophagic turnover of multiple RNA binding proteins interacting with the 5'UTR of *Brca2* enables the translation of this DNA damage repair protein. We also identified that autophagic degradation of p62/SQSTM1 enhances eIF4A1 availability to interact with the m⁷GTP cap. Notably, recent work indicates that p62/SQSTM1 spontaneously undergoes phase separation *in vivo*; the resulting clusters may serve as foci to efficiently capture and sequester proteins such as eIF4A1^{45,46}. There are likely

additional mechanisms by which autophagy regulates protein translation, as our RP study also uncovered mRNAs with increased ribosome occupancy during autophagy inhibition. Although we found no role for autophagy in controlling cap versus IRES translation initiation, we cannot rule out that autophagy may regulate translation from IRES-like or IRES motifs distinct from the viral motif driven reporter systems we employed.

Autophagy enhanced *Brca2* translation may have particular relevance for human health and disease. We found *in vivo* reductions in BRCA2 protein levels and increases in DNA damage in multiple tissues, including a 2-fold reduction in BRCA2 levels and a 3-fold increase in gH2AX levels in the kidney. Polycystic kidney disease has been linked independently to both defects in autophagy and defects in centrosome organization that disrupt primary cilia formation⁴⁷⁻⁴⁹. Our results broach centrosome disorganization as a potential mechanism by which defective autophagy contributes to this disease phenotype. Furthermore, because intestinal stem cells and hematopoietic stem cells are highly dependent on autophagy to maintain genome integrity⁵⁰⁻⁵², our data suggest a previously unrecognized mechanism by which autophagy maintains the genome in stem cells. While ROS has been primarily implicated as the DNA damaging driver in autophagy deficient intestinal stem cells, our results here implicate reduced *Brca2* translation as an aggravating factor.

With regard to cancer, one can speculate autophagy mitigates genomic damage by enabling the translation of *Brca2*, thereby suppressing early tumorigenesis. In support of this idea, a polymorphism in the 5'UTR of BRCA2 which decreases the secondary structure and promotes translation is protective against breast cancer in

patients⁵³. Because autophagy inhibitors are being tested as adjuvant chemotherapies⁵⁴, further defining the effects of autophagy on protein translational control in cancer cells will help refine the proper contexts to effectively employ such strategies. Overall, our findings illuminate roles for autophagy in directing the protein translational landscape in mammalian cells, which maintains genome integrity and promotes cell cycle progression.

Acknowledgements: Grant support includes the NIH (R01AG057462, R01CA213775, R01CA126792 to JD, P30CA082103 to AO), QB3/Calico Longevity Fellowship (to JD), Samuel Waxman Cancer Research Foundation (to JD), and the DOD BCRP (W81XWH-11-1-0130 to JD). JG was supported by the NSF GRFP (DGE -1144247). TM is supported by the NIH (NCI 1F31CA217015). AML is supported by a Banting Postdoctoral Fellowship from the Government of Canada (201409BPF-335868) and a Cancer Research Society Scholarship for Next Generation of Scientists (22805).

Author contributions: Conceptualization, JG and JD; Investigation, JG; Visualization, JG; Formal Analysis, JG; Data Curation, JG; Writing – Original Draft, JG; Writing – Review and Editing, JD, TM, SA and AO; Software, SA and AO; Resources, TM, DS, AML, AO and SA; Funding Acquisition, JD, AO; Supervision, JD.

Figure 1

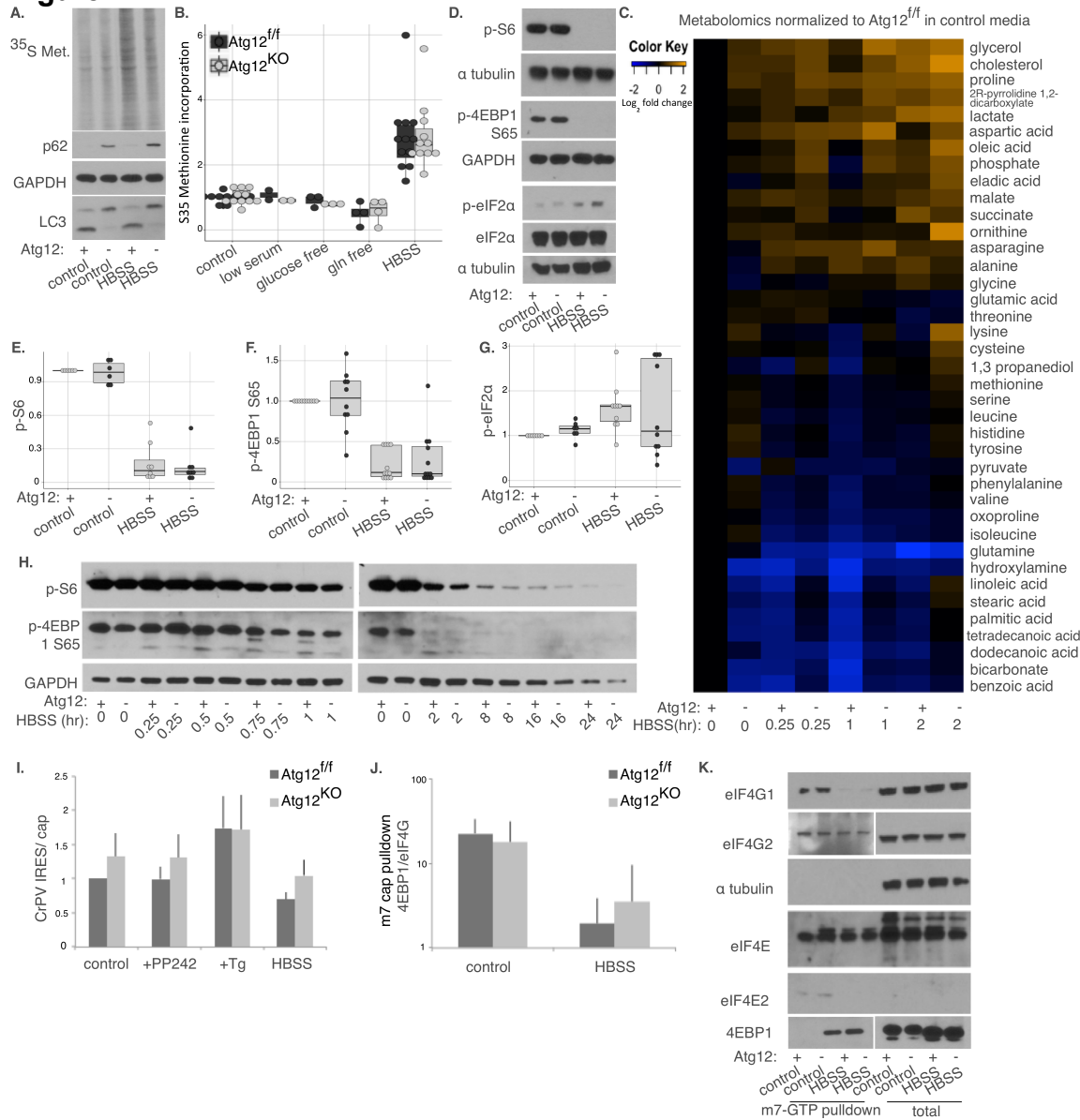


Figure 1: Minimal effects of Atg12 genetic deletion on global translation, intracellular amino acid levels, and mTORC1 signaling

A. Representative ³⁵S-methionine incorporation autoradiogram from *Atg12^{ff}* and *Atg12^{KO}* MEFs in control media (DMEM + 10% serum) without methionine or following 2h HBSS starvation. p62/SQSTM1 and LC3 immunoblotting is shown below.

B. *Atg12^{ff}* or *Atg12^{KO}* MEFs were grown in control media, and 2h prior to lysis were switched to either media lacking methionine, low (1%) serum media lacking methionine, media lacking glucose and methionine, media lacking glutamine and methionine, or HBSS. Cells were labeled with ³⁵S-methionine for 30 min prior to lysis. Relative ³⁵S-

methionine incorporation rate is quantified, shown as a boxplot with dotplot overlay for each biological replicate, normalized to loading control.

C. Changes in intracellular metabolite levels detected by GC-TOF with MTBSTFA (n=4), in Atg12^{ff} and Atg12^{KO} MEFs in control media or following HBSS starvation for the indicated times. Fold change relative to Atg12^{ff} in control media.

D-G. Atg12^{ff} and Atg12^{KO} MEFs in control media or following 2h HBSS starvation were lysed and immunoblotted for markers of mTORC1 signaling (p-S6, p-4EBP1) and cap-dependent protein translation inhibition (p-eIF2 α). Representative immunoblots (D) are shown. Relative protein levels of (E) p-S6, (F) p-4EBP1, and (G) p-eIF2 α were quantified, normalized to loading control, and shown as boxplots with dotplot overlay for each biological replicate.

H. Representative immunoblot for markers of mTORC1 signaling (p-S6, p-4EBP1) in Atg12^{ff} and Atg12^{KO} MEF protein lysate following a timecourse of HBSS starvation.

I. Quantification (mean + SEM, n=5) of Renilla luciferase activity driven by the Cricket paralysis virus IRES motif, normalized to Firefly luciferase activity driven by the cap. Cells were treated with PP242 (2 μ M for 1h) to inhibit mTORC1 signaling, and Thapsigargin (Tg, 1 μ M for 1h) to induce IRES-mediated translation (also see Figure S1P).

J. Protein lysate from Atg12^{ff} and Atg12^{KO} MEFs in control media or following 2h HBSS starvation was subject to pulldown with γ -amino-phenyl-m7 GTP cap analog conjugated to agarose beads (cap pulldown) and 4EBP1 relative to eIF4G1 levels quantified (mean + SD, n=3).

K. Representative immunoblot from cap pulldown assay described in Figure 1J, showing total protein levels of cap binding proteins in indicated cell types in control media and following 2h HBSS starvation.

Figure 2

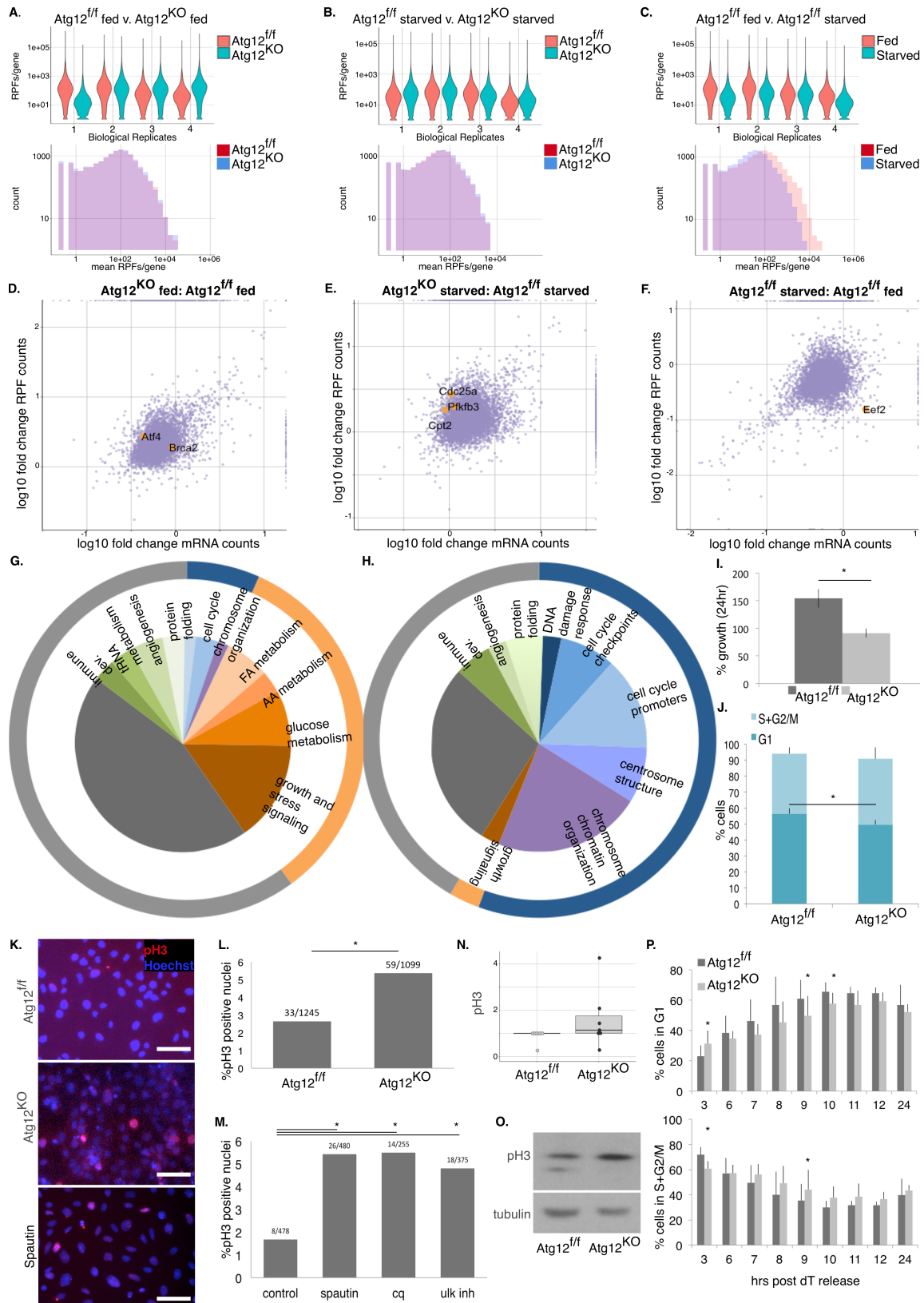


Figure 2: Ribosome profiling reveals that autophagy supports the translation of proteins required for DNA damage response and cell cycle control

A-C. Violin plots of number of read counts of ribosome protected footprints (RPFs) per gene per biological replicate (above) and histogram of the mean of the number of read counts of ribosome protected footprints per gene (below) in (A) Atg12^{ff} and Atg12^{KO} MEFs in control media (B) Atg12^{ff} and Atg12^{KO} MEFs following 2h HBSS starvation or (C) Atg12^{ff} MEFs in control media or following 2h HBSS starvation.

D-F. Fold change of RPF counts versus fold change of mRNA counts. Labeled points in orange are mRNAs whose change in ribosome occupancy was significant, and protein level changes confirmed by immunoblotting (see Figure S2E).

G-H. Molecular functions of mRNAs whose ribosome occupancy is (G) increased (p-value < 0.01, n=36) or (H) decreased (p-value < 0.005, n=60) in Atg12^{KO} cells versus Atg12^{ff} cells in either fed or starved conditions.

I. Quantification (mean ± SEM, n=3) of percent growth of Atg12^{ff} and Atg12^{KO} MEFs over 24h measured by crystal violet staining. Asterisk indicates p-value = 0.05 by t-test.

J. Cell cycle quantification (mean + SD, n=3) of unsynchronized Atg12^{ff} or Atg12^{KO} MEFs. Asterisk indicates p-value = 0.001 by t-test.

K. Representative pH3 (red) immunofluorescence of Atg12^{ff} and Atg12^{KO} MEFs, and MEFs treated with 50µM Spautin-1 for 4h. Nuclei marked by Hoechst (blue). Bar = 100µm.

L. Percent of pH3 positive nuclei in Atg12^{ff} and Atg12^{KO} MEFs. Fraction above bar indicates pH3 positive cells out of total number of cells enumerated from 3 biological replicates. Asterisk indicates p-value =0.001 by two-sided fisher's exact test.

M. Quantification of percent of pH3 positive nuclei in MEFs treated for 4h with control (DMSO), Spautin-1 (50µM), chloroquine (CQ, 20µM), or the Ulk1 inhibitor SBI-0206965 (Ulk inh, 10µM). Fraction above bar indicates pH3 positive cells out of total number of cells enumerated from three biological replicates. Asterisk indicates p-value <0.05 by t-test on logit transformed percent per replicate.

N. Relative pH3 levels in Atg12^{ff} and Atg12^{KO} MEFs were measured by immunoblotting, normalized to loading control, and quantified.

O. Representative immunoblotting for pH3 in Atg12^{ff} and Atg12^{KO} MEFs.

P. Atg12^{ff} and Atg12^{KO} MEFs were double thymidine blocked, released and fixed following hours indicated. Cell cycle stages were quantified by flow cytometry (mean + SD, n=3). Asterisk indicates p-value < 0.05 by t-test.

Figure 3

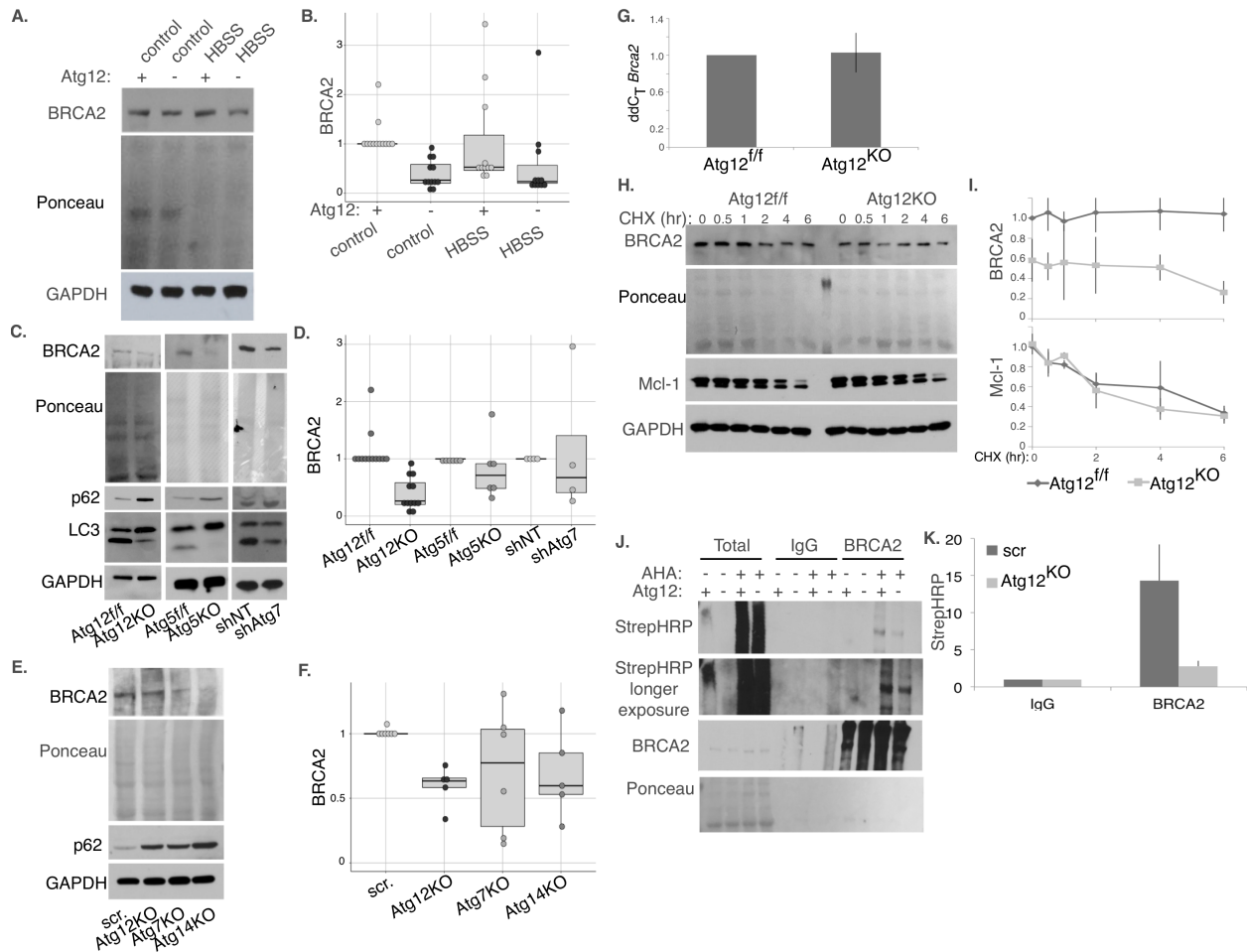


Figure 3: Reduced BRCA2 protein translation in autophagy deficient cells

A-B. Protein lysate was collected from Atg12^{ff/ff} and Atg12^{KO} MEFs in control media or following 2 h HBSS starvation. BRCA2 levels were measured by immunoblotting: (A) representative immunoblot is shown; (B) relative BRCA2 protein levels were normalized to loading control, and quantified shown as a boxplot with dotplot overlay for each biological replicate.

C-D. Protein lysate from Atg12^{ff/ff} and Atg12^{KO} MEFs, Atg5^{ff/ff} and Atg5^{KO} MEFs, and MEFs expressing non-targeting shRNA or shRNA to Atg7 was (C) immunoblotted as indicated and (D) relative BRCA2 levels normalized to loading control was quantified.

E-F. Protein lysate was collected from HEK293T cells with CRISPR deleted Atg12, Atg7, Atg14, or a scrambled sgRNA control, and (E) immunoblotted for the indicated proteins; (F) relative BRCA2 protein levels normalized to loading control was quantified.

G. *Brca2* transcript levels (mean \pm SD, n=7) in Atg12^{ff/ff} and Atg12^{KO} MEFs measured by qPCR, with *Gapdh* as the endogenous control.

H-I. Atg12^{ff/ff} and Atg12^{KO} MEFs following cycloheximide (100 μ g/ml) treatment for time indicated to inhibit protein translation. (H) Representative immunoblots for BRCA2 and

Mcl-1. (I) Quantification (mean \pm SD, n=3) of relative BRCA2 and Mcl-1 levels from immunoblotting, normalized to loading control.

J, K. Newly synthesized BRCA2 protein was measured following 8h AHA incorporation and BRCA2 immunoprecipitation from control or Atg12^{KO} HEK293T cells. (J)

Representative immunoblot is shown. (K) Quantification (mean \pm SD, n=3) of newly synthesized BRCA2 (StrepHRP levels).

Figure 4

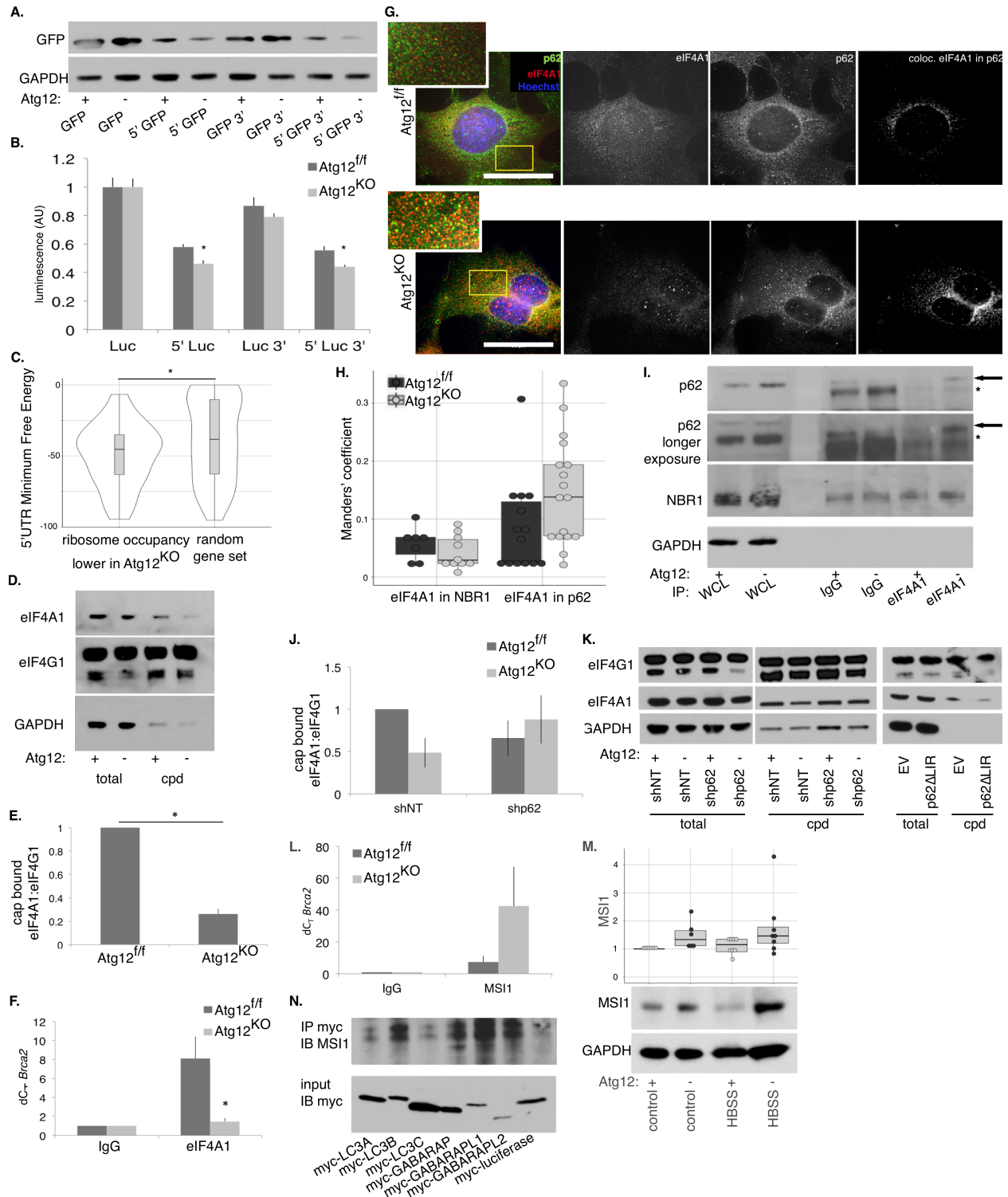


Figure 4: The 5'UTR of *Brca2* determines translational sensitivity to autophagy due to RNA binding protein interactions

- A. Atg12^{ff} and Atg12^{KO} MEFs were transfected with pcDNA3 expressing *Gfp*, *Gfp* preceded by the 5'UTR of *Brca2*, *Gfp* followed by the 3'UTR of *Brca2*, or *Gfp* flanked by both 5' and 3' UTRs of *Brca2*. Representative immunoblots for levels of GFP are shown.
- B. Atg12^{ff} and Atg12^{KO} MEFs were transfected with pNL1.1 driving the expression of *nano-luciferase*, *nano-luciferase* preceded by the 5'UTR of *Brca2*, *nano-luciferase* followed by the 3'UTR of *Brca2*, or *nano-luciferase* flanked by both 5' and 3' UTRs of *Brca2*. Luciferase activity was measured by Nano-glo (Promega). Quantification (mean \pm SEM, n=3) is shown, and asterisks indicate p-value < 0.005 by t-test.
- C. Local minimum free energy (MFE) was predicted by RNALfold in the 5'UTRs from mRNAs with significantly lower than expected ribosome occupancy in Atg12^{KO} MEFs compared to a randomly generated gene set. A violin plot with boxplot overlay of the MFEs is shown, asterisk indicates p-value = 0.05 by Kolmogorov-Smirnov test.
- D. Protein lysate from Atg12^{ff} and Atg12^{KO} MEFs was captured by cap pulldown, and total protein lysate and pulldown was immunoblotted as indicated.
- E. Quantification (mean \pm SD, n=4) of eIF4A1 capture by cap pulldown relative to eIF4G1 capture. Asterisk indicates p-value = 7.4E-08 by t-test.
- F. Quantification (mean \pm SD, n=3) of the fold enrichment of *Brca2* interaction with eIF4A1 over IgG control in Atg12^{ff} or Atg12^{KO} MEFs by RNA immunoprecipitation. Asterisk indicates p-value = 0.05 by t-test.
- G. Representative immunofluorescence images for eIF4A1 (red in merged imaged) and p62/SQSTM1 (green in merged imaged) in Atg12^{ff} and Atg12^{KO} MEFs, nuclei were counterstained with Hoechst (blue). Yellow box indicates region of inset panel in the top left corner. Far right panels show the points of colocalization (white) of eIF4A1 in p62/SQSTM1. Bars = 50 μ m.
- H. Manders' coefficient (percent of colocalization) of eIF4A1 in either NBR1 or p62/SQSTM1 in Atg12^{ff} and Atg12^{KO} MEFs was calculated, and boxplot with dotplot overlay representing one field is shown (n=3). p-value = 0.06 between Atg12^{ff} and Atg12^{KO} for eIF4A1 in p62/SQSTM1 by t-test.
- I. Representative immunoprecipitation of eIF4A1 and immunoblot for the autophagy cargo receptors p62/SQSTM1 and NBR1. Arrow indicates p62/SQSTM1, asterisk indicates immunoglobulin heavy chain.
- J. Protein lysate from Atg12^{ff} and Atg12^{KO} MEFs following p62/SQSTM1 depletion or transduced with non-targeting shRNA was captured by cap pulldown, and the ratio of eIF4A1 to eIF4G1 was quantified (mean \pm SD, n=4).
- K. Protein lysate from Atg12^{ff} and Atg12^{KO} MEFs following p62/SQSTM1 depletion, transduced with non-targeting shRNA or HEK293Ts expressing p62 Δ LIR or empty vector control was captured by cap pulldown, and immunoblotted as indicated.
- L. Quantification (mean \pm SD, n=3) of the fold enrichment of *Brca2* interaction with MSI1 over IgG control in Atg12^{ff} or Atg12^{KO} MEFs by RNA immunoprecipitation.
- M. Boxplot, with dotplot overlay for each biological replicate, of relative MSI1 protein levels normalized to loading control and representative immunoblots from autophagy inhibited MEFs.
- N. Representative immunoblot of immunoprecipitation of myc-tagged LC3/ATG8 family members interacting with MSI1.

Figure 5

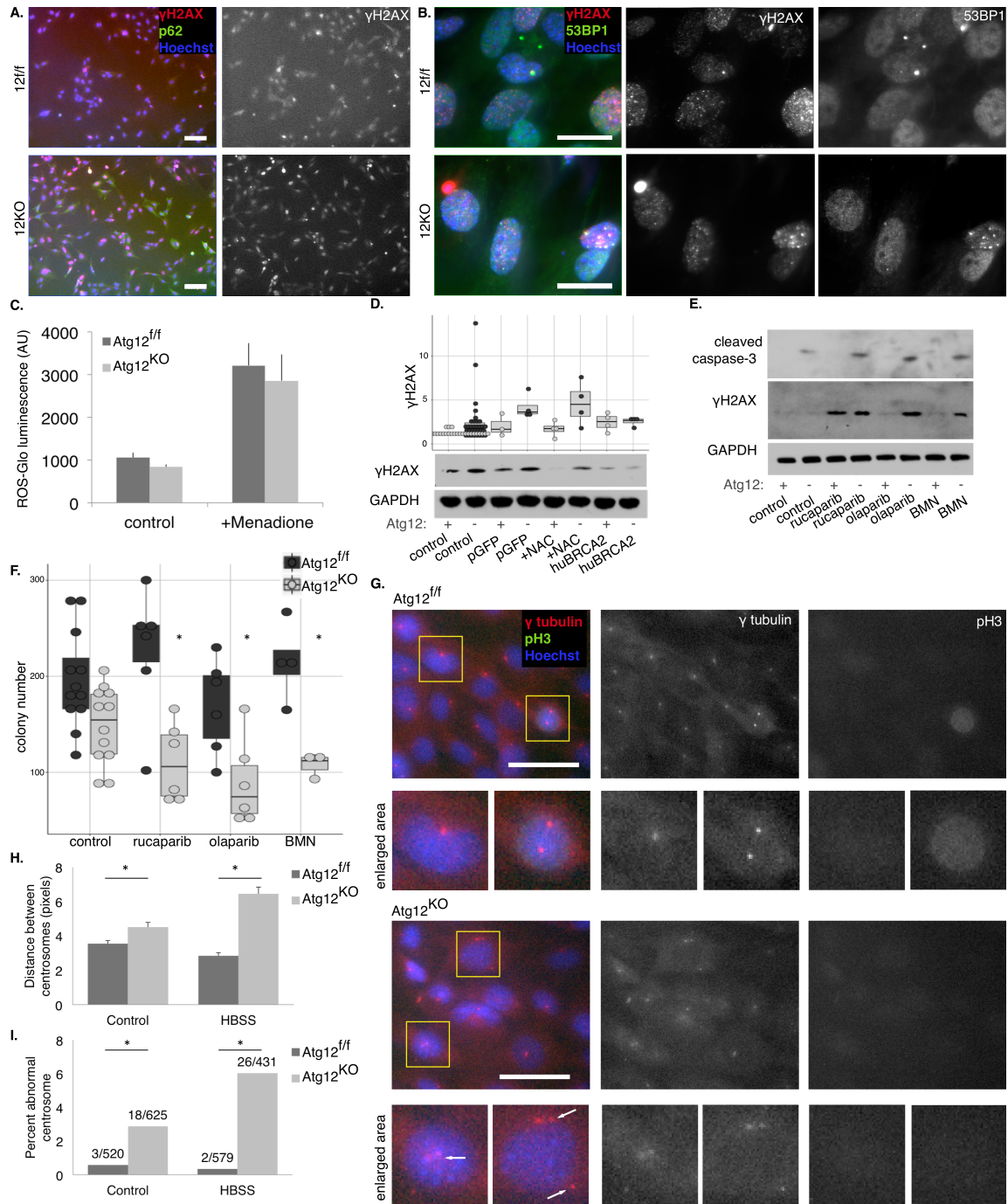


Figure 5: Decreased BRCA2 levels in Atg12 deleted cells results in increased DNA damage and centrosome abnormalities

- A. Representative immunofluorescence for γ H2AX (red in merged image) and p62/SQSTM1 (green in merged image) in Atg12^{ff} and Atg12^{KO} MEFs; nuclei counterstained with Hoechst (blue). Bar = 100 μ m.
- B. Representative immunofluorescence for γ H2AX (red in merged image) and 53BP1 (green in merged image) in Atg12^{ff} and Atg12^{KO} MEF; nuclei counterstained with Hoechst (blue). Bar = 50 μ m.
- C. ROS-glo assay (Promega) in Atg12^{ff} and Atg12^{KO} MEFs treated with vehicle control or menadione (50 μ M for 2h, positive control) was quantified (mean \pm SEM, n=2).
- D. Protein lysate was collected from Atg12^{ff} and Atg12^{KO} MEFs treated with vehicle control or NAC (5mM for 8h), or ectopically overexpressing either GFP (pGFP) or human BRCA2 (huBRCA2). A representative immunoblot for γ H2AX is shown, as well as boxplots with dotplot overlay for biological replicates, for the relative levels of γ H2AX normalized to loading control.
- E. Protein lysate was collected from Atg12^{ff} and Atg12^{KO} MEFs treated for 16h with either vehicle control, rucaparib (100nM), olaparib (100nM), or BMN (2nM). Lysates were immunoblotted as shown.
- F. A clonogenic replating assay was performed on Atg12^{ff} or Atg12^{KO} MEFs treated for 16h with vehicle control, rucaparib (100nM), olaparib (100nM), or BMN (2nM), and colony number was quantified, shown as a boxplot with dotplot overlay for each biological replicate. Asterisk indicates p-value < 0.02 by t-test.
- G. Representative immunofluorescence of centrosomes stained by γ -tubulin (red in merged image) and mitotic cells stained by pH3 (green in merged image), nuclei counterstained by Hoechst (blue in merged image), in Atg12^{ff} and Atg12^{KO} MEFs. Yellow box indicates magnified region below. White arrows indicate non-mitotic cells with multiple centrosomes (3+) or non-clustered centrosomes. Bar = 100 μ m.
- H. Quantification (mean \pm SEM, n=3) of distance between mother and daughter centrosomes measured on immunofluorescence of γ -tubulin in non-pH3 positive cells. Asterisk indicates p-value < 0.005 by t-test.
- I. Quantification of Atg12^{ff} and Atg12^{KO} MEFs with abnormal numbers (3+) of centrosomes from immunofluorescence images (n=4). Asterisk indicates p-value < 0.02 by t-test on logit transformed percent per replicate. Fraction above the bar plots indicates number of cells with abnormal centrosome numbers out of total number of cells enumerated.

Figure 6

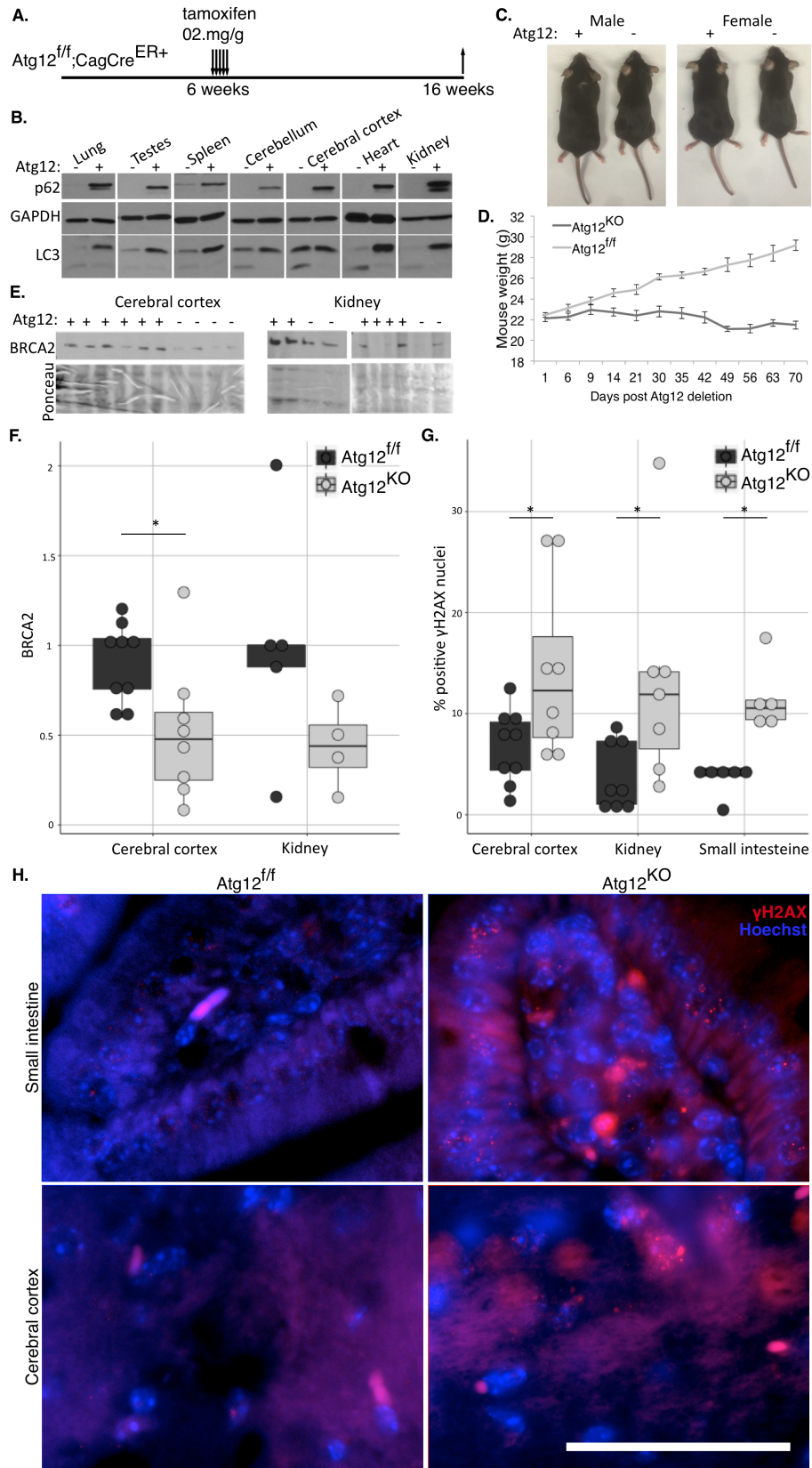


Figure 6: Atg12 deletion *in vivo* leads to reduced BRCA2 and increased DNA damage

- A. Diagram of Atg12^{ff};CagCre^{ER+} mouse treatment and tissue collection.
- B. Protein lysate was collected from tissues 2 weeks following vehicle or 0.2mg/g tamoxifen treatment and immunoblotted for markers of autophagic flux (p62/SQSTM1, LC3).
- C. Representative images of male and female Atg12^{ff} and Atg12^{KO} littermates.
- D. Body weights of mice following Atg12 deletion (Atg12^{ff} n=17, Atg12^{KO} n=14).
- E. Protein lysate was collected from mouse tissues 10 weeks following vehicle or tamoxifen treatment, and immunoblotted for BRCA2.
- F. Boxplot with dotplot overlay for biological replicates of BRCA2 protein levels, normalized to total protein levels, assayed by immunoblotting. Asterisk indicates p-value = 0.02 by t-test.
- G. Boxplot with dotplot overlay for biological replicates of percent of γ H2AX positive nuclei by immunofluorescence, counted over four randomly selected fields of stained tissue per mouse. Asterisk indicates p-value < 0.05 by t-test.
- H. Representative immunofluorescence for γ H2AX (red) in mouse tissues from the cerebral cortex and small intestine, with nuclei counterstained by Hoechst (blue). Bar = 50 μ m.

Table 1: list of top 30 significant changes assessed by ribosome profiling

RP occupancy higher in Fed Atg12KO cells					RP occupancy decreased in Fed Atg12KO cells				
gene ID	mRNA LogFC	P-val	FDR		gene ID	mRNA LogFC	P-val	FDR	
Egfr	ENSMUSG0000020122	0.3715	0.00025	0.1499	Anp32b	ENSMUSG0000028333	-0.7288	3.51E-07	0.001882
181009A15Rik	ENSMUSG0000071653	0.4538	0.00040	0.2150	Egr1	ENSMUSG0000038418	-1.4001	1.84E-06	0.003495
Ank	ENSMUSG0000022265	-0.2724	0.00097	0.3177	Irf7	ENSMUSG0000025498	-2.4639 *	1.95E-06	0.003495
Ptpn9	ENSMUSG0000032290	0.2250	0.00122	0.3398	Kif20b	ENSMUSG0000024795	-0.7614	2.61E-05	0.035003
Ppp1r16a	ENSMUSG0000033819	-0.0917	0.00154	0.3526	Taf15	ENSMUSG0000020680	-0.8102	4.64E-05	0.049837
Sdc2	ENSMUSG0000022261	0.2764	0.00158	0.3526	Srrm1	ENSMUSG0000028809	-0.8857	6.82E-05	0.06108
Atf4	ENSMUSG0000042406	0.3397	0.00226	0.4486	Sp2	ENSMUSG0000018678	-0.5017	8.37E-05	0.064091
Egln2	ENSMUSG0000058709	0.2181	0.00248	0.4576	Hnrpa3	ENSMUSG0000059005	-0.3566	9.55E-05	0.064091
Ppt1	ENSMUSG0000028657	0.1894	0.00271	0.4576	Ppig	ENSMUSG0000042133	-0.8072	0.00050	0.231751
Reb1	ENSMUSG0000039087	-0.1775	0.00290	0.4576	Trp53bp2	ENSMUSG0000026510	-0.4945	0.00052	0.231751
Alg5	ENSMUSG0000036632	0.4846	0.00307	0.4708	Cntin	ENSMUSG0000038070	-0.5310	0.00069	0.276878
Hand2	ENSMUSG0000038193	0.2563	0.00330	0.4796	Sitm	ENSMUSG0000032212	-0.7105	0.00072	0.276878
Angptl2	ENSMUSG0000040405	0.2840	0.00330	0.4796	Dab2	ENSMUSG0000022150	-0.8042	0.00091	0.317169
Ccdc102a	ENSMUSG0000063605	0.7214	0.00356	0.5033	Top1	ENSMUSG0000070544	-0.4617	0.00101	0.317169
Pcnx14	ENSMUSG0000034501	0.2281	0.00404	0.5106	Cenpe	ENSMUSG0000045328	-0.5379	0.00111	0.331874
Tes	ENSMUSG0000029552	-0.1433	0.00404	0.5106	Eapp	ENSMUSG00000054302	-0.4624	0.00127	0.339824
Trapp2c1	ENSMUSG0000015013	0.2788	0.00457	0.5106	Gemin4	ENSMUSG0000049396	-0.2328	0.00134	0.341903
Slc7a2	ENSMUSG0000031596	-0.1303	0.00473	0.5106	Klf17	ENSMUSG0000028986	-0.4527	0.00154	0.352598
Rrf13	ENSMUSG0000036503	0.3582	0.00493	0.5190	Rbm43	ENSMUSG0000038249	-1.5548 *	0.00172	0.369336
Mllt6	ENSMUSG0000038437	0.0134	0.00557	0.6193	Xrn1	ENSMUSG0000032410	-0.8535	0.00205	0.423369
Tmem50a	ENSMUSG0000028822	0.0514	0.00657	0.6193	Bra2	ENSMUSG0000041147	-0.7998	0.00248	0.457551
Large	ENSMUSG0000004383	-0.0079	0.00727	0.6504	Haus3	ENSMUSG0000079555	-0.3752	0.00277	0.457551
Plekha3	ENSMUSG0000002733	0.1405	0.00787	0.6792	Filip1l	ENSMUSG0000043336	-0.8351	0.00279	0.457551
Src	ENSMUSG0000027646	0.2019	0.00803	0.6792	Trp53	ENSMUSG0000059552	-0.5670	0.00284	0.457551
Ibk1	ENSMUSG0000035941	-0.0464	0.00828	0.6792	Rad9a	ENSMUSG0000024824	-0.6054	0.00368	0.507112
Pik3r2	ENSMUSG0000031834	0.1106	0.00865	0.6831	Tbck	ENSMUSG0000028030	-0.2960	0.00413	0.510555
Adcy7	ENSMUSG0000031659	-0.3069	0.00944	0.7144	Cul4b	ENSMUSG0000030195	-0.3956	0.00415	0.510555
Plat	ENSMUSG0000031538	-0.7404	0.00977	0.7144	Fus	ENSMUSG0000030795	-0.3812	0.00430	0.510555
Matn2	ENSMUSG0000022324	0.0573	0.01020	0.7275	Apbb1ip	ENSMUSG0000026786	-0.5264	0.00449	0.510555
Pappa	ENSMUSG0000028370	0.8025	0.01039	0.7275	Tbc1d8b	ENSMUSG0000042473	-0.3252	0.00465	0.510555

RP occupancy higher in Starved Atg12KO cells					RP occupancy lower in Starved Atg12KO cells				
gene ID	mRNA LogFC	P-val	FDR		gene ID	mRNA LogFC	P-val	FDR	
Cdc25a	ENSMUSG0000032477	0.1362	0.00004	0.1002	Irf7	ENSMUSG0000025498	-2.5316 *	5.21E-09	2.80E-05
Nkain1	ENSMUSG0000078532	0.4151	0.00019	0.2842	Ifitm1	ENSMUSG0000025491	-1.3148	0.00028	0.284166
Cpt2	ENSMUSG0000028607	0.5218	0.00026	0.2842	Hist1h2be	ENSMUSG0000047246	-0.2325	0.00057	0.284258
Kif3c	ENSMUSG0000020668	0.5443	0.00032	0.2842	Srgap3	ENSMUSG0000030257	0.2486	0.00077	0.293752
Fam134b	ENSMUSG0000022270	0.2758	0.00050	0.2843	Hist4h4	ENSMUSG0000096010	-0.2521	0.00109	0.364512
Zbtb7b	ENSMUSG0000028042	0.4575	0.00051	0.2843	Cep350	ENSMUSG0000033671	-0.3376	0.00139	0.414586
Vldlr	ENSMUSG0000024924	0.1449	0.00058	0.2843	Rbbp6	ENSMUSG0000030779	-0.6247	0.00173	0.443252
Zfand2b	ENSMUSG0000026197	0.2029	0.00060	0.2843	Rps6ka3	ENSMUSG0000031309	-0.6035	0.00219	0.455529
Pop5	ENSMUSG0000060152	0.7157	0.00066	0.2843	Atrx	ENSMUSG0000031229	-0.7196	0.00237	0.4704
Arfp2	ENSMUSG0000030881	0.4494	0.00069	0.2843	Hist1h2bm	ENSMUSG0000096807	-0.1989	0.00397	0.562075
Bcam	ENSMUSG0000029890	-0.1065	0.00102	0.3645	5830418K08Rik	ENSMUSG0000046111	-0.3621	0.00438	0.562075
2410002F23Rik	ENSMUSG0000045411	0.3523	0.00131	0.4143	Rara	ENSMUSG0000037992	0.0511	0.00455	0.562213
Pmp22	ENSMUSG0000018217	0.6005	0.00155	0.4387	Dek	ENSMUSG0000021377	-0.3718	0.00506	0.565179
Hip1r	ENSMUSG0000000915	0.0619	0.00167	0.4433	Sgol2	ENSMUSG0000026039	-0.5867	0.00548	0.573713
Tbcl1d22a	ENSMUSG0000051864	0.2034	0.00190	0.4549	Pnn	ENSMUSG0000020994	-0.5163	0.00564	0.573713
Gigy1	ENSMUSG0000029714	0.2173	0.00195	0.4549	Smc2	ENSMUSG0000028312	-0.7814	0.00568	0.573713
Slc7a2	ENSMUSG0000031596	0.1968	0.00218	0.4555	Sec2c	ENSMUSG0000027706	-0.5260	0.00589	0.573713
Nin	ENSMUSG0000021710	0.4352	0.00221	0.4555	Cbl	ENSMUSG0000034342	-0.1492	0.00617	0.579643
Bambi	ENSMUSG0000024232	-0.2774	0.00248	0.4760	H2afj	ENSMUSG0000060032	-0.2257	0.00627	0.579643
Zfp622	ENSMUSG0000052553	-0.0688	0.00278	0.5156	Tbc1d22b	ENSMUSG0000042203	-0.0695	0.00648	0.579913
Ctu2	ENSMUSG0000049482	0.1623	0.00317	0.5621	Fryl	ENSMUSG0000070733	-0.4107	0.00686	0.583745
Crabp2	ENSMUSG0000004885	0.4855	0.00325	0.5621	Cc2d1a	ENSMUSG0000036686	-0.3865	0.00727	0.583745
Nfs1	ENSMUSG0000027618	0.3727	0.00340	0.5621	Sirt2	ENSMUSG0000015149	0.0212	0.00743	0.583745
Rnmnd5a	ENSMUSG0000002222	0.4479	0.00355	0.5621	Hist1h2bn	ENSMUSG0000099521	-0.1145	0.00779	0.583745
Pikfb3	ENSMUSG0000026773	0.1066	0.00386	0.5621	Hist1h2bk	ENSMUSG0000062727	-0.1722	0.00790	0.583745
Limk2	ENSMUSG0000020451	-0.1044	0.00390	0.5621	Pbxw17	ENSMUSG0000037816	-1.0364	0.00802	0.583745
Stx4a	ENSMUSG0000030805	0.2904	0.00416	0.5621	Kif21a	ENSMUSG0000022629	-0.0350	0.00820	0.583745
Nes	ENSMUSG0000000491	-0.5295	0.00430	0.5621	2810474019Rik	ENSMUSG0000032712	-0.7653	0.00820	0.583745
Nr1d2	ENSMUSG0000021775	-0.0059	0.00432	0.5621	Ssb	ENSMUSG0000068882	-0.5215	0.00827	0.583745
Zfp143	ENSMUSG0000061079	0.1480	0.00435	0.5621	Rad50	ENSMUSG0000020380	-1.1900	0.00882	0.583745

RP occupancy higher in Starved Atg12i/f cells					RP occupancy lower in Starved Atg12i/f cells				
gene ID	mRNA LogFC	P-val	FDR		gene ID	mRNA LogFC	P-val	FDR	
Gas2l1	ENSMUSG0000034201	0.5015	0.00025	0.0170	Eef1a1	ENSMUSG0000037742	-1.2535 *	1.69E-12	9.09E-09
Cebpb	ENSMUSG0000056501	1.0100	0.00384	0.1625	Eef1b2	ENSMUSG0000025967	-0.5901	7.89E-10	1.12E-06
Itprlp2	ENSMUSG0000095115	1.5805 *	0.00735	0.2861	Rpl17	ENSMUSG0000062328	-0.6946	1.53E-09	2.74E-06
Atf4	ENSMUSG0000044206	0.4882	0.01063	0.3882	Rps24	ENSMUSG0000025290	-0.6555	3.28E-09	3.79E-06
Kifc3	ENSMUSG0000031788	0.5879	0.01334	0.4650	Eef2	ENSMUSG0000034994	-1.4325 *	3.52E-09	3.79E-06
Mphosph9	ENSMUSG0000038126	0.8277	0.01395	0.4742	Tpt1	ENSMUSG0000060126	-0.5643	2.13E-08	1.90E-05
Srsf2	ENSMUSG0000034120	0.8318	0.01532	0.5025	Rps27rt	ENSMUSG0000050621	-0.1222	5.18E-08	3.86E-05
Hist2h2aa1	ENSMUSG0000063954	0.5767	0.01559	0.5041	Rps27	ENSMUSG0000090733	-0.0923	5.75E-08	3.86E-05
Hist1h2ab	ENSMUSG0000061615	0.4144	0.01599	0.5063	Rpl18a	ENSMUSG0000045128	-0.7593	8.15E-08	4.86E-05
Fzd7	ENSMUSG0000041075	1.5212 *	0.01689	0.5186	Rps27a	ENSMUSG0000020460	-0.8120	9.06E-08	4.87E-05
Hist1h2ac	ENSMUSG0000069270	0.3703	0.01702	0.5186	Rpl28	ENSMUSG0000030432	-0.6967	1.15E-07	5.60E-05
Hist1h2ao	ENSMUSG0000094248	0.2730	0.01795	0.5357	Rps4x	ENSMUSG0000031320	-0.8382	1.52E-07	6.82E-05
Hand2	ENSMUSG0000038193	0.1085	0.02003	0.5846	Rpl3	ENSMUSG0000060036	-0.9160 *	1.81E-07	7.49E-05
Nr2f6	ENSMUSG0000002393	0.8287	0.02062	0.5931	Hspa8	ENSMUSG0000015656	-1.2101 *	2.26E-07	8.49E-05
Rab11fp3	ENSMUSG0000037098	0.3356	0.02213	0.6134	Npm1	ENSMUSG0000057113	-0.9757 *	2.37E-07	8.49E-05
Hist1h2ad	ENSMUSG0000071478	0.3001	0.02256	0.6181	Rpl5	ENSMUSG0000058558	-0.9018	2.96E-07	9.93E-05
Hist1h2af	ENSMUSG0000061991	0.3165	0.02295	0.6211	Rps19	ENSMUSG0000040952	-0.3211	3.31E-07	0.000104
Hoxd13	ENSMUSG00000001819	0.5325	0.02342	0.6278	Bgn	ENSMUSG0000031375	-0.8980	3.48E-07	0.000104
Gpx4	ENSMUSG00000075706	0.3285	0.02350	0.6278	Rps3a1	ENSMUSG0000028081	-0.7338	6.09E-07	0.00017
									

Figure S1

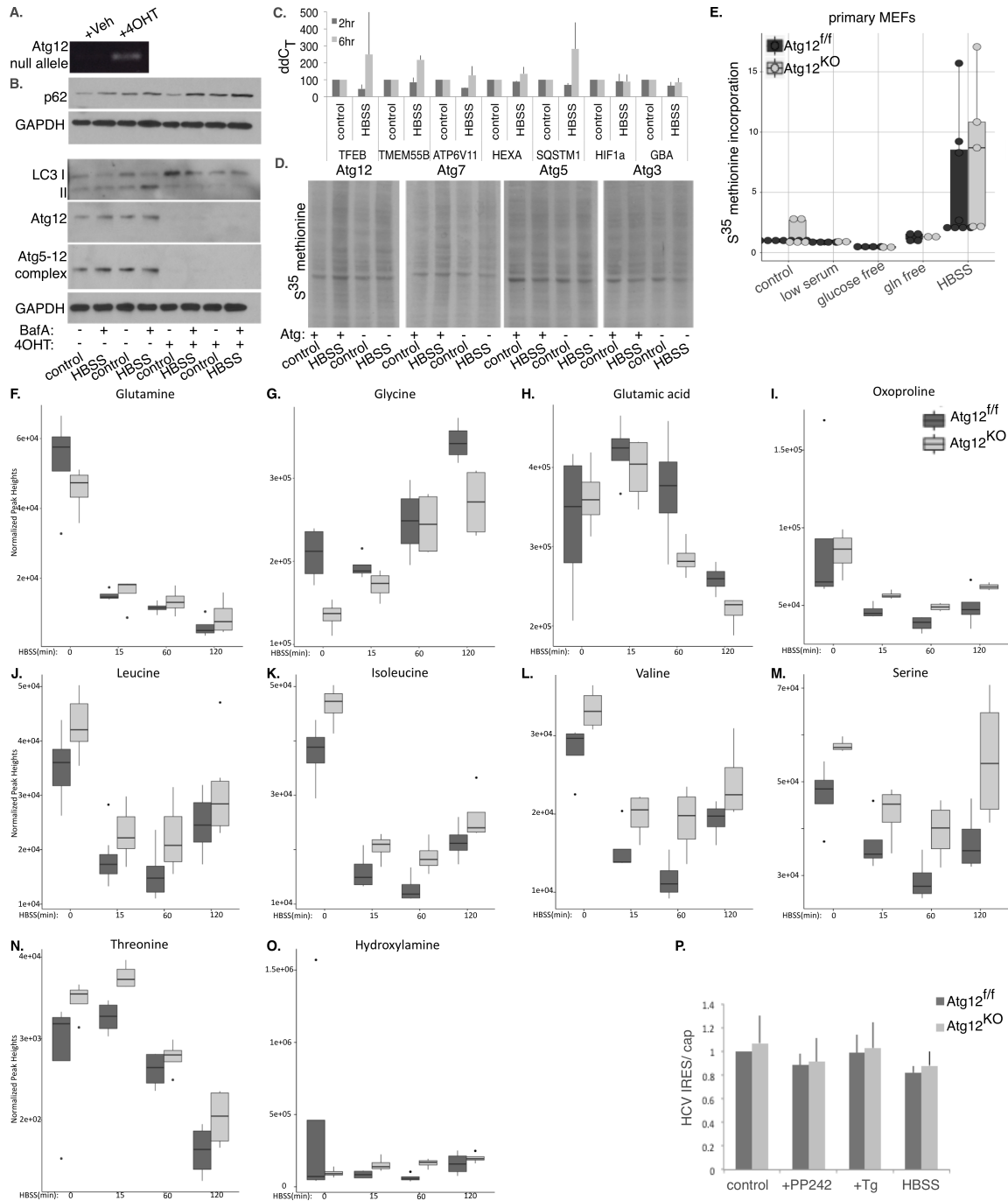


Figure S1: Analysis of Atg deletion in mouse embryonic fibroblasts (related to Figure 1)

- A. PCR of the null allele of Atg12 in immortalized Atg12^{ff} MEFs at 2d following treatment with vehicle control or 4OHT (20 μ M).
- B. Protein lysate collected from Atg12^{ff} MEFs five days following treatment with vehicle control or 4OHT (20 μ M). Indicated cells were incubated with fresh control (nutrient rich) media, or HBSS starved for 2h. When indicated, Bafilomycin A (Baf A, 2.5ng/ml) was added at 30min before lysis. Lysates were immunoblotted as indicated.
- C. Atg12^{ff} MEFs were grown in control media or subject to 2 or 6 hours of HBSS starvation. Quantification (mean \pm SD, n=3) of percent expression of various genes (as indicated) by qPCR with GAPDH as endogenous control is graphed.
- D. Representative ³⁵S-methionine incorporation autoradiogram for immortalized MEFs derived from mice genetically deleted for the indicated Atgs essential for autophagy. Cells were labeled and lysed in either methionine-free control conditions, or following 2h HBSS starvation.
- E. Primary Atg12^{ff} or Atg12^{KO} MEFs were grown in control media, and two hours prior to lysis were switched to control media lacking methionine, low (1%) serum media lacking methionine, media lacking glucose and methionine, media lacking glutamine and methionine, or HBSS. Cells were labeled with ³⁵S-methionine for 30 min prior to lysis. The relative ³⁵S-methionine incorporation rates is quantified and shown is a boxplot with dotplot overlay for each biological replicate, normalized to loading control.
- F-O. Normalized peak height data for individual metabolites from metabolomics profiling using gas chromatography time of flight mass spectrometry with the silylation reagent N-tert-butyldimethylsilyl- N-methyltrifluoroacetamide (GC-TOF with MTBSTFA). Boxplots of normalized peak height of each metabolite as indicated, in Atg12^{ff} or Atg12^{KO} MEFs grown in control media (t=0), or HBSS starved for the indicated times.
- P. Quantification (mean \pm SEM, n=5) of renilla luciferase activity driven by the Hepatitis C viral IRES motif, normalized to firefly luciferase activity driven by the cap. Luminescence was assayed using Dual-Glo reagents (Promega). PP242 (2 μ M for 1h) inhibits mTORC1 signaling, and thapsigargin (Tg, 1 μ M for 1h) induces IRES mediated translation.

Figure S2

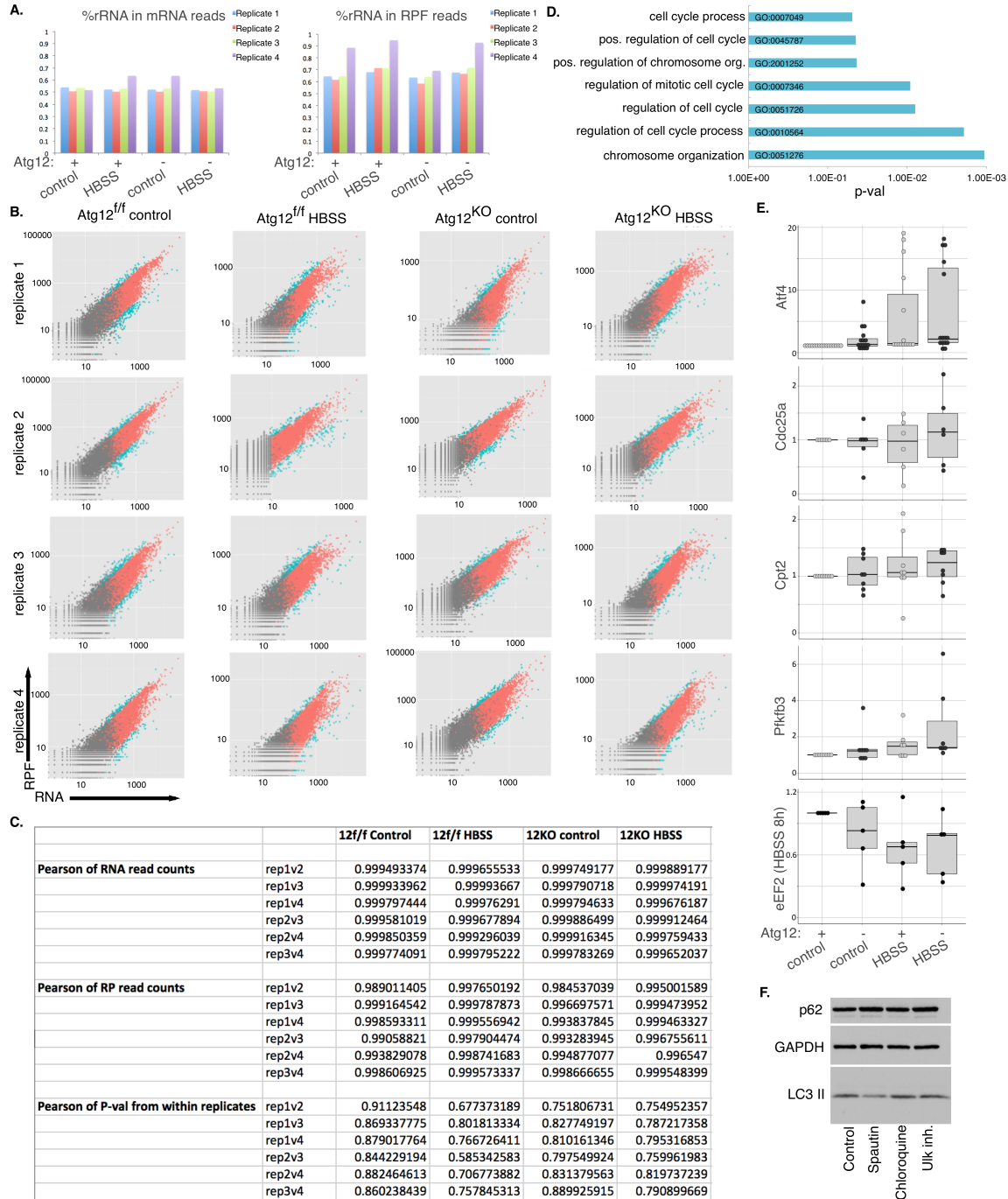


Figure S2: Ribosome profiling quality control metrics (related to Figure 2)
 A. Graph of percent of contaminating rRNA reads in total RNA samples and RPF samples from each biological replicate that were removed in Babel processing.
 B. Read counts of RPF by RNA per condition per biological replicate. Green dots are genes with one-sided p-value < 0.025 corresponding to increased or decreased RPF,

red dots are genes with one-sided p-value between 0.025 and 0.975, grey dots indicate one-sided p-value = NA.

C. Table of calculated Pearson correlation values between biological replicates per condition for RP.

D. Significantly enriched biological processes based on gene ontology (GO) analysis of mRNAs whose ribosome occupancy is significantly decreased in Atg12^{KO} versus Atg12^{ff} cells.

E. Quantification of immunoblot band intensity, normalized to control, for significant hits from RP analysis are shown by boxplots, with dotplot overlay for each biological replicate. Prior to lysis, Atg12^{ff} or Atg12^{KO} MEFs were maintained in control media, or starved in HBSS for 2 hours, unless indicated for 8 hours (last panel, eEF2).

F. Representative immunoblot of MEFs treated with Spautin-1 (50μM, 4h), chloroquine (20μM, 4h), or SBI-0206965 (10μM, 4h), stained for markers of autophagic flux and loading control as indicated.

Figure S3

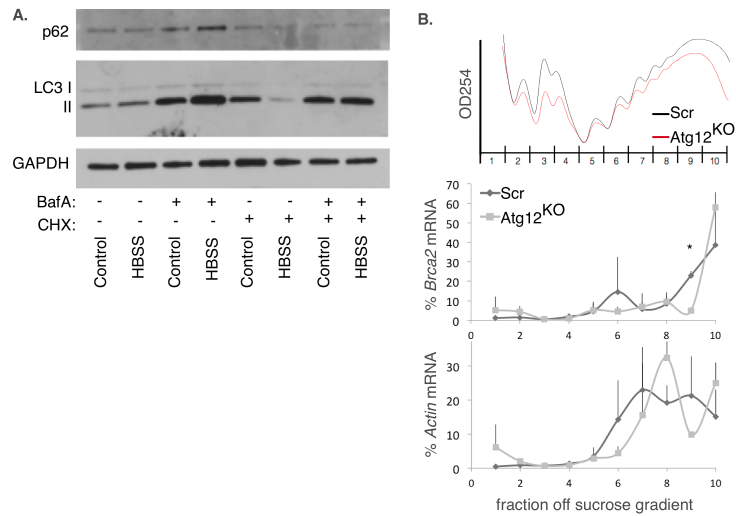


Figure S3: *Brca2* translation is impaired in autophagy deficient cells

A. Protein lysate was collected from MEFs treated with the lysosome inhibitor Bafilomycin A and cycloheximide (CHX) and immunoblotted for markers of autophagic turnover and loading controls as indicated.

B. Polysome profiling of scramble control and Atg12^{KO} HEK293Ts. Top: Representative polysome trace with fractions. Bottom: Percent of total *Brca2* mRNA and *Actin* mRNA per fraction measured by qPCR.

Figure S4

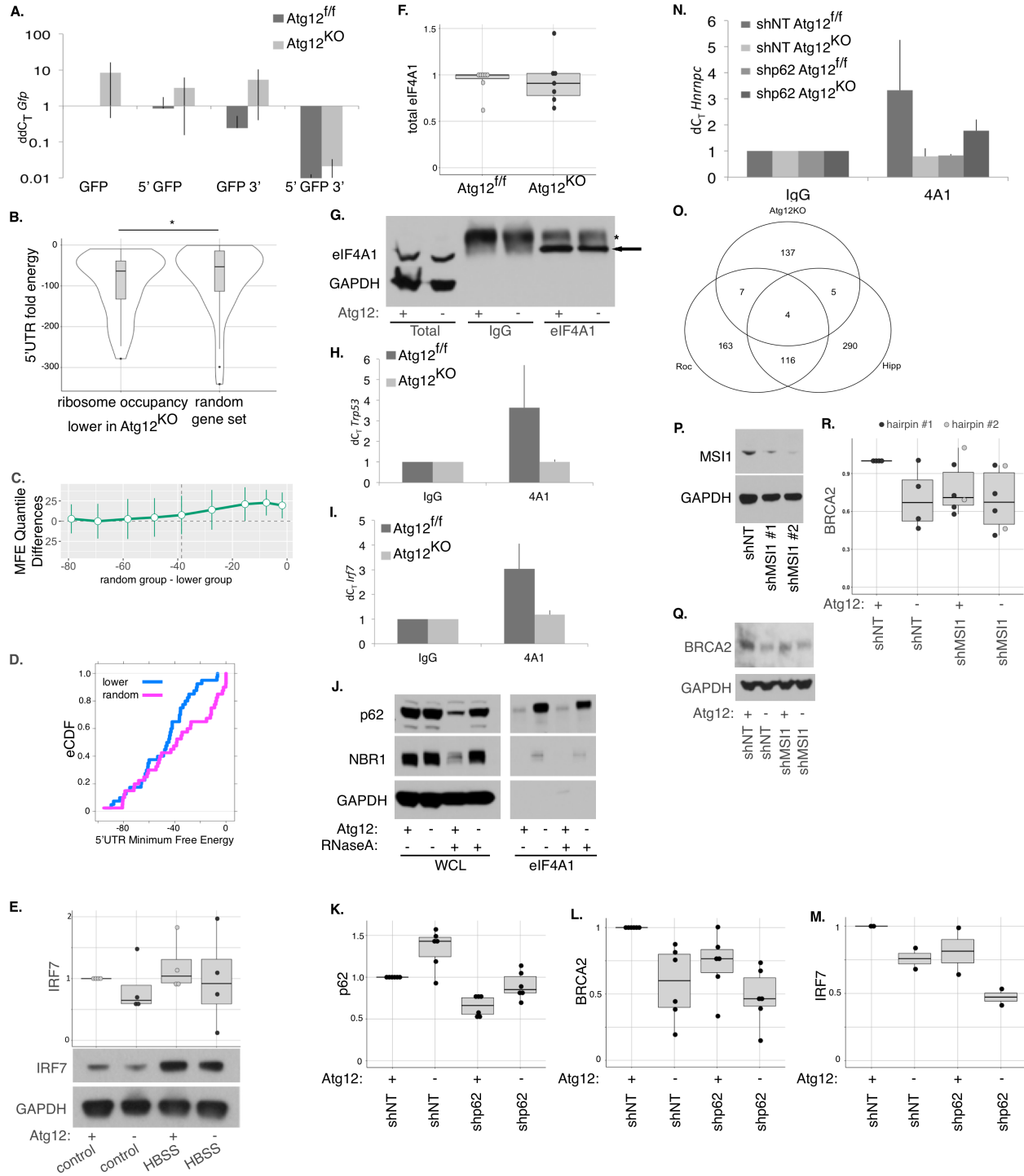


Figure S4: The 5'UTR of *Brca2* determines its translational response to autophagy (related to Figure 4)

A. qPCR for relative levels of *Gfp* in Atg12^{ff} and Atg12^{KO} MEFs transfected with the pcDNA3 *Brca2* UTR reporter plasmids, using *Gapdh* as an endogenous control (mean \pm SD, n=3).

B. Plot of 5'UTR fold energies (boxplots on violin plots) from mRNAs with significantly lower than expected ribosome occupancy in Atg12^{KO} MEFs compared to a randomly generated gene set from the mouse genome of equivalent length. Asterisk indicates p-value = 0.02 by Wilcoxon rank sum test.

C-D. Local minimum free energy (MFE) was predicted by RNALfold in the 5'UTRs from mRNAs with significantly lower than expected ribosome occupancy in Atg12^{KO} MEFs (lower group) compared to a randomly generated gene set (random group). (C) The quantile differences between the MFEs of the two groups is graphed. (D) The empirical cumulative distribution function (eCDF) of the MFEs is plotted.

E. Protein lysate was collected from Atg12^{ff} or Atg12^{KO} MEFs grown in control media or starved in HBSS for 2h. IRF7 levels were measured by immunoblotting. Relative quantification from immunoblots for IRF7 normalized to loading control is shown in the boxplot with dotplot overlay per biological replicate. Bottom: representative immunoblot.

F. Protein lysate from Atg12^{ff} and Atg12^{KO} MEFs was collected and immunoblotted for eIF4A1. Relative levels normalized to loading control were quantified; a boxplot with dotplot overlay for each biological replicate is shown.

G. Representative immunoblot for eIF4A1 and GAPDH following RNA immunoprecipitation is shown. Arrow indicates eIF4A1, asterisk indicates immunoglobulin heavy chain.

H-I. Quantification (mean \pm SD, n=3) of the fold enrichment of (H) *Trp53* and (I) *Irf7* interaction with eIF4A1 over IgG control in Atg12^{ff} or Atg12^{KO} MEFs by RNA immunoprecipitation experiments.

J. Representative immunoblot for the autophagy cargo receptors p62/SQSTM1 and NBR1 following immunoprecipitation for eIF4A1 in Atg12^{ff} or Atg12^{KO} MEFs treated with or without RNaseA (10mg/ml for 30min at RT).

K-M. Protein lysate from Atg12^{ff} or Atg12^{KO} MEFs stably infected with shRNA to p62/SQSTM1 or non-targeting control was collected. Relative quantification from immunoblots for (K) p62/SQSTM1, (L) BRCA2, and (M) IRF7 normalized to loading control is shown in the boxplot with dotplot overlay per biological replicate.

N. Quantification (mean \pm SD, n=3) of the fold enrichment of *Hnrnp35* interaction with eIF4A1 over IgG control in Atg12^{ff} or Atg12^{KO} MEFs that were knocked down for p62/SQSTM1 or treated with non-targeting shRNA, assayed by RNA immunoprecipitation.

O. Venn diagram showing overlap of mRNAs whose translation is sensitive (decreased ribosome occupancy) to autophagy inhibition (Atg12KO), the eIF4A1 inhibitor Rocaglate A (Roc), and the eIF4A1 inhibitor Hippuristanol (Hipp) (data from Iwasaki et al, 2016).

P. Protein lysate was collected from Atg12^{ff} MEFs treated with shRNA to MSI1, and immunoblotted as indicated.

Q. Protein lysate was collected from Atg12^{ff} MEFs that were stably knocked down for MSI1 and subsequently treated with 4OHT or control. Representative immunoblot of BRCA2 and GAPDH is shown.

R. Boxplot, with dotplot overlay for each biological replicate, of relative BRCA2 protein levels normalized to loading control from autophagy inhibited, MSI1 knock down MEFs, assayed by immunoblotting.

Figure S5

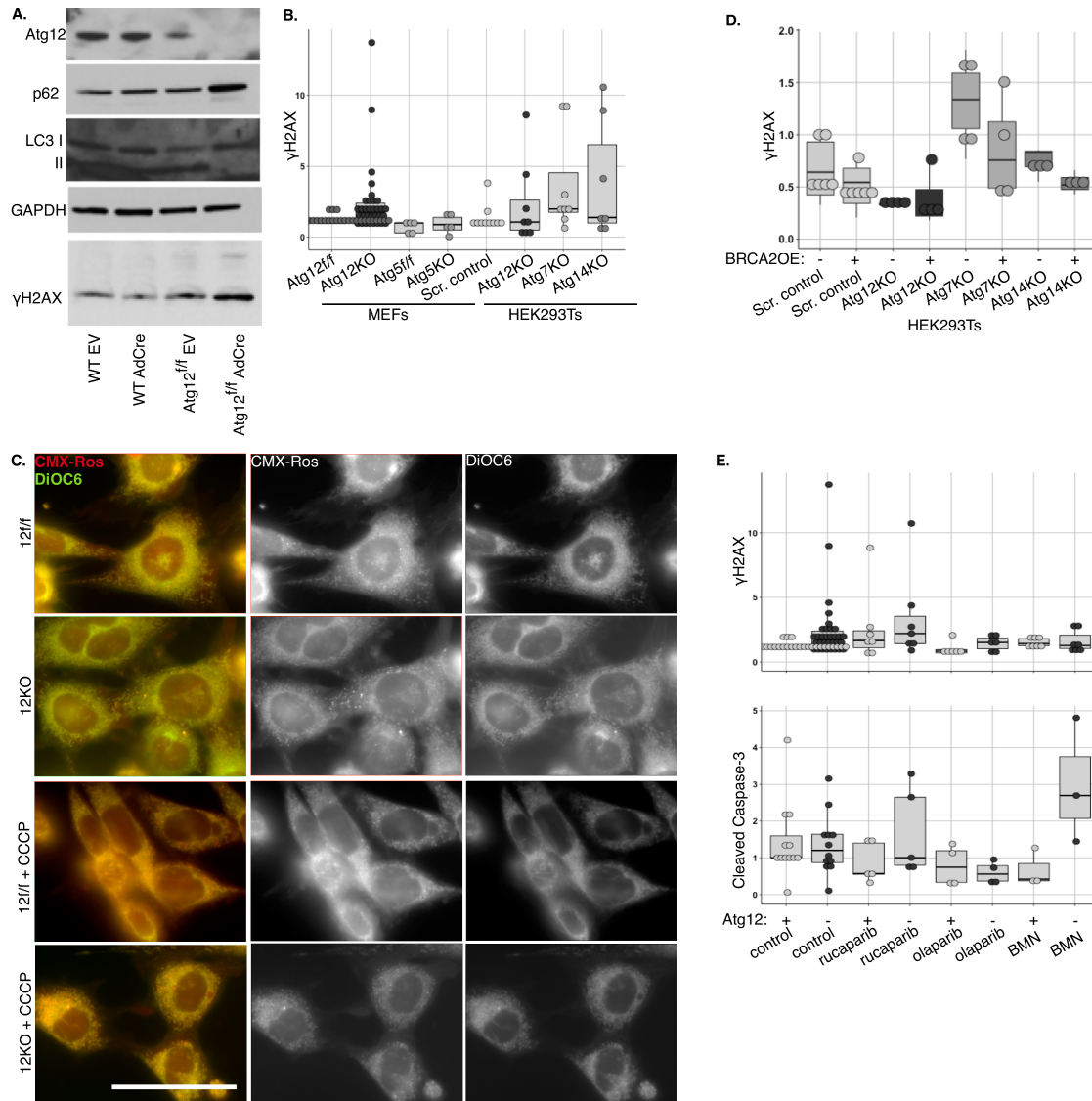


Figure S5: Autophagy inhibition causes increased DNA damage independent of ROS, and sensitizes cells to PARP inhibitors (related to Figure 5)

A. WT MEFs and Atg12^{ff/ff} MEFs were infected with Adenovirus expressing empty vector or Cre and 5d post infection protein lysate was collected and immunoblotted for Atg12, markers of autophagic flux (p62/SQSTM1, LC3), and DNA damage (γH2AX) as indicated.

B. Protein lysate was collected from MEFs and HEK293Ts that were genetically deleted for essential autophagy genes. Relative γH2AX protein levels as detected by immunoblot, normalized to loading control, were quantified and boxplot with dotplot overlay for each biological replicate is shown.

C. Atg12^{ff/ff} or Atg12^{KO} MEFs were stained for mitochondria using MitoTracker Red CMX-Ros (500nM for 15min), and membrane potential of mitochondria by DiOC6(3) (10ng/ml

for 5min), under normal conditions and following CCCP treatment (50 μ M for 30min). Representative immunofluorescence image is shown. Bar = 50 μ m.

D. Ectopic expression of either GFP (BRCA2OE negative) or human BRCA2 (BRCA2OE positive) in HEK293T cells lacking the indicated Atgs was performed. Relative γ H2AX protein levels, normalized to loading control, as detected by immunoblotting were quantified and a boxplot with dotplot overlay for each biological replicate is shown.

E. Atg12^{fl/fl} or Atg12^{KO} MEFs were treated for 16h with vehicle control, or the PARP inhibitors rucaparib (100nM), olaparib (100nM) or BMN (2nM) prior to lysis. Boxplot with dotplot overlay for each biological replicate is shown for relative γ H2AX and cleaved caspase 3 protein levels, normalized to loading control, as detected by immunoblotting.

Materials and Methods

Contact for Reagent and Resource sharing

Please contact J.D. (jayanta.debnath@ucsf.edu) for reagents and resources generated in this study

Experimental models and subject details

Mouse maintenance

Compound transgenic C57Bl/6 mice harboring $Atg12^{ff}$ and $Cag-Cre^{ER}$ were generated by cross-breeding of $Atg12^{ff}$ (Malhotra et al, 2015) and $CagCre^{ER}$ animals (Hayashi, S. & McMahon, 2002) (obtained via the UCSF mouse database). Offspring were genotyped with polymerase chain reaction (PCR) primers listed in the key resources table. At 6 weeks of age, animals of indicated genotypes received either Tamoxifen (0.2mg/gram mouse) or vehicle (peanut oil) via oral gavage for 5 consecutive days. At 10 weeks after the first tamoxifen treatment, animals were sacrificed and tissues were collected for biochemical and histological analysis. All experimental procedures and treatments were conducted in compliance with UCSF Institutional Animal Care and Use Committee guidelines.

Isolation of mouse embryonic fibroblasts

Mouse embryonic fibroblasts were generated from E13.5 mice described above following the protocol from Robertson (1987). Briefly, embryos were collected, heart, liver and head were removed and fibroblasts were minced, digested in trypsin for 30min at 37°C and plated in DMEM with 10% serum and Pen/Strep. Cells were genotyped and

Atg12^{ff};Cag-Cre^{ER+} cells were immortalized by infection with SV40 large T antigen. Cells were plasmocin treated prior to use. Following immortalization and plasmocin treatment, cells were maintained in DMEM 1x (Gibco) supplemented with 10% FBS (Atlas).

Genetic deletion of MEFs

Cells were treated with 2 μ M 4-Hydroxy-tamoxifen (4OHT) or vehicle (100% Ethanol) for three consecutive days. Genetic recombination was achieved following 2 days of 4OHT treatment, and confirmed by PCR.

Additional tissue culture cells

N. Mizushima (University of Tokyo, Japan) provided Atg5^{+/+}, Atg5^{-/-}, Atg7^{+/+} and Atg7^{-/-} MEFs and M. Komatsu (Tokyo Metropolitan Institute, Japan) provided Atg3^{+/+} and Atg3^{-/-} MEFs. Atg12^{+/+} and Atg12^{-/-} MEFs were originally generated in Malhotra et al, 2015. HEK293Ts were cultured in DMEM 1x (Gibco) supplemented with 10% FBS (Atlas) and Pen/Strep. HEK293T knockout cell lines lacking Atg7, Atg12 or Atg14 were generated by CRISPR/Cas9. Human guide sequences (listed in the key resource table) were ligated into pSpCas9(BB)-2A-Puro (PX459) plasmid using the BbsI site. HEK293T cells were transfected with plasmid DNA using Lipofectamine 3000. Cells were selected 48-72 hours post-transfection with 1mg/ml puromycin for 48 h. Polyclonal populations were collected for Surveyor analysis (IDT, 706020) and were sorted into single-cell populations by limiting dilution at 1.5 cells/well per 96-well plate. Monoclonal wells were identified, expanded, and analyzed. For DNA analysis, genomic DNA samples were

prepared using QuickExtract (Epicentre). The PCR products were column purified and analyzed with Surveyor Mutation Detection Kit (IDT). For genotyping of single-sorted cells, PCR amplified products encompassing the edited region were cloned into pCR™4-TOPO® TA vector using the TOPO-TA cloning kit (Thermo Fisher #450030) and sequence verified. Sequencing is available upon request.

Stable RNA interference

pLKO .1blasticidin or pLKO.1puromycin lentiviral plasmids with nontargeting shRNA, which targets no known mammalian genes, or shRNA against mouse ATG7, mouse p62/SQSTM1, or mouse MSI1 were purchased from Sigma-Aldrich. shRNA lentivirus was prepared by cotransfecting HEK293T cells with packaging and envelope vectors and pLKO .1 shRNA expression plasmids. Virus was collected 48 h after transfection, filtered through a 0.45- μ m filter, and stored at -80°C . Cells were seeded in six-well dishes and infected for generation of stable cell lines. Stable pools of knockdown cells were obtained by selecting with 2ng/ml blasticidin or 1-2 μ g/ml puromycin for 48 h.

Plasmid overexpression

MEFs were transfected using the Amaxa Nucleofector device (Lonza), program T-020, MEF 1 nucleofector kit and 2 μ g DNA, according to manufacturer's instructions. For all transfections, efficiency was monitored by qPCR.

Method details

Ribosome profiling

Ribosome profiling experiments were performed using the ARTseq Ribosome profiling kit (Epicentre), with RNA extraction by Trizol LS (Ambion), rRNA depletion via RiboZero Gold (Epicentre), and quality and quantity of small RNA and DNA assayed using Agilent High Sensitivity Small RNA kit and DNA kit respectively (Agilent). Sequencing was performed at the UCSF sequencing core on Illumina HiSeq2000, and analysis of reads was performed using Babel (Olshen et al, 2013). Cycloheximide was made fresh to 50mg/ml in Ethanol for each experiment, used at a concentration of 100µg/ml.

Polysome profiling and qPCR

The protocol was followed from Morita et al, 2013 (Morita et al, 2013. Polysome Profiling Analysis. Bio-protocol 3(14): e833. DOI: 10.21769/BioProtoc.833). Briefly, 4 million cells treated with cyclohexamide as described above were collected in PBS, lysed in 5mM Tris-HCl, pH7.5, 2.5mM MgCl₂, 1.5mM KCl, 0.5% Triton X-100, 0.5% Sodium deoxycholate, with protease inhibitors, cyclohexamide, DTT, and RNase inhibitor added just prior to lysis. OD_{260nm} was measured and equal OD amount of lysate was loaded on each 10-50% sucrose gradient. Cells were centrifuged at 35,000 rpm for 2h at 4C and RNA analysis was performed using the Biocomp gradient station, gradient profiler and Biorad Econo UV monitor. Subsequently, RNA was precipitated and purified using Trizol LS and qPCR was performed using Agilent Brilliant II SYBR green QRT PCR 1 step reagents and read using the Applied Biosystems Step One plus real time PCR system (ThermoFisher).

Immunoblotting

For immunoblot analysis, 200,000 - 300,000 cells were lysed in RIPA buffer (1% Triton X-100, 1% sodium deoxycholate, 0.1% SDS, 25mM Tris, pH 7.6, and 150mM NaCl) plus protease inhibitor cocktail (Sigma-Aldrich), 10mM NaF, 10mM β -glycerophosphate, 1mM Na_3VO_4 , 10nM calyculin A, 0.5mM PMSF, 10 $\mu\text{g}/\text{ml}$ E64d, and 10 $\mu\text{g}/\text{ml}$ pepstatin A. Lysates were freeze-thawed at -20°C , cleared by centrifugation for 30 min at 4°C , protein content was quantified by BCA assay and equal amounts were boiled in sample buffer, resolved by SDS-PAGE, and transferred to polyvinylidene fluoride membrane. Membranes were blocked for 1 h in 5% milk or 5% BSA in PBS with 0.1% Tween 20, incubated in primary antibody overnight at 4°C , washed, incubated for 1 h at RT with HRP-conjugated goat secondary antibodies (1:5,000; Jackson ImmunoResearch Laboratories), washed, and visualized via enhanced chemiluminescence (Thermo Fisher Scientific).

Metabolic labeling

200,000 cells were grown in 6-well plates and incubated for 1.5h DMEM lacking methionine, DMEM lacking methionine and glucose, DMEM lacking methionine and glutamine (UCSF cell culture facility) or HBSS (Gibco), upon which 30 μCi of exogenous $^{35}\text{-S}$ L-Methionine (Perkin Elmer) was added for 30min. Cells were washed in PBS, lysed in RIPA buffer, protein content was quantified by BCA assay and equal total protein per sample was run on SDS-PAGE gels and transferred to PVDF as described above.

AHA labeling

Azidohomoalanine was added to methionine free DMEM at a final concentration of 40uM and left to incorporate in HEK293Ts for 8h. Subsequently, cell lysate was collected for immunoprecipitation. Following immunoprecipitation, the azide-alkyne conjugation reaction was performed using Diazo Biotin alkyne and the ClickIT kit in a quarter volume, according to manufacturer's instructions.

Immunoprecipitation, RNA immunoprecipitation, cap pulldown assays

Antibodies used for immunoprecipitation are listed in the key resources table. Cells were lysed in the following buffers: immunoprecipitation (IP) buffer: 25mM Tris HCl pH 7.4, 150mM NaCl, 1% NP-40, 5% glycerol, 1mM EDTA, 1mM EGTA, 1mM β -glycerophosphate, 10mM NaF, 2.5mM NaP₂O₇, 1 μ M sodium orthovanadate, plus protease inhibitor cocktail. RNA immunoprecipitation (RIP) buffer: 200mM NaCl, 25mM Tris HCl pH 7.4, 5mM EDTA, 5% glycerol, 1mM DTT, 1% NP-40, plus protease inhibitor cocktail and RNase inhibitors. Cap pulldown (CPD) buffer: 10mM Tris HCl pH 7.6, 140mM KCl, 4mM MgCl₂, 1mM DTT, 1mM EDTA, 1% NP-40, 1mM PMSF, protease inhibitor cocktail, 0.2mM sodium orthovanadate.

For immunoprecipitation (IP) and RNA immunoprecipitation (RIP), lysates were precleared with protein A/G (Santa Cruz) and incubated on a rotating shaker overnight at 4°C with protein A/G plus antibody. For IP, beads were washed four times with IP buffer, eluted in 3x sample buffer and analyzed by immunoblotting. For RIP, washed beads were split into a protein fraction and an RNA fraction. The protein fraction was subject to IP as described above. The RNA fraction was extracted with Trizol LS and

bound RNA was analyzed by qPCR. For cap pulldown experiments (CPD), cells were lysed in buffer listed below. 25-50 μ l of m7-GTP beads were added to 250-500 μ g protein at 1 μ g/ μ l and incubated overnight. Beads were washed four times in CPD buffer, eluted in 3x sample buffer and analyzed by immunoblotting.

Immunofluorescence

20,000 cells were grown on fibronectin-coated (10 μ g/ml in PBS) coverslips. Cells were fixed with 4% PFA for 5 min at RT, permeabilized with 0.5% Triton X-100 in PBS, rinsed with PBS-glycine, and blocked overnight at 4°C in blocking buffer (10% goat serum and 0.2% Triton X-100 in PBS). Cells were incubated with primary antibodies for 40min at RT, washed, incubated with Alexa-Fluor 488 or 594 goat secondary antibodies (1:200; Life Technologies) for 40 min at RT, washed, nuclei were stained using Hoescht and mounted using Prolong Gold Anti-Fade mounting medium (Life Technologies).

Tissues were paraffin embedded and sectioned by the UCSF Helen Diller Family Cancer Center mouse pathology core. Deparaffinization in xylene followed by antigen retrieval per manufacturer's instructions (Dako) was performed prior to immunofluorescence staining.

Epifluorescence images were obtained at ambient temperature using an Axiovert 200 microscope (Carl Zeiss) with a 10 \times (NA, 0.25) or 20 \times (NA, 0.4) objective, Spot RT camera (Diagnostic Instruments). High magnification images were taken using the DeltaVision deconvolution microscope (Applied Precision) with a 60 1.42 NA Plan Apo objective (Olympus).

Image analysis

Immunoblot band intensity quantification was performed using ImageJ software.

Immunofluorescence colocalization was performed using ImageJ software (JACoP plugin).

Molecular cloning

GFP and luciferase reporters were created by cloning the UTR sequences of BRCA2 into pcDNA3.EGFP plasmid and pNL1.1nano-luciferase plasmid, using the primers described in the key resources table. The ~500bp 5'UTR of Brca2 that encompasses the region present in the shorter isoform of the Brca2 5'UTR was cloned using Gibson cloning, and the 3'UTR was cloned between restriction enzyme sites XhoI and XbaI.

Human LC3B (NM_022818.4), LC3A (NM_032514.3), LC3C (NM_001004343.2), GABARAP (NM_007278.1), GABARAPL1 (NM_031412.2), and GABARAPL2 (NM_007285.6) were subcloned from mRNA isolated from human cell lines that was reverse transcribed using AccuScript High Fidelity Reverse Transcriptase (Agilent) and cDNA amplified using PfuUltra II Hot Start DNA polymerase and gene specific primers listed in the key resources table. Subsequently, the cDNAs were subcloned into pcDNA3 between the BamHI and XhoI or EcoRI and XhoI restriction sites downstream of an N-terminal myc-tag or 3xFlag-tag. All constructs were verified by sequencing.

IRES reporter assay

HCV and CrPV plasmids were transfected into Atg12^{ff} or Atg12^{KO} MEFs as described above. Ratio of Renilla to Firefly luciferase was assayed using DualGlo reagents (Promega) and luminescence (AU) was read by spectrometer.

Crystal violet assay.

2000 cells were plated per well in 96-well plates. At time (t)=0 and 24h, plates were fixed with 4% paraformaldehyde and stained in 0.3% crystal violet in water for 1hr, and washed in distilled water until control empty wells were rinsed clean. The crystal violet stain was solubilized in 100% methanol, and A590 measured by spectrometer. Percent growth (mean ± SEM) was calculated as $(\text{Abs.t24} - \text{Abs.t0})/\text{Abs.t0}$.

Clonogenic replating assay

Cells were grown in control conditions and treated as indicated for 16h. Following treatment, the cells were trypsinized and 500 live cells were plated in control media, and allowed to grow for 10 days. Colonies were fixed in 4% PFA, stained by crystal violet and counted.

Propidium Iodide staining and double thymidine block and release

Cell cycle analysis was performed either without or with synchronization via thymidine block and release. Briefly, thymidine was added to cells at 2mM for 24h, then released into media containing 25 μ M 2'deoxyctidine for 24h, then washed and released into fresh media and fixed at various time points following the washout. Cells were

trypsinized and fixed in ice cold methanol and stored at -20°C. Cells were stained in 3.8mM sodium citrate, 25µg/ml PI and 10µg/ml RNase A in PBS. Flow was performed on an LSRII SORP machine and analysis of percent of cells in various cell cycle stages was performed using FlowJo. Flow Cytometry data was generated in the UCSF Parnassus Flow Cytometry Core which is supported by the Diabetes Research Center (DRC) grant, NIH P30 DK063720.

Metabolomics

6 million cells per condition (n=4) were washed in PBS and pelleted before being snap frozen. Gas chromatography time of flight mass spectrometry with the silylation reagent N-tert-butyldimethylsilyl- N-methyltrifluoroacetamide (GC-TOF with MTBSTFA) was performed at the West Coast Metabolomics Center at the University of California, Davis.

Statistical analysis

Statistical analysis of ribosome profiling data was performed using Babel (Olshen et al, 2013). Details of statistical analyses of experiments and number of biological replicates (n) can be found in the figure legends. Unless otherwise stated, statistical significance was assessed using the two-sample equal variance t-test with a cutoff of 0.05 for significance. Statistical testing of percentages were performed using either fisher's exact test (Fig2M) after thresholding the data, or the two-sample t-test on logit transformed percentages per biological replicate (Fig5J). The Wilcoxon rank-sum test was used in one case so as not to make distributional assumptions about the data (Fig4G). The

Kolmogorov-Smirnov test was used in Fig4H. Statistical testing was performed in Excel or R.

KEY RESOURCES TABLE

REAGENT or RESOURCE	SOURCE	IDENTIFIER
Antibodies		
anti-BRCA2 rabbit pAb	Bioss USA	bs1210R
anti-p62 guinea pig pAb	Progen	GP-62-C
anti-LC3 mouse pAb	Fung, et al 2008. (commercially available from EMD Millipore)	ABC232
anti-phospho-S6 S240/244 rabbit mAb	Cell signaling	#2215
anti-S6 rabbit mAb	Cell signaling	#2217
anti- α tubulin rabbit mAb	Cell signaling	#2125BC
anti-phospho-4EBP1 S65 rabbit pAb	Cell signaling	#9451
anti-4EBP1 rabbit pAb	Cell signaling	#9452
anti-GAPDH mouse mAb	Millipore	MAB374
anti-phospho-eIF2 α S51 rabbit pAb	Cell signaling	#9721
anti-eIF2 α rabbit pAb	Cell signaling	#9722
anti-eIF4G1 rabbit mAb	Cell signaling	#2469
anti-eIF4G2 rabbit pAb	Cell signaling	#2182
anti-eIF4E rabbit pAb	Cell signaling	#9742
anti-eIF4E2 rabbit pAb	Pierce	#PA5-11798
anti-Atg12 (mouse specific) rabbit pAb	Cell signaling	#2011BC
anti-Atg5 rabbit pAb	Novus Biologicals	NB110-53818
anti-Atg7 rabbit pAb	Cell signaling	#2631
anti-Phospho-histone H3 S10 rabbit pAb	Cell signaling	#9701
anti-Atf4 rabbit mAb	Cell signaling	#11815
anti-Cdc25a rabbit pAb	Cell signaling	#3652
anti-Cpt2 rabbit pAb	Abcam	ab71435
anti-Pfkfb3 rabbit pAb	ABclonal Biotech	A6945
anti-eEF2 rabbit pAb	Cell signaling	#2332
anti-Mcl-1 rabbit pAb	Rockland	800-401-394S
anti-Irf7 rabbit mAb	Abcam	ab109255
anti- γ H2AX S139 mouse mAb (for immunoblot)	Upstate	#05-636
anti- γ H2AX S139 rabbit pAb (for immunofluorescence)	Cell signaling	#9718S
anti-53BP1 rabbit pAb	Abcam	ab21083
anti-Cleaved PARP (Asp214) (mouse specific) rabbit pAb	Cell signaling	#9544S
anti-Cleaved Caspase 3 (Asp175) rabbit pAb	Cell signaling	#9661
anti- γ tubulin mouse mAb	Sigma	T5326-100ul
anti-CREST human pAb	Antibodies Inc.	# 15-234-0001
anti-eIF4A1 rabbit pAb	Cell signaling	#2490
anti-NBR1 (4BR) mouse mAb	Santa Cruz Biotechnology	sc1030380

REAGENT or RESOURCE	SOURCE	IDENTIFIER
normal rabbit IgG	Santa Cruz Biotechnology	sc2027
anti-BRCA2 rabbit pAb (for immunoprecipitation)	Abcam	ab123491
anti-MSI1 rabbit pAb	EMD Millipore	AB5977
streptavidin HRP conjugate	Thermo Scientific Pierce	21130
anti-GFP mouse mAb	Neuromab	N86/8
REAGENT or RESOURCE	SOURCE	IDENTIFIER
Bacterial and Virus Strains		
Biological Samples		
Chemicals, Peptides, and Recombinant Proteins		
Methionine, L-[35S]-Premium stabilized	Perkin Elmer	NEG009A001MC
PP242	Tocris	4257
Thapsigargin	Cayman Chemical Company	10522
Cycloheximide	Sigma-Aldrich	C7698
Propidium iodide	Sigma-Aldrich	P4170-25MG
Paclitaxel	Sigma-Aldrich	T7402-1MG
Hoechst	Intergen	S7304-5
Rucaparib	Selleck Chemicals	S1098
Olaparib	Cellagen Technologies	C2228-5s
BMN 637	Gift from Alan Ashworth (Shen et al, 2013), Commercially available from Selleck Chemicals	S7048
Nocodazole	Sigma-Aldrich	M1404-2MG
Doxorubicin	Sigma-Aldrich	44583-1MG
Actinomycin D	Sigma-Aldrich	A1410
Hydroxyurea	Sigma-Aldrich	H8627
Griseofulvin	Sigma-Aldrich	G4753-5G
Roscovitine	Selleck Chemicals	CYC202
menadione	Sigma-Aldrich	M5625
DiOC6(3) (3,3'-Dihexyloxycarbocyanine Iodide)	Thermo Fisher Scientific	D273
tamoxifen	Sigma-Aldrich	T5648-1G
N-acetyl cysteine	Sigma-Aldrich	A7250
thymidine	Sigma-Aldrich	T9250-5G
2'deoxyctidine	Sigma-Aldrich	D3897-250MG
RNaseA	Sigma-Aldrich	R6513
Superase Inhibitor	Invitrogen	AM2696
4-hydroxy tamoxifen	Sigma-Aldrich	H7904
Protein A/G PLUS-Agarose	Santa Cruz Biotechnology	sc-2003

REAGENT or RESOURCE	SOURCE	IDENTIFIER
Spautin-1	Sigma Aldrich	SML0440-5MG
Chloroquine diphosphate salt	Sigma Aldrich	C6628-25G
SBI-0206965	Cayman Chemical company	18477
Critical Commercial Assays		
γ -amino-phenyl-m7 GTP (C10-spacer)	Jena biosciences	AC155S
Ribo-zero magnetic Gold Kit	Epicenter	MRZG126
Ribosome profiling kit	Epicenter	RPHMR12126
Agilent high sensitivity DNA guide	Agilent	5067-4626
Agilent small RNA guide	Agilent	5067-1548
Ros-glo luciferase assay	Promega	G8820
MitoTracker Red CMX-Ros	Thermo Fisher Scientific	M7512
Dual-Glo Luciferase assay system	Promega	E2920
Nano-glo luciferase assay system	Promega	N1120
Brilliant II SYBR green QRT PCR 1 step	Agilent Technologies	600825
Amaxa nucleofector MEF1 kit	Lonza	VPD-1004
Plasmocin	Invivogen	ant-mpt
Click-iT-AHA	Thermo Fisher Scientific	C10102
Click-iT reaction kit	Thermo Fisher Scientific	C10276
Diazo Biotin Alkyne	Jena Biosciences	CLK-1042-10
RNase A	Sigma Aldrich	R6513
Deposited Data		
Ribosome profiling data	This paper	
Experimental Models: Cell Lines		
Mouse: Embryonic Fibroblast cells, Atg12 tm Cag-Cre ^{ER+}	This paper	NA
Human: HEK293T	ATCC	CRL-3216
Mouse: MEFs Atg3 ^{+/+} and -/-	Gift from M. Komatsu	NA
Mouse: MEFs Atg5 ^{+/+} and -/-	Gift from N. Mizushima	NA
Mouse: MEFs Atg7 ^{+/+} and -/-	Gift from N. Mizushima	NA
Mouse: MEFs Atg12 ^{+/+} and -/-	Malhotra et al, 2015	NA
Experimental Models: Organisms/Strains		
Atg12 tm ;CagCre ^{ER+} transgenic mice	This paper	NA
Oligonucleotides		
msTFEB primers for qPCR: Forward: AGAACCCACCTCCTACCAC Reverse: GGACTGTTGGGAGCACTGTT	This paper	NA

REAGENT or RESOURCE	SOURCE	IDENTIFIER
msTMEM55B primers for qPCR: Forward: CGTACGGAGCCGGTAAACAT Reverse: TGATCGGAGACTGACAGACG	This paper	NA
msATP6V11 primers for qPCR: Forward: GATTGGAATGGAGCCCTGTA Reverse: TGCTCAATAACCCGTTTTCC	This paper	NA
msHEXA primers for qPCR: Forward: GCCATTACCTGCCATTGTCT Reverse: ACCTCCTTCACATCCTGTGC	This paper	NA
msSQSTM1 primers for qPCR: Forward: CCTTGCCCTACAGCTGAGTC Reverse: CTTGTCTTCTGTGCC GTGC	This paper	NA
msHIF1alpha primers for qPCR: Forward: TCAAGTCAGCAACGTGGAAG Reverse: TATCGAGGCTGTGTGCGACTG	This paper	NA
msGBA primers for qPCR: Forward: TGGGTACCTTCAGCCGTTAC Reverse: GAGTAGGTGGGGACAAAGCA	This paper	NA
msBrca2 primers for qPCR: Forward: CTTACCGAGCATCGGAGAAA Reverse: CCGTGGGGCTTATACTCAGA	This paper	NA
GFP primers for qPCR: Forward: CTTCTTCAAGGACGACGGCAA Reverse: CTTGAACTCGATGCCCTTCAGC	This paper	NA
msGAPDH primers for qPCR: Forward: TGTGAGGGAGATGCTCAGTG Reverse: GGCATTGCTCTCAATGACAA	This paper	NA
msAtg12 ^{fl} primers for genotyping PCR: FRT h/h sense 1: ATG TGA ATC AGT CCT TTG CCC FRT-FRT as-2: ACT CTG AAG GCG TTC ACG GC WT-FRT as 2: CTC TGA AGG CGT TCA CAA CA	Malhotra et al, 2015	NA
Cag-CreER primers for genotyping PCR: Forward: GCCTGCATTACCGGTTCGATGC Reverse: CAGGGTGTATAAGCAATCCC	Hayashi and McMahon, 2002	NA
msAtg12 null allele primers for PCR: Forward: CACCCTGCTTTTACGAAGCCCA Reverse: ACTCTGAAGGCGTTCACGGC	Malhotra et al, 2015	NA
Primers for msBrca2 5'UTR cloning: Forward: CGACTCACTATAGGGAGACCCAAGCTTGGTACCGG GCTTTTCGCGGGAGCGGG Reverse: TTTTTGTTCATGGTAGATCCGAGTCTGGTACCTTCT CTACAGTATTTCTCCGATGCTCG	This paper	NA
Primers for msBrca2 3'UTR cloning: Forward: GATCCTCGAGCCTCCCGGTTTGTAAAGATGTGTACAG TTC Reverse: GATCTCTAGATTACAGCTGAAGTTCAGTGAGAGCAT CCAC	This paper	NA

REAGENT or RESOURCE	SOURCE	IDENTIFIER
huBrca2 primers for qPCR: Forward: TGCCTGAAAACCGATGACTATC Reverse: AGGCCAGCAAACCTCCGTTTA	This paper	NA
CRISPR guide sequences scramble: gcactaccagagctaactca	This paper	NA
CRISPR guide sequences huAtg12: CCGTCTTCCGCTGCAGTTTC	This paper	NA
CRISPR guide sequences huAtg7: ACACACTCGAGTCTTTCAAG	This paper	NA
CRISPR guide sequences huAtg14: CTACTTCGACGGCCGCGACC	This paper	NA
primers for genotyping CRISPR deleted HEK293T cells Atg12: Forward: AGCCGGGAACACCAAGTTT Reverse: GTGGCAGCCAAGTATCAGGC	This paper	NA
primers for genotyping CRISPR deleted HEK293T cells Atg7: Forward: TGGGGGACAGTAGAACAGCA Reverse: CCTGGATGTCCTCTCCCTGA	This paper	NA
primers for genotyping CRISPR deleted HEK293T cells Atg14: Forward: AAAATCCCACGTGACTGGCT Reverse: AATGGCAGCAACGGGAAAAC	This paper	NA
huActin primers for qPCR: Forward: AGAGCTACGTGCCTGAC Reverse: CGTACAGGTCTTTGCGGATG	This paper	NA
msHnrnpc primers for qPCR: Forward: TGCAGAGCCAAAAGTGAA Reverse: CACTTTTGCCCTTCGTGAA	This paper	NA
mslrf7 primers for qPCR Forward:AAACCATAGAGGCACCCAAG Reverse:CCCAATAGCCAGTCTCCAAA	This paper	NA
msTrp53 primers for qPCR Forward:CCATCCTGGCTGTAGGTAGC Reverse:CAGACCAAGAGGCTGAGTCG	This paper	NA
primers for molecular cloning of human LC3B: Fwd: agtcggatccatgccgtcggagaagacct; Rev: gactctcgagttacactgacaatt tcatcccg	This paper	NA
primers for molecular cloning of human LC3A: Fwd: agtcggatccatgccctcagaccggcct; Rev: gact ctcgagtcagaagccgaaggttct	This paper	NA
primers for molecular cloning of human LC3C: Fwd: agtcggatccatgccgctccacagaaaat Rev: gact ctcgagctagagaggattgcagggtc	This paper	NA
primers for molecular cloning of human GABARAP: Fwd: agtcggatccatgaagttcgtgtacaagaaga Rev: gactctcgagttaaagaccgtagacactttc	This paper	NA
primers for molecular cloning of human GABARAPL1: Fwd: agtcggatccatgaagttccagtacaaggac Rev: gactctcgagtcatttccatagacactctc	This paper	NA
primers for molecular cloning of human GABARAPL2: Fwd: agtcagatctatgaagtggatgttcaaggag Rev: gactctcgagtcagaagccaaaagtgttctc	This paper	NA

REAGENT or RESOURCE	SOURCE	IDENTIFIER
Recombinant DNA		
pFR-CrPV_xb	Phil Sharp, Petersen et al, 2006	Addgene #11509
pFR_HCV_xb	Phil Sharp, Petersen et al, 2006	Addgene #11510
pcDNA3- EGFP	Doug Golenbock	Addgene #13031
pNL1.1-nano-Luc	Promega	N1001
pcDNA3 236HSC WT (BRCA2)	Mien-Chie Hung, Wang et al 2002	Addgene #16246
pLKO.1blast lentiviral plasmid with shRNA to mouse Atg7: CCA GCT CTG AAC TCA ATA ATA	Sigma-Aldrich	TRC N0000092163
pLKO.1blast lentiviral plasmid with Non targeting shRNA: CAA CAA GAT GAA GAG CAC CAA	Sigma-Aldrich	SHC 002
SV40 1: pBSSVD2005	David Ron	Addgene #21826
pSpCas9(BB)-2A-Puro	Feng Zhang, Ran et al 2013	Addgene #48139
pLKO.1puro lentiviral plasmid with shRNA to mouse MSI1, hairpin#1: CCGG CCTGTTTCAGACCTTGCTCTTCTCGAG AAGAGACAAGGTCTGAACAGG TTTTGG	Sigma Aldrich	TRCN0000098550
pLKO.1puro lentiviral plasmid with shRNA to mouse MSI1, hairpin#2: CCGG CCACTTCCATGAAATCAACAA CTCGAG TTGTTGATTTTCATGGAAGTGG TTTTGG	Sigma Aldrich	TRCN0000098551
pLKO.1blast lentiviral plasmid with shRNA to mouse p62/SQSTM1: CCGGGCTCCTACAGACCAAGAATTACTCGAGTAATTCTTGGTCTGTAGGAGCTTTTGG	Sigma Aldrich	TRCN 0000098617
pMXs.puro empty vector	This paper, cloned from pMXs-puro p62 Δ LIR	NA
pMXs.puro p62 Δ LIR (pMXs-puro GFP-p62 D337, 338, 339A)	Noboru Mizushima	Addgene #38280
Adenovirus Cre (AdCMVCre-eGFP Adenovirus)	Gene Transfer Vector Core at University of Iowa	Ad5CMVCre-eGFP
Software and Algorithms		
Babel	Olshen et al, 2013	https://cran.r-project.org/web/packages/babel/index.html
Integrative Genomics Viewer (IGV)	Robinson et al, 2011, Thorvaldsdottir et al, 2013	https://www.broadinstitute.org/igv/
Random mouse gene set	Vladimír Čermák	http://www.molbiotools.com/randomgenesetgenerator.html
Gene ontology	Paul Thomas	www.pantherdb.org
RNALfold	Lorenz, et al, 2011	https://www.tbi.univie.ac.at/RNA/index.html#

REAGENT or RESOURCE	SOURCE	IDENTIFIER
Shift function	Guillaume Rousselet Bieniek et al, 2016	https://github.com/GRousselet/blog/tree/master/shift_function
Eukaryotic linear motif resource	Dinkel et al, 2016	http://elm.eu.org/search.html
Other		

REFERENCES

1. Murrow, L. & Debnath, J. Autophagy As A Stress Response And Quality Control Mechanism—Implications for Cell Injury and Human Disease. *Annu. Rev. Pathol.* **8**, 105–137 (2013).
2. Sancak, Y. *et al.* Ragulator-Rag complex targets mTORC1 to the lysosomal surface and is necessary for its activation by amino acids. *Cell* **141**, 290–303 (2010).
3. Wang, S. *et al.* Lysosomal amino acid transporter SLC38A9 signals arginine sufficiency to mTORC1. *Science (80-.)*. **347**, 188–194 (2015).
4. Nicklin, P. *et al.* Bidirectional transport of amino acids regulates mTOR and autophagy. *Cell* **136**, 521–534 (2009).
5. Hay, N. & Sonenberg, N. Upstream and downstream of mTOR. *Genes Dev.* **18**, 1926–45 (2004).
6. Onodera, J. & Ohsumi, Y. Autophagy is required for maintenance of amino acid levels and protein synthesis under nitrogen starvation. *J. Biol. Chem.* **280**, 31582–6 (2005).
7. Mizushima, N., Sugita, H., Yoshimori, T. & Ohsumi, Y. A New Protein Conjugation System in Human. *J. Biol. Chem.* **273**, 33889–33892 (1998).
8. Mizushima, N. *et al.* A protein conjugation system essential for autophagy. *Nature* **395**, 395–398 (1998).
9. Malhotra, R., Warne, J., Salas, E., Xu, A. & Debnath, J. Loss of Atg12, but not Atg5, in pro-opiomelanocortin neurons exacerbates diet-induced obesity. *Autophagy* **11**, 145–154 (2015).
10. Settembre, C. *et al.* A lysosome-to-nucleus signalling mechanism senses and regulates the lysosome via mTOR and TFEB. *EMBO J.* **31**, 1095–108 (2012).
11. Thoreen, C. C. *et al.* A unifying model for mTORC1-mediated regulation of mRNA translation. *Nature* **485**, 109–13 (2012).
12. Laplante, M. & Sabatini, D. M. mTOR signaling at a glance. *J. Cell Sci.* **122**, 3589–3594 (2009).
13. Yu, L. *et al.* Autophagy termination and lysosome reformation regulated by mTOR. *Nature* **465**, 942–946 (2010).
14. Coldwell, M. J. & Morley, S. J. Specific isoforms of translation initiation factor 4GI show differences in translational activity. *Mol. Cell. Biol.* **26**, 8448–60 (2006).
15. Lewis, S. M. *et al.* The eIF4G homolog DAP5/p97 supports the translation of select mRNAs during endoplasmic reticulum stress. *Nucleic Acids Res.* **36**, 168–78 (2008).
16. Lee, A. S. Y., Kranzusch, P. J., Doudna, J. A. & Cate, J. H. D. eIF3d is an mRNA cap-binding protein that is required for specialized translation initiation. *Nature* **536**, 96–99 (2016).
17. Fernandez, J., Yaman, I., Sarnow, P., Snider, M. D. & Hatzoglou, M. Regulation of internal ribosomal entry site-mediated translation by phosphorylation of the translation initiation factor eIF2alpha. *J. Biol. Chem.* **277**, 19198–205 (2002).
18. Ingolia, N. T., Brar, G. a, Rouskin, S., McGeachy, A. M. & Weissman, J. S. The ribosome profiling strategy for monitoring translation in vivo by deep sequencing of ribosome-protected mRNA fragments. *Nat. Protoc.* **7**, 1534–50 (2012).

19. Olshen, A. B. *et al.* Assessing gene-level translational control from ribosome profiling. *Bioinformatics* **29**, 2995–3002 (2013).
20. Li, Z., Ji, X., Wang, D., Liu, J. & Zhang, X. Autophagic flux is highly active in early mitosis and differentially regulated throughout the cell cycle. *Oncotarget* **7**, 39705–39718 (2016).
21. Hewitt, G. & Korolchuk, V. I. Repair, Reuse, Recycle: The Expanding Role of Autophagy in Genome Maintenance. *Trends Cell Biol.* **27**, 340–351 (2016).
22. Schwerk, J. & Savan, R. Translating the Untranslated Region. *J. Immunol.* **195**, 2963–2971 (2015).
23. Lorenz, R. *et al.* ViennaRNA Package 2.0. *Algorithms Mol. Biol.* **6**, 1–14 (2011).
24. Kim, Y. M., Choi, W. Y., Oh, C. M., Han, G. H. & Kim, Y. J. Secondary structure of the Irf7 5'-UTR, analyzed using SHAPE (selective 2'-hydroxyl acylation analyzed by primer extension). *BMB Rep.* **47**, 558–562 (2014).
25. Colina, R. *et al.* Translational control of the innate immune response through IRF-7. *Nature* **452**, 323–328 (2008).
26. Araujo, P. R. *et al.* Before it gets started: Regulating translation at the 5' UTR. *Comp. Funct. Genomics* **2012**, 1–8 (2012).
27. Svitkin, Y. *et al.* The requirement for eukaryotic initiation factor 4A (eIF4A) in translation is in direct proportion to *RNA* 382–394 (2001).
28. Ringnér, M. & Krogh, M. Folding free energies of 5'-UTRs impact post-transcriptional regulation on a genomic scale in yeast. *PLoS Comput. Biol.* **1**, 0585–0592 (2005).
29. Jain, A. *et al.* p62/SQSTM1 is a target gene for transcription factor NRF2 and creates a positive feedback loop by inducing antioxidant response element-driven gene transcription. *J. Biol. Chem.* **285**, 22576–22591 (2010).
30. Iwasaki, S., Floor, S. N. & Ingolia, N. T. Rocaglates convert DEAD-box protein eIF4A into a sequence-selective translational repressor. *Nature* **534**, 558–561 (2016).
31. Jadhav, S. *et al.* RNA-binding Protein Musashi Homologue 1 Regulates Kidney Fibrosis by Translational Inhibition of p21 and Numb mRNA. *J. Biol. Chem.* **291**, 14085–14094 (2016).
32. Dinkel, H. *et al.* ELM 2016 — data update and new functionality of the eukaryotic linear motif resource. *Nucleic Acids Res.* **44**, 294–300 (2015).
33. Chen, J. J., Silver, D., Cantor, S., Livingston, D. M. & Scully, R. BRCA1, BRCA2, and Rad51 operate in a common DNA damage response pathway. *Cancer Res.* **59**, 1752–1757 (1999).
34. Liu, E. Y. *et al.* Loss of autophagy causes a synthetic lethal deficiency in DNA repair. *PNAS* **112**, 1–6 (2015).
35. Guo, J. Y. *et al.* Activated Ras requires autophagy to maintain oxidative metabolism and tumorigenesis. *Genes Dev.* **25**, 460–70 (2011).
36. Farmer, H. *et al.* Targeting the DNA repair defect in BRCA mutant cells as a therapeutic strategy. *Nature* **434**, 917–921 (2005).
37. Shen, Y. *et al.* BMN 673, a Novel and Highly Potent PARP1/2 Inhibitor for the Treatment of Human Cancers with DNA Repair Deficiency. *Clin. Cancer Res.* **19**, 5003–5015 (2013).
38. Malik, S., Saito, H., Takaoka, M., Miki, Y. & Nakanishi, A. BRCA2 mediates

- centrosome cohesion via an interaction with cytoplasmic dynein. *Cell Cycle* **15**, 2145–2156 (2016).
39. Cosenza, M. R. *et al.* Asymmetric Centriole Numbers at Spindle Poles Cause Chromosome Missegregation in Cancer Article Asymmetric Centriole Numbers at Spindle Poles Cause Chromosome Missegregation in Cancer. *Cell Rep.* **20**, 1906–1920 (2017).
 40. Hayashi, S. & McMahon, A. P. Efficient recombination in diverse tissues by a tamoxifen-inducible form of Cre: A tool for temporally regulated gene activation/inactivation in the mouse. *Dev. Biol.* **244**, 305–318 (2002).
 41. Karsli-Uzunbas, G. *et al.* Autophagy is required for glucose homeostasis and lung tumor maintenance. *Cancer Discov.* **4**, 914–27 (2014).
 42. Suzuki, S. W., Onodera, J. & Ohsumi, Y. Starvation induced cell death in autophagy-defective yeast mutants is caused by mitochondria dysfunction. *PLoS One* **6**, e17412 (2011).
 43. Schuck, S., Gallagher, C. M. & Walter, P. ER-phagy mediates selective degradation of endoplasmic reticulum independently of the core autophagy machinery. *J. Cell Sci.* **127**, 4078–88 (2014).
 44. Khaminets, A. *et al.* Regulation of endoplasmic reticulum turnover by FAM134B-mediated selective autophagy. *Nature* **522**, 359–62 (2015).
 45. Zaffagnini, G. *et al.* P62 Filaments Capture and Present Ubiquitinated Cargos for Autophagy. *EMBO J.* **37**, e98308 (2018).
 46. Sun, D., Wu, R., Zheng, J., Li, P. & Yu, L. Polyubiquitin chain-induced p62 phase separation drives autophagic cargo segregation. *Cell Res.* **28**, 405–415 (2018).
 47. Zhu, P., Sieben, C. J., Xu, X., Harris, P. C. & Lin, X. Autophagy activators suppress cystogenesis in an autosomal dominant polycystic kidney disease model. *Hum. Mol. Genet.* **26**, 158–172 (2016).
 48. Liu, S. *et al.* Autophagy plays a critical role in kidney tubule maintenance, aging and ischemia-reperfusion injury. *Autophagy* **8**, 826–837 (2012).
 49. Hildebrandt, F. & Otto, E. Cilia and centrosomes: a unifying pathogenic concept for cystic kidney disease? *Nat. Rev. Genet.* **6**, 928–940 (2005).
 50. Asano, J. *et al.* Intrinsic Autophagy Is Required for the Maintenance of Intestinal Stem Cells and for Irradiation-Induced Intestinal Regeneration. *CellReports* **20**, 1050–1060 (2017).
 51. Ho, T. T. *et al.* Autophagy maintains the metabolism and function of young and old stem cells. *Nature* **543**, 205–210 (2017).
 52. Vitale, I., Manic, G., De Maria, R., Kroemer, G. & Galluzzi, L. DNA Damage in Stem Cells. *Mol. Cell* **66**, 306–319 (2017).
 53. Gochhait, S. *et al.* Implication of BRCA2 -26G>A 5' untranslated region polymorphism in susceptibility to sporadic breast cancer and its modulation by p53codon 72 Arg>Pro polymorphism. *Breast Cancer Res.* **9**, R71 (2007).
 54. Chude, C. I. & Amaravadi, R. K. Targeting autophagy in cancer: Update on clinical trials and novel inhibitors. *Int. J. Mol. Sci.* **18**, (2017).

Chapter 3

Autophagy regulates the translation of some metabolic genes and immune response genes

The following chapter describes unpublished work

Contributions: I performed all of the experiments presented in this chapter. Jay Debnath supervised this project.

Introduction

In addition to the extensive validation of cell cycle and DNA damage repair mRNAs that are regulated by autophagy as discussed in Chapter 2, we also identified two other interesting gene ontology groups: genes involved in regulating metabolism and immune response. While these groups were not as significant as the cell cycle cohort, we thought that they both warranted some further investigation because of the known involvement of autophagy in both processes. Autophagy supports the maintenance of metabolites, as evidenced by *in vivo* knockouts of essential autophagy genes and monitoring of serum nutrient levels ¹. Additionally, autophagy has been reported to be necessary for the function and maintenance of T-cells ²⁻⁴, the response to viruses *in vivo* ⁵, and the secretion of IL-6 ⁶.

Results

A. Metabolic group of mRNAs

Certain mRNAs involved in signaling metabolic needs, stress response and cell cycle control are upregulated in autophagy deficient, starved cells

As detailed in the introduction, autophagy directly and indirectly regulates the metabolic state of the cell, as does the metabolic state of the cell regulate autophagy. Both work together to balance the metabolic needs of the cell and maintain homeostasis. We found that in autophagy deficient cells, there was an increase in the ribosome occupancy of mRNAs involved in amino acid, fatty acid, and glucose metabolism, as well as growth factor, nutrient and stress signaling pathways although this was not significant by gene ontology analysis (Figure 1A,B). We validated an

increase in protein in Atg12KO cells for ATF4, CDC25A, CPT2, and PFKFB3 (Figure 1C). ATF4 is a transcription factor that is translationally activated following eIF2 α phosphorylation. It is known to be upregulated through a unique process of translational regulation during stress responses, and as such it was understandable that we observed an increase in response to starvation and autophagy inhibition. Downstream targets of ATF4 include a wide array of genes involved in amino acid transport, cholesterol and glucose metabolism, oxidation status, autophagy, and energy management. CDC25A is required for the progression from G1 to S phase, as well as other stages of cell cycle progression. It is degraded in response to DNA damage and can cooperate with Ras as an oncogene⁷. CPT2 is an obligate enzyme in mitochondrial fatty acid oxidation. PFKFB3 is a critical enzyme in glycolysis and recently it was identified as an important link between the metabolic state of the cell and the cell cycle⁸.

Most of these mRNAs (*Cdc25A*, *Cpt2*, and *Pfkfb3*) had significantly increased ribosome occupancy in Atg12^{KO} cells under starvation conditions only, and the protein levels similarly reflected this fact. We therefore investigated whether the protein increase could be mitigated by the addition of glutamine or serum. We found that addition of exogenous nutrients suppressed the translation enhancement that occurred in autophagy knock out cells (Figure 1D, E). Therefore, we propose a model in which autophagy deficiency leads to a change in the metabolic pool of the cell, most likely lower glutamine levels, which under normal circumstances somehow negatively regulates the translation of this subset of mRNAs through an unknown mechanism (Figure 1F). Of course, there may be other mechanisms that positively regulate the translation of some of these mRNAs during starvation (such as RNA binding proteins

associating with the mRNAs), although we have no direct evidence to support this statement at the moment.

How dependent are autophagy deficient cells on fatty acid transport and metabolism?

Interestingly, autophagy has been found to be required for lipid homeostasis and fatty acid oxidation, particularly in a cancer context ⁹. Because of the small group of mRNAs that are involved in fatty acid metabolism and transport, including the validated CPT2, we investigated whether the Atg12^{KO} MEFs had increased sensitivity to the CPT family inhibitor etomoxir. We did not observe any differences in the ability of the cells following etomoxir treatment to recovery in a colony forming assay, nor were there significant increases in markers of DNA damage or apoptosis, in the same way that we observed sensitivity in response to DNA damage inducing or cell cycle inhibiting drugs (Figure 2A, B). However, none of the experiments were performed in starvation conditions, and perhaps MEFs in HBSS would be more sensitive to etomoxir. If this proves to be the case, the next logical step would be to identify whether solid tumors that are nutrient starved and dependent on fatty acid metabolism, such as certain breast tumors ¹⁰, also have a reliance on autophagy to maintain CPT2 levels for survival.

RBM4 may be a link between autophagy dependent translational upregulation

We identified that there are RBM4 motif sites in the 3'UTR of the mRNAs whose ribosome occupancy is increased in Atg12^{KO} compared to the group whose mRNAs had decreased ribosome occupancy in Atg12^{KO}, although there was no significant difference

between the higher group and a random sampling of mouse mRNAs of equivalent length (Figure 3A). RBM4 is a translational regulator whose activity has been linked to arsenite, hypoxic, and DNA damage stress^{11,12}. We found that RBM4 localization drastically changes from large puncta to cytoplasmically diffuse upon Atg12^{KO} or HBSS starvation (Figure 3B), while the total protein levels remain unchanged (Figure 3C). RBM4 localization has been reported to be dependent upon phosphorylation of p38¹¹, which we see also increased in starvation and in Atg12^{KO} (Figure 3D). The puncta are reminiscent of stress granules but do not costain with TIA-1 or G3BP (Figure 3E). However, RBM4 diffuse localization in HBSS cannot be rescued to puncta by the addition of glutamine (Figure 3F). It remains unclear if the translational control we observe in a nutrient and autophagy-dependent manner is impacted by RBM4 at all.

Discussion

It was surprising to us that we did not significantly enrich for mRNAs involved in metabolism from the RP screen. Given the known role of autophagy in regulating the metabolic homeostasis both *in vitro* and *in vivo*, it seems that translational control is independent from the autophagic degradation that regulates cell metabolism. What does seem to be consistent is the fact that the translational response upregulates mobilization of alternative energy sources such as amino acid import proteins and lipid metabolism. The increase in ribosome occupancy of certain mRNAs, and resulting increases in protein levels like PFKFB3 and CDC25A, seems to overlap with regulation of cell cycle control described in Chapter 2, potentially strengthening the link between these results.

B. Immune response group of mRNAs

Autophagy deficient cells have compromised T-cell proliferation

Atg5 deficient cells are unable to effectively mobilize memory CD44+ T-cells² and we demonstrate that Atg12 deficient T-cells are similarly impaired (Figure 4A, B). We also monitored the translation rates of autophagy competent versus impaired T-cells by ³⁵S methionine incorporation. While not statistically significant, we found that the Atg12^{KO} T-cells had somewhat higher rates of label incorporation, in both unstimulated and stimulated conditions, compared to the Atg12^{fl/fl} cells (Figure 4C, D).

Immune response genes are translationally regulated, in both a positive and negative manner, in response to autophagy inhibition

From our RP dataset, we identified several mRNAs involved in the immune response that have altered ribosome occupancy in Atg12^{KO} cells. *Ibtk* and *Zbtb7b* had increased ribosome occupancy in Atg12^{KO} cells, while *Irf7* and *Ifitm1* had decreased ribosome occupancy in Atg12^{KO} cells.

IRF7 is a transcriptional regulator of type I IFN genes (IFN- α and IFN- β) and IFN-stimulated genes (ISG) by binding to an interferon-stimulated response element (ISRE) in their promoters. It plays a critical role in the innate immune response against DNA and RNA viruses. IFITM1 is an IFN-induced antiviral protein which inhibits the entry of viruses to the host cell cytoplasm, permitting endocytosis, but preventing subsequent viral fusion and release of viral contents into the cytosol. We confirmed a decrease in the protein levels of IRF7 in Atg12^{KO} MEFs (Figure 4E, duplicated from Chapter 2

Figure S4E). A decrease of these proteins in Atg12^{KO} cells may render the cells more sensitive to viral infection.

The immune targets that had increased ribosome occupancy in the Atg12KO cells, ZBTB7B and IBTK, were not validated for protein increases. However, if the translation increase has a biological effect, it would theoretically impair the adaptive immune response to react to stimuli, particularly viral infection, similar to the response that downregulation of IRF7 and IFITM1 might have. ZBTB7B is a transcription factor important in CD4/CD8 cell fate that represses collagen expression. Wang et al.¹³ show Zbtb7b acts in peripheral CD4+ T-cells to suppress CD8-lineage gene expression, including perforin and Granzyme B necessary for effector T-cell function, and is important for the proper repression of interferon- γ (IFN- γ) during effector differentiation. IBTK acts as an inhibitor of BTK tyrosine kinase activity, leading to interference with BTK-mediated calcium mobilization and NF-kappa-B-driven transcription, which is important for the survival of immature B cells in the bone marrow and the development of peripheral B-cells¹⁴. Furthermore, IBTK has previously been demonstrated to be translationally controlled by eIF2 α phosphorylation following stress¹⁵, which fits with the ATF4 translational upregulation data reported in the section above.

Discussion

Autophagy has been previously demonstrated to regulate the immune response, particularly the function and proliferation of T-cells²⁻⁴. Additionally, secretion of IL-6 is impaired in autophagy deficient cells⁶, and IL-6 can induce differentiation of activated B-cells as well as having antiviral activity. Therefore, all of the translational changes that

we report, as well as the published data on T-cell activity and IL-6 secretion, would seem to impair the immune response to viral infection, which indeed has been demonstrated to be the case in autophagy deficient cells⁵. How much these translational changes contribute to T-cell and B-cell proliferation and viral response, compared to autophagy dependent metabolism and secretion, remains to be determined.

Figure 1

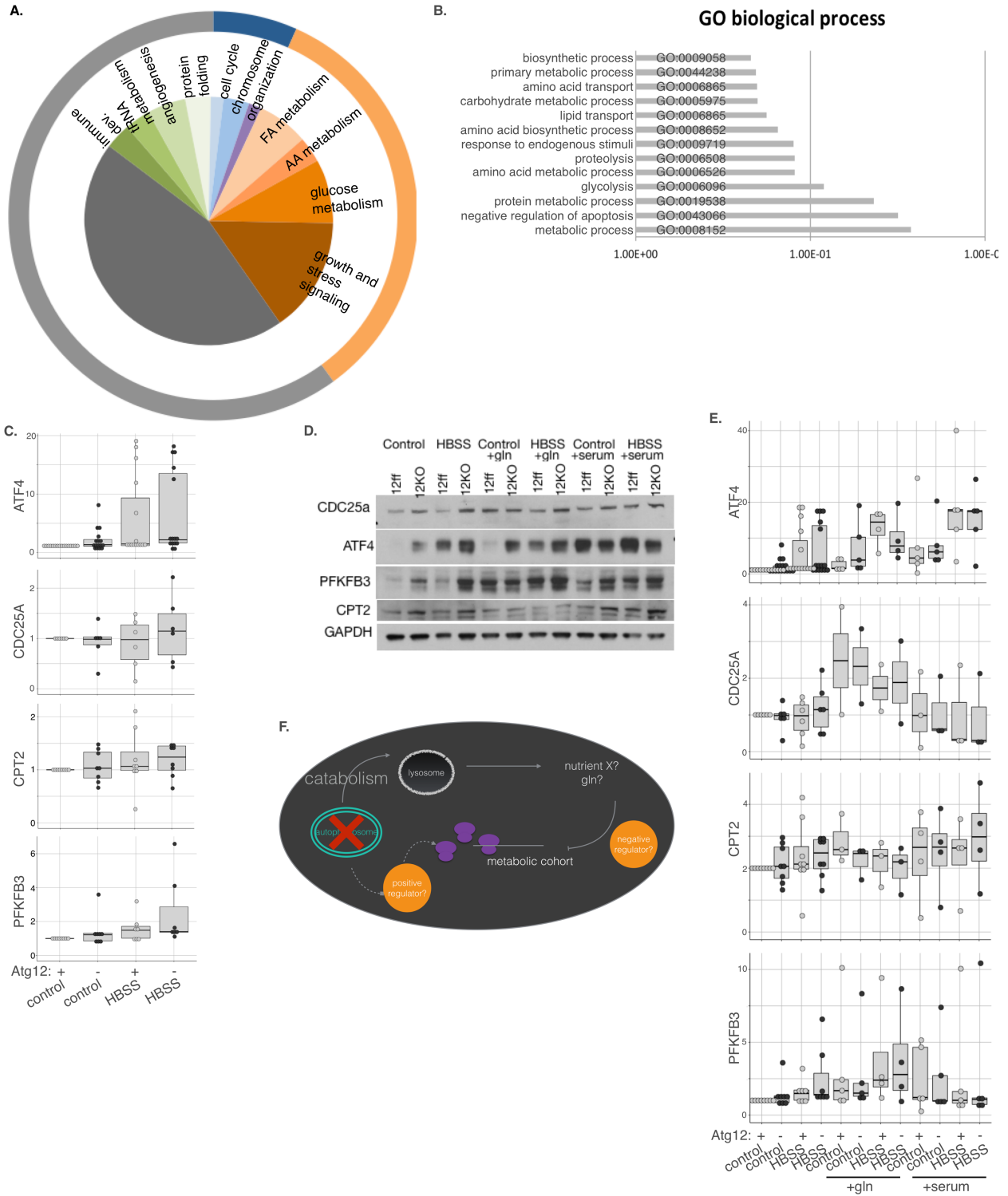


Figure 1: mRNAs that had significantly enriched for ribosomes during autophagy inhibition group loosely to genes involved in metabolism and growth response

A. Reproduction of data from chapter 2 Figure 2G. Molecular functions of mRNAs whose ribosome occupancy is increased (p-value < 0.01, n=36) in Atg12^{KO} cells versus Atg12^{ff} cells in either fed or starved conditions.

B. Enriched biological processes based on gene ontology (GO) analysis of mRNAs whose ribosome occupancy is significantly increased in Atg12^{KO} versus Atg12^{ff} cells.

C. Protein lysate was collected from Atg12^{ff} and Atg12^{KO} MEFs in fed or starved conditions, and immunoblotted for some of the top hits from ribosome profiling. Shown is the quantification (boxplot with dotplot overlay) from immunoblot intensity, normalized to control.

D, E. Protein lysate was collected from Atg12^{ff} and Atg12^{KO} MEFs in fed or starved conditions, and media supplemented with glutamine and serum. (D) Representative immunoblot of metabolic top hits. (E) Quantification (boxplot with dotplot overlay) from immunoblot intensity, normalized to control.

F. Model describing possible mechanisms of autophagic translational control.

Figure 2

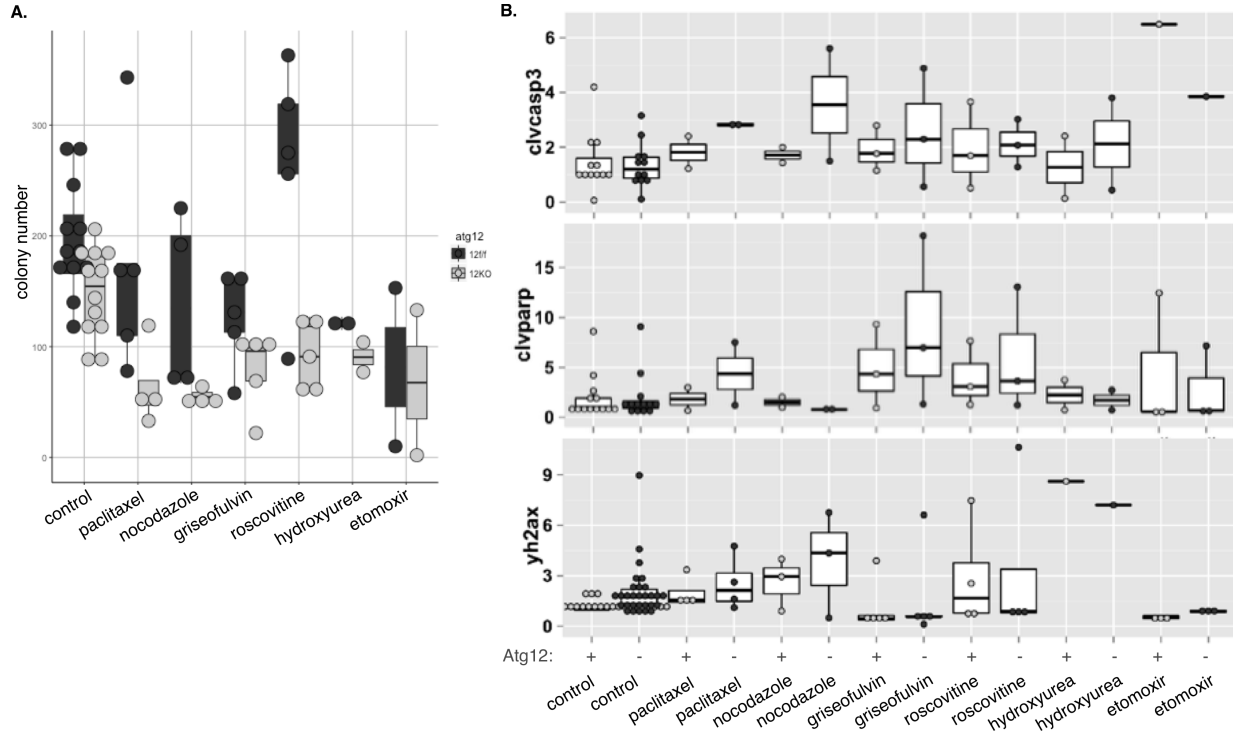


Figure 2: Autophagy deleted cells are sensitive to cell cycle inhibitors, not sensitive to CPT inhibitors, under fed conditions

A. A clonogenic replating assay was performed on Atg12^{ff} or Atg12^{KO} MEFs treated for 16h with vehicle control, cell cycle inhibitors or the CPT inhibitor etomoxir, and colony number was quantified, shown as a boxplot with dotplot overlay for each biological replicate.

B. Quantification of immunoblot intensity, normalized to loading control, of Atg12^{ff} or Atg12^{KO} MEFs treated for 16h with cell cycle inhibitors or the CPT inhibitor etomoxir.

Figure 3

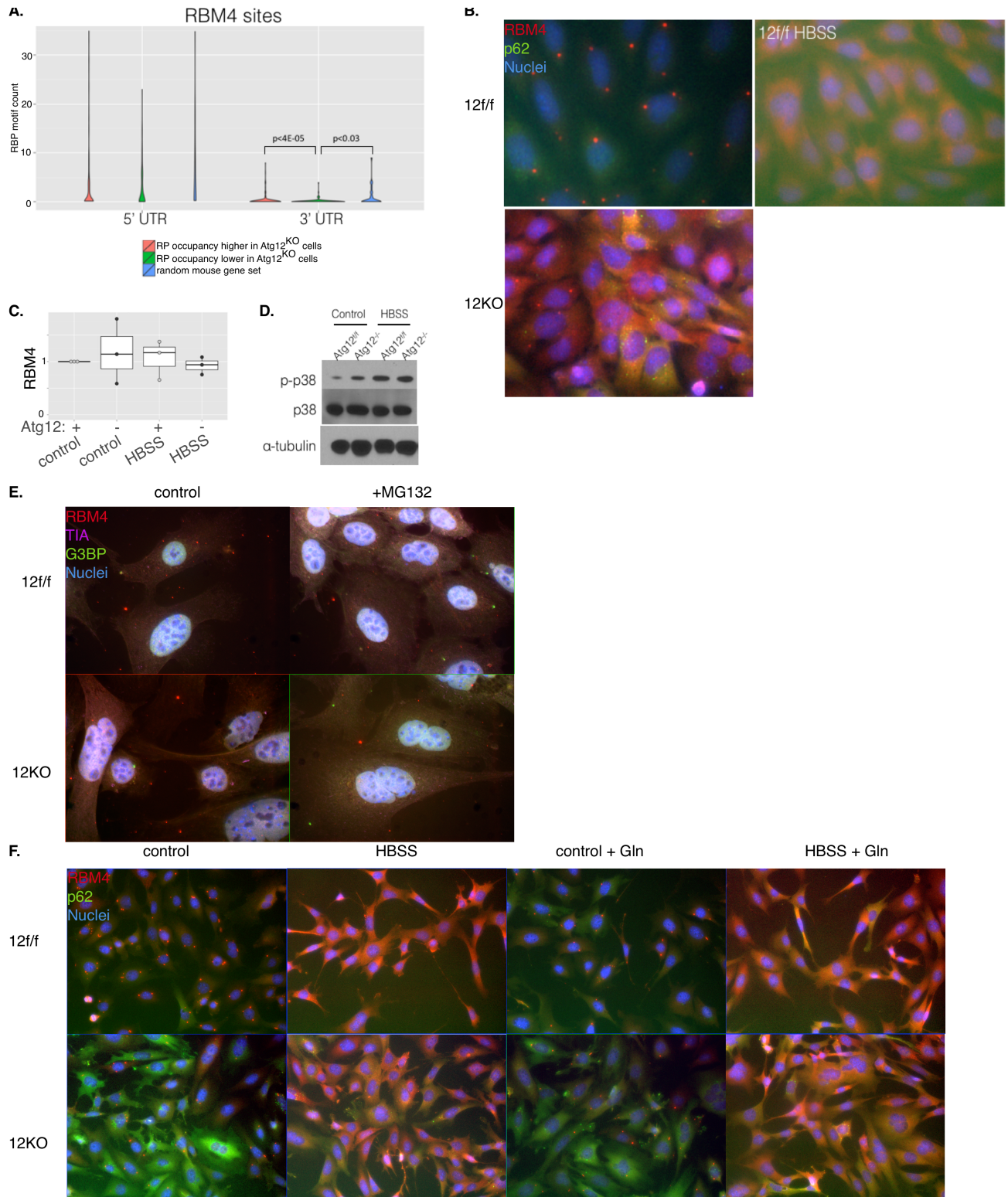


Figure 3: the RNA binding protein RBM4 shows striking relocalization in starvation, autophagy deletion

- A. Violin plot of number of predicted RBM4 binding sites in the 5' and 3'UTRs from the top hits that were significantly enriched for ribosome occupancy in Atg12^{KO} cells, top hits that were significantly decreased for ribosome occupancy in Atg12^{KO} cells, and a random gene set of equivalent length. p-val (t-test) shown for significant differences.
- B. Immunofluorescence staining for RBM4 in Atg12^{ff} and Atg12^{KO} MEFs, and Atg12^{ff} MEFs in HBSS starvation.
- C. Quantification of immunoblot intensity, normalized to loading control, of RBM4 levels in Atg12^{ff} and Atg12^{KO} MEFs, under both fed and starved conditions.
- D. Representative immunoblot from Atg12^{ff} and Atg12^{KO} MEFs, under both fed and starved conditions, for phosphorylated p38.
- E. Immunofluorescence staining for RBM4 and stress granule markers TIA and G3BP in Atg12^{ff} and Atg12^{KO} MEFs, under normal and stress inducing conditions (MG132 5μM for 3h).
- F. Immunofluorescence staining for RBM4 and p62 in Atg12^{ff} and Atg12^{KO} MEFs, under normal and starvation conditions, with exogenous glutamine added.

Figure 4

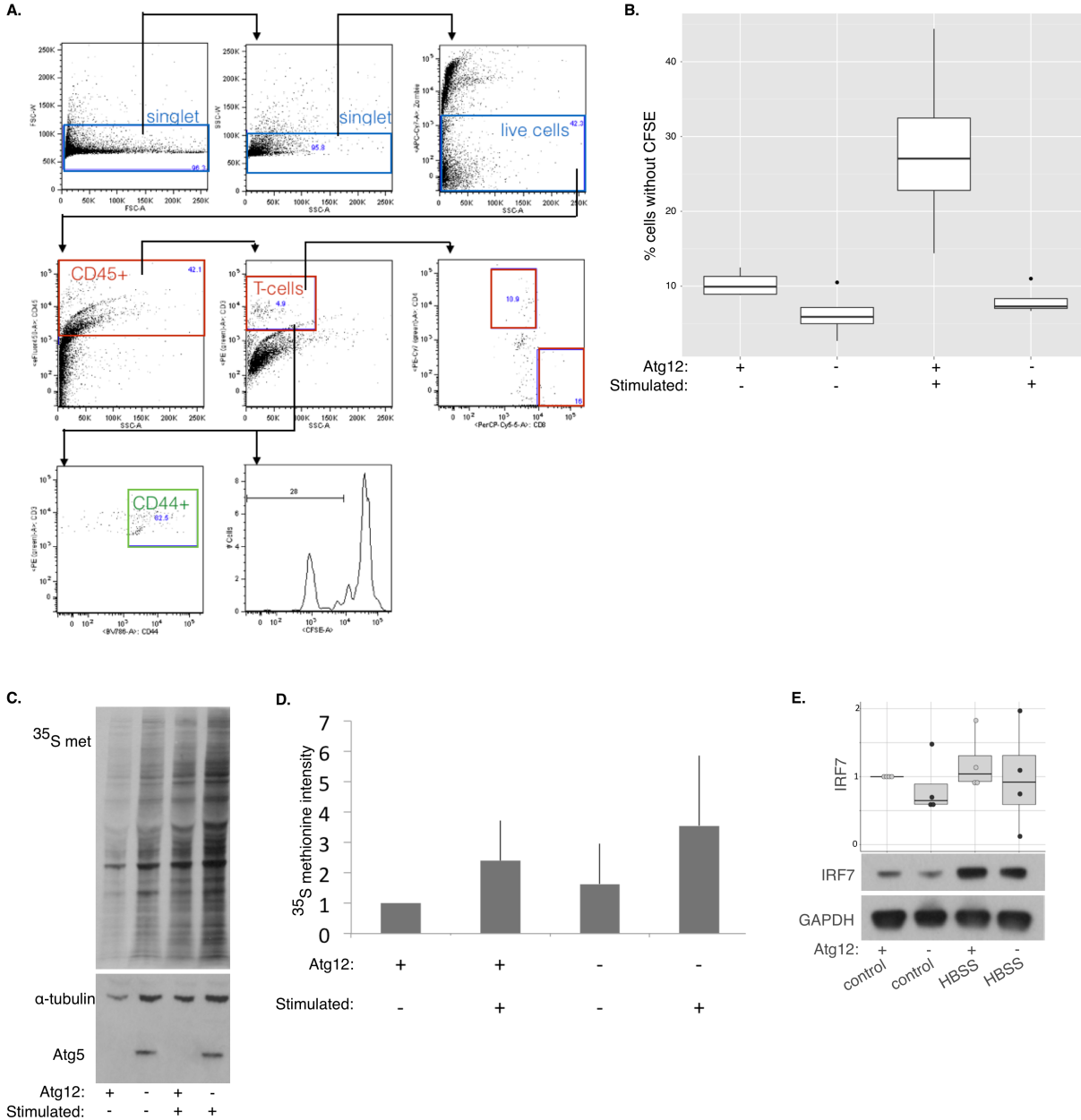


Figure 4: Atg12^{KO} T-cells have impaired proliferation following stimulation, possibly higher translation rates

A. Schema of gating analysis on proliferating T-cells from Atg12^{ff} and Atg12^{KO} splenocytes, marked by CFSE dilution.
 B. Quantification of percent of proliferating CD45+, CD3+ Atg12^{ff} and Atg12^{KO} T-cells.
 C, D. Protein lysate was collected from Atg12^{ff} and Atg12^{KO} splenocytes, either unstimulated or following stimulation. (C) Representative autoradiogram of ³⁵S methionine incorporation (above) and immunoblot for loading control and autophagy

deletion (below). (D) Quantification (mean + SD) of rate of ^{35}S methionine incorporation, normalized to control.

E. Reproduction of figure from chapter 2, Figure S4E. Protein lysate was collected from Atg12^{ff} or Atg12^{KO} MEFs grown in control media or starved in HBSS for 2h. IRF7 levels were measured by immunoblotting. Relative quantification from immunoblots for IRF7 normalized to loading control is shown in the boxplot with dotplot overlay per biological replicate. Bottom: representative immunoblot.

Materials and Methods

Mouse maintenance

Compound transgenic C57Bl/6 mice harboring $Atg12^{ff}$ and $Cag-Cre^{ER}$ were generated by cross-breeding of $Atg12^{ff}$ (Malhotra et al, 2015) and $CagCre^{ER}$ animals (Hayashi, S. & McMahon, 2002) (obtained via the UCSF mouse database). Offspring were genotyped with polymerase chain reaction (PCR) primers listed in the key resources table. At 6 weeks of age, animals of indicated genotypes received either Tamoxifen (0.2mg/gram mouse) or vehicle (peanut oil) via oral gavage for 5 consecutive days. At 10 weeks after the first tamoxifen treatment, animals were sacrificed and tissues were collected for biochemical and histological analysis. All experimental procedures and treatments were conducted in compliance with UCSF Institutional Animal Care and Use Committee guidelines.

Genetic deletion of MEFs

Cells were treated with $2\mu\text{M}$ 4-Hydroxy-tamoxifen (4OHT) or vehicle (100% Ethanol) for three consecutive days. Genetic recombination was achieved following 2 days of 4OHT treatment, and confirmed by PCR.

T-cell isolation and culture

After isolating splenocytes from $Atg12^{ff};Cag-Cre^{ER+}$ C57BL/6 mice, splenocytes were pulsed with CFSE, and subsequently cultured *in vitro* in OpTmizer SFM plus IL-7 in the presence or absence of T-cell stimulating anti CD3e and CD28 for 3 days. Cells were then either fixed for flow cytometry analysis for proliferation of T-cells, or labeled with ^{35}S -methionine for 6h.

KEY RESOURCES TABLE

Reagent or Resource	Source	Identifier	concentration
Antibodies			
RBM4	Protein Tech	11614-1-AP	1:1000 for IB 1:100 for IF
phospho-p38 T180/Y182	Cell Signaling	#9211	1:1000 for IB
Cpt2	Abcam	ab71435	1:500 for IB
Pfkfb3	ABclonal Biotech	A6945	1:500 for IB
Cdc25A	Cell Signaling	#3652	1:500 for IB
Atf4	Cell Signaling	#11815	1:1000 for IB
Atg5	Novus Biologicals	NB110-53818	1:1000 for IB
alpha-tubulin	Cell Signaling	#2125BC	1:1000 for IB
GAPDH	Millipore	MAB374	1:1000 for IB
TIA	Santa Cruz	sc-1751	1:50 for IF
G3BP-488	abcam	ab214946	1:100 for IF
p62	progen	GP-62-C	1:1000 for IB 1:200 for IF
Chemicals			
Paclitaxel	Sigma Aldrich	T7402-1MG	100nM
nocodazole	Sigma Aldrich	M1404-2MG	50nM
griseofulvin	Sigma Aldrich	G4753-5G	10µM
roscovitine	Selleck Chemicals	CYC202	10µM
hydroxyurea	Sigma Aldrich	H8627	50µM
etomoxir	Sigma Aldrich	E1905	1mM
MG132	Sigma Aldrich	C2211	5µM

References

1. Guo, J. Y. *et al.* Autophagy provides metabolic substrates to maintain energy charge and nucleotide pools in Ras-driven lung cancer cells. *Genes Dev.* **30**, 1704–1717 (2016).
2. Pua, H. H., Dzhagalov, I., Chuck, M., Mizushima, N. & He, Y.-W. A critical role for the autophagy gene Atg5 in T cell survival and proliferation. *J. Exp. Med.* **204**, 25–31 (2007).
3. Xu, X., Araki, K., Li, S., Han, J. & Ye, L. Autophagy is essential for effector CD8+ T cell survival and memory formation. *Nat. ...* **15**, (2014).
4. Schlie, K. *et al.* Survival of Effector CD8+ T Cells during Influenza Infection Is Dependent on Autophagy. *J. Immunol.* (2015). doi:10.4049/jimmunol.1402571
5. Kudchodkar, S. & Levine, B. Viruses and autophagy. *Rev Med Virol* **19**, 359–378 (2010).
6. Lock, R. *et al.* Autophagy facilitates glycolysis during Ras-mediated oncogenic transformation. *Mol. Biol. Cell* **22**, 165–78 (2011).
7. Shen, T. & Huang, S. The role of CDC25A in the regulation of cell proliferation and apoptosis. *Anti-Cancer Agents Med. Chem.* (... **12**, 631–639 (2012).
8. Salazar-roa, M. & Malumbres, M. Fueling the Cell Division Cycle. *Trends Cell Biol.* **27**, 69–81 (2017).
9. Guo, J. Y. *et al.* Autophagy suppresses progression of K-ras-induced lung tumors to oncocytomas and maintains lipid homeostasis. *Genes Dev.* **27**, 1447–61 (2013).
10. Camarda, R. *et al.* Inhibition of fatty acid oxidation as a therapy for MYC-overexpressing triple-negative breast cancer. *Nat. Med.* **93**, 292–297 (2016).
11. Lin, J., Hsu, M. & Tarn, W. Cell stress modulates the function of splicing regulatory protein RBM4 in translation control. **104**, 1–6 (2007).
12. Gebauer, F. Versatility of the translational machinery during stress: changing partners to keep dancing. *Cell Res.* **22**, 1634–6 (2012).
13. Wang, L. *et al.* The Zinc Finger Transcription Factor Zbtb7b Represses CD8-Lineage Gene Expression in Peripheral CD4+T Cells. *Immunity* **29**, 876–887 (2008).
14. Liu, W. *et al.* Direct inhibition of Bruton ' s tyrosine kinase by IBtk , a Btk-binding protein. *Nat. Immunol.* **2**, 939–946 (2001).
15. Baird, T. D. *et al.* Selective mRNA translation during eIF2 phosphorylation induces expression of IBTK . *Mol. Biol. Cell* **25**, 1686–1697 (2014).

Chapter 4

Acute starvation induced translation

The following chapter describes unpublished work.

Contributions: I performed all of the experiments presented in this chapter. Jay Debnath supervised this project.

Abstract

Protein translation is necessary for cell growth and function, and it is an incredibly energy demanding process. As such, protein translation is tightly regulated by the metabolic state of the cell. A key regulator of cap-dependent translation is the mammalian target of rapamycin complex 1 (mTORC1), which integrates extracellular and intracellular nutrient status to regulate anabolism and cell growth. It is widely accepted that global translation universally drops in response to nutrient starvation, due to the inactivation of mTORC1. Cap-independent translation is less well understood, and the interplay between these types of translational control during nutrient starvation is only just starting to be elucidated. The prevailing theory is mTOR and eIF2 α coordinately down-regulate cap-dependent translation and maintain cap-independent translation of a select few transcripts during nutrient starvation.

However, my preliminary data challenges this prevailing view in the field. I have surprisingly uncovered an increased, rather than decreased, rate of translation upon starvation in a buffered saline solution that arises independently of mTOR, hereafter termed acute starvation induced translation (ASIT). Notably, previous studies have starved cells by removal of solitary nutrients, which do not necessarily recapitulate physiological starvation. Thus, ASIT may have been previously overlooked if it behaves in a cell type specific manner in response to compound nutrient stresses.

Introduction and background

There are two current models for translation initiation: cap-dependent and cap-independent translation. mTOR in complex C1 is a nutrient sensor and master regulator

of cap-dependent translation through phosphorylation of 4EBP1 and S6K. 4EBP1 when hypo-phosphorylated sequesters the initiation factor eIF4E, preventing translation, and is thought to be the key regulator of translation. The ribosomal protein S6 kinase (S6K) regulates cap-dependent translation, among other cellular processes, by phosphorylation of a number of translation regulators, including initiation factors eIF4A and eIF4B, elongation factor eEF2, and the small ribosomal subunit protein S6¹. Signaling pathways that sense the ratio of ADP to ATP, and the presence of glucose and amino acids such as AMPK, and the Rag/Ragulator complex all converge to regulate the activity of mTORC1. In times of nutrient plenty, mTORC1 is activated at the lysosome and phosphorylates 4EBP1 and S6K to promote translation. During starvation, mTORC1 activity is suppressed and 4EBP1 and S6K lose their phosphorylation, which represses translation. Many studies of nutrient starvation rely on monitoring S6, S6K, or 4EBP phosphorylation status to infer mTOR activity and translation capacity.

While mTORC1 activity is considered the master regulator of cap-dependent protein translation, recent studies performing ribosome profiling on Torin-1 treated cells shows that mTORC1 is responsible for regulating the translation of mainly 5'TOP mRNAs². However, there are mTOR-independent pathways that control cap-dependent translation: MEK, ERK and PI3K pathways can regulate eIF2B, S6, and 4EBP independent of mTOR³⁻⁵; Additionally, direct effects on ribosomal proteins by PKC β II - RACK1⁶ and a recently discovered non-coding RNA in yeast can also decrease translation rates⁷. Furthermore, cap-independent translation is regulated separately, although much less is known about it. The best understood mechanism of cap-

independent translation is internal ribosomal entry site (IRES) dependent translation, which bypasses the need for eIF4E binding and cap-dependent scanning and allows the 40S ribosome to be recruited closer to the start site⁸. The requirement of initiation factors during IRES-mediated translation varies depending on the mRNA and the situation.

Nutrient starvation is a key regulator of translation through both cap-dependent and cap-independent mechanisms. During nutrient rich conditions, mTORC1 phosphorylates 4EBP1 and S6K, allowing translation initiation on the mRNA 5' m⁷-cap. During starvation, abundant evidence suggests that reduced mTORC1 activity abrogates translation via the same mechanism. At the same time, phosphorylated-eIF2 α actively curbs cap-mediated mRNA translation by preventing eIF2B-mediated reformation of the ribosome ternary complex at the start codon. The rate of global translation decreases in yeast and mammalian cells during glucose starvation, and nitrogen or glutamine starvation⁹⁻¹³. However, cap-independent translation of specific transcripts necessary for survival, such as heat shock proteins and amino acid biosynthesis genes, are thought to be maintained via the use of an internal ribosome entry site (IRES) mediated by the freeing up of ribosomes and key initiation factors due to the phosphorylation of eIF2 α ^{2,14-16}. As such, much remains to be learned on how cap-independent pathways contribute to translation in starving cells.

In my preliminary studies, I have unexpectedly found that during nutrient starvation in Hank's balanced salt solution (HBSS), a saline solution that maintains osmotic balance and provides inorganic ions and some glucose, the rate of translation seems to increase. Previous studies that looked at translation rates in cultured cell lines

either only used markers of mTORC1 activation as a proxy for translation rates, or if monitored translation rates by ^{35}S -methionine incorporation used 20x fold the levels of methionine and cysteine. In classical experiments with *Tetrahymena*, several stresses initially lead to a burst in translation which is then followed by a decrease in protein synthesis¹⁷⁻²⁰, indicating there may be a more complex relationship between nutrient starvation and translation than previously described. Nonetheless, the mechanistic underpinnings and biological significance of this translational increase during certain types of starvation remains a mystery.

Results

HBSS, unlike single nutrient starvation, increases ^{35}S -methionine incorporation rates

Upon starvation in HBSS, the rate of ^{35}S methionine incorporation increases 2-3 fold as measured by quantification of autoradiography of lysates run on SDS-PAGE gels, or by CPM measured on a scintillation counter (Figure 1A, B). The rate of *de novo* protein translation rapidly increases within 15 minutes and persists for at least 6 hours (Figure 1C). Similarly, complete nutrient starvation by EBSS or PBS also lead to an increase in the rate of ^{35}S -met incorporation in contrast with glucose and glutamine withdrawal, which reduces the rate of translation in these cells as expected (Figure 1D). Therefore, we termed this phenomenon acute starvation induced translation (ASIT).

ASIT occurs in both primary and SV40 immortalized MEFs, and was consistent over all 6 of the cell lines tested. (Figure 1E, F). ASIT does not rely on transcription to promote the observed translation, as pre-treatment with Actinomycin D to severely

induce DNA damage and inhibit transcription did not affect 35S methionine incorporation, while blocking translation by treatment with cycloheximide prevented 35S methionine incorporation (Figure 1G, H). Chase experiments show that ASIT is rapidly reversible upon wash of HBSS and re-addition of control media (Figure 1I).

Canonical translation signaling markers all indicate that translation should be down in HBSS starvation, ASIT is not dependent on mTORC1 activity

ASIT inversely correlates with canonical mTOR pathway activity, which declines over this time period. Phosphorylation of key downstream translational regulators of mTORC1, 4EBP1, S6K and S6, all show lower levels of phosphorylation in HBSS/EBSS starvation than in control media. Additionally, markers of translation inhibition, phosphorylation of eIF2 α and eEF2, are increased (Figure 2A, B). During amino acid starvation, GCN2 phosphorylates eIF2 α on Ser51, a cardinal feature of the integrated stress response that results in decreased in global translation, as well as the translation of specific mRNAs^{16,21–24}. Phosphorylation of eIF4E, which is associated with a fed state but there is little evidence as to whether this post-translational modification affects the rate of translation, is decreased in HBSS/EBSS starvation. Additionally, using a cap-pulldown assay in which m⁷-GTP is attached by a linker to agarose beads and initiation factors can be pulled down in various conditions shows that HBSS reduces the ratio of eIF4G to 4EBP bound to the cap, similar to other starvation treatments or translation inhibitors thapsigargin (Tg) or the mTORC1/2 inhibitor PP242 (Figure 2C, D). These data suggest that this “hyper-synthetic” phenotype is proceeding via an mTORC1-independent pathway, and that this translation regulation is not cap-dependent.

To further test the independence of ASIT on mTORC1, we treated the cells with the mTORC1/2 inhibitor PP242 and monitored the rate of translation by ³⁵S-methionine incorporation. While PP242 decreased the rate of translation observed in the control media, it had no effect on HBSS starvation, where the rate of translation still increased approximately two fold compared to control media with the inhibitor (Figure 2E,F).

ASIT does not require autophagy, a degradative lysosome or proteasome

Because starvation induces autophagy, which has been proposed to maintain amino acids for translation (although in Chapter 2 we have found this not to be the case), we investigated whether autophagy or a functioning lysosome or proteasome was necessary to support ASIT. However, we found that autophagy deficient MEFs were just as capable of undergoing ASIT (Figure 3A,B), as were cells treated with lysosomal inhibitors Bafilomycin A (Figure 3C), or treatment with chloroquine (Figure 3D). Additionally, treatment with the proteasome inhibitor MG132 had no effect on ASIT (Figure 3E).

ASIT is not controlled by calcium, glucose, vitamins or serum

ASIT is observed in a variety of acute starvation in saline solutions, including HBSS, EBSS and PBS. Because these different ASIT inducing solutions have differences in calcium and magnesium concentrations, glucose concentrations, and pH buffering abilities, we noted therefore that none of those differences affect ASIT. To further confirm these findings, HBSS plus the calcium and magnesium chelators EGTA and EDTA had no affect on ASIT, nor did the addition of calcium or magnesium to PBS,

although this did prevent the cells from detaching and allowed longer starvation time points to be studied (Figure 3F). Similarly, addition of glucose to PBS did not alter ^{35}S -methionine incorporation rates, nor did addition of the glycolysis inhibitor 2-deoxyglucose (2DG) to HBSS alter the two-fold induction in ^{35}S -methionine incorporation rates (Figure 3G, H). Other differences between all of the ASIT inducing saline solutions and control growth media is that DMEM contains a vitamin mix that the saline solutions lack, as well as a complement of essential and non-essential amino acids and often the addition of serum (Table 1). However, addition of 1% serum, vitamin mix, or non-essential amino acids to HBSS had no effect on ASIT (Figure 3I).

ASIT can be prevented by the addition of leucine to HBSS

We therefore investigated the role of essential amino acids in ASIT. DMEM without any amino acids induced ASIT, and addition of up to 20% all amino acids back decreased the ^{35}S -methionine incorporation by about half (Figure 4A). Adding L-leucine to HBSS prevented ASIT (Figure 4B). Other amino acids that seemed to also mitigate ASIT were histidine and tyrosine. There is little similarity between these three amino acids: histidine is basic, although addition of lysine failed to have the same effect; tyrosine and histidine both have bulky side chains, but leucine is a small branched chain amino acid; there is no known common amino acid transporter that transports all three amino acids. We continued to validate that ASIT was leucine sensitive, as leucine had the strongest and most reproducible result. Only L-leucine, the bioactive form, and not D-Leucine, was able to impair ASIT (Figure 4C, D). Interestingly, a very high concentration of cycloleucine was able to impair ASIT (Figure 4E), and I believe that

high concentrations above physiological levels of other amino acids may do the same as well. Leucine prevented ASIT in a dose dependent manner (Figure 4F). We noted that following starvation, after refeeding, the cells grew slower over a 24h period than if they had been maintained in control media consistently. However, addition of leucine had no effect on regrowth rates following starvation (Figure 4G).

The leucine tRNA synthetase is a protein that is very sensitive and responsive to levels of intracellular leucine. Therefore, we investigated whether the leucine tRNA synthetase LARS was necessary for ASIT. We found however that LARS is dispensible for ASIT induction (Figure 4H).

Puromycin, Ribosome profiling, inconsistent in assessing ASIT

One of the major concerns with these results is whether ASIT is an artifact of radiolabeling. We first checked that HBSS was not increasing the presence of the surface transporter for methionine, SNAT2, which may lead to more label being incorporated. We found that SNAT2 surface levels do not change after 4 hours of HBSS starvation (Figure 5A). While ³⁵S-methionine is the gold standard for measuring the rate of translation, we investigated whether ASIT could be captured by another labeling approach. Part of the puromycin molecule mimics the shape of aminoacylated tRNA, and it is incorporated into the nascent polypeptide and terminates translation. The rate of puromycin incorporation in the short term before the cell begins to suffer due to an inhibition of translation can be assayed by a primary antibody against puromycin in the lysate run on an SDS-PAGE gel. Puromycin incorporation was decreased in acute

starvation, although not significantly, but drastically impaired in glutamine starvation (Figure 5B,C).

Additionally, we investigated whether the polysome profile was altered in HBSS starvation. During glutamine starvation, the polysome peak amplitudes are diminished and the monosome peaks increase. Because we observed approximately a two-fold increase in the rate of ^{35}S -methionine incorporation during starvation that seems to be consistent across all proteins analyzed by the SDS-PAGE analysis, we expected to see an increase in the polysome peaks measured by profiling. However, we were unable to detect any change in the amplitude of polysome peaks in MEFs during HBSS starvation (Figure 5D).

Further, we performed ribosome profiling on MEFs either maintained in control media or following 2h of HBSS starvation. By comparing the number of ribosome bound fragments on an mRNA by mRNA basis, we found that there seemed to be fewer ribosomes binding after starvation, indicating that translation rates should be decreased (Figure 5E). We also investigated what mRNAs seemed to have higher translation rates normalized to mRNA levels and based on the average RP:RNA counts per group; therefore, this analysis would not show whether translation rates were globally upregulated during starvation, only the mRNAs whose translation rates were more increased in starvation relative to the mean rates of translation of this group. The top 30 significant mRNAs had relatively high p-values and FDRs, and did not group by gene ontology analysis (Tables 2,3). It would be very interesting to see if we can observe in the data whether ribosomes are stalling at particular amino acid codons preferentially, for example leucine, since we know that addition of leucine, even in the absence of all

other amino acids, can rescue the ASIT phenotype. However, whether the coverage from our MEF ribosome profiling is sufficient to obtain this resolution is unknown, and perhaps repeating the ribosome profiling in a cell type more amenable to ribosome profiling, such as HEK293Ts, may be more informative.

Much more dramatically and with more significant values, we found that many ribosomal proteins have halted translation during starvation (Tables 3,4). As this would indicate a slowing of translation rates, contradicting our findings of ASIT by ³⁵S-methionine labeling, it is unclear how to reconcile these data.

Discussion

In this chapter, we present a model in which amino acids normally act to repress a type of global translation independent of mTORC1 that we term ASIT. When all amino acids are removed, repression of ASIT is removed and we observe a two-fold increase in translation across most proteins. Supplementation of single essential amino acids, in particular leucine, can prevent ASIT, even in the absence of all other amino acids.

This unexpected increase in protein synthesis upon general nutrient limitation has little precedent in research; In starved and deciliated or starved and heat-shock impaired Tetrahymena, a similar although seemingly less robust increase in translation rate has been previously observed, but its precise biological function remains obscure¹⁷⁻²⁰. Additionally, in Cocksackie B virus infected HeLa cells, an increase in translation capacity is observed prior to the expected decrease in protein synthesis²⁵. However, in a study published in Oncogene in 2012, Yoon and colleagues show that HeLa cells at 50% confluency when starved in HBSS decrease the incorporation of 500

μCi of ^{35}S Met/Cys over 2-15 hours. Potentially, the discrepancies observed between their data and our data is the combination and ~ 20 fold higher levels of radiolabeled methionine and cysteine added. As we have found that addition of single amino acids back into HBSS can reduce ASIT and high concentrations of cycloleucine can inhibit ASIT, potentially high concentrations of methionine or cysteine can have a similar effect.

Verification of the observed increase in translation was unsatisfactory by polysome profiling and puromycin incorporation in MEFs. Potentially, polysome profiling in HEK293Ts, which yield more reproducible polysome profiles would give a clearer answer. Additionally, because puromycin also terminates translation, a better method would be to use azidohomoalanine labeling, a methionine analog that contains a reactive azide that can then be “click” covalently bonded to biotin conjugated alkyne, and quantified by streptavidin HRP immunoblots, or potentially by SILAC and quantitative mass spectrometry.

There are many remaining questions that arise from this data, assuming that the increase in ^{35}S -methionine is indicating a real increase in translation rates across the proteome. First, how is leucine sensed and how does it regulate translation? While we demonstrated that LARS is not necessary for ASIT, there are other leucine sensitive proteins in the cell that we haven't investigated yet, such as Sestrin2, Slc38a9, or Slc7a5 (LATS1)²⁶⁻²⁸. The subsequent question would be are leucine-sensing proteins normally repressive of translation under fed conditions? Additionally, as ASIT is mTOR independent but appears to affect translation across all of the proteins identified on an SDS-PAGE gel, is the translation dependent on the m^7 -GTP cap? Is the translation

machinery the same as during fed conditions, or are there different initiation factors, elongation factors or ribosome subunits associated with ASIT?

The other looming question is whether ASIT occurs *in vivo*, and what is its physiological relevance? If there is normally a repression of translation that is relieved by loss of amino acids, does this process go haywire in cancer, which is known to depend on an increase of translational capacity for growth²⁹? Additionally, are there normal physiological situations in which there is an amino acid starvation strong enough to induce ASIT? Models for further investigation would be malnutrition syndromes kwashiorkor, in which patients have sufficient calorie intake but insufficient protein consumption, and marasmus, in which patients have insufficient levels of all nutrients. Hypoproteinemia induced by nephrosis has been shown to increase the incorporation of radiolabelled amino acids in the liver³⁰; whether hypoproteinemia induced by other stimuli such as sepsis also leads to increased protein translation, or whether other organs also become hypersynthetic, is unknown. Leucine, and the other branched chain amino acids isoleucine and valine, have more dramatic fluctuations in plasma levels compared to other amino acids, whose plasma concentrations are more tightly regulated by liver metabolism. Would high levels of dietary leucine prevent ASIT in a model such as kwashiorkor? Another model to investigate ASIT induction is exercise. During exercise, local nutrient and oxygen depletion potentially primes the cells for increased growth upon refeeding. How leucine fits in this model however is unclear, as there has been data indicating that leucine promotes muscle growth after exercise^{31,32}.

On a smaller scale, lack of blood flow, for example to cells in the center of a solid tumor, may evoke a similar amino acid starving to induce ASIT. Outside of a disease

model, during development many cells are transiently nutrient depleted during the first half of gestation. Does ASIT support continued translation during these stages of development? Cerebrospinal fluid has lower levels of protein and glucose compared to plasma^{33,34}. In sleep, the CSF flow increases in brain to clear out unwanted proteins³⁵, it would be interesting to monitor the rate of translation in neurons during a CSF wash.

Another potential *in vivo* model in which there is severe acute nutrient depletion is cardiac ischemia. An established *ex vivo* model of cardiomyopathy is isolated heart cells cultured in a pellet under oil,³⁶ which is reminiscent of the HBSS starvation that induces ASIT. During heart attacks, ischemia and reperfusion to the muscle leads to severe tissue damage. While the adult heart has limited potential for regeneration, there is evidence that cardiomyocytes can slowly self renew^{37,38}. Enhancement of these processes offers the potential to immensely benefit patients following a myocardial infarction. Protein translation is necessary to maintain, build, and repair muscle cells in basal conditions³⁹. Translation rapidly responds to changes in metabolism and oxygen whereas transcriptional responses can take hours; moreover, translation is required for productive muscle regrowth, either by cardiac hypertrophy or regeneration. Therefore, translational changes can be the first and last response to any damage to the heart. In a preliminary study, I found that mimicking hypoxia by the addition of cobalt chloride decreases ³⁵S-methionine incorporation slightly in MEFs, but still has no effect on ASIT. If ASIT occurs during ischemic cardiomyopathy, can it also be modulated to mitigate the damage done or promote repair?

Additionally, a cardiac model to study ASIT and starvation induced translational changes is somewhat prompted by the ribosome profiling data obtained, from which I

identified two proteins, Hand2⁴⁰ and Chchd2⁴¹⁻⁴³, that exhibit increased ribosome occupancy in response to starvation. These transcription factors are primed to affect heart repair following injury. For example, heart function has been restored in mice by reprogramming non-myocytes into cardiomyocytes by expressing a slew of transcription factors, including Hand2^{44,45}. Whether Hand2 or Chchd2 are helpful or harmful in rebuilding heart tissue following damage normally remains to be elucidated^{37,40,46,47}. Firstly, the increase of Hand2 and Chchd2 translation during starvation would need to be validated by label incorporation and immunoprecipitation, and polysome profiling and qPCR. Secondly, whether this increase in translation leads to an observable increase in protein levels would need to be confirmed. Unfortunately, the downstream genes that are transcriptionally regulated by these two proteins are poorly characterized, but a qPCR screen with some of the reported downstream targets will show whether the increased protein levels of Chchd2 and Hand2 are having a functional effect on rewiring the cells during stress^{41,42,48,49}. Subsequent studies on the necessity of these proteins for cardiac survival following starvation could then be performed.

Figure 1

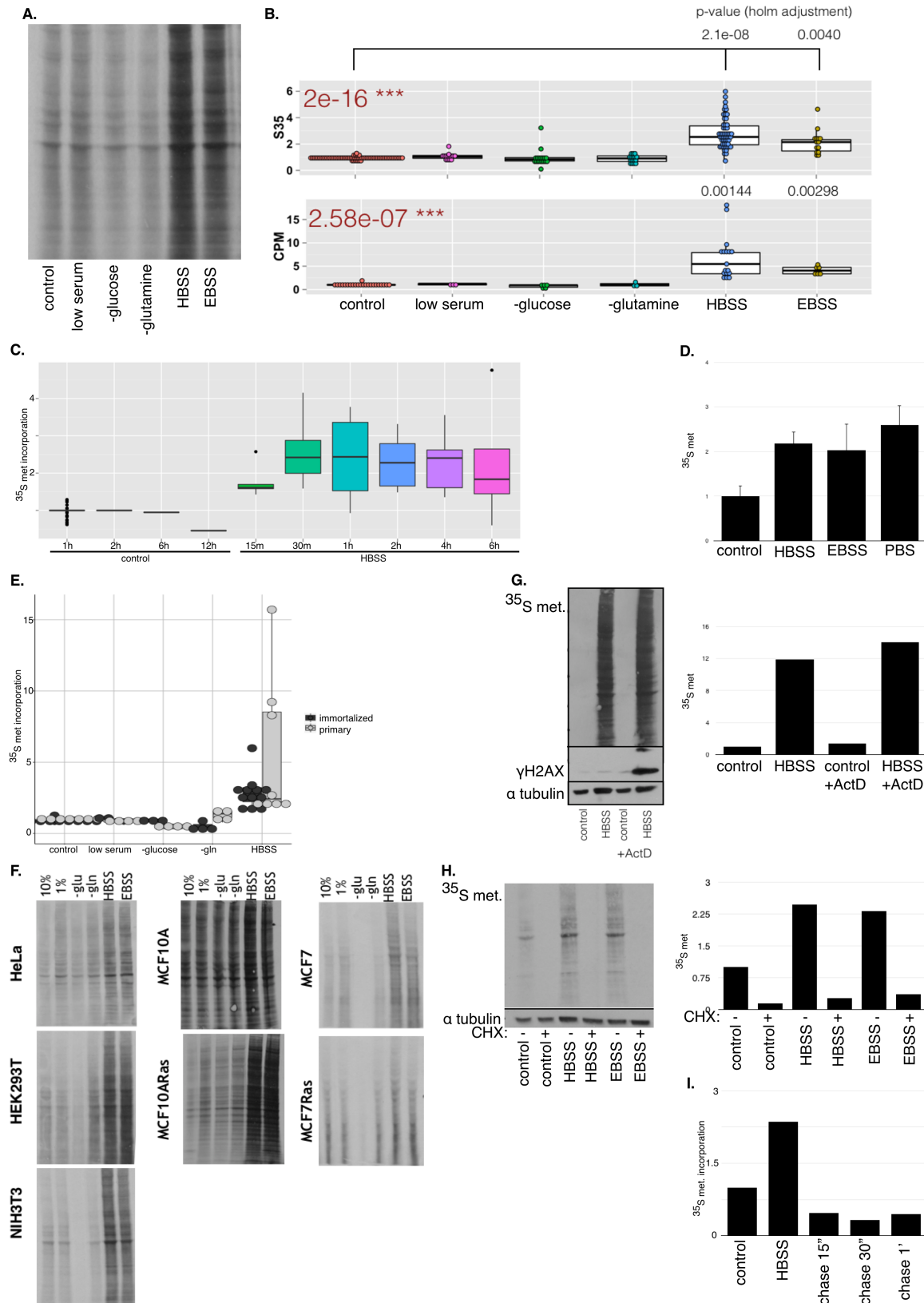


Figure 1: Acute starvation induced translation is rapid and sustained in a variety of cell types

A. Protein lysate was collected cells pulsed with ^{35}S methionine for 30min following 2h of culture in methionine-free media lacking various nutrients, and an autoradiogram was performed.

B. Quantification of ^{35}S methionine incorporation, normalized to control conditions, from autoradiograms (above) and scintillation counter (below). p-val by ANOVA listed in red in top left corner, p-val by t-test indicated for HBSS and EBSS conditions.

C. Quantification of ^{35}S methionine incorporation rates over the final 30min of starvation treatment, assayed by radiogram and normalized to control, are shown for various timepoints as indicated of HBSS starvation.

D. Quantification (mean + SD) of ^{35}S methionine incorporation rates, assayed by radiogram and normalized to control, in various acute starvation conditions.

E. ^{35}S methionine incorporation rates, assayed by radiogram and normalized to control, in various starvation conditions in primary and immortalized MEFs.

F. ^{35}S methionine incorporation in various starvation conditions in a panel of cell lines as indicated.

G, H. ^{35}S methionine incorporation rates in immortalized MEFs pretreated with Actinomycin D (10 $\mu\text{g}/\text{ml}$ for 1h) (G) or cycloheximide (25 $\mu\text{g}/\text{ml}$ for 15m) (H) and placed in fed or starved conditions. Representative autoradiogram immunoblotted as indicated (left) and quantification of ^{35}S methionine incorporation rates, assayed by radiogram and normalized to control (right) shown.

I. ^{35}S methionine incorporation rates over 15 min in immortalized MEFs in fed or starved conditions, or following starvation chased with full media for the time indicated.

Figure 2

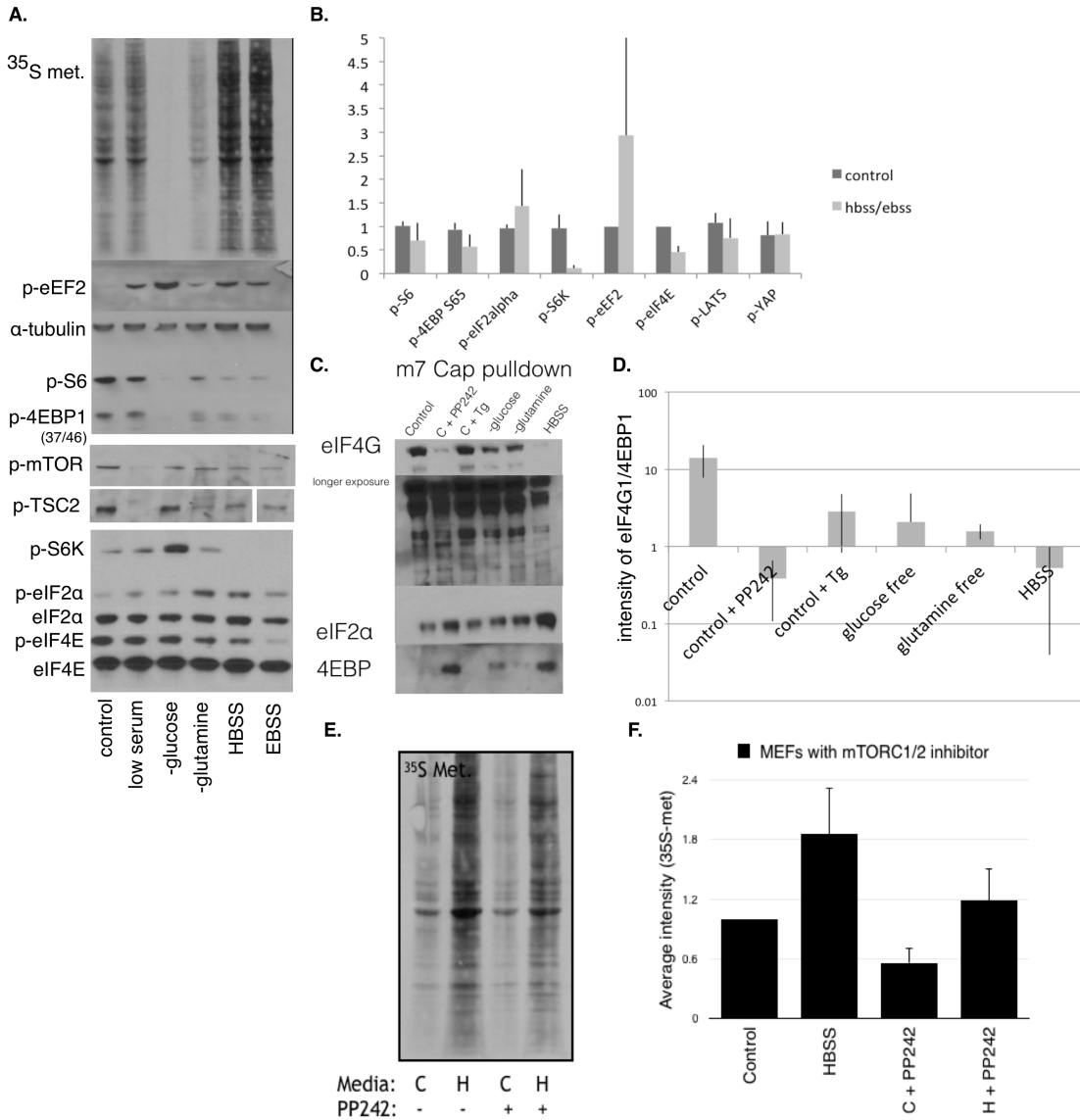


Figure 2: Canonical markers of translation indicate that protein translation should be attenuated in acute starvation conditions

A. Representative autoradiogram and immunoblots of immortalized MEFs cultured in various starvation conditions.

B. Quantification (mean + SD) of immunoblot intensity, normalized to control conditions, of immortalized MEFs in fed or starved conditions.

C. Representative immunoblot of m⁷-GTP cap pulldown assay of immortalized MEFs treated with various translation inhibitors and starvation conditions as indicated.

D. Quantification (mean ± SD) of m⁷-GTP cap pulldown assay, showing ratio of immunoblot intensity of eIF4G1 to 4EBP1 in immortalized MEFs treated with various translation inhibitors and starvation conditions as indicated.

E, F. ^{35}S methionine incorporation rates in immortalized MEFs treated with the mTORC1/2 inhibitor PP242 (2 μM for 1h) and placed in control media (C) or HBSS (H). (E) Representative autoradiogram. (F) Quantification (mean + SD) of ^{35}S methionine incorporation rates, assayed by radiogram and normalized to control.

Figure 3

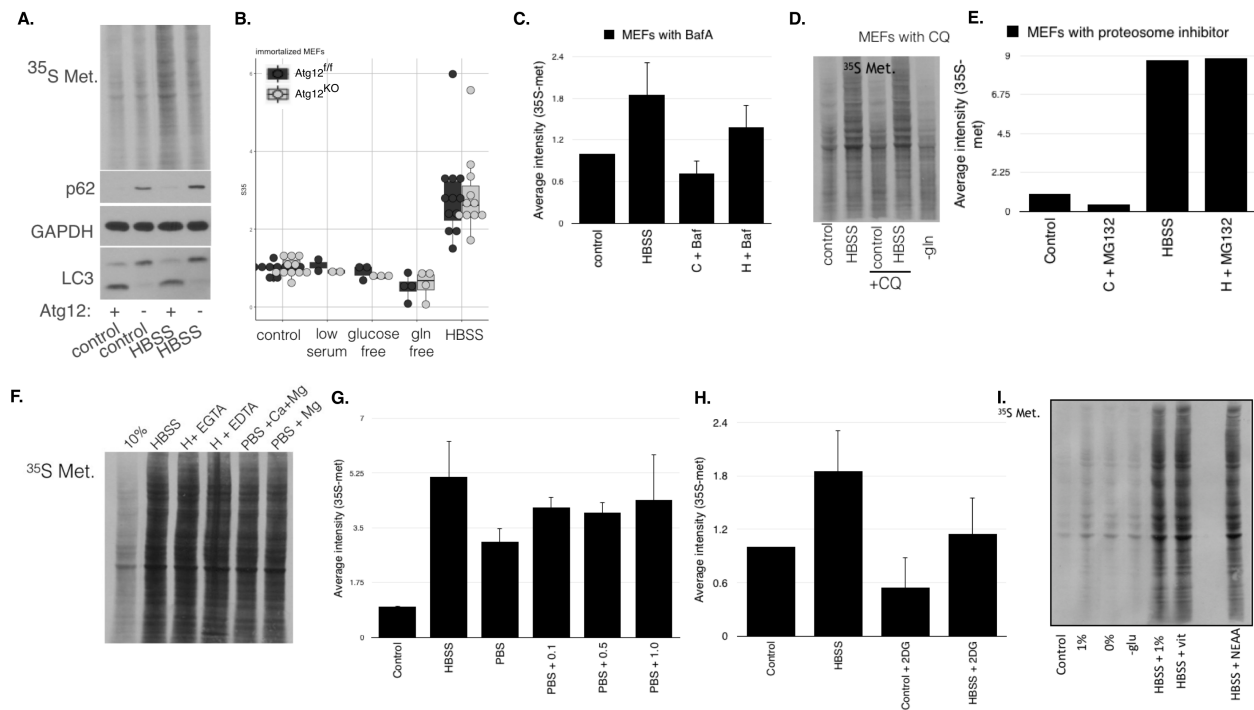


Figure 3: Protein turnover, calcium, glucose, serum, vitamins and non-essential amino acids, do not prevent ASIT

A, B. ^{35}S methionine incorporation rates in immortalized MEFs that deleted for Atg12 and placed in control media or HBSS. (A) Representative autoradiogram, with immunoblot for markers of autophagy inhibition. (B) Quantification (boxplot with dotplot overlay) of ^{35}S methionine incorporation rates, assayed by radiogram and normalized to Atg12^{fl/fl} control levels.

C. Quantification (mean + SD) of ^{35}S methionine incorporation rates, assayed by radiogram and normalized to control, in immortalized MEFs treated with the lysosomal inhibitor Bafilomycin A (25nM for 6h) in control media or HBSS for 2h.

D. Representative autoradiogram of immortalized MEFs treated with the lysosomal inhibitor chloroquine (25 μM for 8h) in control media or HBSS for 2h.

E. Quantification of ^{35}S methionine incorporation rates, assayed by radiogram and normalized to control, in immortalized MEFs treated with the proteasome inhibitor MG132 (5 μM for 1h) in control media or HBSS for 2h.

F. Representative autoradiogram of ^{35}S methionine incorporation in immortalized MEFs in control, HBSS, HBSS supplemented with calcium chelators EGTA or EDTA, or PBS supplemented with calcium and magnesium, or magnesium only.

G. Quantification (mean + SD) of ^{35}S methionine incorporation rates in immortalized MEFs in control media, HBSS, PBS, or PBS supplemented with glucose as indicated (mg/L for 2h).

H. Quantification (mean + SD) of ^{35}S methionine incorporation rates in immortalized MEFs in control media or HBSS treated with the glycolysis inhibitor 2-deoxyglucose (50mM for 1h).

I. Representative autoradiogram of ^{35}S methionine incorporation in immortalized MEFs in various starvation conditions and HBSS supplemented with low serum, vitamin mix or non-essential amino acids as indicated.

Figure 4

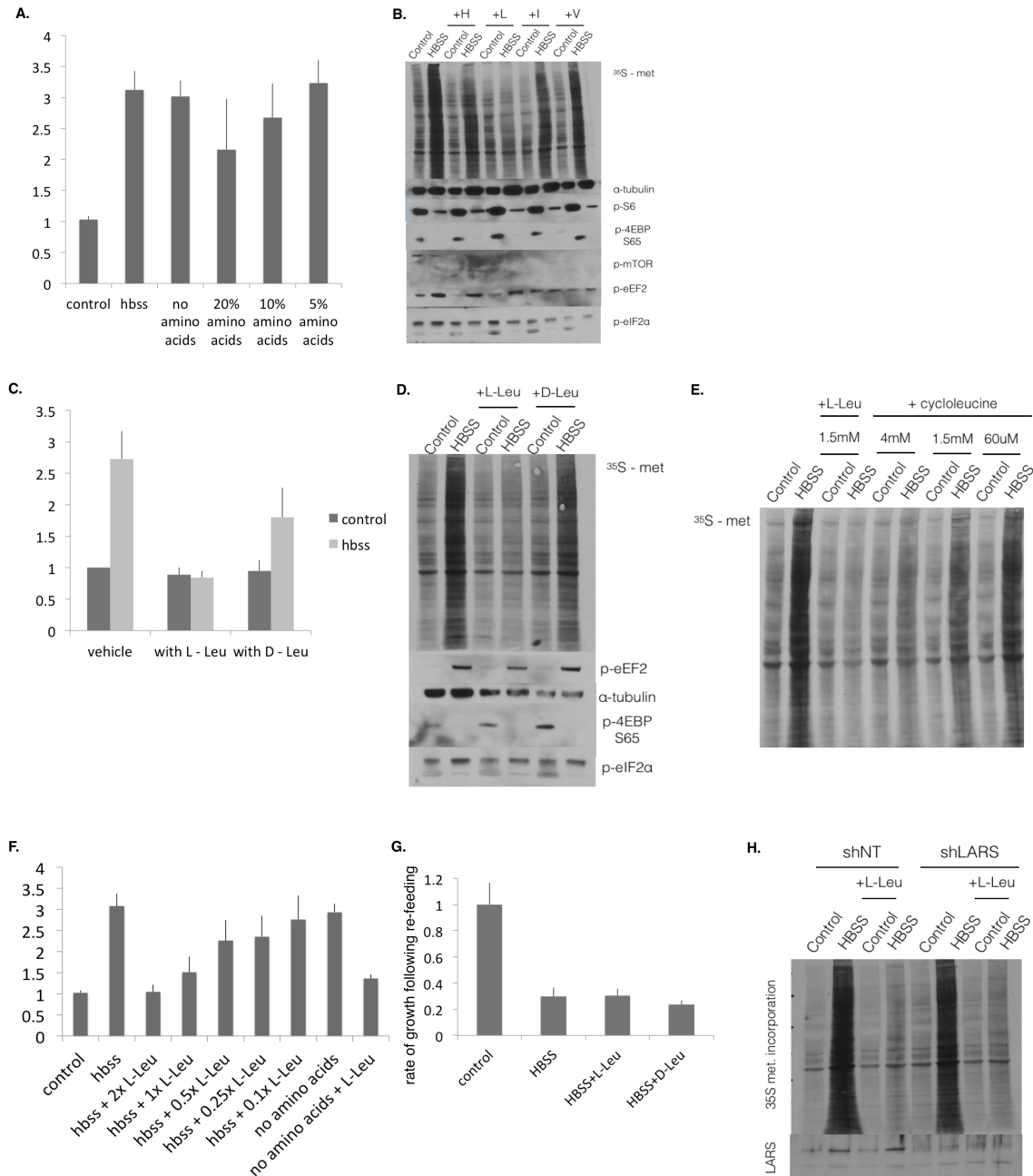


Figure 4: L-Leucine prevents ASIT

A. Quantification (mean + SD) of ^{35}S methionine incorporation rates in immortalized MEFs in control media, HBSS, DMEM without amino acids, and DMEM with decreased levels of amino acids.

B. Representative autoradiogram of ^{35}S methionine incorporation in immortalized MEFs in control media or HBSS, supplemented with single amino acids (to double the concentration present in DMEM) as indicated. Immunoblots for markers of active translation below.

- C. Quantification (mean + SD) of ^{35}S methionine incorporation rate in immortalized MEFs, normalized to control, in control media or HBSS supplemented with bioactive L-Leucine or bio-inactive D-Leucine.
- D. Representative autoradiogram of ^{35}S methionine incorporation in immortalized MEFs in control media or HBSS, supplemented with L-Leucine or D-Leucine as indicated. Immunoblots for markers of active translation below.
- E. Representative autoradiogram of ^{35}S methionine incorporation in immortalized MEFs in control media or HBSS, supplemented with L-Leucine or cycloleucine at various concentrations as indicated.
- F. Quantification (mean + SD) of ^{35}S methionine incorporation rate in immortalized MEFs, normalized to control, in control media, HBSS, or HBSS supplemented with L-Leucine at a range of doses relative to levels in DMEM, DMEM without amino acids, and DMEM supplemented with L-Leucine as indicated.
- G. Quantification of rate of growth (mean + SEM), assayed by crystal violet staining and normalized to control, in cells starved for 2h as indicated, and then switched to DMEM for 24h.
- H. Representative autoradiogram of ^{35}S methionine incorporation (above) and immunoblot of LARS (below) in immortalized MEFs knocked down for LARS and switched to HBSS with or without additional L-Leucine, as indicated.

Figure 5

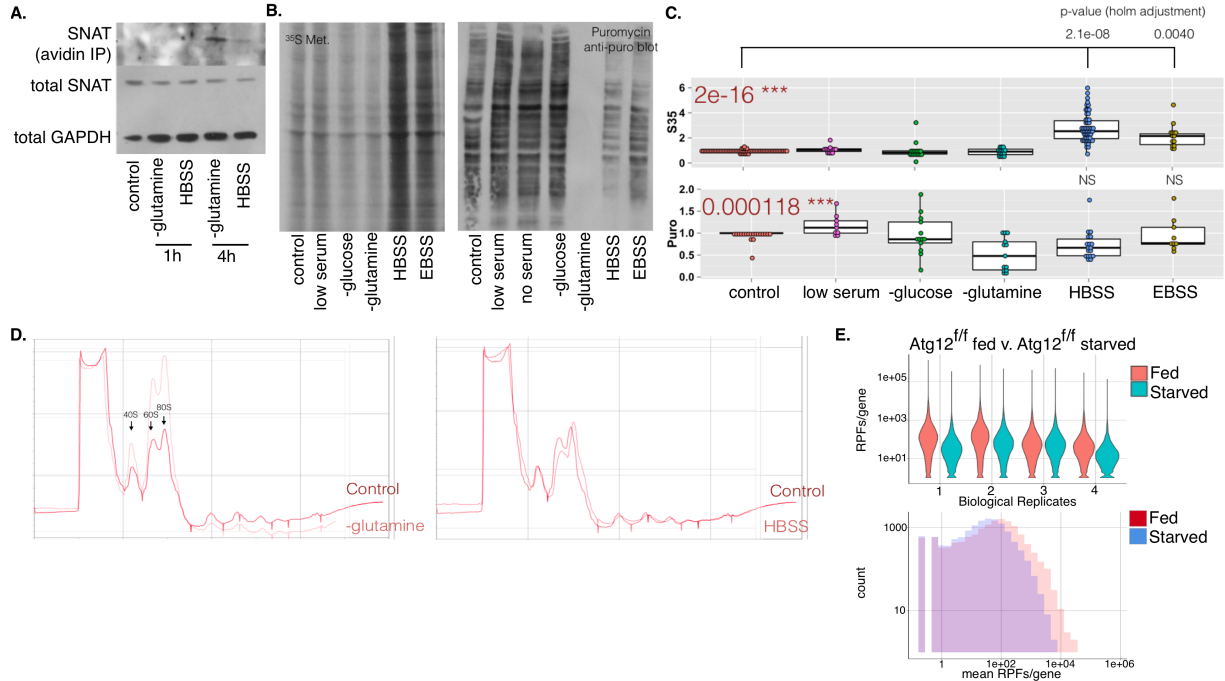


Figure 5: Experiments to confirm increased translation rates are inconclusive

A. Immunoblot of surface levels of SNAT, assayed by surface biotinylation, and total levels of SNAT and GAPDH in various starvation conditions for time indicated.

B. Representative autoradiogram and immunoblot of ^{35}S methionine incorporation (left) and puromycin incorporation (right) in various starvation conditions in immortalized MEFs.

C. Quantification of ^{35}S methionine incorporation rate (top) and puromycin incorporation rate (bottom) in various starvation conditions, normalized to control. p-val by ANOVA in red at top left, p-val by t-test comparing control to acute starvation indicated.

D. Polysome profile of immortalized MEFs in control, glutamine free and HBSS starvation conditions.

E. Reproduction of data presented in chapter 2, Figure 2C. Violin plots of number of read counts of ribosome protected footprints (RPFs) per gene per biological replicate (above) and histogram of the mean of the number of read counts of ribosome protected footprints per gene (below) in Atg12^{ff} MEFs in control media or following 2h HBSS starvation.

Table 1: comparison chart of various acute starvation media

	DMEM	HBSS	EBSS	PBS
sodium chloride	6400mg/L	8000mg/L	6800mg/L	8000mg/L
sodium phosphate	125mg/L	90mg/L	140mg/L	2160mg/L
potassium chloride	400mg/L	400 mg/L	400mg/L	200mg/L
sodium bicarbonate	3700mg/L	350mg/L	2200mg/L	--
D-glucose	4500mg/L	1000mg/L	1000mg/L	--
calcium chloride	200mg/L	140mg/L	200mg/L	--
magnesium sulfate	200mg/L	100mg/L	97mg/L	--
ferric nitrate	0.1 mg/L	--	--	--
phenol red	15mg/L	--	10mg/L	--
magnesium chloride	--	100mg/L	--	200mg/L
potassium phosphate monobasic	--	60mg/L	--	No
Amino acids	Yes	No	No	No
Vitamin mix	Yes	No	No	No
pH after 1hr on cells	8.2	7.5	8.1	7.5

Table 2: list of top 30 significantly enriched ribosome occupancies in starved versus fed conditions

High ribosome occupancy of Starved:Fed cells

	gene ID	mRNA LogFC	P-val	FDR
Gas2l1	ENSMUSG00000034201	0.5015	0.00025	0.0170
Cebpb	ENSMUSG00000056501	1.0100	0.00384	0.1625
Itpril2	ENSMUSG00000095115	1.5805 *	0.00735	0.2861
Atf4	ENSMUSG00000042406	0.4882	0.01063	0.3882
Kifc3	ENSMUSG00000031788	0.5879	0.01334	0.4650
Mphosph9	ENSMUSG00000038126	0.2877	0.01395	0.4742
Srsf2	ENSMUSG00000034120	0.8318	0.01532	0.5025
Hist2h2aa1	ENSMUSG00000063954	0.5767	0.01559	0.5041
Hist1h2ab	ENSMUSG00000061615	0.4144	0.01599	0.5063
Fzd7	ENSMUSG00000041075	1.5212 *	0.01689	0.5186
Hist1h2ac	ENSMUSG00000069270	0.3703	0.01702	0.5186
Hist1h2ao	ENSMUSG00000094248	0.2730	0.01795	0.5357
Hand2	ENSMUSG00000038193	0.1085	0.02003	0.5846
Nr2f6	ENSMUSG00000002393	0.8287	0.02062	0.5931
Rab11fip3	ENSMUSG00000037098	0.3356	0.02213	0.6134
Hist1h2ad	ENSMUSG00000071478	0.3001	0.02256	0.6181
Hist1h2af	ENSMUSG00000061991	0.3165	0.02295	0.6211
Hoxd13	ENSMUSG00000001819	0.5325	0.02342	0.6278
Gpx4	ENSMUSG00000075706	0.3285	0.02350	0.6278
Adra1b	ENSMUSG00000050541	0.5988	0.02392	0.6327
Egln2	ENSMUSG00000058709	0.3497	0.02484	0.6507
Ier5	ENSMUSG00000056708	2.6947 *	0.02565	0.6608
Hist1h2ah	ENSMUSG00000069302	0.3354	0.02590	0.6623
Mapk6	ENSMUSG00000042688	1.1797 *	0.02630	0.6662
Jund	ENSMUSG00000071076	0.6380	0.02695	0.6717
Arhgef10l	ENSMUSG00000040964	0.3566	0.02736	0.6770
Adamts13	ENSMUSG00000070469	0.8678	0.02776	0.6838
Hnrnpa0	ENSMUSG00000007836	0.6285	0.02867	0.6914
Chchd2	ENSMUSG00000070493	0.5581	0.02897	0.6914
Polh	ENSMUSG00000023953	0.5476	0.03205	0.7458

* = both ribosome occupancy and mRNA changes

Table 3: Gene ontology of mRNAs with significantly enriched ribosome occupancy during starvation

PANTHER GO-Slim Biological Process	#	#	expected	Fold Enrichment	+/-	▲ raw P value	FDR
regulation of gene expression, epigenetic	72	4	.09	45.81	+	2.06E-06	5.04E-04
chromatin organization	258	4	.31	12.78	+	2.65E-04	3.23E-02
regulation of nucleobase-containing compound metabolic process	560	5	.68	7.36	+	5.23E-04	4.25E-02
metabolic process	6009	15	7.29	2.06	+	1.81E-03	1.10E-01
nitrogen compound metabolic process	2462	9	2.99	3.01	+	1.81E-03	8.84E-02
organelle organization	1133	6	1.37	4.37	+	2.06E-03	8.38E-02
nucleobase-containing compound metabolic process	2710	9	3.29	2.74	+	3.53E-03	1.23E-01
biosynthetic process	1719	7	2.08	3.36	+	3.68E-03	1.12E-01
mesoderm development	265	3	.32	9.33	+	4.06E-03	1.10E-01
transcription, DNA-dependent	998	5	1.21	4.13	+	6.46E-03	1.58E-01
regulation of vasoconstriction	5	1	.01	> 100	+	7.25E-03	1.61E-01
primary metabolic process	4839	12	5.87	2.04	+	8.39E-03	1.71E-01
RNA metabolic process	1536	6	1.86	3.22	+	9.11E-03	1.71E-01
Unclassified	10492	6	12.73	.47	-	1.11E-02	1.94E-01
regulation of biological process	3320	9	4.03	2.24	+	1.34E-02	2.18E-01
digestive tract mesoderm development	18	1	.02	45.81	+	2.28E-02	3.47E-01
blood circulation	19	1	.02	43.40	+	2.40E-02	3.44E-01
response to toxic substance	21	1	.03	39.26	+	2.63E-02	3.57E-01
cellular component organization	1961	6	2.38	2.52	+	2.76E-02	3.54E-01
cellular component organization or biogenesis	2099	6	2.55	2.36	+	3.69E-02	4.51E-01
biological regulation	3899	9	4.73	1.90	+	4.09E-02	4.75E-01
cell cycle	650	3	.79	3.81	+	4.35E-02	4.82E-01
response to stress	785	3	.95	3.15	+	6.87E-02	7.29E-01
behavior	61	1	.07	13.52	+	7.25E-02	7.37E-01
cell proliferation	66	1	.08	12.49	+	7.81E-02	7.62E-01
response to abiotic stimulus	70	1	.08	11.78	+	8.26E-02	7.75E-01

Table 4: list of top 30 significantly decreased ribosome occupancies in starved versus fed conditions

Low ribosome occupancy of Starved:Fed cells

	gene ID	mRNA LogFC		P-val	FDR
Eef1a1	ENSMUSG00000037742	-1.2535	*	1.69E-12	9.09E-09
Eef1b2	ENSMUSG00000025967	-0.5901		7.89E-10	2.12E-06
Rpl17	ENSMUSG00000062328	-0.6946		1.53E-09	2.74E-06
Rps24	ENSMUSG00000025290	-0.6555		3.28E-09	3.79E-06
Eef2	ENSMUSG00000034994	-1.4325	*	3.52E-09	3.79E-06
Tpt1	ENSMUSG00000060126	-0.5643		2.13E-08	1.90E-05
Rps27rt	ENSMUSG00000050621	-0.1222		5.18E-08	3.86E-05
Rps27	ENSMUSG00000090733	-0.0923		5.75E-08	3.86E-05
Rpl18a	ENSMUSG00000045128	-0.7593		8.15E-08	4.86E-05
Rps27a	ENSMUSG00000020460	-0.8120		9.06E-08	4.87E-05
Rpl28	ENSMUSG00000030432	-0.6967		1.15E-07	5.60E-05
Rps4x	ENSMUSG00000031320	-0.8382		1.52E-07	6.82E-05
Rpl3	ENSMUSG00000060036	-0.9160	*	1.81E-07	7.49E-05
Hspa8	ENSMUSG00000015656	-1.2101	*	2.26E-07	8.49E-05
Npm1	ENSMUSG00000057113	-0.9757	*	2.37E-07	8.49E-05
Rpl5	ENSMUSG00000058558	-0.9018		2.96E-07	9.93E-05
Rps19	ENSMUSG00000040952	-0.3211		3.31E-07	0.000103782
Bgn	ENSMUSG00000031375	-0.8980		3.48E-07	0.000103782
Rps3a1	ENSMUSG00000028081	-0.7338		6.09E-07	0.000170094
Rpl30	ENSMUSG00000058600	-0.3448		6.33E-07	0.000170094
Rpl31	ENSMUSG00000073702	-0.3883		8.64E-07	0.000221012
Vim	ENSMUSG00000026728	-1.0521	*	1.02E-06	0.000249454
Pabpc1	ENSMUSG00000022283	-0.5094		1.11E-06	0.00025884
Rpl22l1	ENSMUSG00000039221	-0.4286		1.22E-06	0.000272028
Hsp90ab1	ENSMUSG00000023944	-1.2991	*	1.59E-06	0.000340994
Rpl10	ENSMUSG00000008682	-0.5821		1.88E-06	0.000387717
Rps20	ENSMUSG00000028234	-0.3299		2.19E-06	0.000433982
Rps18	ENSMUSG00000008668	-0.2418		2.26E-06	0.000433982
Rps6	ENSMUSG00000028495	-0.6000		2.46E-06	0.000455249
Rpl39	ENSMUSG00000079641	-0.2957		2.75E-06	0.000492798

* = both ribosome occupancy and mRNA changes

Table 5: Gene ontology of mRNAs with significantly decreased ribosome occupancy during starvation

GO biological process complete	#	# expected	Fold Enrichment	+/-	▲ raw P value	FDR	
translation	293	16	.38	41.92	+	7.27E-23	1.13E-18
peptide biosynthetic process	312	16	.41	39.37	+	1.91E-22	1.49E-18
peptide metabolic process	420	17	.55	31.07	+	2.87E-22	1.48E-18
amide biosynthetic process	398	16	.52	30.86	+	8.18E-21	3.18E-17
cellular amide metabolic process	627	17	.82	20.81	+	2.08E-19	6.46E-16
organonitrogen compound biosynthetic process	1065	16	1.39	11.53	+	3.14E-14	8.14E-11
gene expression	3007	21	3.92	5.36	+	8.34E-13	1.85E-09
cellular nitrogen compound biosynthetic process	2677	19	3.49	5.45	+	2.09E-11	4.07E-08
cellular macromolecule biosynthetic process	2694	19	3.51	5.41	+	2.34E-11	4.04E-08
macromolecule biosynthetic process	2721	19	3.54	5.36	+	2.79E-11	4.34E-08
cellular nitrogen compound metabolic process	4147	22	5.40	4.07	+	3.63E-11	5.13E-08
cellular protein metabolic process	2800	18	3.65	4.93	+	5.58E-10	7.22E-07
ribonucleoprotein complex biogenesis	398	9	.52	17.36	+	1.50E-09	1.79E-06
ribosome biogenesis	265	8	.35	23.17	+	1.57E-09	1.74E-06
cellular biosynthetic process	3474	19	4.53	4.20	+	1.97E-09	2.04E-06
organic substance biosynthetic process	3557	19	4.63	4.10	+	2.96E-09	2.88E-06
biosynthetic process	3617	19	4.71	4.03	+	3.94E-09	3.60E-06
macromolecule metabolic process	6252	23	8.14	2.82	+	1.54E-08	1.33E-05
cellular macromolecule metabolic process	5065	21	6.60	3.18	+	1.97E-08	1.61E-05
cytoplasmic translation	62	5	.08	61.91	+	2.37E-08	1.84E-05
ribosomal small subunit biogenesis	63	5	.08	60.93	+	2.55E-08	1.89E-05
protein metabolic process	3581	18	4.66	3.86	+	3.03E-08	2.14E-05
ribosome assembly	70	5	.09	54.83	+	4.20E-08	2.84E-05
nitrogen compound metabolic process	6998	23	9.12	2.52	+	1.56E-07	1.01E-04
ribonucleoprotein complex assembly	208	6	.27	22.14	+	2.88E-07	1.79E-04
positive regulation of translation	108	5	.14	35.54	+	3.30E-07	1.97E-04

Materials and Methods

Isolation of mouse embryonic fibroblasts

Mouse embryonic fibroblasts were generated from E13.5 mice described above and C57Bl/6 mice following the protocol from Robertson (1987). Briefly, embryos were collected, heart, liver and head were removed and fibroblasts were minced, digested in trypsin for 30min at 37°C and plated in DMEM with 10% serum and Pen/Strep. Cells were genotyped and Atg12^{ff};Cag-Cre^{ER+} and Atg12^{WT} cells were immortalized by infection with SV40 large T antigen. Cells were plasmocin treated prior to use. Following immortalization and plasmocin treatment, cells were maintained in DMEM 1x (Gibco) supplemented with 10% FBS (Atlas).

Genetic deletion of MEFs

Cells were treated with 2µM 4-Hydroxy-tamoxifen (4OHT) or vehicle (100% Ethanol) for three consecutive days. Genetic recombination was achieved following 2 days of 4OHT treatment, and confirmed by PCR.

Cell culture

HeLa cells, HEK293T cells, NIH3T3 cells were all cultured in DMEM with 10% fetal bovine serum, penicillin and streptomycin. MCF10A and MCF10ARas cells were cultured in DMEM/F12 supplemented with 5% horse serum, 20ng/ml EGF, 0.5 µg/ml hydrocortisone, 100ng/ml cholera toxin, 10 µg/ml insulin, penicillin and streptomycin.

³⁵S methionine radiolabeling assay

200,000 cells in a 6-well plate were plated the night before in control media and allowed to adhere overnight. The next day, cells were washed once in PBS and media was replaced with either DMEM + 10% FBS lacking methionine (control) or HBSS or some

other starvation condition for the indicated amount of time. All labeling was done in the absence of cold methionine. Unless otherwise indicated, starvation time was 2 hours. 30 min prior to collection, 20 μ Ci of 35 S methionine was added to the wells. After 30 min of label incorporation, the media was removed and disposed of in a manner in accordance with radiation safety at UCSF, as was all subsequent washes and protein lysate. Cells were washed once in PBS and lysed in RIPA buffer containing protease and phosphatase inhibitors. Lysates were frozen at -80C, thawed and the insoluble fraction was centrifuged out. Then the protein concentration in the lysates was measured by BCA assay, and equal protein amounts were boiled in sample buffer, loaded onto SDS-PAGE gels and run for 80 min at 150V, just before the dye-front left the gel. The samples were then transferred onto PVDF at 45V for 2h, and the membrane was sandwiched in cling film, taped in a cassette and film placed on the membrane for 5-7 days before developing.

Puromycin labeling assay

The labeling with puromycin was mostly the same as the 35 S methionine labeling. However, the cells did not need to be switched to methionine free media prior to labeling. Puromycin was added to cells in various media conditions for at a concentration of 10 μ M for 30min. Following transfer onto PVDF, the membrane was immunoblotted using an anti-puromycin antibody.

Immunoblotting

For immunoblot analysis, 200,000 - 300,000 cells were lysed in RIPA buffer (1% Triton X-100, 1% sodium deoxycholate, 0.1% SDS, 25mM Tris, pH 7.6, and 150mM NaCl) plus protease inhibitor cocktail (Sigma-Aldrich), 10mM NaF, 10mM β -glycerophosphate,

1mM Na₃VO₄, 10nM calyculin A, 0.5mM PMSF, 10µg/ml E64d, and 10µg/ml pepstatin A. Lysates were freeze-thawed at –20°C, cleared by centrifugation for 30 min at 4°C, protein content was quantified by BCA assay and equal amounts were boiled in sample buffer, resolved by SDS -PAGE, and transferred to polyvinylidene fluoride membrane. Membranes were blocked for 1 h in 5% milk or 5% BSA in PBS with 0.1% Tween 20, incubated in primary antibody overnight at 4°C, washed, incubated for 1 h at RT with HRP-conjugated goat secondary antibodies (1:5,000; Jackson ImmunoResearch Laboratories), washed, and visualized via enhanced chemiluminescence (Thermo Fisher Scientific).

cap pulldown assay

For cap pulldown experiments (CPD), cells were lysed in buffer listed. 25-50µl of m7-GTP beads were added to 250-500µg protein at 1µg/µl and incubated overnight. Beads were washed four times in CPD buffer, eluted in 3x sample buffer and analyzed by immunoblotting.

Cap pulldown (CPD) buffer: 10mM Tris HCl pH 7.6, 140mM KCl, 4mM MgCl₂, 1mM DTT, 1mM EDTA, 1% NP-40, 1mM PMSF, protease inhibitor cocktail, 0.2mM sodium orthovanadate.

Surface biotinylation assay

Surface proteins were labeled with biotin and captured using the Pierce Cell surface protein isolation kit (89881) according to manufacturer's instructions.

Crystal violet assay.

2000 cells were plated per well in 96-well plates. At time (t)=0 and 24h, plates were fixed with 4% paraformaldehyde and stained in 0.3% crystal violet in water for 1hr, and

washed in distilled water until control empty wells were rinsed clean. The crystal violet stain was solubilized in 100% methanol, and A590 measured by spectrometer. Percent growth (mean \pm SEM) was calculated as $(\text{Abs.t}_{24} - \text{Abs.t}_0)/\text{Abs.t}_0$.

Ribosome profiling

Ribosome profiling experiments were performed using the ARTseq Ribosome profiling kit (Epicentre), with RNA extraction by Trizol LS (Ambion), rRNA depletion via RiboZero Gold (Epicentre), and quality and quantity of small RNA and DNA assayed using Agilent High Sensitivity Small RNA kit and DNA kit respectively (Agilent). Sequencing was performed at the UCSF sequencing core on Illumina HiSeq2000, and analysis of reads was performed using Babel (Olshen et al, 2013). Cycloheximide was made fresh to 50mg/ml in Ethanol for each experiment, used at a concentration of 100 μ g/ml.

Polysome profiling

The protocol was followed from Morita et al, 2013 (Morita et al, 2013. Polysome Profiling Analysis. Bio-protocol 3(14): e833. DOI: 10.21769/BioProtoc.833). Briefly, 4 million cells treated with cyclohexamide as described above were collected in PBS, lysed in 5mM Tris-HCl, pH7.5, 2.5mM MgCl₂, 1.5mM KCl, 0.5% Triton X-100, 0.5% Sodium deoxycholate, with protease inhibitors, cyclohexamide, DTT, and RNase inhibitor added just prior to lysis. OD_{260nm} was measured and equal OD amount of lysate was loaded on each 10-50% sucrose gradient. Cells were centrifuged at 35,000 rpm for 2h at 4C and RNA analysis was performed using the Biocomp gradient station, gradient profiler and Biorad Econo UV monitor.

KEY RESOURCES TABLE

Reagent or Resource	source	identifier	concentration
Antibodies			
alpha-tubulin	Cell Signaling	#2125BC	1:1000 for IB
gamma-H2AX	Upstate	#05-636	1:1000 for IB
phospho-S6	Cell Signaling	#2215	1:2000 for IB
S6	Cell Signaling	#2217	1:2000 for IB
phospho-4EBP1 S65	Cell Signaling	#9451	1:1000 for IB
phospho-4EBP1 S37/46	Cell Signaling	#2855	1:1000 for IB
4EBP1	Cell Signaling	#9452	1:1000 for IB
phospho-S6K	Cell Signaling	#9206S	1:1000 for IB
S6K	Cell Signaling	#9202	1:1000 for IB
phospho-eIF2alpha	Cell Signaling	#9721	1:1000 for IB
eIF2alpha	Cell Signaling	#9722	1:1000 for IB
phospho-eIF4E S209	Cell Signaling	#9741P	1:1000 for IB
eIF4E	Cell Signaling	#9742	1:1000 for IB
eIF4G	Cell Signaling	#2469	1:1000 for IB
phospho-eEF2	Cell signaling	#2331S	1:2000 for IB
eEF2	Cell Signaling	#2332	1:2000 for IB
phospho-LATS (Ser909)	Cell Signaling	#9517	1:500 for IB
LATS	Cell Signaling	#9153S	1:500 for IB
phospho-YAP (Ser109)	Cell Signaling	#43961	1:500 for IB
YAP	Cell Signaling	#4912S	1:500 for IB
p62	Progen	GP-62-C	1:1000 for IB
GAPDH	Millipore	MAB374	1:2000 for IB
LC3	Fung, et al 2008. (commercially available from EMD Millipore)	ABC232	1:1000 for IB
LARS	Bethyl	A304-316A-M	1:1000 for IB
phospho-TSC2	Cell Signaling	#3615S	1:500 for IB
phospho-mTOR S2448	Cell Signaling	2971S	1:500 for IB
Puromycin	Kerafast	EQ0001	1:1000 for IB

Reagent or Resource	source	identifier	concentration
Chemicals			
PP242	Tocris	4257	2uM
Thapsigargin	Cayman Chemical Company	10522	1uM
Bafilomycin A	Sigma Aldrich	B1793	25nM
Chloroquine	Sigma Aldrich	C6628-25G	25µM
MG132	Sigma Aldrich	C2211	5uM
2Deoxy Glucose	Sigma Aldrich	D6134	50mM
Cycloheximide	Sigma Aldrich	C7698	25ug/ml
35S methionine	Perkin Elmer	NEG009A001MC	20µCi
Actinomycin D	Sigma Aldrich	A1410	10 ug/ml
Puromycin	Sigma Aldrich	P7255	10µM
L-Leucine	Sigma Aldrich	L8912	4mM (2X) (200mg/ml)
D-Leucine	Sigma Aldrich	855448	4mM (2X) (200mg/ml)

References

1. Magnuson, B., Ekim, B. & Fingar, D. C. Regulation and function of ribosomal protein S6 kinase (S6K) within mTOR signalling networks. *Biochem. J.* **441**, 1–21 (2012).
2. Thoreen, C. C. *et al.* A unifying model for mTORC1-mediated regulation of mRNA translation. *Nature* **485**, 109–13 (2012).
3. Kelleher, R. J., Govindarajan, A., Jung, H.-Y., Kang, H. & Tonegawa, S. Translational control by MAPK signaling in long-term synaptic plasticity and memory. *Cell* **116**, 467–79 (2004).
4. Kuemmerle, J. F. IGF-I elicits growth of human intestinal smooth muscle cells by activation of PI3K, PDK-1, and p70S6 kinase. *Am. J. Physiol. Gastrointest. Liver Physiol.* **284**, G411-22 (2003).
5. Welsh, G. I., Miller, C. M., Loughlin, a J., Price, N. T. & Proud, C. G. Regulation of eukaryotic initiation factor eIF2B: glycogen synthase kinase-3 phosphorylates a conserved serine which undergoes dephosphorylation in response to insulin. *FEBS Lett.* **421**, 125–30 (1998).
6. Grosso, S. *et al.* PKC β 1 modulates translation independently from mTOR and through RACK1. *Biochem. J.* **415**, 77–85 (2008).
7. Pircher, A., Bakowska-Zywicka, K., Schneider, L., Zywicki, M. & Polacek, N. An mRNA-Derived Noncoding RNA Targets and Regulates the Ribosome. *Mol. Cell* 1–9 (2014). doi:10.1016/j.molcel.2014.02.024
8. Komar, A. a. & Hatzoglou, M. Cellular IRES-mediated translation: The war of ITAFs in pathophysiological states. *Cell Cycle* **10**, 229–240 (2011).
9. Ashe, M. P., Long, S. K. De & Sachs, A. B. Glucose depletion rapidly inhibits translation initiation in Yeast. *Mol. Biol. Cell* **11**, 833–848 (2000).
10. Castelli, L. M. *et al.* Glucose depletion inhibits translation initiation via eIF4A loss and subsequent 48S preinitiation complex accumulation, while the pentose phosphate pathway is coordinately up-regulated. *Mol. Biol. Cell* **22**, 3379–93 (2011).
11. Onodera, J. & Ohsumi, Y. Autophagy is required for maintenance of amino acid levels and protein synthesis under nitrogen starvation. *J. Biol. Chem.* **280**, 31582–6 (2005).
12. Yoon, S. *et al.* NF- κ B and STAT3 cooperatively induce IL6 in starved cancer cells. *Oncogene* **31**, 3467–81 (2012).
13. Zhang, P. *et al.* The GCN2 eIF2 α Kinase Is Required for Adaptation to Amino Acid Deprivation in Mice. *Mol. Cell. Biol.* **22**, 6681–6688 (2002).
14. Hinnebusch, A. G. & Lorsch, J. R. The mechanism of eukaryotic translation initiation: new insights and challenges. *Cold Spring Harb. Perspect. Biol.* **4**, (2012).
15. Hinnebusch, a. G. Translational Regulation of Yeast GCN4: A WINDOW ON FACTORS THAT CONTROL INITIATOR-tRNA BINDING TO THE RIBOSOME. *J. Biol. Chem.* **272**, 21661–21664 (1997).
16. Fernandez, J., Yaman, I., Sarnow, P., Snider, M. D. & Hatzoglou, M. Regulation of internal ribosomal entry site-mediated translation by phosphorylation of the translation initiation factor eIF2 α . *J. Biol. Chem.* **277**, 19198–205 (2002).
17. Hallberg, R. L., Kraus, K. W. & Findly, R. C. Starved *Tetrahymena thermophila*

- Cells That Are Unable to Mount an Effective Heat Shock Response Selectively Degrade Their rRNA. *Mol. Cell. Biol.* **4**, 2170–2179 (1984).
18. Galego, L., Barahona, I. & Rodrigues-pousada, C. Response of *Tetrahymena pyriformis* to stress induced by starvation. *FEBS* **139**, 163–171 (1984).
 19. Levy, M. R. & Elliott, A. M. Biochemical and Ultrastructural Changes in *Tetrahymena pyriformis* During Starvation. *J. Protozool.* **15**, 208–222 (1968).
 20. Calzones, F. J., Angerer, R. C. & Gorovsky, M. A. Regulation of Protein Synthesis in *Tetrahymena*. *J. Biol. Chem.* **258**, 6887–6898 (1983).
 21. Stead, R. L. & Proud, C. G. Rapamycin enhances eIF4E phosphorylation by activating MAP kinase-interacting kinase 2a (Mnk2a). *FEBS Lett.* **587**, 2623–8 (2013).
 22. Ye, J. *et al.* The GCN2-ATF4 pathway is critical for tumour cell survival and proliferation in response to nutrient deprivation. *EMBO J.* **29**, 2082–96 (2010).
 23. B'chir, W. *et al.* The eIF2 α /ATF4 pathway is essential for stress-induced autophagy gene expression. *Nucleic Acids Res.* **41**, 7683–99 (2013).
 24. Han, K. *et al.* Parallel measurement of dynamic changes in translation rates in single cells. *Nat. Methods* **11**, 86–93 (2014).
 25. Lerner, R. S. & Nicchitta, C. V. mRNA translation is compartmentalized to the endoplasmic reticulum following physiological inhibition of cap-dependent translation. *RNA* **12**, 775–789 (2006).
 26. Wolfson, R. L. *et al.* Sestrin2 is a leucine sensor for the mTORC1 pathway. *Science (80-.)*. **351**, 43–48 (2016).
 27. Nicklin, P. *et al.* Bidirectional transport of amino acids regulates mTOR and autophagy. *Cell* **136**, 521–534 (2009).
 28. Wyant, G. A. *et al.* mTORC1 Activator SLC38A9 Is Required to Efflux Essential Amino Acids from Lysosomes and Use Protein as a Nutrient. *Cell* **171**, 642–654.e12 (2017).
 29. Ruggero, D. *et al.* The translation factor eIF-4E promotes tumor formation and cooperates with c-Myc in lymphomagenesis. *Nat. Med.* **10**, 484–6 (2004).
 30. Brenner, T. & Shafir, E. Lipoprotein lipid and protein synthesis in experimental nephrosis and plasmapheresis: II. Perfused rat liver. *Lipids* **15**, 637–43 (1980).
 31. Manjarín, R. *et al.* Leucine supplementation of a chronically restricted protein and energy diet enhances mTOR pathway activation but not muscle protein synthesis in neonatal pigs. *Amino Acids* **48**, 257–267 (2016).
 32. Norton, L. E., Norton, L. E., Layman, D. K. & Layman, D. K. Leucine regulates translation initiation of protein synthesis in skeletal muscle after exercise. *J. Nutr.* **136**, 533S–537S (2006).
 33. Di Terlizzi, R. & Platt, S. The function, composition and analysis of cerebrospinal fluid in companion animals: part I - function and composition. *Vet. J.* **172**, 422–31 (2006).
 34. Johanson, C. E. *et al.* Multiplicity of cerebrospinal fluid functions: New challenges in health and disease. *Cerebrospinal Fluid Res.* **5**, 10 (2008).
 35. Xie, L. *et al.* Sleep drives metabolite clearance from the adult brain. *Science* **342**, 373–7 (2013).
 36. Vander Heide, R. S., Rim, D., Hohl, C. M. & Ganote, C. E. An in vitro model of myocardial ischemia utilizing isolated adult rat myocytes. *J. Mol. Cell. Cardiol.* **22**,

- 165–181 (1990).
37. Xin, M., Olson, E. N. & Bassel-duby, R. Mending broken hearts: cardiac development as a basis for adult heart regeneration and repair. *Nat. Rev. Mol. Cell Biol.* **14**, 529–541 (2013).
 38. Haubner, B. J. *et al.* Complete cardiac regeneration in a mouse model of myocardial infarction. *Aging (Albany NY)* **4**, 966–977 (2012).
 39. Schiaffino, S., Dyar, K. A., Ciciliot, S., Blaauw, B. & Sandri, M. Mechanisms regulating skeletal muscle growth and atrophy. *FEBS J.* **280**, 4294–4314 (2013).
 40. Tsuchihashi, T. *et al.* Hand2 function in second heart field progenitors is essential for cardiogenesis. *Dev. Biol.* **351**, 62–69 (2011).
 41. Liu, Y. *et al.* CHCHD2 inhibits apoptosis by interacting with Bcl-x L to regulate Bax activation. *Cell Death Differ.* 1–12 (2014). doi:10.1038/cdd.2014.194
 42. Aras, S. *et al.* Oxygen-dependent expression of cytochrome c oxidase subunit 4-2 gene expression is mediated by transcription factors RBPJ, CXXC5 and CHCHD2. *Nucleic Acids Res.* **41**, 2255–2266 (2013).
 43. Roselló-Lletí, E. *et al.* Cardiac protein changes in ischaemic and dilated cardiomyopathy: A proteomic study of human left ventricular tissue. *J. Cell. Mol. Med.* **16**, 2471–2486 (2012).
 44. Fu, Y. *et al.* Direct reprogramming of mouse fibroblasts into cardiomyocytes with chemical cocktails. *Cell Res.* **25**, 1013–24 (2015).
 45. Ieda, M. *et al.* Direct Reprogramming of Fibroblasts into Functional Cardiomyocytes by Defined Factors. *Cell* **306**, 1895 (2010).
 46. Thattaliyath, B. D., Livi, C. B., Steinhilber, M. E., Toney, G. M. & Firulli, A. B. HAND1 and HAND2 are expressed in the adult-rodent heart and are modulated during cardiac hypertrophy. *Biochem. Biophys. Res. Commun.* **297**, 870–875 (2002).
 47. Dirkx, E. *et al.* Nfat and miR-25 cooperate to reactivate the transcription factor Hand2 in heart failure. *Nat. Cell Biol.* **15**, 1282–93 (2013).
 48. Osterwalder, M. *et al.* HAND2 targets define a network of transcriptional regulators that compartmentalize the early limb bud mesenchyme. *Dev. Cell* **31**, 345–357 (2014).
 49. Zhu, L. *et al.* The mitochondrial protein CHCHD2 primes the differentiation potential of human induced pluripotent stem cells to neuroectodermal lineages. *J. Cell Biol.* **215**, 187–202 (2016).

Chapter 5

Autophagy and cancer metabolism

Content in the following chapter includes text modified from:

Autophagy and cancer metabolism by Juliet Goldsmith, Beth Levine and Jayanta Debnath, published in *Methods in Enzymology* in 2014 (PubMed PMID: 24862259).

Contributions: I was primarily responsible for writing the content in the first draft of this manuscript. Jay Debnath supervised this project and Beth Levine provided critical comments. We all edited and revised subsequent drafts.

Abstract

Cancer metabolism is dramatically altered in order to maintain survival and promote the expansion of tumor cells under stress. Autophagy is an intracellular recycling process that maintains basal levels of metabolites and biosynthetic intermediates under starvation or other forms of stress, thereby serving as an important mechanism for metabolic adaptation in cancer cells. Although it is widely acknowledged that autophagy sustains metabolism in tumor cells under duress, many questions remain with regard to the inter-relationships between autophagy and metabolism in cancer. Importantly, autophagy has often been described as a “double-edged sword” that can both impede or promote cancer initiation and progression. This review overviews these dual functions of autophagy in tumorigenesis, and details our current understanding of the coordinated regulation of autophagy and cancer cell metabolism in the control of tumor growth, progression, and therapeutic resistance.

Keywords

Autophagy; cancer metabolism; cancer therapy; glycolysis; glutaminolysis; hypoxia

1. Introduction

The ability of cells to adapt to stress requires diverse changes in cellular metabolism. One of the principal pathways contributing to this metabolic adaptive response is macroautophagy (commonly termed autophagy), a tightly regulated lysosomal digestion process. Because degradation through autophagy allows recycling of nutrients, autophagy serves as an important survival and fitness pathway induced by a wide array of stresses including nutrient deprivation, growth factor withdrawal, oxidative stress, infection, and hypoxia¹⁻⁴. In addition to its role in the stress-induced response, autophagy plays an essential homeostatic function by selectively removing damaged or non-functional proteins and organelles. These quality control functions have been demonstrated to be especially crucial in certain cell types: liver cells are reliant on autophagy for breakdown of stored metabolites, pancreatic β -cells utilize autophagy to manage high levels of ER stress, and post-mitotic neurons require autophagy to remove potentially damaging proteins that cannot be diluted by cell division⁵⁻⁹.

Given these key functions of autophagy in normal cells and tissues, it is not surprising that disruptions in autophagy have been implicated in numerous human diseases, including neurodegeneration, liver disease, inflammation, type 2 diabetes and cancer¹⁰⁻¹². While autophagy has been demonstrated to improve disease outcome in many cases by facilitating stress-induced metabolic adaptation or cellular homeostasis, the role of autophagy is more complex in cancer. Autophagy serves as an important tumor suppressor mechanism that impedes cancer initiation; at the same time, autophagy can promote the survival of tumor cells in response to diverse micro-

environmental and therapeutic stresses as well as support anabolic capacity in fast-replicating, metabolically-stressed tumor cells¹²⁻¹⁴. Despite this widely accepted notion that autophagy critically fuels metabolism in tumor cells under duress, many questions remain with regard to the inter-relationships between autophagy and metabolism in cancer. This review focuses on the coordinated regulation of autophagy and cancer cell metabolism, controlling tumor growth, progression, and resistance.

2. Autophagy and tumor suppression

Scientific evidence supports both tumor promoting and suppressive functions for autophagy and the exact role of autophagy during cancer progression depends on tumor type, context, and stage. Here, we discuss the genetic evidence supporting the role of autophagy-related proteins (ATGs) as tumor suppressors and review the potential mechanisms through which autophagy impairs tumor initiation and progression (Figure 1).

2.1. ATGs as tumor suppressors

Genetic evidence that autophagy can prevent tumor formation first emerged through studies of *beclin 1*¹⁵, which was found to be monoallelically deleted in 40-75% of cases of sporadic human breast, ovarian and prostate cancer. Furthermore, mice lacking a single copy of *beclin 1* developed spontaneous lymphoma, hepatocellular carcinoma, and lung adenocarcinomas^{16,17}. Notably, the second allele of *beclin 1* was not lost in these tumors, further corroborating that *beclin 1* functioned as a haploinsufficient tumor suppressor. In addition, multiple Beclin 1-interacting partners have been implicated as tumor suppressors. UV irradiation Resistance-Associated

Gene (UVRAG), a Beclin 1-interacting protein that positively regulates autophagy, is allelically deleted in human colon carcinoma^{18,19}. Moreover, frameshift mutations in the polyadenine tract of the UVRAG gene resulting in decreased autophagy are present in gastric carcinomas²⁰. Mice lacking SH3GLB1/Bif-1, which interacts with Beclin 1 via UVRAG, exhibit a significantly higher rate of spontaneous tumors²¹, and reduced SH3GLB1/Bif-1 expression, which correlates with decreased autophagy, is observed in gastric carcinoma²². Besides the well-characterized oncoprotein BCL-2 interaction with Beclin 1, two other oncoproteins have been more recently shown to interact with Beclin 1 leading to autophagy suppression and oncogenesis. AKT-mediated Beclin 1 serine phosphorylation enhances its interaction with vimentin and decreases autophagy. Depletion of vimentin or expression of a non-phosphorylatable Beclin 1 mutant in AKT-overexpressing cells increases autophagy and inhibits transformation, supporting the hypothesis that autophagy suppresses tumor initiation in AKT-driven tumors²³. EGFR-mediated Beclin 1 tyrosine phosphorylation suppresses the formation of the pro-autophagy Beclin 1/VPS34 complex, which may contribute to tumor progression and chemoresistance in human non-small cell lung cancer xenografts harboring oncogenic EGFR mutations²⁴.

In addition to Beclin 1 and its associated proteins, other ATGs have been implicated as suppressors of spontaneous tumorigenesis. Mice with systemic mosaic deletion of *Atg5* and liver-specific *Atg7*^{-/-} mice develop liver adenomas^{25,26}. *Atg4C* knockout mice exhibit increased susceptibility to fibrosarcomas in a chemical carcinogen model²⁷. Mice with hematopoietic stem cell deletion of *Atg7* develop an atypical myeloproliferation resembling human myelodysplastic syndrome and acute

myeloid leukemia²⁸. Frameshift mutations in *ATG2B*, *ATG5*, and *ATG9B* have been reported in gastric and colorectal carcinomas, further suggesting that components of the core autophagic machinery act as tumor suppressors in human cancers²⁹.

2.2. Autophagy-dependent degradation of p62/SQSTM1

The accumulation of p62/SQSTM1, an autophagy cargo receptor, promotes tumorigenesis: liver tumor size is reduced in *Atg7*^{-/-} mice by simultaneous *p62* deletion²⁶; *p62* gene targeting reduces anchorage-independent growth of human hepatocellular carcinoma cells²⁵; *p62*^{-/-} mice fail to develop RAS-induced lung carcinomas³⁰; and *p62* null cells have impaired RAS transformation³¹. In K-RAS-driven tumor cells, p62 activates Nrf2 and NF-κB, which stimulate pro-angiogenic and pro-inflammatory responses respectively, thereby contributing to aggressive tumor progression. Thus, increased autophagy enhances p62 degradation, leading to diminished angiogenic and inflammatory responses^{30,32,33}.

p62/SQSTM1 activation of the Nrf2 pathway in autophagy-deficient cells is especially important in tumor progression³⁴. Notably, the Nrf2 pathway, due to inactivating somatic mutations in the E3 ubiquitin ligase Keap1, has been implicated as a survival pathway in non-small cell lung carcinomas³⁵. The transcription factor Nrf2 (nuclear regulatory factor 2) regulates the expression of a wide range of genes that promote angiogenesis and facilitate cell survival. Keap1 ubiquitinates Nrf2 resulting in its degradation under normal conditions. Accumulated p62/SQSTM1 in autophagy-deficient cells directly binds to Keap1, disrupting Keap1-mediated degradation of Nrf2 and promoting aberrant Nrf2-mediated transcription³⁴. Thus, aberrant regulation of Nrf2 in autophagy-deficient cells may be an important pathway in tumor cell survival

(Figure 1A). Indeed, this pathway has been implicated in the spontaneous tumorigenesis of autophagy-defective liver cells^{25,26} and in the early growth acceleration of BRAF driven lung cancers lacking Atg7³⁶.

2.3. Autophagy prevents pro-tumor inflammation and facilitates senescence

Because autophagy promotes tumor cell adaptation and survival during hypoxic and metabolic stress, it may suppress tumor progression by inhibiting necrosis. In solid tumors, necrotic cell death causes macrophage infiltration and pro-inflammatory cytokine production, and chronic inflammation generally favors cancer growth and progression³⁷. Thus, by limiting necrosis, autophagy may actually suppress tumor growth by preventing leukocyte infiltration of the primary tumor site (Figure 1B). Indeed, this ability of autophagy to restrict necrosis prevented macrophage-associated tumor inflammation and inhibited primary tumor growth in apoptosis-resistant cells³⁸. Additionally, autophagy can facilitate the transition to senescence (Figure 1C), which also prevents immune activation due to necrosis, and can lead to elimination of premalignant cells by senescence-mediated surveillance³⁹⁻⁴¹. Autophagy allows the cancer cells to quietly survive, but helps to restrict proliferation by facilitating senescence, thereby overall suppressing tumor growth.

2.4. Autophagy clears dysfunctional mitochondria and regulates DNA damage

Autophagy is an important mechanism for the clearance of damaged mitochondria, a process termed mitophagy. Mitochondrial number may indirectly regulate tumor progression as mitochondria produce ROS, which can promote tumor progression via damage to proteins or DNA causing chromosomal instability⁴². In

response to ROS, mitophagy is upregulated to remove excess mitochondria and mitigate ROS production (Figure 1D). Increased ROS production from increased metabolic rate can damage mitochondria, which in turn can increase metabolic stress in the cell. Accordingly, in autophagy-defective cells, metabolic stress induces more DNA damage, increased genomic instability, and increased accumulation of damaged mitochondria than in wild type control cells.^{32,43} By clearing damaged mitochondria and controlling intracellular ROS levels, autophagy may exert a tumor suppressor function.

Additionally, in chapter 1 we identify protein translational control as another mechanism by which autophagy mitigates DNA damage. *Brca2* mRNA as well as some other cell cycle regulators are under translational control that is regulated by autophagy, so that in autophagy deficient cells there is a resulting decrease in BRCA2 levels, an increase in DNA damage and longer time spent in mitosis leading to slower cell cycling.

3. Tumor promoting functions of autophagy

Although reduced autophagy can promote tumor development, autophagy provides cancer cells with certain selective advantages to cope with stress and promote metabolic adaptation. Hence, a basal level of autophagy appears to be necessary for the optimal survival and fitness of cancer cells. The following section provides an overview of several potential mechanisms by which autophagy may promote tumor progression (Figure 2).

3.1. Autophagy and metabolic adaptation in cancer

Autophagy and oxidative mitochondrial metabolism:

Strong oncogenic insults like RAS activation lead to increased autophagy. In pancreatic ductal adenocarcinoma (PDAC), where activating K-RAS mutations are present in greater than 90% of tumors, elevated autophagy is found in both primary PDAC tumors and cell lines. Genetic inhibition of autophagy in PDAC cells potently suppresses proliferation *in vitro* and elicits robust tumor regression and prolonged survival in pancreatic cancer xenografts and genetic mouse models⁴⁴. Because RAS activation is marked by profound metabolic alterations that promote energy production and support the biosynthesis of macromolecules needed for rapid proliferation, it has been hypothesized that autophagy maintains key metabolic pathways in RAS-transformed cells. In support, the loss of autophagy during RAS transformation is associated with reduced mitochondrial oxygen consumption and decreased levels of tricarboxylic acid (TCA) cycle intermediates^{31,44}. This requirement for autophagy to maintain oxidative mitochondrial metabolism of RAS-transformed cells indicates that the pro-tumor effects of autophagy are not limited to survival functions in response to external stresses. Rather, autophagy contributes to the metabolic fitness of the entire tumor population. Remarkably, this requirement for autophagy may be oncogene dependent, as autophagy has been demonstrated to restrict, rather than promote, proliferation driven by oncogenic PI3K in a three-dimensional mammary culture model⁴⁵. As RAS is one of the few oncogenes that stimulates – rather than suppresses – autophagy, it will be interesting to determine whether this requirement for autophagy is conserved in other oncogenic contexts.

Glucose metabolism:

Many tumors preferentially use aerobic glycolysis, which allows for the accumulation of metabolic intermediates required for anabolism⁴⁶. CMA and selective macroautophagy both play important roles in regulating the shift to aerobic glycolysis in cancer cells. CMA is upregulated in diverse tumor types, is necessary for tumor growth and metastasis in lung cancer cells, and inhibition of CMA decreases the rate of glycolysis characteristic of tumor growth⁴⁷. More specifically, CMA controls levels of the metabolic enzyme PKM2 (Figure 2A), which is often upregulated in many tumor types and particularly glioblastoma. The PKM2 isoform of pyruvate kinase is slower at metabolically converting phosphoenolpyruvate to pyruvate than the M1 isoform; this causes glycolytic intermediates to accumulate, and drives tumor cell proliferation and growth by promoting key biosynthetic side reactions in the glycolytic pathway. CMA can selectively degrade PKM2, thereby regulating levels of the metabolic intermediates, glucose-6-phosphate and fructose-1,6-bisphosphate, as well as levels of ATP⁴⁸. Recently, PKM2-specific deletion was shown to have increased mammary tumor formation driven by *Brca-1* deletion⁴⁹, consistent with the notion that cancer cells prefer low pyruvate kinase activity. Therefore, the degradation of PKM2 by CMA may promote tumor progression.

The number of mitochondria present also regulates the shift to anaerobic metabolism. BRAF driven melanoma cells decrease the rate of mitochondrial biogenesis in order to shift from oxidative phosphorylation to glycolysis⁵⁰⁻⁵². If mitophagy is aberrantly activated, decreased numbers of mitochondria shift the cells to glycolysis in a similar mechanism to BRAF regulation of mitochondrial biogenesis

(Figure 2B). RCAN1-1L, whose expression is increased in response to oxidative stress, can open the MPT pore and decrease ATP levels. This inhibits MTOR signalling via AMPK, resulting in increased mitophagy and a shift to glycolysis⁵³. In addition to shifting the metabolic pathways to preferentially use glucose, autophagy also facilitates glucose uptake (Figure 2A) and glycolytic flux in RAS transformed cells, which is required for adhesion independent proliferation^{54,55}.

Amino acids:

In addition to glucose, amino acids are necessary for cancer cell growth. Amino acids feed into cataplerotic pathways and can be used to maintain biosynthetic capacity in rapidly dividing cancer cells. In yeast, autophagic breakdown of proteins during starvation generates cytosolic amino acid pools crucial for survival⁵⁶. It had been thought that autophagy would support the maintenance of all amino acids. However, as discussed in chapter 1, we have found that in mammalian cells, loss of autophagy has little impact on the majority of amino acids in fed and starved conditions – the only three responsive amino acids being glutamine, glutamate and glycine. Yet these specific defects in amino acid levels in autophagy deficient cells may be particularly important in the context of cancer. Glutamine, the most abundant amino acid in mammalian cells, is important in cancer progression as a metabolic intermediate^{57,58}. As glycolytic rates increase, tumor cells rely increasingly on glutamine to replenish the TCA cycle and maintain ATP production⁵⁹. In pancreatic cancer, glutamine feeds into glutaminolysis, utilizing steps in the TCA cycle to generate NADPH, maintain the cellular redox state and provide metabolites for anaplerosis⁶⁰. In an independent, previously published

study, loss of autophagy in wild type MEFs was also found to decrease the levels of intracellular glutamine and also mimic the metabolic changes associated with glutamine depletion; indicating that autophagy normally helps to maintain intracellular stores of glutamine. However, in the same study, glutamine deprivation did not increase levels of autophagy, and the *Atg5* mRNA level decreased⁶¹. Therefore, how autophagy may increase specific amino acids during deprivation remains to be defined.

Lipids:

Lipid metabolism is altered in cancer – tumor cells reactivate *de novo* lipid synthesis, ATP-citrate lyase is required for transformation *in vitro*, cholesterol synthesis in prostate cancer is increased, and fatty acid oxidation is an important source of energy for prostate cancer cells⁶². Autophagy in the specific form of lipophagy is important for the degradation of lipid droplets in adipose tissue⁶³, and autophagy regulates lipid metabolism in hepatocytes as triglyceride hydrolysis is impaired in *Atg5*^{-/-} cells⁶⁴. Whether these processes affect tumor lipid metabolism requires further study.

Additionally, autophagy impacts lipid metabolism by altering mitochondrial number. *Atg7* deleted, p53 mutant cells in a KRAS-driven NSCLC model have intracellular lipid accumulation because of increased dysfunctional mitochondria that compromises fatty acid oxidation, suggesting that autophagy is crucial to maintain lipid metabolism in KRAS and p53 mutant cells. This prevents the efficient growth of tumor cells and turns them into lipid cysts instead of tumors⁶⁵.

3.2. Autophagy promotes cell survival under metabolic stress

As discussed above, autophagy is strongly activated under periods of oxidative and metabolic stress, and depending on the extent and severity of stress, autophagy serves to prolong cell survival in the primary tumor, and possibly also during tumor dissemination and metastasis (Figure 2C). In melanoma cells driven by oncogenic Ras or MEK, the removal of leucine does not induce autophagy to the same extent as non-transformed, immortalized melanocytes. The aberrant activation of mTOR via Ras prevents autophagy induction and the cells are sensitized to apoptosis, presumably because translation continues although the lost leucine is not recycled intracellularly⁶⁶. Following growth factor withdrawal, autophagy is essential for maintaining cell survival in apoptosis-deficient hematopoietic cells, and can sustain viability for several weeks. IL3-deprived cells become less glycolytic and use autophagy as a catabolic process to maintain mitochondrial respiration and levels of ATP¹. Increased autophagy regulated by the PI3K/AKT/MTOR pathway prolongs cancer cell survival under acidic environment stress produced by glycolysis⁶⁷. Autophagy also prevents ER-stress-induced cell death during protein over-production (for example, induced by oncogenes such as Myc) by clearing excess and misfolded proteins⁶⁸. Indeed, Myc-driven tumors have increased cell growth, ER stress, and metabolic rate, and autophagy inhibition enhances therapy-induced apoptosis in a Myc-driven model of lymphoma⁶⁹⁻⁷¹.

3.3. Autophagy in the tumor stroma

Autophagy prolongs tumor cell survival under stressful conditions. It should be noted that the acidic, hypoxic, or nutrient-starved environment also induces autophagy

in the surrounding stromal cells, which promotes tumor growth (Figure 2D). Serum-deprived mesenchymal stem cells induce autophagy and support MCF7 growth in xenograft models by secreting growth factors and anti-apoptotic factors ⁷². While autophagy-induced senescence in cancer cells limits growth, autophagy-induced senescence in the tumor stroma may promote cancer by enhancing the SASP phenotype and promoting secretion of growth factors and cytokines that enhance tumor progression ^{73–76}.

In addition to modulating secretion in senescent fibroblasts, autophagy in cancer-associated fibroblasts (CAFs) may directly fuel cancer cell metabolism. Autophagic senescent CAFs release metabolites such as glutamine, ketone bodies, and glycolytic intermediates which may promote tumor growth and metastasis. These studies raise the possibility that autophagy in the tumor stroma is important for the continued growth of the tumor ^{77–79}.

3.4. Autophagy inhibition in cancer therapy

The increased dependence of tumors on altered metabolism is an attractive therapeutic target. In addition to targeting metabolic enzymes, targeting autophagy may provide a similar benefit. However, such an approach is complicated by the multifaceted role of autophagy in tumor formation and progression ⁸⁰. Increased autophagy has been observed in tumor cells following numerous anti-cancer treatments and is proposed to represent a common adaptive stress response that enables tumor cells to survive these therapeutic insults (Figure 2C). This has motivated significant interest in

combining autophagy inhibition with other agents to synergistically eliminate cancer cells. Readers are referred to several reviews for additional information ^{81–83}.

Notably, certain targeted therapies that enhance autophagy *in vitro* may benefit from combined autophagy inhibition. Autophagy is upregulated in response to erlotinib in NSCLC cell lines and combined treatment with chloroquine, an anti-malarial that inhibits autophagy, enhances erlotinib sensitivity ⁸⁴. Similarly, gastrointestinal stromal tumors exhibit enhanced autophagy in response to imatinib, which lessens the therapeutic benefit. Combined inhibition of autophagy with imatinib treatment increased the number of cells undergoing apoptosis, both *in vitro* and *in vivo*, and reduced the outgrowth of resistant cells ⁸⁵. Moreover, upon treatment with the VEGF-neutralizing antibody bevacizumab, increased autophagy due to hypoxia promotes tumor cell survival and resistance to this anti-angiogenic therapy ⁸⁶. In contrast, inhibition of erlotinib-induced autophagy in human NSCLC xenografts *in vivo* by inducible expression of a Beclin 1 tyrosine phosphomimetic mutant resulted in partial chemoresistance ²⁴, suggesting that the effects of autophagy inhibition may vary depending upon the autophagy step targeted, *in vitro* versus *in vivo* studies, or due to other differences in tumor type or experimental systems.

In the above examples, autophagy is targeted due to its induction in response to therapy, but autophagy inhibition can also synergize with therapies that do not normally promote autophagic flux. For example, combining autophagy inhibition with immunotherapy could increase efficacy. Hypoxia-induced autophagy prevents lung cancer cells from cytolytic T-cell mediated cell death, but inhibition of autophagy combined with immunotherapy may provide a powerful and tumor-specific therapy ⁸⁷.

Another synergistic approach involves targeting the proteasome pathway and autophagy in tumor cells that are prone to ER stress. Autophagy inhibitors in combination with proteasome inhibitors increase suppression of proliferation and induce apoptosis in hepatocellular carcinoma⁸⁸. Additional studies in multiple myeloma cells also show the same increased sensitivity to combination proteasome inhibitors and autophagy inhibitors *in vitro*⁸⁹.

Importantly, one should recognize that many studies of autophagy inhibition as anticancer therapy have employed the lysosomal inhibitor HCQ. Hence, an important caveat for these experiments is that the cytotoxic effects of HCQ and similar agents are likely to involve processes other than autophagy. To date, the precise contributions of autophagy inhibition toward the efficacy of these anti-malarials remain uncertain. Moreover, compensatory pathways, such as CMA, may influence the efficacy of autophagy inhibition as a therapeutic approach. For example, autophagy inhibition in combination with the HDACi vorinostat in a sensitive T-cell lymphoma cell line results in decreased cell death, but the resulting vorinostat-resistant subclones become partially resensitized by inhibition of CMA⁹⁰.

While it remains controversial whether autophagy can mediate cell death, several studies demonstrate that genetic knockdown of autophagy blocks tumor cell death induced by oncogenic RAS⁹¹ or by various chemotherapeutic agents^{92,93}. Furthermore, acute inhibition of autophagy can limit chemotherapy responses *in vivo* by preventing autophagy-dependent anticancer immune responses⁹⁴. Thus, additional studies are needed to further clarify the contexts in which autophagy inhibition will be beneficial in

the treatment of cancer, but as these studies have shown, autophagy inhibition as a clinical therapy will not be straightforward.

Conclusion

Autophagy and metabolism in cancer cells are inexorably linked. The cross-regulation of these processes acts to buffer cancer cells from the environmental and internal stresses caused by excessive proliferation. As more targeted therapies are being designed and tested, unintended consequences on autophagy, both positive and negative, must be considered in order to predict and combat side effects and resistance mechanisms. Therefore, further understanding of how autophagy contributes to cancer cell metabolism will provide insight into how to better treat cancers.

Figure 1

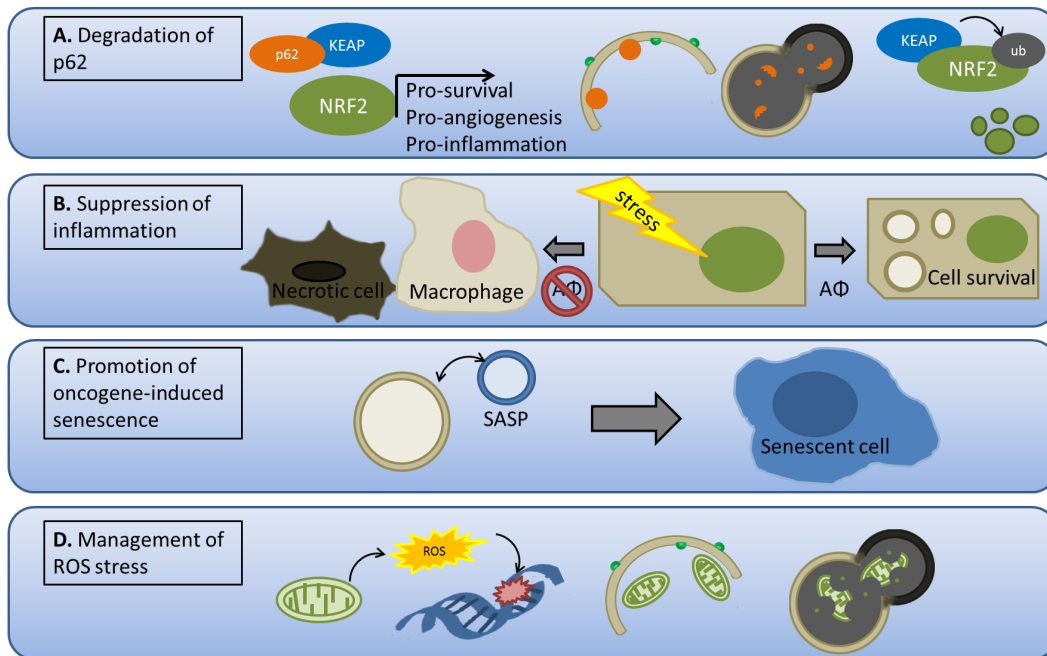


Figure 1: Tumor suppressive roles for autophagy in cancer

(A) Autophagy prevents p62/NRF2 pathway pro-survival, pro-angiogenic and pro-inflammatory signalling. During hypoxia, p62 binds to and sequesters KEAP, thereby preventing ubiquitination of NRF2. NRF2 can then promote transcription of pro-survival, pro-angiogenic and pro-inflammatory genes that enhance tumor growth. When autophagy is active, p62 is degraded by sequestration within the autophagolysosome, thereby allowing ubiquitination and degradation of NRF2. **(B)** Autophagy prevents necrosis and inflammation by promoting survival in stressed cells. Tumor cells with decreased autophagy (AΦ) are more prone to necrosis following stress, which recruits macrophages, promotes inflammation, and fuels tumor growth. **(C)** Autophagy promotes oncogene-induced senescence by enhancing the senescence-associated secretory phenotype (SASP). **(D)** Autophagy suppresses reactive oxygen species (ROS) accumulation and genomic damage, which helps prevent genomic instability – an important driver of tumorigenesis. Mitochondria produce ROS under normal metabolic conditions, and may increase the production of ROS when damaged. Mitophagy is upregulated in response to ROS, and clears excess and damaged mitochondria, which then mitigates ROS production.

Figure 2

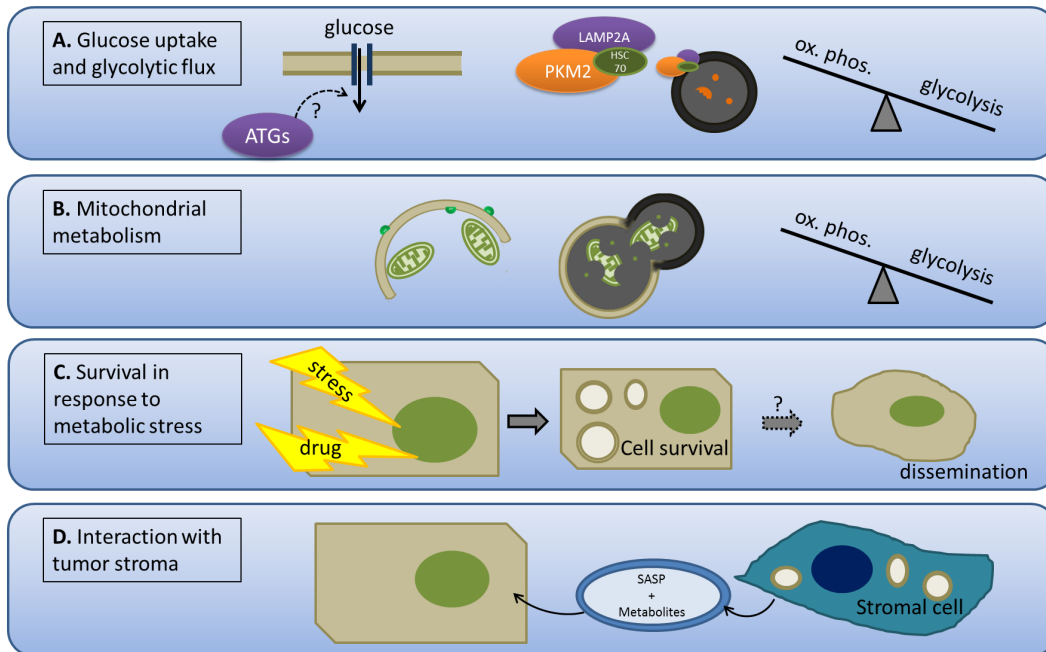


Figure 2: Tumor-promoting roles for autophagy in cancer

(A) Autophagy promotes glucose uptake and glycolytic flux. Autophagy has been shown to promote glucose uptake in cancer cells, although the mechanism remains to be elucidated. Additionally, increased chaperone-mediated autophagy (CMA) promotes degradation of PKM2, a rate limiting glycolytic enzyme. Thus CMA can control the rate of flux through glycolysis, and whether glycolytic intermediates are used for energy production or anaplerosis. **(B)** Autophagy selectively degrades mitochondria, and therefore the machinery necessary for fatty acid oxidation and oxidative phosphorylation. This enhances the shift to glycolysis, which is characteristic of cancer cells. **(C)** Autophagy promotes survival in response to metabolic stress such as growth factor deprivation, acidic environment and ER stress by recycling cytoplasmic material in order to maintain the basal energy state and clear damaged, misfolded proteins. This process may also be important for survival during tumor dissemination and metastasis. **(D)** Autophagy in stromal cells induced by the hypoxic and acidic tumor microenvironment promotes secretion of metabolites and growth signals via senescence-associated secretion phenotype (SASP) that enhances tumor cell growth.

References

1. Lum, J. J. *et al.* Growth factor regulation of autophagy and cell survival in the absence of apoptosis. *Cell* **120**, 237–48 (2005).
2. Avivar-Valderas, A. *et al.* PERK integrates autophagy and oxidative stress responses to promote survival during extracellular matrix detachment. *Mol. Cell. Biol.* **31**, 3616–29 (2011).
3. Boya, P., Reggiori, F. & Codogno, P. Emerging regulation and functions of autophagy. *Nat. Cell Biol.* **15**, 713–20 (2013).
4. Yin, L. I., Kharbanda, S. & Kufe, D. MUC1 oncoprotein promotes autophagy in a survival response to glucose deprivation. *Int. J. Oncol.* 1691–1699 (2009). doi:10.3892/ijo
5. Komatsu, M. *et al.* Impairment of starvation-induced and constitutive autophagy in Atg7-deficient mice. *J. Cell Biol.* **169**, 425–34 (2005).
6. Wu, J. J. *et al.* Mitochondrial dysfunction and oxidative stress mediate the physiological impairment induced by the disruption of autophagy. *Aging (Albany, NY)*. **1**, 425–37 (2009).
7. Jung, H. S. *et al.* Loss of autophagy diminishes pancreatic beta cell mass and function with resultant hyperglycemia. *Cell Metab.* **8**, 318–24 (2008).
8. Hara, T. *et al.* Suppression of basal autophagy in neural cells causes neurodegenerative disease in mice. *Nature* **441**, 885–9 (2006).
9. Komatsu, M. *et al.* Loss of autophagy in the central nervous system causes neurodegeneration in mice. *Nature* **441**, 880–4 (2006).
10. Debnath, J. The multifaceted roles of autophagy in tumors-implications for breast cancer. *J. Mammary Gland Biol. Neoplasia* **16**, 173–87 (2011).
11. Murrow, L. & Debnath, J. Autophagy as a stress-response and quality-control mechanism: implications for cell injury and human disease. *Annu. Rev. Pathol.* **8**, 105–37 (2013).
12. Levine, B. & Kroemer, G. Autophagy in the pathogenesis of disease. *Cell* **132**, 27–42 (2008).
13. Rabinowitz, J. D. & White, E. Autophagy and metabolism. *Science (80-.)*. **330**, 1344–8 (2010).
14. Kimmelman, A. C. The dynamic nature of autophagy in cancer. *Genes Dev.* **25**, 1999–2010 (2011).
15. Liang, X. H. *et al.* Induction of autophagy and inhibition of tumorigenesis by beclin 1. *Nature* **402**, 672–6 (1999).
16. Qu, X. *et al.* Promotion of tumorigenesis by heterozygous disruption of the beclin 1 autophagy gene. *J. Clin. Invest.* **112**, 1809–1820 (2003).
17. Yue, Z., Jin, S., Yang, C., Levine, A. J. & Heintz, N. Beclin 1, an autophagy gene essential for early embryonic development, is a haploinsufficient tumor suppressor. *Proc. Natl. Acad. Sci. U. S. A.* **100**, 15077–82 (2003).
18. Liang, C. *et al.* Autophagic and tumour suppressor activity of a novel Beclin1-binding protein UVRAG. *Nat. Cell Biol.* **8**, 688–99 (2006).
19. Liang, C., Feng, P., Ku, B. & Oh, B. UVRAG: a new player in autophagy and tumor cell growth. *Autophagy* **3**, 69–71 (2007).
20. Kim, M. S. *et al.* Frameshift mutation of UVRAG, an autophagy-related gene, in

- gastric carcinomas with microsatellite instability. *Hum. Pathol.* **39**, 1059–63 (2008).
21. Takahashi, Y. *et al.* Bif-1 interacts with Beclin 1 through UVRAG and regulates autophagy and tumorigenesis. *Nat. Cell Biol.* **9**, 1142–51 (2007).
 22. Lee, J. W. *et al.* Decreased expression of tumour suppressor Bax-interacting factor-1 (Bif-1), a Bax activator, in gastric carcinomas. *Pathology* **38**, 312–5 (2006).
 23. Wang, R. C. *et al.* Akt-mediated regulation of autophagy and tumorigenesis through Beclin 1 phosphorylation. *Science (80-.)*. **338**, 956–9 (2012).
 24. Wei, Y. *et al.* EGFR-Mediated Beclin 1 Phosphorylation in Autophagy Suppression , Tumor Progression , and Tumor Chemoresistance. *Cell* **154**, 1–16 (2013).
 25. Inami, Y. *et al.* Persistent activation of Nrf2 through p62 in hepatocellular carcinoma cells. *J. Cell Biol.* **193**, 275–84 (2011).
 26. Takamura, A. *et al.* Autophagy-deficient mice develop multiple liver tumors. *Genes Dev.* **25**, 795–800 (2011).
 27. Mariño, G. *et al.* Tissue-specific autophagy alterations and increased tumorigenesis in mice deficient in Atg4C/autophagin-3. *J. Biol. Chem.* **282**, 18573–83 (2007).
 28. Mortensen, M. *et al.* The autophagy protein Atg7 is essential for hematopoietic stem cell maintenance. *J. Exp. Med.* **208**, 455–67 (2011).
 29. Kang, M. R. *et al.* Frameshift mutations of autophagy-related genes ATG2B , ATG5 , ATG9B and ATG12 in gastric and colorectal cancers with microsatellite instability. *J. Pathol.* **217**, 702–706 (2009).
 30. Duran, A. *et al.* The signaling adaptor p62 is an important NF-kappaB mediator in tumorigenesis. *Cancer Cell* **13**, 343–54 (2008).
 31. Guo, J. Y. *et al.* Activated Ras requires autophagy to maintain oxidative metabolism and tumorigenesis. *Genes Dev.* **25**, 460–70 (2011).
 32. Mathew, R. *et al.* Autophagy suppresses tumorigenesis through elimination of p62. *Cell* **137**, 1062–75 (2009).
 33. Kim, T.-H. *et al.* NRF2 blockade suppresses colon tumor angiogenesis by inhibiting hypoxia-induced activation of HIF-1 α . *Cancer Res.* **71**, 2260–75 (2011).
 34. Komatsu, M. *et al.* The selective autophagy substrate p62 activates the stress responsive transcription factor Nrf2 through inactivation of Keap1. *Nat. Cell Biol.* **12**, 213–23 (2010).
 35. Singh, A. *et al.* Dysfunctional KEAP1-NRF2 interaction in non-small-cell lung cancer. *PLoS Med.* **3**, e420 (2006).
 36. Strohecker, A. M. *et al.* Autophagy Sustains Mitochondrial Glutamine Metabolism and Growth of BRAFV600E-Driven Lung Tumors. *Cancer Discov.* (2013). doi:10.1158/2159-8290.CD-13-0397
 37. DeNardo, D. G., Johansson, M. & Coussens, L. M. Immune cells as mediators of solid tumor metastasis. *Cancer Metastasis Rev* **27**, 11–18 (2008).
 38. Degenhardt, K. *et al.* Autophagy promotes tumor cell survival and restricts necrosis, inflammation, and tumorigenesis. *Cancer Cell* **10**, 51–64 (2006).
 39. Narita, M. *et al.* Spatial coupling of mTOR and autophagy augments secretory phenotypes. *Science (80-.)*. **332**, 966–70 (2011).

40. Young, A. R. J. *et al.* Autophagy mediates the mitotic senescence transition. *Genes Dev.* **23**, 798–803 (2009).
41. Kang, T.-W. *et al.* Senescence surveillance of pre-malignant hepatocytes limits liver cancer development. *Nature* **479**, 547–51 (2011).
42. Ishikawa, K. *et al.* ROS-generating mitochondrial DNA mutations can regulate tumor cell metastasis. *Science (80-.)*. **320**, 661–4 (2008).
43. Belaid, A. *et al.* Autophagy plays a critical role in the degradation of active RHOA, the control of cell cytokinesis and genomic stability. *Cancer Res.* **73**, 4311–4322 (2013).
44. Yang, S. *et al.* Pancreatic cancers require autophagy for tumor growth. *Genes Dev.* **25**, 717–729 (2011).
45. Chen, N., Eritja, N., Lock, R. & Debnath, J. Autophagy restricts proliferation driven by oncogenic phosphatidylinositol 3-kinase in three-dimensional culture. *Oncogene* **32**, 2543–54 (2013).
46. Hsu, P. P. & Sabatini, D. M. Cancer cell metabolism: Warburg and beyond. *Cell* **134**, 703–7 (2008).
47. Kon, M. *et al.* Chaperone-mediated autophagy is required for tumor growth. *Sci. Transl. Med.* **3**, 109ra117 (2011).
48. Lv, L. *et al.* Acetylation targets the M2 isoform of pyruvate kinase for degradation through chaperone-mediated autophagy and promotes tumor growth. *Mol. Cell* **42**, 719–30 (2011).
49. Israelsen, W. J. *et al.* PKM2 Isoform-Specific Deletion Reveals a Differential Requirement for Pyruvate Kinase in Tumor Cells. *Cell* **155**, 397–409 (2013).
50. Vazquez, F. *et al.* PGC1 α expression defines a subset of human melanoma tumors with increased mitochondrial capacity and resistance to oxidative stress. *Cancer Cell* **23**, 287–301 (2013).
51. Ho, J. *et al.* Importance of glycolysis and oxidative phosphorylation in advanced melanoma. *Mol. Cancer* **11**, 76 (2012).
52. Haq, R. *et al.* Oncogenic BRAF regulates oxidative metabolism via PGC1 α and MITF. *Cancer Cell* **23**, 302–15 (2013).
53. Ermak, G. *et al.* Chronic expression of RCAN1-1L protein induces mitochondrial autophagy and metabolic shift from oxidative phosphorylation to glycolysis in neuronal cells. *J. Biol. Chem.* **287**, 14088–98 (2012).
54. Lock, R. *et al.* Autophagy facilitates glycolysis during Ras-mediated oncogenic transformation. *Mol. Biol. Cell* **22**, 165–78 (2011).
55. Lock, R. & Debnath, J. Ras, autophagy and glycolysis. *Cell Cycle* **10**, 1516–1517 (2011).
56. Onodera, J. & Ohsumi, Y. Autophagy is required for maintenance of amino acid levels and protein synthesis under nitrogen starvation. *J. Biol. Chem.* **280**, 31582–6 (2005).
57. DeBerardinis, R. J., Lum, J. J., Hatzivassiliou, G. & Thompson, C. B. The biology of cancer: metabolic reprogramming fuels cell growth and proliferation. *Cell Metab.* **7**, 11–20 (2008).
58. Gaglio, D. *et al.* Oncogenic K-Ras decouples glucose and glutamine metabolism to support cancer cell growth. *Mol. Syst. Biol.* **7**, 523 (2011).
59. Burgess, D. J. Metabolism: Glutamine connections. *Nat. Rev. Cancer* **13**, 293

- (2013).
60. Son, J. *et al.* Glutamine supports pancreatic cancer growth through a KRAS-regulated metabolic pathway. *Nature* **496**, 101–5 (2013).
 61. Lin, T. *et al.* Resetting glutamine-dependent metabolism and oxygen consumption Autophagy. *Autophagy* **8**, 1477–1493 (2012).
 62. Santos, C. R. & Schulze, A. Lipid metabolism in cancer. *FEBS J.* **279**, 2610–23 (2012).
 63. Singh, R. & Cuervo, A. M. Lipophagy: connecting autophagy and lipid metabolism. *Int. J. Cell Biol.* **2012**, 282041 (2012).
 64. Singh, R. *et al.* Autophagy regulates lipid metabolism. *Nature* **458**, 1131–5 (2009).
 65. Guo, J. Y. *et al.* Autophagy suppresses progression of K-ras-induced lung tumors to oncocytomas and maintains lipid homeostasis. *Genes Dev.* **27**, 1447–61 (2013).
 66. Sheen, J.-H., Zoncu, R., Kim, D. & Sabatini, D. M. Defective regulation of autophagy upon leucine deprivation reveals a targetable liability of human melanoma cells in vitro and in vivo. *Cancer Cell* **19**, 613–28 (2011).
 67. Wojtkowiak, J. W. *et al.* Chronic autophagy is a cellular adaptation to tumor acidic pH microenvironments. *Cancer Res.* **72**, 3938–47 (2012).
 68. Tomohiro, Y. & Klionsky, D. J. Endoplasmic reticulum stress: a new pathway to induce autophagy. *Autophagy* **3**, 160–162 (2007).
 69. Miller, D. M., Thomas, S. D., Islam, A., Muench, D. & Sedoris, K. c-Myc and cancer metabolism. *Clin. cancer Res.* **18**, 5546–53 (2012).
 70. Dang, C. V. c-Myc Target Genes Involved in Cell Growth , Apoptosis, and Metabolism. *Mol. Cell. Biol.* **19**, 1–11 (1999).
 71. Amaravadi, R., Yu, D. & Lum, J. Autophagy inhibition enhances therapy-induced apoptosis in a Myc-induced model of lymphoma. *J. Clin. Invest.* **117**, 326–336 (2007).
 72. Sanchez, C. G. *et al.* Activation of autophagy in mesenchymal stem cells provides tumor stromal support. *Carcinogenesis* **32**, 964–72 (2011).
 73. Capparelli, C. *et al.* CDK inhibitors (p16/p19/p21) induce senescence and autophagy in cancer-associated fibroblasts, “fueling” tumor growth via paracrine interactions, without an increase in neo-angiogenesis. *Cell Cycle* **11**, 3599–3610 (2012).
 74. Capparelli, C. *et al.* Autophagy and senescence in cancer-associated fibroblasts metabolically supports tumor growth and metastasis via glycolysis and ketone production. *Cell Cycle* **11**, 2285–2302 (2012).
 75. Capparelli, C. *et al.* CTGF drives autophagy, glycolysis and senescence in cancer-associated fibroblasts via HIF1 activation, metabolically promoting tumor growth. *Cell Cycle* **11**, 2272–2284 (2012).
 76. Maes, H., Rubio, N., Garg, A. D. & Agostinis, P. Autophagy: shaping the tumor microenvironment and therapeutic response. *Trends Mol. Med.* 1–19 (2013). doi:10.1016/j.molmed.2013.04.005
 77. Martinez-Outschoorn, U. E. *et al.* Autophagy in cancer associated fibroblasts promotes tumor cell survival: Role of hypoxia, HIF1 induction and NFκB activation in the tumor stromal microenvironment. *Cell Cycle* **9**, 3515–3533 (2010).
 78. Ko, Y.-H. *et al.* Glutamine fuels a vicious cycle of autophagy in the tumor stroma

- and oxidative mitochondrial metabolism in epithelial cancer cells. *Cancer Biol. Ther.* **12**, 1085–1097 (2011).
79. Salem, A. F. *et al.* Two-compartment tumor metabolism: Autophagy in the tumor microenvironment and oxidative mitochondrial metabolism (OXPHOS) in cancer cells. *Cell Cycle* **11**, 2545–2556 (2012).
 80. Cheong, H., Lu, C., Lindsten, T. & Thompson, C. B. Therapeutic targets in cancer cell metabolism and autophagy. *Nat. Biotechnol.* **30**, 671–8 (2012).
 81. Amaravadi, R. K. *et al.* Principles and current strategies for targeting autophagy for cancer treatment. *Clin. Cancer Res.* **17**, 654–666 (2011).
 82. Eisenberg-Lerner, A. & Kimchi, A. The paradox of autophagy and its implication in cancer etiology and therapy. *Apoptosis* **14**, 376–91 (2009).
 83. Høyer-hansen, M. & Jäättelä, M. Autophagy: an emerging target for cancer therapy. *Autophagy* **4**, 574–580 (2008).
 84. Li, Y.-Y., Lam, S.-K., Mak, J. C.-W., Zheng, C.-Y. & Ho, J. C.-M. Erlotinib-induced autophagy in epidermal growth factor receptor mutated non-small cell lung cancer. *Lung cancer* 1–8 (2013). doi:10.1016/j.lungcan.2013.05.012
 85. Gupta, A. *et al.* Autophagy inhibition and antimalarials promote cell death in gastrointestinal stromal tumor (GIST). *Proc. Natl. Acad. Sci. U. S. A.* **107**, 14333–8 (2010).
 86. Hu, Y.-L. *et al.* Hypoxia-induced autophagy promotes tumor cell survival and adaptation to antiangiogenic treatment in glioblastoma. *Cancer Res.* **72**, 1773–83 (2012).
 87. Noman, M. Z. *et al.* Blocking hypoxia-induced autophagy in tumors restores cytotoxic T-cell activity and promotes regression. *Cancer Res.* **71**, 5976–86 (2011).
 88. Hui, B. *et al.* Proteasome inhibitor interacts synergistically with autophagy inhibitor to suppress proliferation and induce apoptosis in hepatocellular carcinoma. *Cancer* **118**, 5560–71 (2012).
 89. Kawaguchi, T. *et al.* Combined treatment with bortezomib plus bafilomycin A1 enhances the cytotoxic effect and induces endoplasmic reticulum stress in U266 myeloma cells: crosstalk among proteasome, autophagy-lysosome and ER stress. *Int. J. Oncol.* **38**, 643–54 (2011).
 90. Dupéré-Richer, D. *et al.* Vorinostat-induced autophagy switches from a death-promoting to a cytoprotective signal to drive acquired resistance. *Cell Death Dis.* **4**, e486 (2013).
 91. Elgendy, M., Sheridan, C., Brumatti, G. & Martin, S. J. Oncogenic Ras-induced expression of Noxa and Beclin-1 promotes autophagic cell death and limits clonogenic survival. *Mol. Cell* **42**, 23–35 (2011).
 92. Janku, F., McConkey, D., Hong, D. & Kurzrock, R. Autophagy as a target for anticancer therapy. *Nat Rev Clin Oncol.* **8**, 528–39 (2011).
 93. Notte, A., Leclere, L. & Michiels, C. Autophagy as a mediator of chemotherapy-induced cell death in cancer. *Biochem. Pharmacol.* **82**, 427–34 (2011).
 94. Michaud, M. *et al.* Autophagy-dependent anticancer immune responses induced by chemotherapeutic agents in mice. *Science (80-.).* **334**, 1573–1577 (2011).

Chapter 6

Concluding remarks

Overall, the theme that has linked my thesis research has been investigating various metabolic stresses on protein translation, and that these stresses have not regulated translation as we expected them to. I have found novel mechanisms of regulation of protein translation by autophagy and by acute starvation.

The first subtle metabolic perturbation that I introduced was inhibiting autophagy. We found surprisingly that autophagy inhibition did not globally impact translation, as we would have expected from a large metabolic perturbation. In fact, genetically inhibiting autophagy had minimal impacts on the amino acid levels in the cells, excepting glutamine. And yet, we found that autophagy plays a role in regulating the translation of specific groups of mRNAs, particularly mRNAs involved in regulating the cell cycle and DNA damage repair. I focused mainly on validating the autophagy-enhanced translational control of BRCA2, which is detailed in Chapter 2. We provide evidence that autophagy regulates the levels of RNA binding proteins, including MSI1 and eIF4A1, in the cell, which promotes the translation of certain mRNAs. Additionally, we show evidence that accumulation of p62 in autophagy deficient cells leads to the sequestration of eIF4A1, which prevents its interaction at the m⁷-GTP cap. However, neither of these mechanisms alone seem to be sufficient to rescue *Brca2* translation in autophagy deficient cells, and therefore a combination of factors or other proteins we have not yet identified, may be further regulating these processes. Nevertheless, autophagy enabled translation of *Brca2* seems to be important for repairing DNA damage, both *in vitro* and *in vivo*, and the resulting decreased in BRCA2 in autophagy deficient cells leads to defects in cell cycle progression, increased DNA damage, centrosome defects and increased sensitivity to PARP inhibitors.

We also describe in Chapter 3 other mRNAs that seem to be translationally regulated by autophagy, although the validation and mechanism is not as thorough as with BRCA2. We describe two other groups of mRNAs, mRNAs involved in metabolic regulation and mRNAs involved in immune signaling. We speculate that these translational changes will maintain the metabolic homeostasis in the cell and impair viral immune responses in autophagy deficient cells.

Lastly, we present data regarding translational regulation under acute starvation stress. To our surprise, we find that the rate of ³⁵S-methionine label incorporation more than doubles in a rapid and sustained manner following withdrawal of amino acids. Additionally, we find that this acute starvation induced translation can be prevented by addition of the bioactive L-Leucine, but not D-Leucine, in the absence of all other amino acids. Our findings are contrary to the current dogma that translation rates are decreased during starvation, and although we find evidence that mTORC1 signaling is repressed during amino acid withdrawal, our ³⁵S-methionine data is at odds with these results. We have not yet identified the mechanism to reconcile these data, but we hope that in the future, the research presented here will be the foundation to a new understanding of translational control.

Appendix A

NBR1 enables autophagy-dependent focal adhesion turnover

The following appendix is published work

Kenific, CM., Stehbens, SJ., **Goldsmith, J.**, Leidal, AM., Faure, N., Ye, J., Wittman, T.,
Debnath, J.

Contributions: Candia Kenific, a former graduate student in the lab, performed all of the experiments and analyzed all the data. Jayanta Debnath supervised the project. I contributed to the validation of knockdown reagents and antibodies for data in Figure 5A, 5B, and S2A, and performed the immunoblot for p62 in Figure S2A. Thank you Candia for guiding me as a rotation student, and including me in your research!

NBR1 enables autophagy-dependent focal adhesion turnover

Candia M. Kenific,^{1,3} Samantha J. Stehbens,² Juliet Goldsmith,^{1,3} Andrew M. Leidal,¹ Nathalie Faure,¹ Jordan Ye,¹ Torsten Wittmann,² and Jayanta Debnath¹

¹Department of Pathology and Helen Diller Family Comprehensive Cancer Center, ²Department of Cell and Tissue Biology, and ³Biomedical Sciences Graduate Program, University of California, San Francisco, San Francisco, CA 94143

Autophagy is a catabolic pathway involving the sequestration of cellular contents into a double-membrane vesicle, the autophagosome. Although recent studies have demonstrated that autophagy supports cell migration, the underlying mechanisms remain unknown. Using live-cell imaging, we uncover that autophagy promotes optimal migratory rate and facilitates the dynamic assembly and disassembly of cell-matrix focal adhesions (FAs), which is essential for efficient motility. Additionally, our studies reveal that autophagosomes associate with FAs primarily during disassembly, suggesting autophagy locally facilitates the destabilization of cell-matrix contact sites. Furthermore, we identify the selective autophagy cargo receptor neighbor of BRCA1 (NBR1) as a key mediator of autophagy-dependent FA remodeling. NBR1 depletion impairs FA turnover and decreases targeting of autophagosomes to FAs, whereas ectopic expression of autophagy-competent, but not autophagy-defective, NBR1 enhances FA disassembly and reduces FA lifetime during migration. Our findings provide mechanistic insight into how autophagy promotes migration by revealing a requirement for NBR1-mediated selective autophagy in enabling FA disassembly in motile cells.

Introduction

Cell migration is essential for tissue morphogenesis during development, immune function, and wound healing and is deregulated during pathological processes such as cancer (Ridley et al., 2003; Friedl and Wolf, 2010). Migration is a highly integrated process involving tight spatiotemporal control of signaling and structural networks throughout the cell. Chief among these are integrin-based focal adhesions (FAs) through which cells engage in adhesive contacts with the surrounding ECM. In addition to integrins, FAs are comprised of signaling and adapter proteins that serve as large, macromolecular biochemical and physical scaffolds linking the ECM to the intracellular actin cytoskeleton (Gardel et al., 2010; Geiger and Yamada, 2011). As such, FAs direct migration in part by mechanically generating forces for movement. Specifically, rapid cycles of FA assembly and disassembly, or turnover, at the leading edge of migrating cells are necessary for productive migration. FA assembly allows cells to establish traction for forward movement, whereas subsequent disassembly of FAs enables efficient displacement of the advancing cell (Gardel et al., 2010; Geiger and Yamada, 2011; Wolfenson et al., 2013).

Given the prominent role of cell migration in many physiological and pathological processes, understanding the regulation

of FA dynamics is a topic of intense study. It is well established that FA assembly involves hierarchical recruitment of FA proteins because of phosphorylation and tension-induced conformational changes that progressively enable protein-protein interactions, but it is not completely certain how these events are regulated (Wolfenson et al., 2013). Although FA disassembly has also been shown to require phosphorylation of FA proteins (Webb et al., 2004) and recent work demonstrates that microtubule-induced FA disassembly involves extracellular proteolysis (Stehbens et al., 2014), how FA disassembly is spatiotemporally coordinated at the leading edge of migrating cells remains unclear.

Autophagy is an evolutionarily conserved process of cellular self-degradation that involves formation of a double-membrane vesicle, the autophagosome, which sequesters cytoplasmic material for delivery to lysosomes (Feng et al., 2014). Although traditionally viewed as a vital pathway supporting cellular homeostasis and adaptation to stress, autophagy is implicated in a growing list of cellular functions (Morrow and Debnath, 2013). Recent studies demonstrate that autophagy inhibition impacts cell migration (Galavotti et al., 2013; Tuloup-Minguez et al., 2013; Lock et al., 2014; Zhan et al., 2014). However, apart from establishing a genetic requirement for essential autophagy

Correspondence to Jayanta Debnath: Jayanta.Debnath@ucsf.edu

Abbreviations used in this paper: ATG, autophagy regulator; FA, focal adhesion; iBMK, immortalized baby mouse kidney; LC3, microtubule-associated protein 1 light chain 3; LIR, LC3-interacting region; NBR1, neighbor of BRCA1; NDP52, nuclear dot protein 52; OPTN, optineurin; p62, p62/sequestosome 1; PyMT, polyoma middle T; SIM, structured illumination microscopy; TIRF, total internal reflection fluorescence; UBA, ubiquitin-binding domain.

© 2016 Kenific et al. This article is distributed under the terms of an Attribution-Noncommercial-Share Alike-No Mirror Sites license for the first six months after the publication date (see <http://www.rupress.org/terms>). After six months it is available under a Creative Commons License (Attribution-Noncommercial-Share Alike 3.0 Unported license, as described at <http://creativecommons.org/licenses/by-nc-sa/3.0/>).



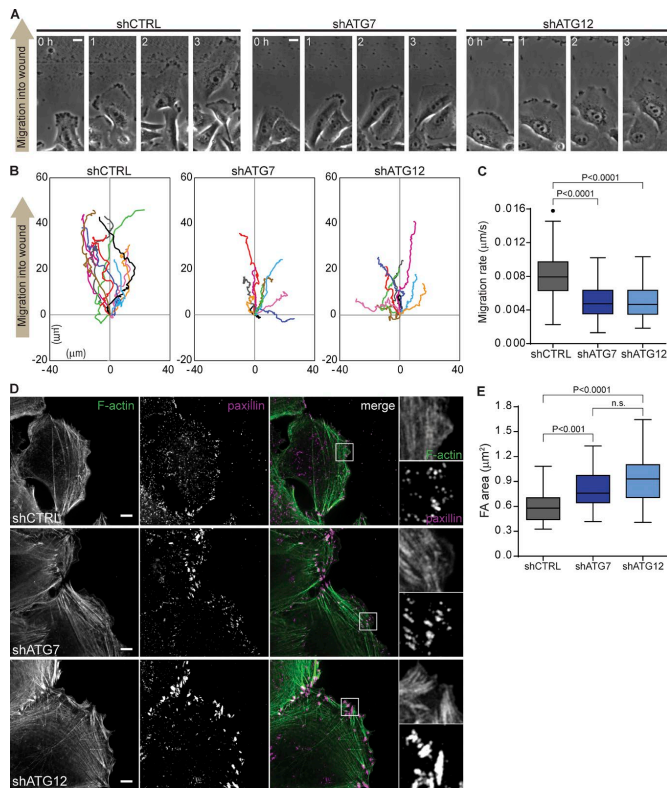


Figure 1. Impaired migration rate and increased FA size in autophagy-deficient cells. (A) Representative phase-contrast microscopy time-lapse sequences of single cells expressing shCTRL (CTRL; left), shATG7 (middle), or shATG12 (right) tracked over 3 h after wounding. Elapsed time (h) in top left of images. Bars, 10 μm . These images correspond to Video 1. (B) Migration paths of individual shCTRL (left), shATG7 (middle), or shATG12 (right) cells showing total distance traveled over 3 h. Cell position over time was used to generate paths and was determined by manually tracking cell nucleoli in each frame over the course of the time lapse. $n = 10$ representative cells shown per condition, and each colored track represents an independent cell. The starting position for each cell was normalized to 0 μm , 0 μm on the x , y axes. (C) Quantification of migration rate of individual tracked cells determined as total distance traveled divided by the total time of migration ($d/t_f - t_0$). Data presented as median (line), first and third quartile (box), and whiskers extend to ± 1.5 times the interquartile range. Individual data points outside of this range are shown. $n = 155$ cells for shCTRL, $n = 121$ cells for shATG7, and $n = 115$ cells for shATG12, pooled from three independent experiments. P-values calculated using a nonparametric Kruskal-Wallis test followed by Dunn post-hoc test. (D) Representative immunofluorescence images of migrating wound edge cells expressing shCTRL (top), shATG7 (middle), or shATG12 (bottom) stained for endogenous F-actin (green) and paxillin (magenta) to mark FAs. Right panels show enlarged insets of boxed region in merged images. Bars, 5 μm . Insets are magnified 3.7-fold. (E) Quantification of the area of leading edge FAs in migrating wound edge cells determined by manually outlining anti-paxillin-labeled FAs. Data presented as median (line), first and third quartile (box), and whiskers extend to ± 1.5 times the interquartile range. $n = 713$ FAs for shCTRL, $n = 511$ FAs for shATG7, and $n = 430$ FAs for shATG12, pooled from two independent experiments. P-values calculated using a nonparametric Kruskal-Wallis test followed by Dunn post-hoc test. n.s., not significant.

exhibited a significant increase in cell area compared with autophagy-competent cells (Fig. 3, B and C). Together with our quantitative analysis of FAs in migrating cells, these findings point to a broader role for autophagy in modulating adhesion-dependent phenotypes.

Autophagosomes localize to FAs during disassembly in migrating cells

Typically, autophagy functions through the local and direct sequestration of cellular material into the forming autophagosome, which eventually fuses with lysosomes for cargo degradation (Murrow and Debnath, 2013; Feng et al., 2014). Hence, we reasoned that autophagy-dependent FA turnover may entail the close local apposition of autophagosomes with dynamic FAs during migration. To test this prediction, we generated cells coexpressing paxillin-mCherry and GFP-LC3, which marks autophagosomes, and observed that autophagosomes localized throughout the leading edge of migrating cells (Fig. 4 A and Video 4). We enumerated adhesions targeted by GFP-LC3, defined as GFP-LC3 puncta in direct contact with paxillin-mCherry-labeled FAs and found that 40% of dynamic FAs were directly targeted by autophagosomes and that autophagosomes were enriched by 40-fold at FAs compared with

non-FA areas at the leading edge (Fig. 4, B–F; and Videos 5 and 6). Of note, these experiments may underestimate the actual number of targeted FAs because of the rapid intracellular dynamics of GFP-LC3-labeled vesicles. In addition, we used structured illumination microscopy (SIM) and total internal reflection fluorescence (TIRF) microscopy to better observe the spatial relationship between autophagosomes and FAs. SIM, which provides improved resolution over confocal imaging, corroborated that autophagosomes localize to leading edge FAs (Fig. S2 A). Likewise, TIRF imaging further verified that autophagosomes are localized to leading edge FAs at the basal surface of migrating cells (Fig. S2 B). Furthermore, during cell spreading, we similarly observed GFP-LC3 puncta to be associated with dynamic FAs throughout the periphery of the cell, further confirming that autophagosomes are locally targeted to FAs (Fig. S2 C).

We next determined if autophagosome targeting to FAs proceeds in a temporally specific manner. Interestingly, a limited number of targeting events occurred during FA assembly or when FAs were relatively stable; rather, most GFP-LC3 targeting events occurred during FA disassembly (Fig. 4, E–G; and Video 6). Together with our data showing that autophagy is functionally required for FA turnover, these results support

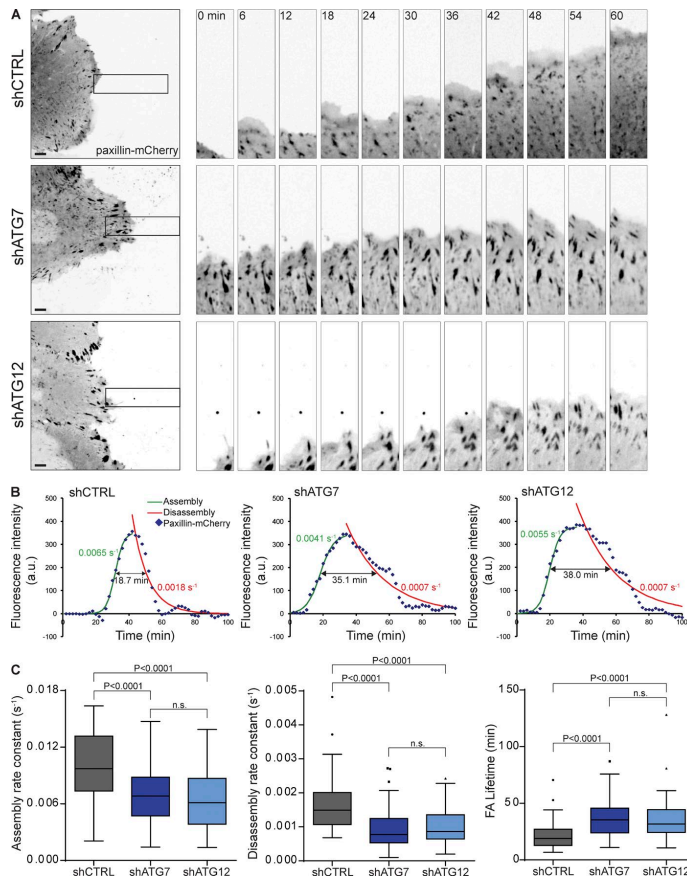


Figure 2. Autophagy promotes FA turnover in migrating cells. (A) Spinning disk confocal microscopy time-lapse sequences of migrating cells expressing paxillin-mCherry (black) to monitor FA dynamics. Left panels show representative cells expressing shCTRL (top), shATG7 (middle), or shATG12 (bottom). Image sequences of boxed regions have been rotated such that the cell edge with dynamic FAs is moving upward vertically. Elapsed time (min) shown in top left. Bars, 5 μ m. Insets are magnified twofold. These images correspond to Videos 2 and 3. (B) Example plots of paxillin-mCherry fluorescence intensity (y axis) over time (x axis) for shCTRL (left), shATG7 (middle), and shATG12 (right) cells used for calculating FA turnover parameters in C. Plots generated by manually tracking individual FAs over time, and each data point is a three-frame running mean of intensity value. The green line represents FA assembly fitted with a logistic function, and the red line represents FA disassembly fitted with an exponential decay function. The lifetime is the time spent above half-maximum fluorescence intensity (double arrow). The values of each parameter are indicated for the specific curves shown (assembly rate constant in green, disassembly rate constant in red, and lifetime in black). (C) Quantification of assembly rate constants (left), disassembly rate constants (middle), and lifetime (right) for FAs in cells expressing shCTRL, shATG7, or shATG12. Data presented as median (line), first and third quartile (box), and whiskers extend to ± 1.5 times the interquartile range. Individual data points outside of this range are shown. $n = 62$ FAs for shCTRL, $n = 64$ FAs for shATG7, and $n = 51$ FAs for shATG12, pooled from four independent experiments. P-values calculated using a non-parametric Kruskal-Wallis test followed by Dunn post-hoc test. n.s., not significant.

that autophagy impacts leading edge FAs by proximally facilitating disassembly. This autophagy-dependent FA remodeling may involve the local sequestration of FA components into autophagosomes to promote FA destabilization and disassembly. In support, multiple FA proteins, including paxillin, vinculin, and zyxin, were present in GFP-LC3-labeled autophagosomes of migrating cells (Fig. S2 D).

The selective autophagy cargo receptor NBR1 promotes cell migration and FA turnover

Given the highly specific targeting of autophagosomes to FAs during disassembly, and because FA turnover is exquisitely coordinated to optimize migration and adhesion (Gardel et al., 2010; Geiger and Yamada, 2011; Wolfenson et al., 2013), we hypothesized that a tightly controlled mechanism would be necessary to direct autophagic targeting of FAs. Notably, FAs are large protein complexes (Geiger and Zaidel-Bar, 2012), and autophagy has been shown to target large intracellular macromolecular assemblies, such as iron-containing ferritin complexes (Dowdle et al., 2014; Mancias et al., 2014) and midbody derivatives during the final stages of cytokinesis (Pohl and Jentsch, 2009; Kuo et

al., 2011). The autophagic targeting of these structures is mediated by autophagy cargo receptors, which promote the selective degradation of cellular substrates (Johansen and Lamark, 2011; Rogov et al., 2014). These molecules bind cargo marked with degradation signals, most commonly ubiquitin, through their ubiquitin-binding domains (UBAs; Kraft et al., 2010) and typically possess an LC3-interacting region (LIR) motif, which allows them to bind to LC3 and other ATG8 isoforms present on developing autophagosomes (Birgisdottir et al., 2013). Because of these unique characteristics, we sought to determine if autophagy cargo receptors support migration and FA dynamics.

To initially establish if individual autophagy cargo receptors regulate migration, we performed scratch-wound closure assays with cells transiently depleted for several of the major known receptors, including p62/sequestosome 1 (p62), NBR1, optineurin (OPTN), and nuclear dot protein 52 (NDP52). We identified NBR1 as the only cargo receptor whose knockdown significantly attenuated wound closure (Fig. 5, A and B; and Fig. S3 A). To verify this result, we generated stable pools of cells with shRNA against NBR1 (Fig. S3 B). In agreement with our findings using transient, siRNA-mediated depletion, stable NBR1 knockdown also significantly inhibited migration (Fig. 5,

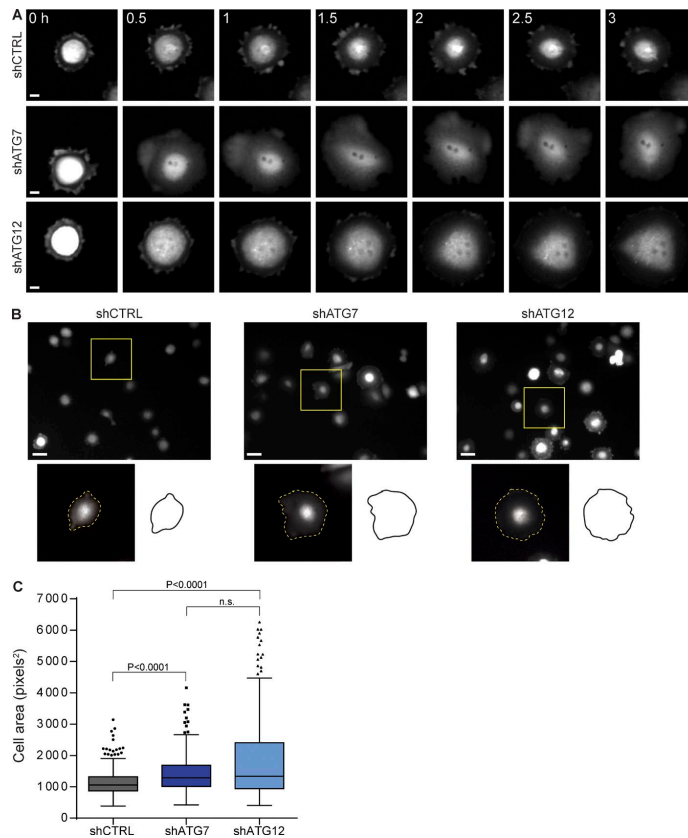


Figure 3. Autophagy inhibition results in enhanced cell spreading. (A) Spinning disk confocal microscopy time-lapse sequences of cells expressing ZsGreen during spreading after replating. Representative shCTRL (top), shATG7 (middle), or shATG12 (bottom) cells shown over a 3-h time course. Elapsed time (h) indicated in top left of images. Bars, 10 μ m. (B) Representative images of ZsGreen-expressing cells fixed 1 h after replating used for quantification of cell area in C. Whole field images shown with enlarged boxed insets of individual cells at bottom left. Tracing of individual cell in inset shown at bottom right. Bars, 50 μ m. Insets are magnified 2.4-fold. (C) Quantification of area of cells fixed 1 h after replating. Area determined by manually outlining individual ZsGreen-expressing cell borders. Data presented as median (line), first and third quartile (box), and whiskers extend to ± 1.5 times the interquartile range. Individual data points outside of this range are shown. $n = 315$ cells for shCTRL, $n = 351$ cells for shATG7, and $n = 306$ cells for shATG12, pooled from three independent experiments. P-values were calculated using a nonparametric Kruskal-Wallis test followed by Dunn post-hoc test. n.s., not significant.

C and D). Importantly, in contrast with ATG knockdown, NBR1 depletion did not affect basal autophagy levels (Fig. S3 C).

To further dissect the role of NBR1 in motility, we measured FA dynamics in paxillin-mCherry-expressing cells after stable NBR1 knockdown. Similar to ATG depletion, NBR1 loss of function decreased the rates of FA assembly and disassembly by 32% and 41%, respectively, leading to an overall 81% increase in FA lifetime compared with controls (Fig. 5, E and F; and Videos 7 and 8). Consistent with this role for NBR1 in facilitating FA turnover, endogenous NBR1 colocalized with anti-paxillin-labeled FAs, and GFP-NBR1 associated with and was significantly enriched at leading edge FAs in live migrating cells (Fig. S3, D–F; and Video 9). Furthermore, NBR1-depleted ZsGreen-expressing cells underwent prolonged spreading compared with control cells and exhibited increased cell area at 1 h after replating (Fig. S4, A–C). Collectively, these results demonstrate that NBR1 loss of function phenocopies the effects of autophagy inhibition on both FA turnover and adhesion-dependent processes, indicating NBR1 and autophagy may coordinately facilitate FA remodeling through a common pathway of NBR1-mediated selective autophagy. Moreover, we uncover that NBR1, like autophagosomes, localizes to FAs, further supporting that NBR1-mediated selective autophagy proximally impacts FA remodeling.

NBR1-dependent selective autophagy promotes FA disassembly

Because NBR1 is a multidomain scaffold protein that may serve both autophagy-dependent and -independent functions, we next sought to more precisely ascertain if NBR1-mediated FA turnover is associated with its role in selective autophagy. NBR1-dependent selective autophagy requires that it locally promote targeting of autophagosomes to substrates destined for autophagic turnover; therefore, we hypothesized that NBR1 would colocalize with a high proportion of FA-associated autophagosomes. Indeed, in migrating cells stably expressing paxillin-mTurquoise, Venus-LC3, and mCherry-NBR1, NBR1 was localized to 80% of FA-associated autophagosomes (Fig. 6, A and B). Most importantly, we uncovered that NBR1 depletion significantly attenuated the targeting of autophagosomes to dynamic, leading edge FAs (Fig. 6 C), thereby confirming the functional requirement of NBR1 in locally facilitating autophagic targeting of FAs. Collectively, these data provide evidence for a localized pathway of NBR1-mediated autophagic targeting of FAs.

Autophagy cargo recognition by NBR1 requires that it interact with both potential substrates and forming autophagosomes. Accordingly, we first assessed whether NBR1 interacts with FA components in cells ectopically expressing low levels

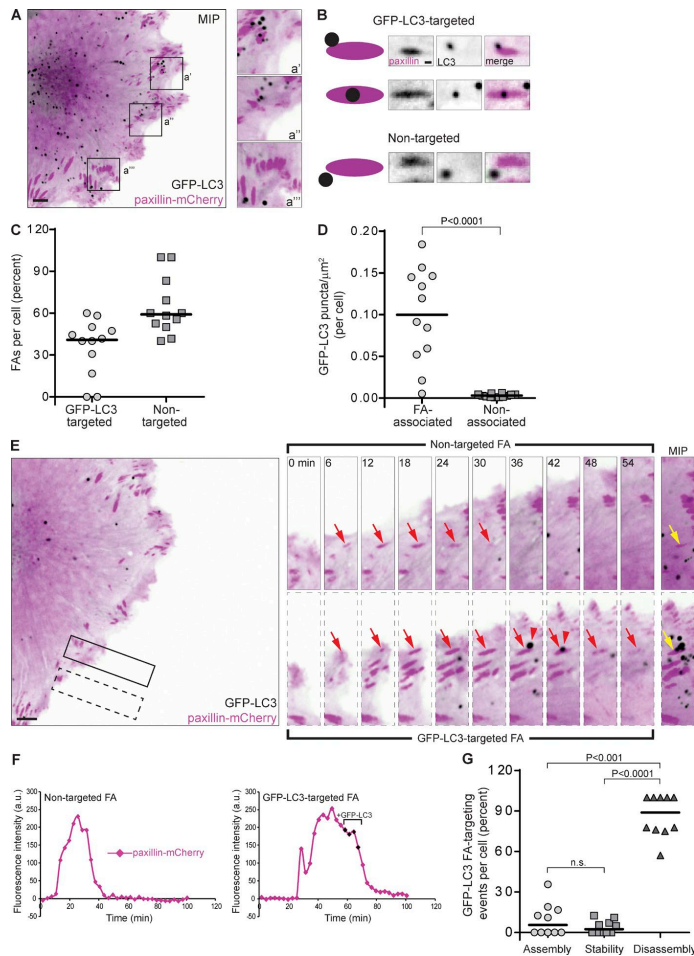


Figure 4. Autophagosomes associate with dynamic FAs during disassembly. (A) Spinning disk confocal microscopy of a migrating cell expressing GFP-LC3 (black) to label autophagosomes and paxillin-mCherry (magenta) to label FAs. Left panel shows maximum intensity projection (MIP) of a cell over 21 min, illustrating multiple associations between autophagosomes and FAs. Boxed inset areas are enlarged in right panel. Bar, 5 μ m. Insets are magnified twofold. (B) Criteria for distinguishing GFP-LC3-targeted FAs versus nontargeted FAs. Left illustration depicts representations of targeted FAs (top and middle) and nontargeted FAs (bottom). Right images are examples of targeted and nontargeted FAs. Bar, 0.5 μ m. (C) Quantification of the percentage of dynamic leading edge FAs per cell targeted by autophagosomes. FAs were randomly chosen independent of the GFP channel and then manually tracked from their appearance to disappearance for evidence of direct contact by GFP-LC3 vesicles. Scatter plot shows individual single cells ($n = 12$ total cells) and median (line), representing 129 total FAs analyzed from two independent experiments. (D) Analysis of GFP-LC3 vesicles in FA areas and non-FA areas at the leading edge of migrating cells. The total number of vesicles at FAs or in non-FA areas was counted and normalized to the total area for FA or non-FA regions, respectively. Scatter plot shows individual single cells ($n = 12$ total cells) and median (line), representing 196 total leading edge GFP-LC3 vesicles analyzed from two independent experiments. P-value determined using unpaired t test. (E) Spinning disk confocal microscopy time-lapse sequences of representative targeted (box with dotted border, bottom) and nontargeted (box with solid border, top) FAs. Insets rotated such that leading edge is moving upward vertically. Arrows track single FAs over time, with autophagosome targeting indicated by arrowheads. Elapsed time (min) shown in top left of images. Right-most panels show MIP for each FA (arrow) shown in the corresponding time-lapse sequence. Bar, 5 μ m. Insets are magnified 1.5-fold. (F) Representative paxillin-mCherry fluorescence intensity (y axis) plots over time (x axis) for the FAs shown in E. Frames in which GFP-LC3 was in direct contact with FAs are indicated by black data points and bracketing (right plot). (G) Temporal analysis of GFP-LC3 targeting to FAs.

The phase during which GFP-LC3 associated with FAs was determined by counting the total number of GFP-LC3 targeting events in C and determining when during FA turnover each event occurred; if FAs were targeted multiple times during their lifetime, each event was independently counted. Scatter plot shows individual cells ($n = 12$ total cells) and median (line), representing 114 total targeting events analyzed from two independent experiments. P-values were calculated using a nonparametric Kruskal-Wallis test followed by Dunn post-hoc test. n.s., not significant. Images in this figure correspond to Videos 4–6.

of GFP-NBR1. GFP-NBR1 interacted with multiple endogenous FA proteins, including paxillin, vinculin, zyxin, and FAK, indicating that such biochemical interactions may enable localization of NBR1 to FAs (Fig. S5 A). As a positive control, we confirmed the previously established interaction of GFP-NBR1 with p62 in these cells (Lange et al., 2005; Kirkin et al., 2009; Fig. S5 A). Next, we used a gain-of-function approach to scrutinize the requirement of NBR1 interaction with LC3 in autophagy-dependent FA turnover. We generated cells overexpressing wild-type GFP-NBR1 or a mutant NBR1 lacking the LIR motif (GFP-NBR1 Δ LIR) required for binding to LC3/ATG8, thereby rendering it autophagy-incompetent (Kirkin et al., 2009; Waters et al., 2009; Fig. 6 D). In contrast to wild-type GFP-NBR1,

GFP-NBR1 Δ LIR was resistant to nutrient starvation-induced autophagic degradation, confirming this mutant to be autophagy-incompetent (Fig. 6 E). GFP-NBR1 was ectopically expressed in paxillin-mCherry cells to test if increased NBR1 was sufficient to enhance FA turnover. Compared with GFP alone, expression of GFP-NBR1 significantly increased FA turnover. Although GFP-NBR1 did not impact FA assembly, it significantly enhanced FA disassembly by 46%, leading to an overall 29% decrease in FA lifetime (Figs. 6 F and S5 B). In contrast, GFP-NBR1 Δ LIR did not significantly affect FA assembly, disassembly, or lifetime (Figs. 6 F and S5 B). Therefore, the interaction of NBR1 with LC3, and hence the ability of this cargo receptor to facilitate selective autophagy, is absolutely essential

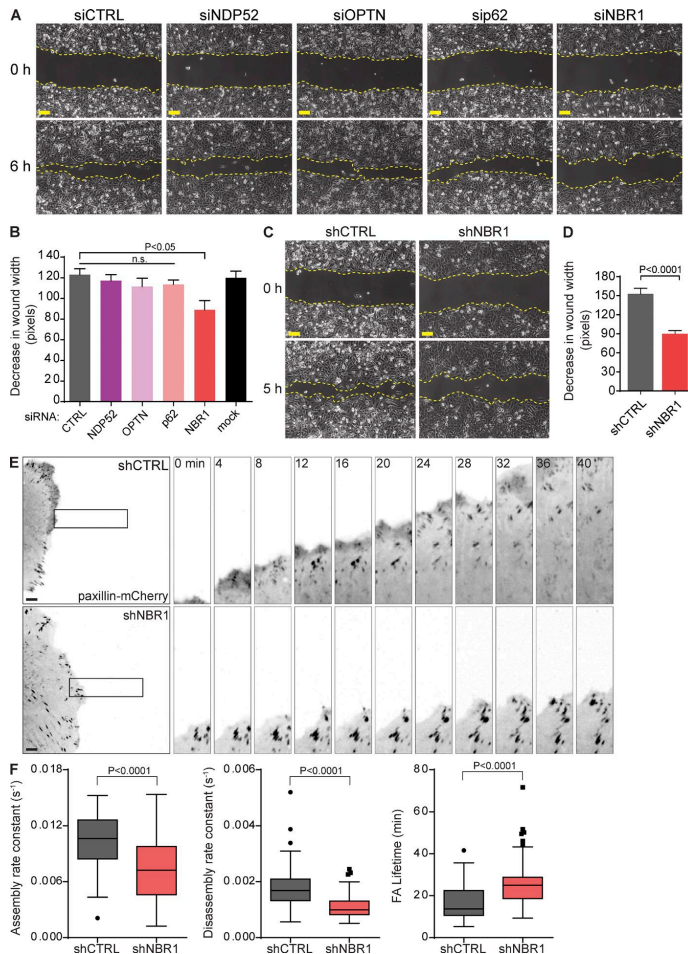


Figure 5. NBR1 facilitates cell migration and FA turnover.

(A) Representative phase-contrast microscopy images at time of wounding (0 h) and 6 h after wounding for cells expressing control siRNA (CTRL) or siRNA against NDP52, OPTN, p62, or NBR1. Dashed yellow lines highlight wound boundaries. Bars, 100 μ m. (B) Quantification of wound closure over 6 h by cells expressing indicated siRNAs. The decrease in wound width was determined by subtracting the final width at 6 h from the initial width at 0 h. Bar graph shows mean + SEM, representing $n = 8$ wounds for siCTRL, $n = 8$ wounds for siNDP52, $n = 8$ wounds for siOPTN, $n = 6$ wounds for sip62, $n = 6$ wounds for siNBR1, and $n = 5$ wounds for mock (no siRNA) pooled from four independent experiments. P-values calculated using one-way analysis of variance followed by Tukey post-hoc test. n.s., not significant. (C) Representative phase-contrast microscopy images of cells expressing shCTRL or shNBR1 at time of wounding (0 h) and at 5 h after wounding. Dashed yellow lines highlight wound boundaries. Bars, 100 μ m. (D) Quantification of wound closure over 5 h by shCTRL and shNBR1 cells. Bar graph shows mean + SEM, representing $n = 12$ wounds for shCTRL and $n = 15$ wounds for shNBR1 pooled from three independent experiments. P-value determined using unpaired t test. (E) Spinning disk confocal microscopy time-lapse sequences of cells expressing paxillin-mCherry (black) to monitor FA dynamics. Left panels show representative cells expressing shCTRL (top) or shNBR1 (bottom). Image sequences of boxed regions on the right have been rotated such that the cell edge with dynamic FAs is moving upward vertically. Elapsed time (min) in top left of images. Bars, 5 μ m. Insets are magnified twofold. These images correspond to Videos 7 and 8. (F) Quantification of FA assembly rate constants (left), disassembly rate constants (middle), and lifetime (right) for FAs in shCTRL or shNBR1 cells. Data presented as median (line), first and third quartile (box), and whiskers extend to ± 1.5 times the interquartile range. Individual data points outside of this range are shown. $n = 53$ FAs for shCTRL and $n = 58$ FAs for shNBR1, pooled from three independent experiments. P-value calculated using a nonparametric Mann-Whitney test.

for its role in enabling FA turnover. Finally, because autophagy cargo recognition by NBR1 also involves the binding of ubiquitinated substrates via its UBA, we tested the effects of a mutant NBR1 lacking this UBA (GFP-NBR1 Δ UBA) on FA dynamics. Similar to GFP-NBR1 Δ LIR, GFP-NBR1 Δ UBA did not significantly impact FA disassembly or turnover (Figs. 6 F and S5 B). Overall, these results delineate a specific role for NBR1-mediated selective autophagy in regulating FA turnover by promoting FA disassembly in migrating cells.

Discussion

In summary, we present evidence for autophagy as a mechanism for FA turnover at the leading edge of migrating cells and implicate the selective autophagy cargo receptor, NBR1, as a key mediator of this process. Using live-cell imaging to directly visualize FAs, we uncover that autophagy supports

FA turnover and that autophagosomes target FAs during disassembly. Overall, these data suggest a role for autophagy in facilitating FA turnover by locally promoting FA disassembly. Although autophagosomes are found preferentially associated with disassembling FAs, it is important to note that ATG knock-down functionally impairs both FA assembly and disassembly. Therefore, although disassembly may be proximally modulated by autophagy, we cannot rule out that autophagy regulates FA assembly by more indirect mechanisms that do not necessarily involve the localization of autophagosomes to FAs.

There is evidence that autophagy directs the endocytic recycling of β 1-integrins. However, the activation of this pathway is only observed during extreme nutrient deprivation conditions in which cells are incubated in HBSS to induce autophagy. As a result, it remains uncertain whether the autophagy pathway alters integrin recycling to impact migration in broader contexts (Tuloup-Minguez et al., 2013). Although autophagy may impact cell motility via multiple mechanisms, our results

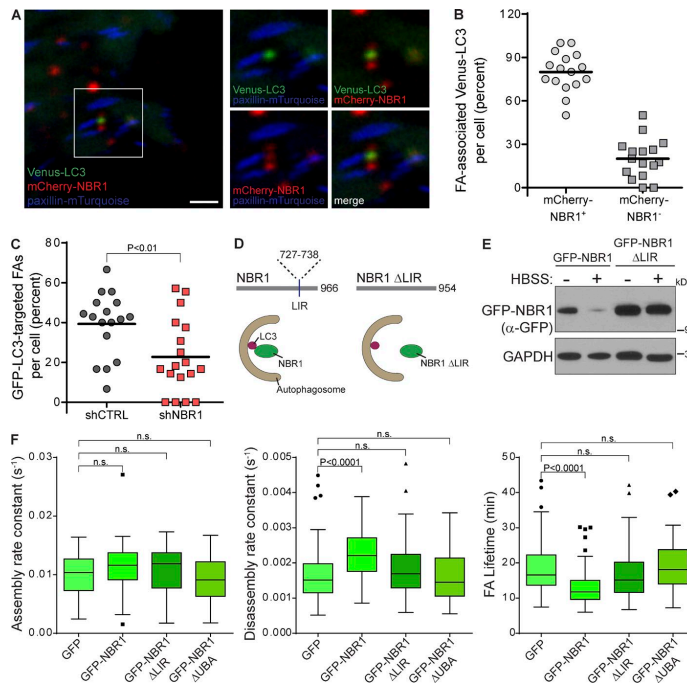


Figure 6. NBR1-mediated selective autophagy promotes FA disassembly. (A) Representative spinning disk confocal image of a migrating cell stably expressing paxillin-mTurquoise, Venus-LC3, and mCherry-NBR1. Whole-cell merged image shown at left and enlarged boxed insets of two- and three-color merged images shown at right. Bar, 2.5 μ m. Insets are magnified 1.4-fold. (B) Quantification of mCherry-NBR1 colocalization with FA-associated Venus-LC3 vesicles. FA-associated Venus-LC3 vesicles were identified as described in Fig. 4 B, and then the number of mCherry-NBR1-positive and -negative vesicles were enumerated. Scatter plot shows individual single cells ($n = 16$ total cells) and mean (line), representing 170 total FA-associated Venus-LC3 vesicles analyzed from two independent experiments. (C) Quantification of the percentage of dynamic leading edge FAs per cell targeted by autophagosomes in shCTRL or shNBR1 cells. FAs were randomly chosen independent of the GFP channel and then manually tracked for evidence of direct contact by GFP-LC3 vesicles as described in Fig. 4 B. Scatter plot shows individual single cells ($n = 17$ cells for shCTRL and $n = 18$ cells for shNBR1) and mean (line), representing 165 FAs for shCTRL and 159 FAs for shNBR1 analyzed from two independent experiments. P-value determined using unpaired t test. (D) Schematic of wild-type NBR1 (left) and autophagy-defective NBR1 Δ LIR (right) resulting from deletion of the LIR (aa 727–738, depicted as vertical line). Bottom diagram demonstrates inability of NBR1 Δ LIR to bind LC3 (right) and be recruited into autophagosomes, unlike wild-type NBR1 (left). (E) Nutrient-starved (HBSS, 4 h) HEK-293T cells ectopically expressing wild-type GFP-NBR1 or GFP-NBR1 Δ LIR. GAPDH is loading control. (F) Quantification of FA assembly rate constants (left), disassembly rate constants (middle), and lifetime (right) for FAs in cells expressing GFP control, GFP-NBR1, GFP-NBR1 Δ LIR, or GFP-NBR1 Δ UBA. Data presented as median (line), first and third quartile (box), and whiskers extend to ± 1.5 times the interquartile range. Individual data points outside of this are shown. $n = 99$ FAs for GFP control, $n = 84$ FAs for GFP-NBR1, $n = 62$ FAs for GFP-NBR1 Δ LIR, and $n = 62$ FAs for GFP-NBR1 Δ UBA, pooled from four independent experiments. P-values calculated using a nonparametric Kruskal-Wallis test followed by Dunn post-hoc test. n.s., not significant.

here most clearly implicate autophagy in promoting leading edge FA turnover, which functions as a crucial and distinct contributor to migration.

Significantly, our results expand on the growing importance of selective autophagy receptors, namely NBR1, in controlling essential cellular functions. Our findings that loss of NBR1 function inhibits migration and leading edge FA turnover, that NBR1 is required for efficient targeting of autophagosomes to FAs, that only autophagy-competent NBR1 is sufficient to specifically drive FA disassembly, and that NBR1 colocalizes with autophagosomes at dynamic FAs all support that cargo receptor-mediated autophagy fine-tunes migratory capacity by optimizing adhesion site turnover. Like other autophagy cargo receptors, NBR1 enables the selective capture of cellular substrates into autophagosomes. Therefore, our work broaches the hypothesis that NBR1 interacts with FA-associated proteins and recruits autophagosomes to FAs via binding of NBR1 to LC3. This recruitment triggers autophagic sequestration or consumption of FA components, which facilitates FA disassembly. In support, we demonstrate that NBR1 biochemically interacts with multiple FA proteins and that FA components are localized to autophagosomes in migrating cells. Indeed, selective autophagy is an attractive candidate for mediating turnover of large macromolecular complexes, such as FAs, because it is the

major homeostatic pathway through which bulky cellular cargo, such as organelles and protein aggregates, are sequestered and degraded (Murrow and Debnath, 2013).

During autophagy, cargo selection is often specified by ubiquitination of substrates (Kraft et al., 2010; Johansen and Lamark, 2011). E3 ubiquitin ligases constitute an integral arm of the adhesome, and FA proteins can be modified by ubiquitination (Schiller and Fässler, 2013; Wolfenson et al., 2013; Deng and Huang, 2014; Winograd-Katz et al., 2014). Despite being an important pathway for the turnover of ubiquitinated substrates, the role of autophagy in dictating the fate of FAs harboring ubiquitinated proteins has not been investigated. Our data demonstrate that the UBA of NBR1 is required for NBR1-dependent FA disassembly, indicating a potentially important role for the recognition of ubiquitinated cargoes during autophagy-mediated FA turnover. In addition, ubiquitin-independent mechanisms of autophagy substrate selection also exist (Kraft et al., 2010), and FAs consist of hundreds of proteins (Geiger and Zaidel-Bar, 2012). Furthermore, NBR1 is a large multidomain scaffold (Whitehouse et al., 2002; Müller et al., 2006; Kirkin et al., 2009; Waters et al., 2009) with the ability to engage in many interactions. Given these potentially diverse mechanisms of cargo recognition, numerous interactions between NBR1 and FAs likely exist; accordingly, our biochemical studies indicate

that multiple FA proteins are able to interact with NBR1. Therefore, important topics for future study are to more comprehensively identify NBR1 binding partners at FAs and to elucidate how such interactions are regulated, both by ubiquitination and other pathways, to promote autophagosome recruitment to dynamic FAs during adhesion-dependent processes.

Finally, our results demonstrating that FA turnover is partially inhibited in autophagy-deficient cells reinforce that selective autophagic targeting of FAs only serves as one destabilizing mechanism to promote disassembly. Additional pathways, including phosphorylation mediated by FAK-Src signaling (Webb et al., 2004), endocytosis (Ezraty et al., 2005, 2009; Chao and Kunz, 2009), calpain cleavage (Franco et al., 2004; Chan et al., 2010; Cortesio et al., 2011), and ECM proteolysis (Shi and Sotile, 2011; Stehbins et al., 2014), have all been implicated in FA disassembly. Together with our current results demonstrating that autophagy supports FA turnover, these findings illustrate how cells engage diverse mechanisms to direct adhesion and migration. Going forward, a crucial unanswered question is how autophagy acts in concert with these other pathways to orchestrate FA remodeling.

Materials and methods

Cell culture

MCF10A and MCF10A-Ras mammary epithelial cells were cultured in DMEM/F12 supplemented with 5% horse serum, 20 ng/ml EGF, 0.5 µg/ml hydrocortisone, 100 ng/ml cholera toxin, 10 µg/ml insulin, penicillin, and streptomycin. PyMT mammary carcinoma cells (R221A clone; Martin et al., 2008; gift from B. Fingleton, Vanderbilt University, Nashville, TN) and HEK-293T cells were cultured in DMEM with 10% FBS, penicillin, and streptomycin. iBMK cells were a gift from E. White (Rutgers University, New Brunswick, NJ) and are now commercially available from Applied Biological Materials (T0082 and T3027). They were originally derived via stable transformation of primary kidney epithelial cells isolated from *Atg5^{+/+}* and *Atg5^{-/-}* isogenic newborn littermates (postnatal day 1, C57BL/6 genetic background) with adenovirus E1A and dominant negative p53 (p53DD; Mathew et al., 2008). They were cultured in DMEM with 10% FBS, penicillin, and streptomycin. For experiments, MCF10A-Ras cells were routinely incubated in assay media (DMEM/F12, 2% horse serum, 0.5 µg/ml hydrocortisone, 100 ng/ml cholera toxin, 10 µg/ml insulin, penicillin, and streptomycin; Debnath et al., 2003); 20 mM Hepes was added to the culture medium during live-cell imaging experiments.

cDNA constructs, retroviral and lentiviral vectors, and generation of stable cell lines

We previously generated pBabeneo-HRas^{V12}, pBabepuro-GFP-LC3 (22405; Addgene), pBabehydro-GFP-LC3, and pLentiblast-paxillin-mCherry; our subcloning strategy for these plasmids has been described elsewhere (Hu et al., 2007; Fung et al., 2008; Lock et al., 2014; Stehbins et al., 2014). pMXs-IP-GFP-NBR1 and pMRX-IP-Venus-LC3 were gifts from N. Mizushima (University of Tokyo, Tokyo, Japan; 38283 and 58740; Addgene; Itakura and Mizushima, 2011; Koyama-Honda et al., 2013). pHIV-ZsGreen was provided by B. Welm (University of Utah School of Medicine, Salt Lake City, Utah; 18121; Addgene; Welm et al., 2008). pDest-mCherry-NBR1 was a gift from P. Kim (University of Toronto, Toronto, Ontario, Canada) and T. Johansen (University of Tromsø, Tromsø, Norway; Kirkin et al., 2009; Deosaran et al., 2013). Paxillin-mTurquoise, mCherry-vinculin, and zyxin-mCherry were from M. Davidson (Florida State University,

Tallahassee, FL; 55573, 55159, and 55166; Addgene), and pLentiblast-GFP was provided by E. Campeau (University of Massachusetts Medical School, Worcester, MA; 19069; Addgene; Campeau et al., 2009). Lentiviral packaging and envelope plasmids pRSV-REV, pMD2Lg/pRRE, and pMD2.g were gifts from D. Trono (École Polytechnique Fédérale de Lausanne, Lausanne, Switzerland; 12253, 12251, and 12259; Addgene).

To generate pMXspuro-GFP, pMXspuro-GFP-NBR1, pMXspuro-GFP-NBR1 ΔLIR, and pMXspuro-GFP-NBR1 ΔUBA, GFP alone and GFP-NBR1 were first amplified from pMXs-IP-GFP-NBR1 and subcloned into pcDNA3 (Life Technologies). Site-directed mutagenesis was then performed for deletion of aa 727–738 in NBR1 (NBR1 ΔLIR) or to change aa 877 to a premature stop (NBR1 ΔUBA); GFP, GFP-NBR1, GFP-NBR1 ΔLIR, and GFP-NBR1 ΔUBA were subsequently subcloned into BamHI–XhoI sites of pMXspuro for retroviral expression (Kitamura et al., 2003). mCherry-NBR1 was PCR amplified from pDest-mCherry-NBR1 and subcloned into the BamHI–XhoI sites of pMXspuro to generate pMXspuro-mCherry-NBR1 for retroviral expression. To generate pLentiblast-paxillin-mTurquoise, paxillin-mTurquoise was PCR amplified and subcloned into the BamHI–SalI sites of pLentiblast-GFP for lentiviral expression.

Vesicular stomatitis virus G pseudotyped retroviruses were produced by transfection of a 293GPG retrovirus producer cell line (Ory et al., 1996) with 15 µg of expression cDNA using Lipofectamine 2000 (Life Technologies). Retroviral supernatants were collected at days 5–7 after transfection, filtered through a 0.45-µm filter, and stored at –80°C. Lentivirus was made using a four-plasmid, third-generation producer system (Dull et al., 1998) by cotransfecting HEK-293T cells with packaging and envelope vectors (2 µg of pRSV-REV, 2 µg of pMD2Lg/pRRE, and 4 µg of pMD2.g) and 12 µg of expression cDNA using Lipofectamine LTX/PLUS (Life Technologies). Lentiviral supernatants were collected 48 h after transfection, filtered through a 0.45-µm filter, and stored at –80°C. For infection with retroviruses and lentiviruses, 100,000 cells were seeded per well in six-well dishes the day before infection and incubated overnight with virus-containing supernatants supplemented with 8 µg/ml polybrene (Sigma-Aldrich). Stable cell lines were obtained by selecting with 200 µg/ml G418 (Sigma-Aldrich), 0.5–2 µg/ml puromycin (Sigma-Aldrich), 6 µg/ml blasticidin (Life Technologies), or 200 µg/ml hygromycin (Life Technologies). After stable pools were obtained, cells were cultured in the absence of selection agents.

RNA interference

For stable RNA interference, pLKO.1puro lentiviral plasmids with nontargeting shRNA or shRNA against ATG7 (human: NM_006395, mouse: NM_028835), human ATG12 (NM_004707), and human NBR1 (NM_031858) were purchased from Sigma-Aldrich. The target sequence for shRNA against human ATG7 (TRCN0000007587) is 5'-CCCAGCTATTGGAACACTGTA-3', against human ATG12 (TRCN0000007394) is 5'-TGGAACCTCTATGAGTGTTT-3', against mouse ATG7 (TRCN0000092163) is 5'-CCAGCTCTGAACCAATAATA-3', and against human NBR1 (TRCN0000123161) is 5'-GCCAGGAACCAAGTTTATCAA-3'. The sequence of the nontargeting shRNA (SHC002; Sigma-Aldrich), which targets no known mammalian genes, is 5'-CAACAAGATGAAGAGCACC-3'. shRNA lentivirus was prepared as described above for lentiviral vectors. In brief, HEK-293T cells were cotransfected with packaging and envelope vectors and pLKO.1 shRNA expression plasmids. Virus was collected 48 h after transfection, filtered through a 0.45-µm filter, and stored at –80°C. Cells were seeded in six-well dishes and infected as described for generation of stable cell lines. Stable pools of knockdown cells were obtained by selecting with 2 µg/ml puromycin for 48 h. Cells were

used within one to two passages after selection for experiments. New stable pools were generated for each experimental repeat, and knock-down was verified by immunoblotting for each individual experiment.

For siRNA-mediated knockdown, ON-TARGETplus SMART-pool siRNAs were purchased from Dharmacon. The sense sequences of the individual duplexes comprising each pool are as follows: human p62/SQSTM1 (L-010230-00): 5'-GAACAGAUAGGAGUCGGAUA-3', 5'-GCAUUGAAGUUGAUUCGA-3', 5'-CCACAGGCUGAAGG AAGC-3', and 5'-GGACCCAUUCUGUCUCAA-3'; human NBR1 (L-010522-00): 5'-GAGAACAAGUGGUUAACGA-3', 5'-CCACAU GACAGUCCUUUA-3', 5'-GAACGUUAUCUCCAUUG-3', and 5'-AGAAGCCACUUGCACAUA-3'; human OPTN (L-016269-00): 5'-GGGUCAGAUAGGAAGUUUA-3', 5'-CCAUGAAGCUAAAUAUCA-3', 5'-CUUGCAACUGAGGAGUUA-3', and 5'-CUAUGGCCUUGAGUCAUG-3'; human CALCOCO2/NDP52 (L-010637-00): 5'-GGAAACCCAUUUCUGGUA-3', 5'-GGAUUGGAUUGGCAUCUUU-3', 5'-GGACGUCACAUGUCAUUUAU-3', and 5'-GGAAGACAACCCGUGAGUA-3'; and nontargeting control (D-001810-10): 5'-UGGUUUACAUGUCGACUA-3', 5'-UGGUUUACAUGUUUCUGA-3', and 5'-UGGUUUACAUGUUUCCUA-3'.

The Amaxa Nucleofector device (Lonza) was used to electro-porate cells using program T-024 and nucleofector kit V according to manufacturer's instructions.

Antibodies, immunoblotting, immunoprecipitation, and immunofluorescence

The following antibodies were used for immunoblotting: goat anti-ATG7 for human (sc-8668, 1:200; Santa Cruz Biotechnology, Inc.), rabbit anti-ATG12 for human (2010, 1:500; Cell Signaling), rabbit anti-ATG7 for mouse (2631, 1:500; Cell Signaling), rabbit anti-ATG12 for mouse (2011, 1:500; Cell Signaling), guinea pig anti-p62/SQSTM1 (GP62-C, 1:1,000; Progen Biotechnik), mouse anti-NBR1 (H00004077-A01, 1:500; Abnova), rabbit anti-OPTN (ab23666, 1:1,000; Abcam), rabbit anti-CALCOCO2/NDP52 (ab68588, 1:500; Abcam), mouse anti-GFP (390394, 1:500; Santa Cruz Biotechnology, Inc.), mouse anti-paxillin (610051, 1:1,000; BD Biosciences), mouse anti-FAK (610087, 1:500; BD Biosciences), mouse anti-vinculin (V9131, 1:1,000; Sigma-Aldrich), mouse anti-zyxin (H00007791-M01, 1:500; Abnova), mouse anti-TUBA (T6199, 1:5,000; Sigma Aldrich), and mouse anti-GAPDH (AB2302, 1:5,000; Millipore). A rabbit polyclonal antibody against MAP1LC3 has been previously described (Fung et al., 2008) and is now commercially available (ABC232, 1:1,000; Millipore).

For immunoblot analysis, cells were lysed in RIPA buffer (1% Triton X-100, 1% sodium deoxycholate, 0.1% SDS, 25 mM Tris, pH 7.6, and 150 mM NaCl) plus protease inhibitor cocktail (Sigma-Aldrich), 10 mM NaF, 10 mM β -glycerophosphate, 1 mM Na_2VO_4 , 10 nM calyculin A, 0.5 mM PMSF, 10 $\mu\text{g}/\text{ml}$ E64d, and 10 $\mu\text{g}/\text{ml}$ pepstatin A. Lysates were freeze-thawed at -80°C , cleared by centrifugation for 30 min at 4°C , boiled in sample buffer, resolved by SDS-PAGE, and transferred to polyvinylidene fluoride membrane. Membranes were blocked for 1 h in 5% milk in PBS with 0.1% Tween 20, incubated in primary antibody overnight at 4°C , washed, incubated for 1 h at RT with HRP-conjugated goat secondary antibodies (1:5,000; Jackson ImmunoResearch Laboratories), washed, and visualized via enhanced chemiluminescence (Thermo Fisher Scientific).

For immunoprecipitation, cells expressing GFP or GFP-NBR1 were sparsely plated on fibronectin-coated (10 $\mu\text{g}/\text{ml}$ in PBS) dishes and were lysed in nondenaturing lysis buffer (1% Triton X-100, 25 mM Tris HCl, pH 7.4, and 150 mM NaCl) plus protease inhibitor cocktail (Sigma-Aldrich), 10 mM N-ethylmaleimide, 10 mM NaF, 10 mM

β -glycerophosphate, 1 mM Na_2VO_4 , 10 nM calyculin A, 0.5 mM PMSF, 10 $\mu\text{g}/\text{ml}$ E64d, and 10 $\mu\text{g}/\text{ml}$ pepstatin A. Lysates were precleared with protein A/G beads (Santa Cruz Biotechnology, Inc.) and normal rabbit IgG (Santa Cruz Biotechnology, Inc.) at 4°C and incubated overnight with rabbit anti-GFP primary antibody (ab6556; Abcam; 1 $\mu\text{g}/200$ –300 μg lysate) at 4°C . Immune complexes were captured by incubation with protein A/G beads for 4 h at 4°C and then washed six times with PBS plus inhibitors, eluted with sample buffer, and analyzed by immunoblotting. For immunoblot analysis of paxillin from anti-GFP immunoprecipitates, rat anti-mouse HRP TrueBlot (18-8817-33, 1:1,000; Rockland Immunochemicals) was used.

For immunofluorescence, mouse anti-paxillin (610619, 1:200; BD Biosciences) and rabbit anti-NBR1 (71703, 1:200; Novus) were used. Alexa Fluor 488-conjugated phalloidin (A12379, 1:200; Life Technologies) was used for imaging the F-actin cytoskeleton. Cells were fixed with 4% PFA for 20 min at RT, permeabilized with 0.5% Triton X-100 in PBS, rinsed with PBS-glycine, and blocked overnight at 4°C in blocking buffer (10% goat serum and 0.2% Triton X-100 in PBS). Cells were incubated with primary antibodies for 1 h at RT, washed, incubated with Alexa Fluor 488 or 594 goat secondary antibodies (1:500; Life Technologies) for 40 min at RT, washed, and mounted using Prolong Gold Anti-Fade mounting medium (Life Technologies).

Microscopy

For all live-cell imaging and static images of cells during wound healing, cells were imaged in the assay media described for scratch wound-healing migration assay. For cells expressing paxillin-mTurquoise, phenol red-free DMEM/F12 was used to prepare assay media. Fixed specimens for immunofluorescence and SIM were mounted with hard-set Prolong Gold Anti-Fade mounting medium for imaging. Fixed cells for cell spreading assays were imaged in PBS.

Static phase contrast and epifluorescence images were obtained at ambient temperature using an Axiovert 200 microscope (Carl Zeiss) with a 10 \times (NA, 0.25) or 20 \times (NA, 0.4) objective, Spot RT camera (Diagnostic Instruments), and mercury lamp (for ZsGreen). Images were acquired using MetaMorph software (v6.0; Molecular Devices). Phase-contrast microscopy time-lapse sequences were acquired on a TE 2000-inverted microscope stand (Nikon) with a CoolSNAP HQ2 scientific grade interline charge coupled device camera (Photometrics) and a 40 \times (NA, 0.6) objective (CFI Plan Fluor ELWD DM; Nikon) housed in an environmentally controlled chamber at 37°C . Microscope hardware and image acquisition were controlled by NIS-Elements software (Nikon).

Spinning disk confocal imaging was performed as previously described (Stehbens et al., 2014; Stehbens and Wittmann, 2014) using an environmentally controlled TI-inverted microscope stand (Nikon) equipped with a Borealis-modified Yokogawa CSU-X1 confocal head (Spectral Applied Research), solid-state 442-nm (for mTurquoise), 488-nm (for GFP, ZsGreen, and Alexa Fluor 488), 515-nm (for Venus), and 561-nm (for mCherry and Alexa Fluor 594) lasers, and a Clara cooled scientific-grade interline CCD camera (Andor) or a CoolSNAP MYO cooled scientific-grade CCD camera (Photometrics). Intracellular fluorescent-tagged protein dynamics in live cells were imaged at 37°C using a 60 \times (NA, 1.49; oil) objective (CFI Apochromat TIRF; Nikon), and immunofluorescence images were acquired at 37°C using a 100 \times (NA, 1.49; oil) objective (CFI Apochromat; Nikon). Live-cell spreading of ZsGreen cells was imaged at 37°C using a 10 \times (NA, 0.45) objective (CFI Plan Apochromat; Nikon). TIRF microscopy of live cells was performed at 37°C on the same Nikon TI-inverted microscope stand equipped with a motorized TIRF illuminator (Nikon) and an iXon electron-multiplying CCD camera (Andor). TIRF images were acquired using a 100 \times objective

(NA, 1.49; oil), with 1.5× intermediate magnification. Microscope hardware was controlled with NIS-Elements.

Super-resolution SIM was performed on a Ti-E-inverted microscope stand (Nikon) with 488-nm (for GFP) and 561-nm (for mCherry) lasers and an iXon DU-897 electron multiplying CCD camera (Andor). Imaging was performed on fixed samples at ambient temperature using a 100× (NA, 1.49; oil) objective (CFI Achromat; Nikon). Microscope hardware was controlled with NIS-Elements.

For analysis of all microscopy images, raw image data were used. Details of image analysis for each experimental technique and image processing for presentation are described in the following sections.

Scratch-wound healing migration assay

For assessment of wound closure by different cell types, monolayers were grown to confluency and incubated in the following media: assay media supplemented with 5 ng/ml EGF for wild-type MCF10A cells, DMEM with 2% FBS, 50 ng/ml EGF, penicillin, and streptomycin for PyMT cells, and DMEM supplemented with 2% FBS, penicillin, and streptomycin for iBMK cells. The proliferation inhibitor mitomycin C (1 μg/ml) was added to the cultures during assays. Confluent monolayers were wounded using a 200-μl pipette tip, washed several times to remove cell debris, and imaged at time of wounding (0 h) and the indicated time points. Wound widths were determined using MetaMorph software and were taken as the mean of six to nine measurements across the wound; to account for differences in starting wound width, data are reported as the decrease in wound width calculated by subtracting the final width from the initial width.

For live-cell phase contrast imaging of migrating MCF10A-Ras cells, cells were grown to confluency on 3.5-cm glass bottom dishes (Mattek), incubated in assay media, and wounded. Image fields were randomly chosen along the length of the wound, and images were acquired every 3 min for 3 h. Single-cell tracking analysis was performed in NIS-Elements by randomly choosing one to two cells per image field and using the “Tracking” feature to manually track cell nucleoli (discerned as dark spots in the nucleus) for each frame over the time course; time and position data were then used to create single-cell migration paths and calculate migration speed as the total distance traveled divided by total time ($dt_j - t_0$) for each cell over 3 h.

Cell-spreading assay

Coverslips in 24-well dishes and glass bottom six-well dishes (Mattek) were prepared by coating overnight at 4°C with 10 μg/ml fibronectin in PBS and then blocking with 1% BSA in DMEM/F12 for 30 min at 37°C. Subconfluent monolayers of MCF10A-Ras cells expressing ZsGreen were incubated overnight in assay media, harvested with fresh aliquots of 0.05% trypsin/EDTA diluted 1:1 with PBS, and sparsely plated in assay media. To synchronize attachment and initiation of spreading, plates were spun at 300 rpm in a swinging bucket rotor for 5 min immediately on plating cells. For live-cell confocal imaging of spreading, cells in six-well dishes were imaged every 5 min for 3 h. Cells on coverslips were incubated for 1 h, fixed in 4% PFA for 20 min at RT, and stored in PBS for imaging; epifluorescence images of fixed ZsGreen-expressing cells were used to quantify cell area using ImageJ (National Institutes of Health) by manually outlining cell borders. For each experiment, two coverslips per condition were plated, and four random fields per coverslip were imaged. All cells entirely present in each image field were measured.

FA size analysis

MCF10A-Ras cells were plated at confluency in assay media on coverslips coated with 10 μg/ml fibronectin, wounded, and fixed 4–6 h after wounding for anti-paxillin immunostaining. Confocal images of migrating

cells were acquired randomly along the wound edge, and FAs at the leading edge of cells were manually outlined for area measurements using NIS-Elements. FAs from one to three cells were measured in each field, and the mean area of FAs per field was determined and plotted.

FA turnover assay and analysis

Analysis of dynamic FA turnover in live cells was performed as previously described (Stehbens et al., 2014; Stehbens and Wittmann, 2014). In brief, MCF10A-Ras cells expressing paxillin-mCherry were plated at confluency in assay media on 3.5-cm glass bottom dishes coated with 10 μg/ml fibronectin and wounded. 15–25 image fields were taken along the wound edge, and cells were imaged every 2–3 min for 1.5–3 h. For analysis, FAs were randomly chosen, and three to five FAs were measured per cell; only FAs that could be tracked completely from their appearance through disappearance were measured. To track FAs, the Bezier ROI tool was used to manually outline individual FAs and was redrawn in each frame as necessary over time if the FA significantly changed in size or location. The “Time Measurement” feature in NIS-Elements was used to generate fluorescence intensity data for each tracked FA, and background intensity was similarly determined using a duplicated region of interest placed adjacent to the FA. Background corrected intensity data were smoothed with a three-frame running mean and plotted against time. Smoothed fluorescence intensity curve plots were used to calculate FA assembly rate constant, disassembly rate constant, and lifetime by curve fitting in Excel (Microsoft). Assembly was determined by curve fitting the initial portion of the intensity plot during which fluorescence intensity steadily increases (when the FA is assembling) with a logistic function (Fig. 2 B, green line). Disassembly was determined by curve fitting the latter portion of the intensity plot when fluorescence intensity is decreasing (FA disassembly) with an exponential function (Fig. 2 B, red line). Rate constants for each parameter were obtained from these functions for each FA. The assembly and disassembly curve fits were also used to calculate FA lifetime, the time during which fluorescence intensity remained above half of the maximum intensity value (Fig. 2 B, double black arrow).

Analysis of GFP-LC3 and GFP-NBR1 targeting to FAs in live cells

MCF10A-Ras cells coexpressing GFP-LC3 and paxillin-mCherry were imaged every 3 min during migration as described under FA turnover assay and analysis. For enumeration of GFP-LC3 targeting to FAs, 5–10 FAs were first randomly chosen per cell independent of the GFP channel, and then, the number of GFP-LC3 vesicles that associated with each FA was counted. Note that targeting was strictly defined as observable physical contact of GFP-LC3 vesicles with FAs (Fig. 4 B). Multiple targeting events were counted if the FA was targeted more than once over its lifetime or by multiple vesicles at the same time. Then, FAs were tracked and measured as described in FA turnover assay and analysis for generation of paxillin-mCherry fluorescence intensity plots to delineate assembly, stability, and disassembly phases of each targeted FA to determine the phase during which GFP-LC3 targeting events occurred. Qualitative live-cell analysis of GFP-LC3 association with dynamic FAs during spreading was performed by imaging cells within 30 min of plating at 1-min intervals.

For analysis of enrichment of GFP-LC3 at FAs, three random frames per time lapse were chosen for each cell, and GFP-LC3 puncta at FAs and in non-FA areas were enumerated in the leading edge region. Total FA area and non-FA areas were manually measured for the leading edge, and the number of puncta per square micrometer FA or non-FA area was determined by dividing the total number of puncta for that region by the total area for that region. GFP-NBR1 enrichment at FAs was quantified in the same manner.

Localization of mCherry-tagged FA proteins to autophagosomes

For two-color imaging of paxillin and autophagosomes, MCF10A-Ras cells stably coexpressing GFP-LC3 and paxillin-mCherry as described for analysis of GFP-LC3 targeting to FAs were used. For two-color imaging of vinculin or zyxin and autophagosomes, MCF10A-Ras cells stably expressing GFP-LC3 were electroporated using the Amaxa nucleofector device as described for RNA interference with mCherry-vinculin or zyxin-mCherry. Cells were plated, wounded, and imaged by spinning disk confocal microscopy as described for FA turnover and analysis, and GFP/mCherry double-positive puncta were identified in migrating cells.

Analysis of Venus-LC3 and mCherry-NBR1 colocalization at FAs

MCF10A-Ras cells stably coexpressing paxillin-mTurquoise, Venus-LC3, and mCherry-NBR1 were plated and imaged by spinning disk confocal microscopy after wounding as described in FA turnover assay and analysis. For analysis, three random frames per time lapse were chosen for each cell. FA-associated Venus-LC3 puncta were identified using the paxillin-mTurquoise and Venus-LC3 channels. Then, the Venus-LC3 and mCherry-NBR1 channels were used to count the number of FA-associated Venus-LC3 puncta that were also mCherry-NBR1 positive.

Image processing

All image analysis was performed on raw image data; however, for presentation purposes, images were processed using established methods (Stehbens et al., 2014). In NIS-Elements, 14-bit spinning disk confocal microscopy time-lapse sequences of paxillin-mCherry were corrected for photobleaching over time using the "Equalize Intensity in Time" tool, and reduction of pixel noise and enhancement of contrast were performed using a low-pass filter and unsharp mask, respectively. Images were then linearly adjusted as needed for brightness and contrast and converted to 8 bit. "Complement Colors" was used to contrast invert images for visualization of black FAs on a white background. Throughout the figures, leading edge inset areas were cropped and rotated for closer visualization of FA dynamics.

To generate two-color black/magenta images as previously described (Stehbens et al., 2014) of GFP-LC3 and paxillin-mCherry or GFP-NBR1 and paxillin-mCherry, the GFP and mCherry channels were first separated and processed individually to 8-bit images as detailed for single-color time-lapse sequences of paxillin-mCherry. Next, the images were added using ND Image Arithmetics: GFP + mCherry, and subsequently combined by merging channels (red: GFP, green: GFP + mCherry (from ND Arithmetics), and blue: GFP). The merged image was then contrast inverted using "Complement Colors" to create black/magenta overlays with magenta FAs and black vesicles on a white background.

Two-color immunofluorescence (Alexa Fluor 488/Alexa Fluor 594) and live-cell (GFP/mCherry) images were processed to 8 bit as described for single-color time-lapse sequences of paxillin-mCherry, and green/magenta overlays were created in NIS-Elements using merge channels (red: 561 nm, green: 488 nm, and blue: 561 nm). Three-color (mTurquoise/Venus/mCherry) live-cell images were also processed as described for two-color images in NIS-Elements. Finally, both phase contrast and epifluorescence images were linearly brightened and contrast adjusted to better discern cell bodies and outlines in MetaMorph or ImageJ.

Statistical analysis

All statistical analyses were performed using GraphPad Prism 6 (GraphPad Software). The normality of the distribution of datasets was determined by a Shapiro-Wilk normality test ($P < 0.05$, indicating a

non-normal distribution); for datasets in which the sample size was not large enough ($n \leq 6$) for determination of normality, a normal distribution was assumed. For normal distributions, groups were compared using unpaired *t* test or one-way analysis of variance followed by Tukey post-hoc test for multiple comparisons. For nonparametric statistics, a Mann-Whitney test or Kruskal-Wallis test followed by Dunn's post-hoc test for multiple comparisons was used. $P < 0.05$ was considered to be significant for all tests.

Online supplemental materials

Fig. S1 shows that inhibition of autophagy caused by loss of ATGs impairs migration and leads to enlarged FAs in multiple epithelial cell types. Fig. S2 shows SIM and TIRF imaging of autophagosomes at FAs and presence of mCherry-tagged FA proteins at autophagosomes. Fig. S3 shows validation of RNA interference against autophagy cargo receptors, no changes in basal autophagic flux with NBR1 depletion, and localization of NBR1 to FAs. Fig. S4 shows that loss of NBR1 leads to enhanced cell spreading. Fig. S5 shows interaction of GFP-NBR1 with endogenous FA proteins and representative paxillin-mCherry time-lapse sequences of cells expressing GFP, GFP-NBR1, GFP-NBR1 Δ LR, or GFP-NBR1 Δ UBA. Video 1 shows migration of autophagy-inhibited cells. Videos 2 and 3 show FA dynamics upon autophagy inhibition in migrating cells expressing paxillin-mCherry. Video 4 shows a migrating cell expressing GFP-LC3 and paxillin-mCherry. Videos 5 and 6 show FA dynamics in a migrating cell expressing GFP-LC3 and paxillin-mCherry. Videos 7 and 8 show FA dynamics upon depletion of NBR1 in migrating cells expressing paxillin-mCherry. Video 9 shows the leading edge of a migrating cell expressing GFP-NBR1 and paxillin-mCherry. Online supplemental material is available at <http://www.jcb.org/cgi/content/full/jcb.201503075/DC1>.

Acknowledgments

Confocal and TIRF microscopy and image analysis were performed in the Biological Imaging Development Center at University of California, San Francisco (UCSF). SIM was performed in the Nikon Imaging Center at UCSF. We thank D. Sheppard and N. Reed for advice on spreading adhesion assays.

Grant support to J. Debnath includes National Institutes of Health (CA126792 and CA188404), Department of Defense Breast Cancer Research Program (W81XWH-11-1-0130 and W81XWH-12-1-0505), and Samuel Waxman Cancer Research Foundation. Grant support to T. Wittmann includes National Institutes of Health (GM079139 and S10 RR26758). C.M. Kenific was supported by a National Institutes of Health Predoctoral Fellowship (F31CA167905), and J. Goldsmith is supported by a National Science Foundation Graduate Student Fellowship (DGE-1144247).

The authors declare no competing financial interests.

Author contributions: C.M. Kenific and J. Debnath conceived the study. C.M. Kenific and J. Debnath designed the experiments with input from S.J. Stehbens and T. Wittmann. C.M. Kenific, J. Goldsmith, A.M. Leidal, N. Faure, and J. Ye performed experiments. C.M. Kenific and J. Debnath analyzed the data. S.J. Stehbens and T. Wittmann created analytical tools crucial for quantitative assessment of dynamic FA turnover. C.M. Kenific and J. Debnath wrote the manuscript, with input from the other authors.

Submitted: 16 March 2015

Accepted: 19 January 2016

References

- Birgisdottir, A.B., T. Lamark, and T. Johansen. 2013. The LIR motif - crucial for selective autophagy. *J. Cell Sci.* 126:3237–3247. <http://dx.doi.org/10.1242/jcs.12612>
- Campeau, E., V.E. Ruhl, F. Rodier, C.L. Smith, B.L. Rahmberg, J.O. Fuss, J. Campisi, P. Yaswen, P.K. Cooper, and P.D. Kaufman. 2009. A versatile viral system for expression and depletion of proteins in mammalian cells. *PLoS One*. 4:e6529. <http://dx.doi.org/10.1371/journal.pone.0006529>
- Cavalcanti-Adam, E.A., T. Volberg, A. Micoulet, H. Kessler, B. Geiger, and J.P. Spatz. 2007. Cell spreading and focal adhesion dynamics are regulated by spacing of integrin ligands. *Biophys. J.* 92:2964–2974. <http://dx.doi.org/10.1529/biophysj.106.089730>
- Chan, K.T., D.A. Bennis, and A. Huttenlocher. 2010. Regulation of adhesion dynamics by calpain-mediated proteolysis of focal adhesion kinase (FAK). *J. Biol. Chem.* 285:11418–11426. <http://dx.doi.org/10.1074/jbc.M109.090746>
- Chao, W.T., and J. Kunz. 2009. Focal adhesion disassembly requires clathrin-dependent endocytosis of integrins. *FEBS Lett.* 583:1337–1343. <http://dx.doi.org/10.1016/j.febslet.2009.03.037>
- Corteso, C.L., L.R. Boateng, T.M. Piazza, D.A. Bennis, and A. Huttenlocher. 2011. Calpain-mediated proteolysis of paxillin negatively regulates focal adhesion dynamics and cell migration. *J. Biol. Chem.* 286:9998–10006. <http://dx.doi.org/10.1074/jbc.M110.187294>
- Debnath, J., S.K. Muthuswamy, and J.S. Brugge. 2003. Morphogenesis and oncogenesis of MCF-10A mammary epithelial acini grown in three-dimensional basement membrane cultures. *Methods*. 30:256–268. [http://dx.doi.org/10.1016/S1046-2023\(03\)00032-X](http://dx.doi.org/10.1016/S1046-2023(03)00032-X)
- Deng, S., and C. Huang. 2014. E3 ubiquitin ligases in regulating stress fiber, lamellipodium, and focal adhesion dynamics. *Cell Adhes. Migr.* 8:49–54. <http://dx.doi.org/10.4161/cam.27480>
- Deosaran, E., K.B. Larsen, R. Hua, G. Sargent, Y. Wang, S. Kim, T. Lamark, M. Jauregui, K. Law, J. Lippincott-Schwartz, et al. 2013. NBR1 acts as an autophagy receptor for peroxisomes. *J. Cell Sci.* 126:939–952. <http://dx.doi.org/10.1242/jcs.114819>
- DiMilla, P.A., K. Barbee, and D.A. Lauffenburger. 1991. Mathematical model for the effects of adhesion and mechanics on cell migration speed. *Biophys. J.* 60:15–37. [http://dx.doi.org/10.1016/S0006-3495\(91\)82027-6](http://dx.doi.org/10.1016/S0006-3495(91)82027-6)
- DiMilla, P.A., J.A. Stone, J.A. Quinn, S.M. Albelda, and D.A. Lauffenburger. 1993. Maximal migration of human smooth muscle cells on fibronectin and type IV collagen occurs at an intermediate attachment strength. *J. Cell Biol.* 122:729–737. <http://dx.doi.org/10.1083/jcb.122.3.729>
- Dowdle, W.E., B. Nyfeler, J. Nagel, R.A. Elling, S. Liu, E. Triantafellow, S. Menon, Z. Wang, A. Honda, G. Pardee, et al. 2014. Selective VPS34 inhibitor blocks autophagy and uncovers a role for NCOA4 in ferritin degradation and iron homeostasis in vivo. *Nat. Cell Biol.* 16:1069–1079. <http://dx.doi.org/10.1038/ncb3053>
- Dull, T., R. Zufferey, M. Kelly, R.J. Mandel, M. Nguyen, D. Trono, and L. Naldini. 1998. A third-generation lentivirus vector with a conditional packaging system. *J. Virol.* 72:8463–8471.
- Ezratty, E.J., M.A. Partridge, and G.G. Gundersen. 2005. Microtubule-induced focal adhesion disassembly is mediated by dynamin and focal adhesion kinase. *Nat. Cell Biol.* 7:581–590. <http://dx.doi.org/10.1038/ncb1262>
- Ezratty, E.J., C. Bertaux, E.E. Marcantonio, and G.G. Gundersen. 2009. Clathrin mediates integrin endocytosis for focal adhesion disassembly in migrating cells. *J. Cell Biol.* 187:733–747. <http://dx.doi.org/10.1083/jcb.200904054>
- Feng, Y., D. He, Z. Yao, and D.J. Klionsky. 2014. The machinery of macroautophagy. *Cell Res.* 24:24–41. <http://dx.doi.org/10.1038/cr.2013.168>
- Franco, S.J., M.A. Rodgers, B.J. Perrin, J. Han, D.A. Bennis, D.R. Critchley, and A. Huttenlocher. 2004. Calpain-mediated proteolysis of talin regulates adhesion dynamics. *Nat. Cell Biol.* 6:977–983. <http://dx.doi.org/10.1038/ncb1175>
- Friedl, P., and K. Wolf. 2010. Plasticity of cell migration: a multiscale tuning model. *J. Cell Biol.* 188:11–19. <http://dx.doi.org/10.1083/jcb.200909003>
- Fung, C., R. Lock, S. Gao, E. Salas, and J. Debnath. 2008. Induction of autophagy during extracellular matrix detachment promotes cell survival. *Mol. Biol. Cell.* 19:797–806. <http://dx.doi.org/10.1091/mbc.E07-10-1092>
- Galavotti, S., S. Bartesaghi, D. Faccenda, M. Shaked-Rabi, S. Sanzone, A. McEvoy, D. Dinsdale, F. Condorelli, S. Brandner, M. Campanella, et al. 2013. The autophagy-associated factors DRAM1 and p62 regulate cell migration and invasion in glioblastoma stem cells. *Oncogene*. 32:699–712. <http://dx.doi.org/10.1038/onc.2012.111>
- Gardel, M.L., I.C. Schneider, Y. Aratyn-Schaus, and C.M. Waterman. 2010. Mechanical integration of actin and adhesion dynamics in cell migration. *Annu. Rev. Cell Dev. Biol.* 26:315–333. <http://dx.doi.org/10.1146/annurev.cellbio.011209.122036>
- Geiger, B., and K.M. Yamada. 2011. Molecular architecture and function of matrix adhesions. *Cold Spring Harb. Perspect. Biol.* 3:a005033. <http://dx.doi.org/10.1101/cshperspect.a005033>
- Geiger, T., and R. Zaidel-Bar. 2012. Opening the floodgates: proteomics and the integrin adhesome. *Curr. Opin. Cell Biol.* 24:562–568. <http://dx.doi.org/10.1016/j.cob.2012.05.004>
- Gupton, S.L., and C.M. Waterman-Storer. 2006. Spatiotemporal feedback between actomyosin and focal-adhesion systems optimizes rapid cell migration. *Cell*. 125:1361–1374. <http://dx.doi.org/10.1016/j.cell.2006.05.029>
- Hu, K., L. Ji, K.T. Applegate, G. Danuser, and C.M. Waterman-Storer. 2007. Differential transmission of actin motion within focal adhesions. *Science*. 315:1111–1115. <http://dx.doi.org/10.1126/science.1135085>
- Huttenlocher, A., M.H. Ginsberg, and A.F. Horwitz. 1996. Modulation of cell migration by integrin-mediated cytoskeletal linkages and ligand-binding affinity. *J. Cell Biol.* 134:1551–1562. <http://dx.doi.org/10.1083/jcb.134.6.1551>
- Itakura, E., and N. Mizushima. 2011. p62 Targeting to the autophagosome formation site requires self-oligomerization but not LC3 binding. *J. Cell Biol.* 192:17–27. <http://dx.doi.org/10.1083/jcb.201009067>
- Johansen, T., and T. Lamark. 2011. Selective autophagy mediated by autophagic adapter proteins. *Autophagy*. 7:279–296. <http://dx.doi.org/10.4161/aut.7.3.14487>
- Kirkin, V., T. Lamark, Y.S. Sou, G. Bjørkøy, J.L. Nunn, J.A. Bruun, E. Shvets, D.G. McEwan, T.H. Clausen, P. Wild, et al. 2009. A role for NBR1 in autophagosomal degradation of ubiquitinated substrates. *Mol. Cell*. 33:505–516. <http://dx.doi.org/10.1016/j.molcel.2009.01.020>
- Kitamura, T., Y. Koshino, F. Shibata, T. Oki, H. Nakajima, T. Nosaka, and H. Kumagai. 2003. Retrovirus-mediated gene transfer and expression cloning: powerful tools in functional genomics. *Exp. Hematol.* 31:1007–1014. [http://dx.doi.org/10.1016/S0301-472X\(03\)00260-1](http://dx.doi.org/10.1016/S0301-472X(03)00260-1)
- Koyama-Honda, I., E. Itakura, T.K. Fujiwara, and N. Mizushima. 2013. Temporal analysis of recruitment of mammalian ATG proteins to the autophagosome formation site. *Autophagy*. 9:1491–1499. <http://dx.doi.org/10.4161/aut.25529>
- Kraft, C., M. Peter, and K. Hofmann. 2010. Selective autophagy: ubiquitin-mediated recognition and beyond. *Nat. Cell Biol.* 12:836–841. <http://dx.doi.org/10.1038/ncb0910-836>
- Kuo, T.C., C.T. Chen, D. Baron, T.T. Onder, S. Loewer, S. Almeida, C.M. Weismann, P. Xu, J.M. Houghton, F.B. Gao, et al. 2011. Midbody accumulation through evasion of autophagy contributes to cellular reprogramming and tumorigenicity. *Nat. Cell Biol.* 13:1214–1223. <http://dx.doi.org/10.1038/ncb2332>
- Lange, S., F. Xiang, A. Yakovenko, A. Vihola, P. Hackman, E. Rostkova, J. Kristensen, B. Brandmeier, G. Franzen, B. Hedberg, et al. 2005. The kinase domain of titin controls muscle gene expression and protein turnover. *Science*. 308:1599–1603. <http://dx.doi.org/10.1126/science.1110463>
- Lock, R., C.M. Kenific, A.M. Leidal, E. Salas, and J. Debnath. 2014. Autophagy-dependent production of secreted factors facilitates oncogenic RAS-driven invasion. *Cancer Discov.* 4:466–479. <http://dx.doi.org/10.1158/2159-8290.CD-13-0841>
- Mancias, J.D., X. Wang, S.P. Gygi, J.W. Harper, and A.C. Kimmelman. 2014. Quantitative proteomics identifies NCOA4 as the cargo receptor mediating ferritinophagy. *Nature*. 509:105–109. <http://dx.doi.org/10.1038/nature13148>
- Martin, M.D., K.J. Carter, S.R. Jean-Philippe, M. Chang, S. Mobashery, S. Thiolloy, C.C. Lynch, L.M. Matrisian, and B. Fingleton. 2008. Effect of ablation or inhibition of stromal matrix metalloproteinase-9 on lung metastasis in a breast cancer model is dependent on genetic background. *Cancer Res.* 68:6251–6259. <http://dx.doi.org/10.1158/0008-5472.CAN-08-0537>
- Mathew, R., K. Degenhardt, L. Haramaty, C.M. Karp, and E. White. 2008. Immortalized mouse epithelial cell models to study the role of apoptosis in cancer. *Methods Enzymol.* 446:77–106. [http://dx.doi.org/10.1016/S0076-6879\(08\)01605-4](http://dx.doi.org/10.1016/S0076-6879(08)01605-4)
- Meenderink, L.M., L.M. Ryzhova, D.M. Donato, D.F. Gochberg, I. Kaverina, and S.K. Hanks. 2010. P130Cas Src-binding and substrate domains have distinct roles in sustaining focal adhesion disassembly and promoting cell migration. *PLoS One*. 5:e13412. <http://dx.doi.org/10.1371/journal.pone.0013412>
- Müller, S., I. Kursula, P. Zou, and M. Wilmanns. 2006. Crystal structure of the PB1 domain of NBR1. *FEBS Lett.* 580:341–344. <http://dx.doi.org/10.1016/j.febslet.2005.12.021>
- Murrow, L., and J. Debnath. 2013. Autophagy as a stress-response and quality-control mechanism: implications for cell injury and human disease. *Annu. Rev. Pathol.* 8:105–137. <http://dx.doi.org/10.1146/annurev-pathol-020712-163918>

- Ory, D.S., B.A. Neugeboren, and R.C. Mulligan. 1996. A stable human-derived packaging cell line for production of high titer retrovirus/vesicular stomatitis virus G pseudotypes. *Proc. Natl. Acad. Sci. USA*. 93:11400–11406. <http://dx.doi.org/10.1073/pnas.93.21.11400>
- Palecek, S.P., J.C. Loftus, M.H. Ginsberg, D.A. Lauffenburger, and A.F. Horwitz. 1997. Integrin-ligand binding properties govern cell migration speed through cell-substratum adhesiveness. *Nature*. 385:537–540. <http://dx.doi.org/10.1038/385537a0>
- Pohl, C., and S. Jentsch. 2009. Midbody ring disposal by autophagy is a post-abscission event of cytokinesis. *Nat. Cell Biol.* 11:65–70. <http://dx.doi.org/10.1038/ncb1813>
- Ridley, A.J., M.A. Schwartz, K. Burridge, R.A. Firtel, M.H. Ginsberg, G. Borisy, J.T. Parsons, and A.R. Horwitz. 2003. Cell migration: integrating signals from front to back. *Science*. 302:1704–1709. <http://dx.doi.org/10.1126/science.1092053>
- Rogov, V., V. Dötsch, T. Johansen, and V. Kirkin. 2014. Interactions between autophagy receptors and ubiquitin-like proteins form the molecular basis for selective autophagy. *Mol. Cell*. 53:167–178. <http://dx.doi.org/10.1016/j.molcel.2013.12.014>
- Schiller, H.B., and R. Fassler. 2013. Mechanosensitivity and compositional dynamics of cell-matrix adhesions. *EMBO Rep.* 14:509–519. <http://dx.doi.org/10.1038/embor.2013.49>
- Shi, F., and J. Sottile. 2011. MT1-MMP regulates the turnover and endocytosis of extracellular matrix fibronectin. *J. Cell Sci.* 124:4039–4050. <http://dx.doi.org/10.1242/jcs.087858>
- Stehbens, S.J., and T. Wittmann. 2014. Analysis of focal adhesion turnover: a quantitative live-cell imaging example. *Methods Cell Biol.* 123:335–346. <http://dx.doi.org/10.1016/B978-0-12-420138-5.00018-5>
- Stehbens, S.J., M. Paszek, H. Pemble, A. Eitinger, S. Gierke, and T. Wittmann. 2014. CLASPs link focal-adhesion-associated microtubule capture to localized exocytosis and adhesion site turnover. *Nat. Cell Biol.* 16:561–573. <http://dx.doi.org/10.1038/ncb2975>
- Tuloup-Minguez, V., A. Hamañ, A. Greffard, V. Nicolas, P. Codogno, and J. Botti. 2013. Autophagy modulates cell migration and $\beta 1$ integrin membrane recycling. *Cell Cycle*. 12:3317–3328. <http://dx.doi.org/10.4161/cc.26298>
- Waters, S., K. Marchbank, E. Solomon, C. Whitehouse, and M. Gantel. 2009. Interactions with LC3 and polyubiquitin chains link nbr1 to autophagic protein turnover. *FEBS Lett.* 583:1846–1852. <http://dx.doi.org/10.1016/j.febslet.2009.04.049>
- Webb, D.J., K. Donais, L.A. Whitmore, S.M. Thomas, C.E. Turner, J.T. Parsons, and A.F. Horwitz. 2004. FAK-Src signalling through paxillin, ERK and MLCK regulates adhesion disassembly. *Nat. Cell Biol.* 6:154–161. <http://dx.doi.org/10.1038/ncb1094>
- Welm, B.E., G.J. Dijkgraaf, A.S. Bledau, A.L. Welm, and Z. Werb. 2008. Lentiviral transduction of mammary stem cells for analysis of gene function during development and cancer. *Cell Stem Cell*. 2:90–102. <http://dx.doi.org/10.1016/j.stem.2007.10.002>
- Whitehouse, C., J. Chambers, K. Howe, M. Cobourne, P. Sharpe, and E. Solomon. 2002. NBR1 interacts with fasciculation and elongation protein zeta-1 (FEZ1) and calcium and integrin binding protein (CIB) and shows developmentally restricted expression in the neural tube. *Eur. J. Biochem.* 269:538–545. <http://dx.doi.org/10.1046/j.0014-2956.2001.02681.x>
- Winograd-Katz, S.E., R. Fassler, B. Geiger, and K.R. Legate. 2014. The integrin adhesome: from genes and proteins to human disease. *Nat. Rev. Mol. Cell Biol.* 15:273–288. <http://dx.doi.org/10.1038/nrm3769>
- Wolfenson, H., I. Lavelin, and B. Geiger. 2013. Dynamic regulation of the structure and functions of integrin adhesions. *Dev. Cell*. 24:447–458. <http://dx.doi.org/10.1016/j.devcel.2013.02.012>
- Zhan, Z., X. Xie, H. Cao, X. Zhou, X.D. Zhang, H. Fan, and Z. Liu. 2014. Autophagy facilitates TLR4- and TLR3-triggered migration and invasion of lung cancer cells through the promotion of TRAF6 ubiquitination. *Autophagy*. 10:257–268. <http://dx.doi.org/10.4161/autophagy.27162>

Supplemental material

JCB

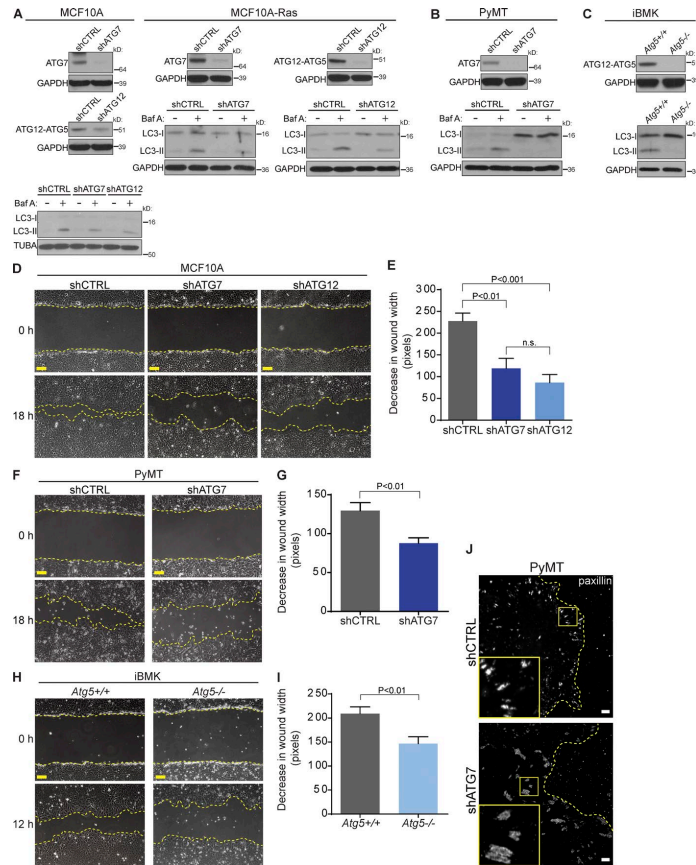
Kenific et al., <http://www.jcb.org/cgi/content/full/jcb.201503075/DC1>

Figure S1. Autophagy enables migration of multiple cell types. (A) Stable shRNA-mediated depletion of ATG7 or ATG12 inhibits autophagy in wild-type MCF10A (left) and MCF10A-Ras (right) cells. ATG12 knockdown results in decrease of the ATG12-ATG5 complex required for autophagosome formation. Autophagy inhibition in ATG7- or ATG12-depleted cells shown by reduced LC3-II turnover in the presence versus absence of the lysosomal inhibitor bafilomycin A (Baf A, 20 nM for 30 min). GAPDH or α -tubulin used as loading control. (B) shRNA-mediated depletion of ATG7 inhibits autophagy in PyMT cells. LC3-II turnover was assessed as in A. GAPDH is the loading control. (C) Absence of ATG12-ATG5 and loss of autophagy (LC3-II) in iBMK cells derived from *Atg5^{-/-}* mice but not *Atg5^{+/+}* controls. GAPDH used as loading control. (D) Representative phase-contrast microscopy images of MCF10A cells expressing indicated shRNAs at time of wounding (0 h) and at 18 h. Dashed yellow lines highlight wound boundaries. Bars, 100 μ m. (E) Quantification of wound closure over 18 h for MCF10A cells. Decrease in wound width determined by subtracting the final width at 18 h from the initial width at 0 h. Bar graph shows mean \pm SEM, representing $n = 12$ wounds for shCTRL, $n = 12$ wounds for shATG7, and $n = 8$ wounds for shATG12 pooled from six independent experiments. P-values determined using a one-way analysis of variance followed by Tukey post-hoc test. n.s., not significant. (F) Representative phase-contrast microscopy images of PyMT cells expressing shCTRL or shATG7 at time of wounding (0 h) and 18 h. Dashed yellow lines highlight wound boundaries. Bars, 100 μ m. (G) Quantification of wound closure over 18 h for PyMT cells. Bar graph shows mean \pm SEM, representing $n = 16$ wounds for shCTRL and $n = 20$ wounds for shATG7 pooled from eight independent experiments. P-value determined using unpaired *t* test. (H) Representative phase-contrast microscopy images of *Atg5^{+/+}* and *Atg5^{-/-}* iBMK cells at time of wounding (0 h) and 12 h. Dashed yellow lines highlight wound boundaries. Bars, 100 μ m. (I) Quantification of wound closure over 12 h for iBMK cells. Bar graph shows mean \pm SEM, representing $n = 10$ wounds each for *Atg5^{+/+}* and *Atg5^{-/-}* pooled from four independent experiments. P-value determined using unpaired *t* test. (J) Representative immunofluorescence images of wound edge PyMT cells expressing shCTRL (top) or shATG7 (bottom) stained for endogenous paxillin to mark FAs. Cell edges outlined with dotted yellow line. Enlarged insets of boxed regions are shown. Bars, 5 μ m. Insets are magnified 3.3-fold.

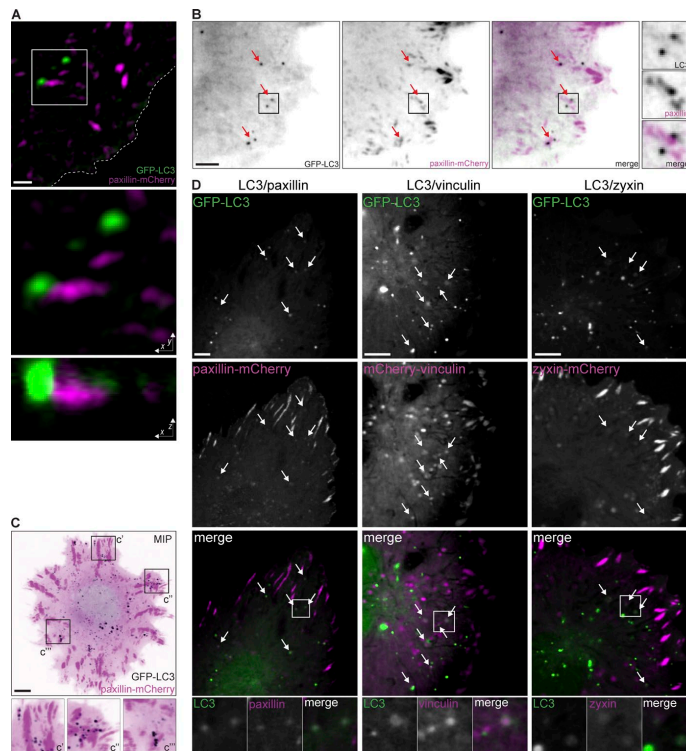


Figure S2. **Autophagosomes localize to FAs.** (A) Super-resolution SIM imaging of wound edge cells expressing GFP-LC3 to mark autophagosomes and paxillin-mCherry to mark FAs. Middle and bottom panels show x-y and x-z images of inset in boxed region, respectively. Bar, 1 μ m. Insets are magnified threefold. (B) TIRF microscopy of wound edge cells expressing GFP-LC3 (black in merged image) and paxillin-mCherry (magenta in merged image). Red arrows in whole-cell images show autophagosomes localized to FAs. Right-most panel shows single-channel and merged insets of boxed region. Bar, 5 μ m. Insets are magnified 2.4-fold. (C) Spinning disk confocal microscopy of a spreading cell expressing GFP-LC3 (black) and paxillin-mCherry (magenta). Top panel shows MIP of a cell over 40 min to show autophagosomes near dynamic FAs throughout the cell periphery during spreading. Boxed inset areas are shown enlarged at bottom. Bar, 5 μ m. Insets are magnified 2.2-fold. (D) Spinning disk confocal microscopy of cells expressing GFP-LC3 and paxillin-mCherry (left), mCherry-vinculin (middle), or zyxin-mCherry (right). White arrows in whole-cell images indicate GFP-positive and mCherry-positive puncta. Bottom panel shows single-channel and merged insets of boxed region. Bars, 5 μ m. Insets for LC3/paxillin are magnified 3.2-fold, and insets for LC3/vinculin and LC3/zyxin are magnified 2.7-fold.

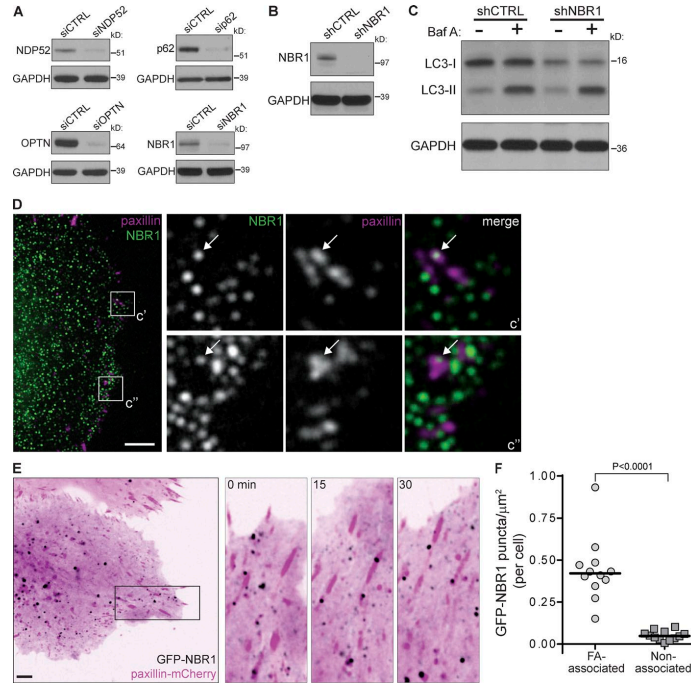


Figure S3. Regulation of migration and FAs by the autophagy cargo receptor NBR1. (A) siRNA-mediated depletion of the indicated autophagy cargo receptors used for scratch-wound closure assays. GAPDH is loading control. (B) shRNA knockdown of NBR1. GAPDH is loading control. (C) LC3-II turnover in the absence or presence of bafilomycin A (Baf A, 20 nM for 30 min). GAPDH is loading control. (D) Representative immunofluorescence images of wound edge cells stained for endogenous paxillin (magenta) to mark FAs and endogenous NBR1 (green). Whole-cell merged image shown at left, and enlarged boxed insets of merged and single-channel paxillin and NBR1 images shown at right. Arrow points to colocalization in insets. Bar, 5 μm . Insets are magnified 4.9-fold. (E) Spinning disk confocal microscopy of a migrating cell expressing GFP-NBR1 (black) and paxillin-mCherry (magenta). Boxed region is shown as enlarged insets to the right, rotated such that the cell edge is moving upward vertically. Elapsed time (min) indicated in top left of images. Bar, 5 μm . Insets are magnified 2.4-fold. These images correspond to Video 9. (F) Analysis of GFP-NBR1 in FA areas and non-FA areas at the leading edge of migrating cells. Total GFP-NBR1 puncta at FAs or in non-FA areas was counted and normalized to the total area for FA or non-FA regions, respectively. Scatter plot shows individual single cells ($n = 12$ total cells) and median (line), representing 963 total leading edge GFP-NBR1 puncta analyzed from two independent experiments. P-value calculated using a nonparametric Mann-Whitney test.

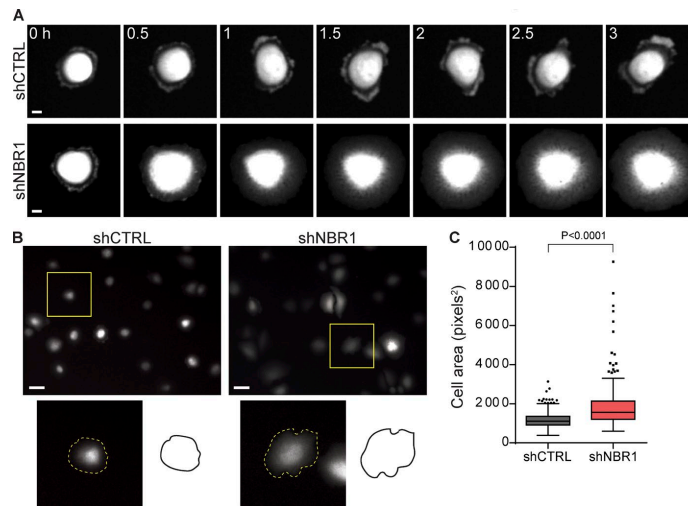


Figure S4. NBR1 knockdown leads to enhanced cell spreading. (A) Spinning disk confocal microscopy time-lapse sequences of cells expressing ZsGreen during spreading after replating. Representative images of shCTRL (top) and shNBR1 (bottom) cells are shown over 3 h. Elapsed time (h) indicated at top left. Bars, 10 μ m. (B) Representative images of ZsGreen-labeled cells fixed at 1 h after replating. Whole-field images shown with boxed insets of individual cells enlarged at bottom left. Tracing of individual cell in inset at bottom right. Bars, 50 μ m. Insets are magnified 2.4-fold. (C) Quantification of area of shCTRL- and shNBR1-expressing cells fixed 1 h after replating. Area determined by manually outlining individual ZsGreen-expressing cell borders. Data presented as median (line), first and third quartile (box), and whiskers extend to ± 1.5 times the interquartile range. Individual data points outside of this range are shown. $n = 211$ cells for shCTRL and $n = 195$ cells for shNBR1, pooled from two independent experiments. These experiments were run in conjunction with two out of the three experimental repeats in Fig. 3 (B and C); therefore, quantitative data for shCTRL from those experiments are also included as part of Fig. S3 C. P-values were calculated using a nonparametric Mann-Whitney test.

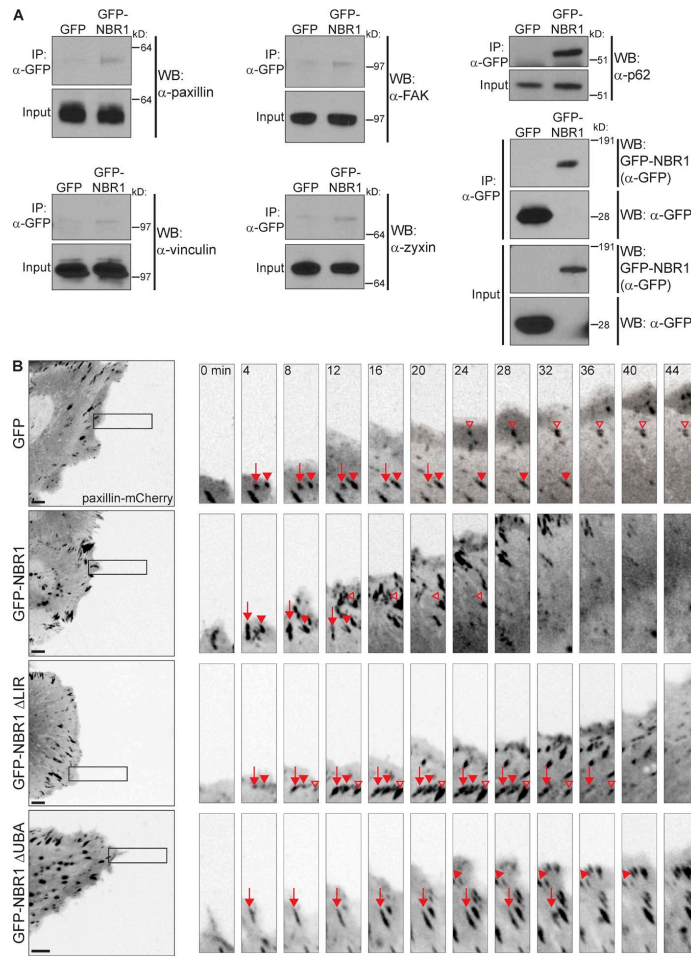
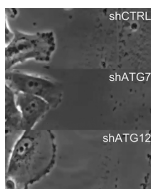
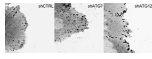


Figure S5. NBR1 interacts with FA proteins and promotes FA disassembly. (A) Cells stably expressing GFP or GFP-NBR1 were lysed, immunoprecipitated (IP) with anti-GFP, and immunoblotted (WB) with the indicated antibodies. (B) Spinning disk confocal microscopy time-lapse sequences of paxillin-mCherry-labeled FAs (black) in migrating cells. Left panels show representative cells expressing GFP control, GFP-NBR1, GFP-NBR1 Δ LIR, or GFP-NBR1 Δ UBA. Image sequences of boxed regions on the right have been rotated such that the cell edge with dynamic FAs is moving upward vertically. Arrows, closed arrowheads, and open arrowheads track individual FAs over time. Elapsed time (min) shown in top left of images. Bars, 5 μ m. Insets are magnified 2.4-fold.



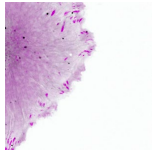
Video 1. Single-cell tracking of migrating shCTRL-, shATG7-, and shATG12-expressing cells. Phase-contrast microscopy of single-cell migration of shCTRL- (top), shATG7- (middle), and shATG12-expressing (bottom) cells. Images were acquired every 3 min. The video plays at 24 frames per second and is accelerated 4,320 times. This video is related to Fig. 1.



Video 2. **FA dynamics in shCTRL-, shATG7-, and shATG12-expressing cells.** Spinning disk confocal microscopy of FA turnover dynamics in shCTRL- (left), shATG7- (middle), and shATG12-expressing (right) cells. FAs are marked by paxillin-mCherry (black). Images were acquired every 2 min. The video plays at 6 frames per second and is accelerated 720 times. This video is related to Fig. 2.



Video 3. **FA dynamics at the leading edge of shCTRL-, shATG7-, and shATG12-expressing cells.** Spinning disk confocal microscopy of FA turnover dynamics at the leading edge of shCTRL- (left), shATG7- (middle), and shATG12-expressing (right) cells. These are insets from the same cells shown in Video 2. FAs are marked by paxillin-mCherry (black). Images were acquired every 2 min. The video plays at 6 frames per second and is accelerated 720 times. This video is related to Fig. 2.



Video 4. **Migrating cell coexpressing GFP-LC3 and paxillin-mCherry.** Spinning disk confocal microscopy of a migrating cell expressing GFP-LC3 (black) to mark autophagosomes and paxillin-mCherry (magenta) to mark FAs. Images were acquired every 3 min. The video plays at 2 frames per second and is accelerated 360 times. This video is related to Fig. 4.



Video 5. **Dynamics of a nontargeted FA.** Spinning disk confocal microscopy of a leading edge nontargeted FA from a cell expressing GFP-LC3 (black) and paxillin-mCherry (magenta). This is an inset from the cell in Video 4. Images were acquired every 3 min. The video plays at 2 frames per second and is accelerated 360 times. This video is related to Fig. 4.



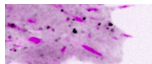
Video 6. **Dynamics of a GFP-LC3-targeted FA.** Spinning disk confocal microscopy of a leading edge GFP-LC3-targeted FA from a cell expressing GFP-LC3 (black) and paxillin-mCherry (magenta). This is an inset from the cell in Video 4. Images were acquired every 3 min. The video plays at 2 frames per second and is accelerated 360 times. This video is related to Fig. 4.



Video 7. **FA dynamics in shCTRL- and shNBR1-expressing cells.** Spinning disk confocal microscopy of FA turnover dynamics in shCTRL- (left) and shNBR1-expressing (right) cells. FAs are marked by paxillin-mCherry (black). Images were acquired every 2 min. The video plays at 6 frames per second and is accelerated 720 times. This video is related to Fig. 5.



Video 8. **FA dynamics at the leading edge of shCTRL- and shNBR1-expressing cells.** Spinning disk confocal microscopy of FA turnover dynamics at the leading edge of shCTRL- (left) and shNBR1-expressing (right) cells. These are insets from the same cells shown in Video 7. FAs are marked by paxillin-mCherry (black). Images were acquired every 2 min. The video plays at 6 frames per second and is accelerated 720 times. This video is related to Fig. 5.



Video 9. **Migrating cell coexpressing GFP-NBR1 and paxillin-mCherry.** Spinning disk confocal microscopy of the leading edge of a migrating cell expressing GFP-NBR1 (black) and paxillin-mCherry (magenta). Images were acquired every 1.5 min. The video plays at 2 frames per second and is accelerated 180 times. This video is related to Fig. S3.

Appendix B

Antitumor adaptive immunity remains intact following inhibition of autophagy and antimalarial treatment

The following appendix is published work

Starobinets, H., Ye, J., Broz, M., Barry, K., **Goldsmith, J.**, Marsh, T., Rostker, F., Krummel, M., Debnath, J.

Contributions: Hanna Starobinets, a former graduate student in the lab, primarily performed the research presented in this paper. Jayanta Debnath supervised the project. I contributed to the collection of tumor and splenocyte material in many of the figures, validated shRNA hairpins in different cell lines, and performed the cell viability assay in Figure S5B. Thank you Hanna for including me in your research!

Antitumor adaptive immunity remains intact following inhibition of autophagy and antimalarial treatment

Hanna Starobinets, Jordan Ye, Miranda Broz, Kevin Barry, Juliet Goldsmith, Timothy Marsh, Fanya Rostker, Matthew Krummel, and Jayanta Debnath

Department of Pathology and Helen Diller Family Comprehensive Cancer Center, UCSF, San Francisco, California, USA.

The rising success of cancer immunotherapy has produced immense interest in defining the clinical contexts that may benefit from this therapeutic approach. To this end, there is a need to ascertain how the therapeutic modulation of intrinsic cancer cell programs influences the anticancer immune response. For example, the role of autophagy as a tumor cell survival and metabolic fitness pathway is being therapeutically targeted in ongoing clinical trials that combine cancer therapies with antimalarial drugs for the treatment of a broad spectrum of cancers, many of which will likely benefit from immunotherapy. However, our current understanding of the interplay between autophagy and the immune response remains incomplete. Here, we have evaluated how autophagy inhibition impacts the antitumor immune response in immune-competent mouse models of melanoma and mammary cancer. We observed equivalent levels of T cell infiltration and function within autophagy-competent and -deficient tumors, even upon treatment with the anthracycline chemotherapeutic doxorubicin. Similarly, we found equivalent T cell responses upon systemic treatment of tumor-bearing mice with antimalarial drugs. Our findings demonstrate that antitumor adaptive immunity is not adversely impaired by autophagy inhibition in these models, allowing for the future possibility of combining autophagy inhibitors with immunotherapy in certain clinical contexts.

Introduction

Autophagy is a tightly regulated cellular program that results in the engulfment and sequestration of cytoplasmic protein and organelle cargo into double-membrane structures termed autophagosomes, which are subsequently delivered to the lysosome for degradation (1). Autophagy occurs both at basal conditions to maintain cellular homeostasis, and in response to environmental stresses such as nutrient starvation or hypoxia. Most studies investigating autophagy in cancer have focused on its cell-intrinsic effects, including aiding cancer cell survival during extrinsic stress (2, 3) as well as promoting drug resistance (4). Importantly, several clinical trials have combined traditional chemotherapy or targeted therapy with antimalarial lysosomotropic agents, such as hydroxychloroquine, which block the late stages of autophagic proteolysis (5–12). Despite interest in inhibiting autophagy in the clinical oncology setting in combination with chemotherapies or other targeted therapies, emerging evidence has raised questions with regard to the efficacy of such approaches to cancer treatment. It is now appreciated that certain chemotherapies, particularly anthracycline agents, can kill tumors through combined cytotoxic and immunogenic mechanisms, via the process of immunogenic cell death (ICD), in which dying cells release damage-associated molecular patterns (DAMPs) to elicit an immune response (13, 14). ICD is believed to be an important effector of both chemotherapy and radiation therapy, but the precise contributions of ICD to treatment-mediated tumor killing are varied and context-dependent (15).

Importantly, autophagy has been shown to promote certain hallmarks of ICD *in vitro*, including the secretion of ATP and high-motility group protein B1 (HMGB1), both of which act as DAMPs (16). In support of the notion that autophagy facilitates antitumor immunity *in vivo* are the observations that loss of either autophagy or adaptive immunity impairs the regression of some mouse tumors during anthracycline therapy, and autophagy-deficient mouse colon tumors exhibit decreases in recruitment and activation of T cells (16, 17).

Overall, these potentially adverse effects on the adaptive immune system argue against the use of autophagy inhibitors in anticancer therapy. Nonetheless, autophagy inhibition may be a very useful anticancer therapy not only in undermining tumor cell growth but also in preventing the survival of quiescent cells during chemotherapy (18). These discrepancies become especially important considerations in light of the recent success of cancer immunotherapies. Notably, immune checkpoint blockade therapies, which leverage monoclonal antibodies targeting cytotoxic T lymphocyte-associated protein 4 (CTLA4) (19, 20) and programmed cell death protein 1 (PD-1) (21, 22) to reinvigorate existing T cell responses within tumors, have produced long-term remission in certain patients (23, 24). Currently, the best indication of a powerful response to these therapies is a high number of cancer-expressed neoantigens; thus, melanomas and smoking-associated lung carcinomas, which carry a high mutational load and express high levels of neoantigens, exhibit the highest response rates to immune checkpoint blockade (25). Even so, only a portion of patients with these cancers responds well to immunotherapy. With the promise of the impressive durable responses achieved with these therapeutic modalities comes a pressing need to better define the clinical contexts in which immunotherapies will be effective (26). Further-

Conflict of interest: The authors have declared that no conflict of interest exists.

Submitted: November 24, 2015; **Accepted:** September 15, 2016.

Reference information: *J Clin Invest.* 2016;126(12):4417–4429. doi:10.1172/JCI85705.

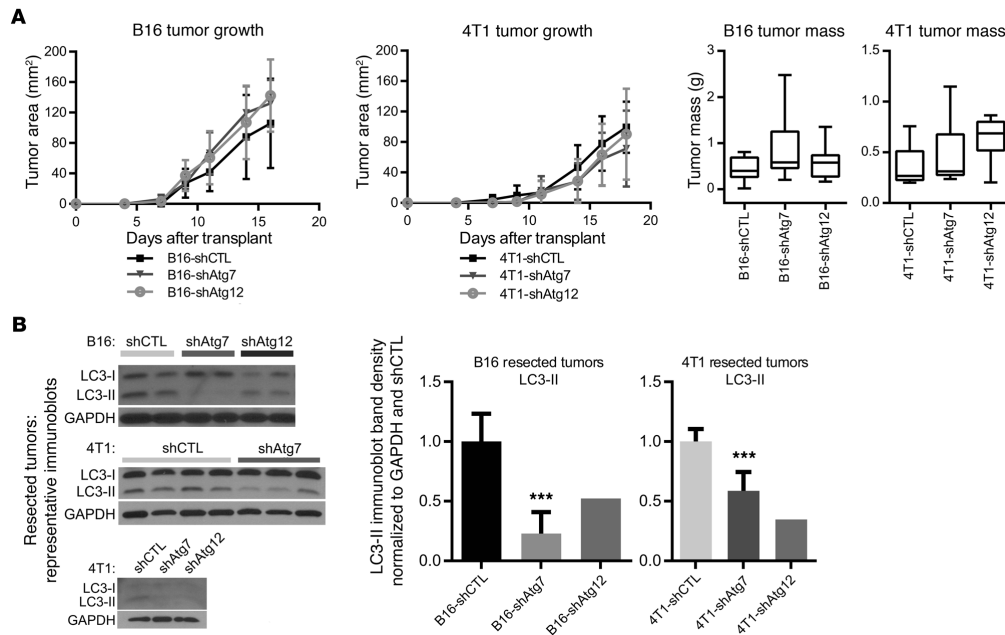


Figure 1. Genetic models of autophagy deficiency in mouse melanoma and mammary cancer. B16 mouse melanoma or 4T1 mouse mammary cancer cells bearing nontargeting shRNA (shCTL) or shRNA directed against autophagy-related genes (ATGs) were transplanted into immune-competent host mice. **(A)** Top: Primary tumor growth of autophagy-competent and -deficient subcutaneous B16 tumors (shCTL: $n = 6$; shATG7: $n = 7$; shATG12: $n = 6$) and orthotopic 4T1 tumors (shCTL: $n = 5$; shATG7: $n = 5$; shATG12: $n = 8$) in syngeneic host mice, as assessed by caliper measurements of tumor area. Error bars represent SD. Bottom: Tumor mass at experimental endpoint (day 16–18). For B16 tumors, shCTL: $n = 14$; shATG7: $n = 15$; shATG12: $n = 9$; and for 4T1 tumors, shCTL: $n = 13$; shATG7: $n = 13$; shATG12: $n = 8$. Box and whisker plots indicate minimum, median, and maximum values. Two-way ANOVA not significant. **(B)** Lysates from resected tumors subject to α -LC3 immunoblotting; band densities for LC3-II were normalized to GAPDH and to the control average within each experiment. For B16 tumors, shCTL: $n = 5$; shATG7: $n = 6$; shATG12: $n = 2$; and for 4T1 tumors, shCTL: $n = 6$; shATG7: $n = 5$; shATG12: $n = 2$. Error bars represent SD. *** $P < 0.001$ using unpaired t test.

more, leveraging the durable responses in immunotherapy in combination with short-term responses in other strategies is an alluring approach to further improve cancer treatment outcomes (27).

In this study, we sought to more fully delineate the effects of autophagy on the tumor-associated T cell response in order to better ascertain whether autophagy inhibition can be effectively combined with chemotherapy in the clinic. Using established immunogenic models of mouse melanoma and mammary cancer, we assessed the effects of autophagy inhibition on the functional status of tumor-infiltrating T cells, both at baseline and following doxorubicin (Dox) chemotherapy. We interrogated the functional status of tumor-associated CD4⁺ T helper cells and CD8⁺ cytotoxic T cells by flow cytometry for a variety of markers of T cell activation (28, 29) as well as immune checkpoint modulators. Our results demonstrate that genetic autophagy inhibition in tumor cells *in vivo* does not significantly impact T cell infiltration, activation, or immune checkpoint regulation. Similarly, we observe no changes in the T cell response upon systemic treatment of tumor-bearing mice with antimalarials that inhibit autophagy. We further confirm that autophagy inhibition does not impact the functional activation of adoptively transferred

ovalbumin-specific transgenic T cell receptor (OT-I) CD8⁺ T cells (30) in ovalbumin-expressing tumors. Hence, autophagy does not modulate the antitumor T lymphocyte response in multiple immune-competent mouse cancer models. Based on these results, we propose that certain clinical contexts exist in which autophagy inhibition may be utilized as a therapeutic strategy against cancer without adversely affecting the antitumor immune response.

Results

Genetic inhibition of autophagy in tumor cells does not alter primary tumor growth. To dissect the effect of tumor cell-intrinsic autophagy on the extrinsic antitumor immune response, we generated B16 murine melanoma cells stably expressing shRNAs against the essential autophagy-related genes *Atg7* and *Atg12*. Cells expressing nontargeting shRNA (shCTL) served as autophagy-competent controls. Stable ATG7 or ATG12 knockdown (Supplemental Figure 1A; supplemental material available online with this article; doi:10.1172/JCI85705DS1) led to reduced autophagic flux, evidenced by reduced LC3-II formation and lysosomal turnover (Supplemental Figure 1B). Control and autophagy-deficient B16 tumors were introduced *s.c.* into C57BL/6 mice, and palpable tumors

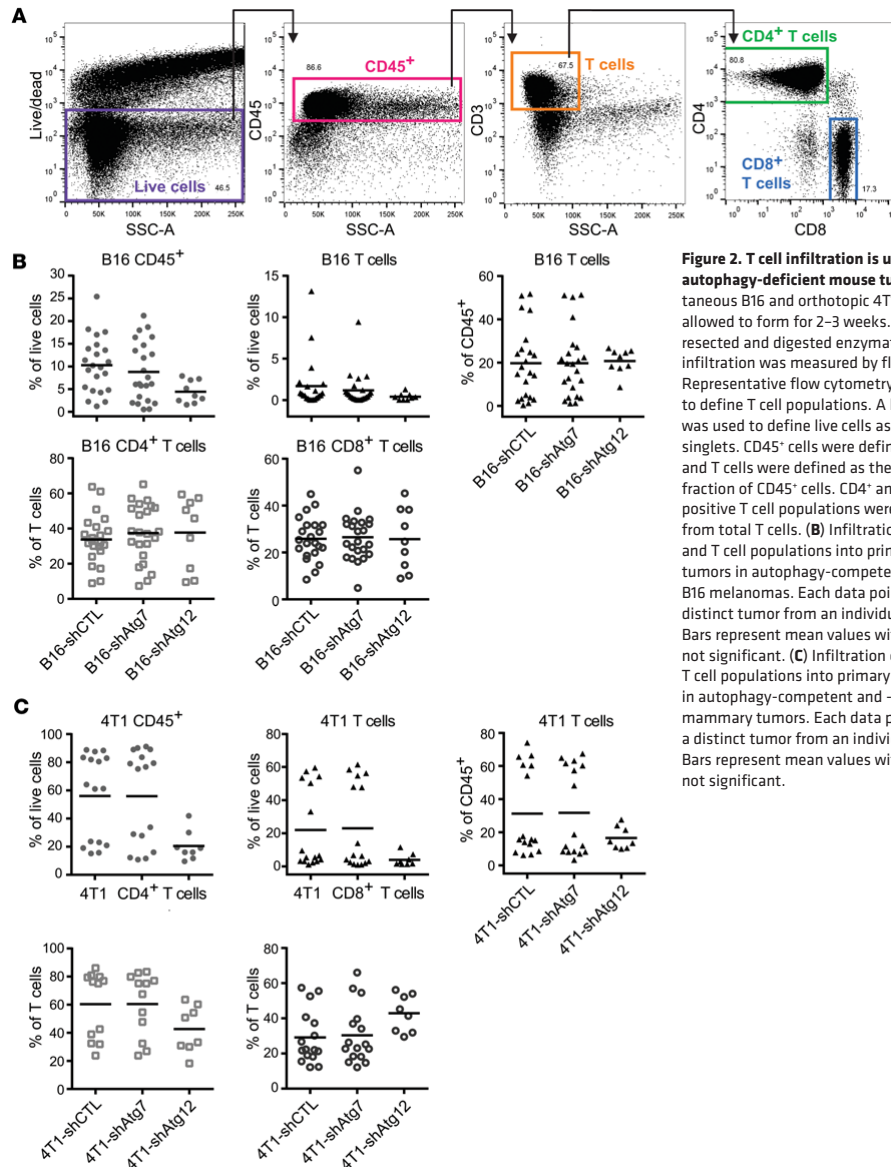


Figure 2. T cell infiltration is unchanged in autophagy-deficient mouse tumors. Subcutaneous B16 and orthotopic 4T1 tumors were allowed to form for 2–3 weeks. Tumors were resected and digested enzymatically, and T cell infiltration was measured by flow cytometry. **(A)** Representative flow cytometry gating strategy to define T cell populations. A live/dead marker was used to define live cells as a subset of singlets. CD45⁺ cells were defined from live cells, and T cells were defined as the CD3⁺SSC-A^{lo} fraction of CD45⁺ cells. CD4⁺ and CD8⁺ single-positive T cell populations were subdivided from total T cells. **(B)** Infiltration of CD45⁺ cells and T cell populations into primary mouse tumors in autophagy-competent and -deficient B16 melanomas. Each data point represents a distinct tumor from an individual host mouse. Bars represent mean values with 2-way ANOVA not significant. **(C)** Infiltration of CD45⁺ cells and T cell populations into primary mouse tumors in autophagy-competent and -deficient 4T1 mammary tumors. Each data point represents a distinct tumor from an individual host mouse. Bars represent mean values with 2-way ANOVA not significant.

formed 7–10 days after transplantation. Primary tumor growth was unchanged between autophagy-competent and -deficient tumors, based on caliper measurements of tumor area over time as well as resected tumor mass at experimental endpoint (Figure 1A). Similarly, autophagy inhibition in 4T1 mammary cancer cells, achieved via stable ATG7 or ATG12 knockdown (Supplemental Figure 1A), significantly impaired autophagic flux (Supplemental Figure 1C) but did not impact primary tumor growth following orthotopic transplantation into the mammary fat pad of 6- to 7-week-old female

BALB/c mice (Figure 1A). In both models, we confirmed that robust autophagy inhibition was maintained over the duration of the experiment, evidenced by the loss of LC3-II in lysates generated from resected tumors harvested at 2–3 weeks after transplant (Figure 1B).

Autophagy-competent and -deficient tumors elicit equivalent T cell responses. Having developed 2 models of tumor cell autophagy deficiency in distinct mouse genetic backgrounds, we evaluated the immune response to tumors arising from these cells. To quantify and interrogate the function of tumor-associated T cells,

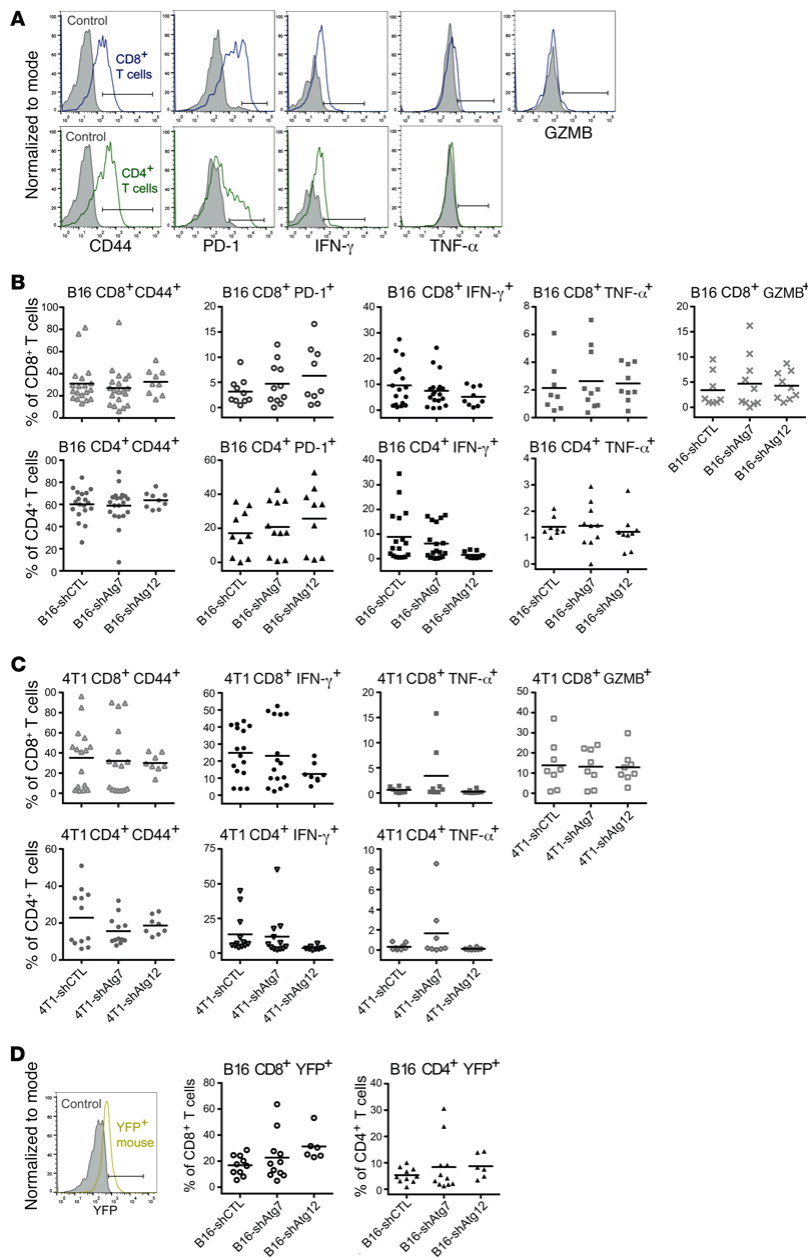


Figure 3. T cell functional status is unchanged in autophagy-deficient mouse tumors. Expression of T cell activation markers (CD44, IFN- γ , TNF- α , GZMB) and immune checkpoint marker PD-1 was measured by flow cytometry in CD8⁺ and CD4⁺ T cell populations. **(A)** Representative histograms of functional marker staining of CD8⁺ and CD4⁺ T cell populations. Solid gray plots represent unstained controls (CD44, CD4, CD8) and isotype controls (PD-1, IFN- γ , TNF- α , GZMB). The same unstained control was used for the CD4⁺ and CD8⁺ T cell panels. Positive staining is indicated by gate and defined as that above the unstained or isotype control. **(B)** Functional status of T cells isolated from autophagy-competent (shCTL) and -deficient (shAtg7 or shAtg12) B16 tumors. Each data point represents a distinct tumor from an individual host mouse. Bars represent mean values with 2-way ANOVA not significant. **(C)** Functional status of T cells isolated from autophagy-competent (shCTL) and -deficient (shAtg7 or shAtg12) 4T1 tumors. Each data point represents a distinct tumor from an individual host mouse. Bars represent mean values with 2-way ANOVA not significant. **(D)** B16 tumors were grown in GREAT reporter mice bearing the IFN- γ -IRES-eYFP reporter cassette. Representative histogram shows YFP-negative control (solid gray plot) and cells isolated from a GREAT reporter mouse (yellow plot). Positive signal was defined as that above the control and is indicated by a gate. Endogenous eYFP expression was measured in tumor-infiltrating T cell populations by flow cytometry without BFA injection. Each data point represents a distinct tumor from an individual host mouse. Bars represent mean values with 2-way ANOVA not significant.

we prepared single-cell suspensions from resected tumors and subsequently stained a variety of surface and intracellular markers for flow cytometric analysis. To accurately measure intracellular cytokines in T cells, we injected mice with brefeldin A (BFA) before tumor resection to prevent cytokine secretion. T cells were identified as the CD45⁺CD3⁺SSC-A^{lo} fraction of total live cells

defined by a live/dead marker; from these, CD4⁺ and CD8⁺ T cell subpopulations were identified (Figure 2A). Autophagy-deficient B16 and 4T1 tumors did not exhibit significant differences in the infiltration of CD45⁺ cells, total T cells, or CD4⁺ or CD8⁺ subsets, when compared with autophagy-competent controls (Figure 2, B and C). While biological variation occurred across the littermates

used for the experimental repeats, autophagy-competent and -deficient tumors generated in littermates exhibited equivalent levels of immune infiltration; hence, statistical analyses of both individual and batched data sets were not significant.

We next assessed the functional activation status of CD8⁺ and CD4⁺ T cells that had infiltrated B16 tumors by analyzing cell surface expression of the activation and memory marker CD44 and intracellular expression of the inflammatory cytokines IFN- γ and TNF- α . By these measures, we observed no differences in the T cell activation phenotype between control and autophagy-deficient B16 tumors (Figure 3, A and B, and Supplemental Figure 2A). Similarly, we found no differences between cohorts in the activation of the CD8⁺ T cell cytotoxic program based on intracellular expression of the serine protease granzyme B (GZMB) (Figure 3, A and B, and Supplemental Figure 2A). We also measured the surface expression of the immune checkpoint regulator programmed cell death protein 1 (PD-1) and found no differences in either CD4⁺ or CD8⁺ T cells between autophagy-competent and -deficient tumors (Figure 3, A and B, and Supplemental Figure 2A). In agreement with these results from B16 tumors, T cell functional status and activation phenotype were unchanged between autophagy-competent and -deficient 4T1 tumors (Figure 3C). As before, statistical analyses of both individual and batched data sets were not significant. Together, these findings indicate that reduced tumor cell autophagy in both mouse melanomas and mammary tumors does not influence the ability of the host adaptive immune system to infiltrate and become functionally active within these tumors.

To further corroborate the observation that T cell activation was independent of autophagy status, we generated autophagy-competent and -deficient B16 tumors in mice carrying an IFN- γ -IRES-eYFP reporter cassette (also known as the "IFN- γ reporter with endogenous polyA transcript," or GREAT allele), in which expression of IFN- γ and expression of enhanced yellow fluorescent protein (eYFP) are separated by an internal ribosome entry site (IRES) and dually controlled by the endogenous *Ifng* promoter/enhancer region (31). While IFN- γ is a secreted protein, eYFP accumulates intracellularly upon IFN- γ transcription; thus, T cell activation in resected tumors is measured using endogenous eYFP fluorescence, obviating the need for BFA treatment or intracellular staining. No differences in eYFP expression in CD4⁺ or CD8⁺ T cells were observed by this method, providing further evidence for an autophagy-independent T cell response (Figure 3D). Remarkably, based on eYFP reporter levels, the IFN- γ response was comparable to that obtained with intracellular IFN- γ staining.

To address whether tumor cell autophagy status modulates immunosuppression, we evaluated the quantity and function of regulatory T cells (Tregs) associated with autophagy-competent and -deficient B16 tumors (Supplemental Figure 3A). Once again, neither the number of Tregs (CD45⁺CD3⁺CD4⁺Foxp3⁺) nor their activation (CD44⁺) was changed upon genetic autophagy inhibition, further supporting that T cell responses were unaffected by autophagy status in these tumors.

Finally, to assess tumor-associated T cell activation potential, we isolated CD8⁺ T cells from 4T1 tumors by FACS or negative bead selection and cultured them with CD3 and CD28 antibodies to incite robust ex vivo antigen-independent restimulation. We

measured IFN- γ secretion in conditioned medium by ELISA and observed equivalent levels of secretion from T cells derived from either autophagy-competent or -deficient 4T1 tumors (Supplemental Figure 3B). Thus, tumor-associated T cells possess equivalent activation in situ as well as equivalent activation potential, regardless of the autophagy status of tumor cells.

Autophagy-competent and -deficient OVA-expressing tumors stimulate comparable transgenic T cell responses. Studies using T cells expressing a transgenic T cell receptor matched to a specific antigen (e.g., ovalbumin) have been valuable in defining a tumor-specific adaptive immune response. To evaluate cancer cell recognition by T cells, we generated autophagy-competent (shCTL) and autophagy-deficient (*Atg7* or *Atg12* shRNA) B78 melanoma cells (a variant of B16) expressing ovalbumin (OVA). We confirmed stable suppression of *ATG7* and *ATG12* (Supplemental Figure 4A) and reduction of autophagic flux by reduced LC3-II and increased P62 (also known as SQSTM1), an autophagic cargo receptor that accumulates upon autophagy inhibition, in cell culture lysates (Supplemental Figure 4B). B78-OVA cells were injected s.c. into WT C57BL/6 mice and allowed to form palpable primary tumors. Freshly isolated OVA-specific OT-I CD8⁺ T cells expressing green fluorescent protein (GFP) were then adoptively transferred by retro-orbital injection into tumor-bearing mice, and tumors were resected 1 week later. Tumor growth kinetics was unchanged between autophagy-competent and -deficient groups (Figure 4A). Autophagy inhibition was confirmed by the accumulation of P62 aggregates in B78-OVA cells isolated from digested tumors (Figure 4B).

Endogenous and adoptively transferred tumor-associated T cells were defined by flow cytometric analysis based on expression of CD45, CD3, CD4, CD8, and GFP; no differences were observed in the tumor infiltration of total T cells, endogenous CD4⁺ or CD8⁺ T cells, or adoptively transferred OT-I CD8⁺ T cells (Figure 4C). We next measured T cell activation by expression of surface CD44 and intracellular IFN- γ , TNF- α , and GZMB. We observed no significant differences in expression of activation markers in either OT-I or endogenous populations of T cells between autophagy-competent and -deficient B78-OVA tumors, with the exception of an increase in TNF- α -expressing OT-I cells associated with autophagy-deficient tumors (Figure 4D and Supplemental Figure 2B). Importantly, autophagy deficiency did not blunt the T cell response. As expected, the activation of OT-I T cells was higher than that of endogenous CD8⁺ T cells, as evidenced by higher percentages of CD44⁺ and TNF- α ⁺ cells. Overall, the T cell response remained intact in both the endogenous and the antigen-matched setting upon genetic autophagy inhibition.

Dox-treated autophagy-competent and -deficient tumors stimulate equivalent T cell responses. Because our results indicated that tumor cell-intrinsic autophagy is dispensable for stimulating a T cell response, we next tested whether autophagy was required for the immune response in tumor-bearing mice following acute treatment with chemotherapy. Previous work with murine colon cancer suggests that autophagy is necessary for the immunogenic cell death (ICD) associated with the efficacy of anthracycline chemotherapy (16). Thus, genetic inhibition of autophagy may hinder the chemotherapeutic drug response by blunting immune responses. We treated autophagy-competent and -deficient B16 melanoma cells with the anthracycline Dox in vitro, and measured the secreted levels of ATP and HMGB1, 2 immunomodulatory factors impli-

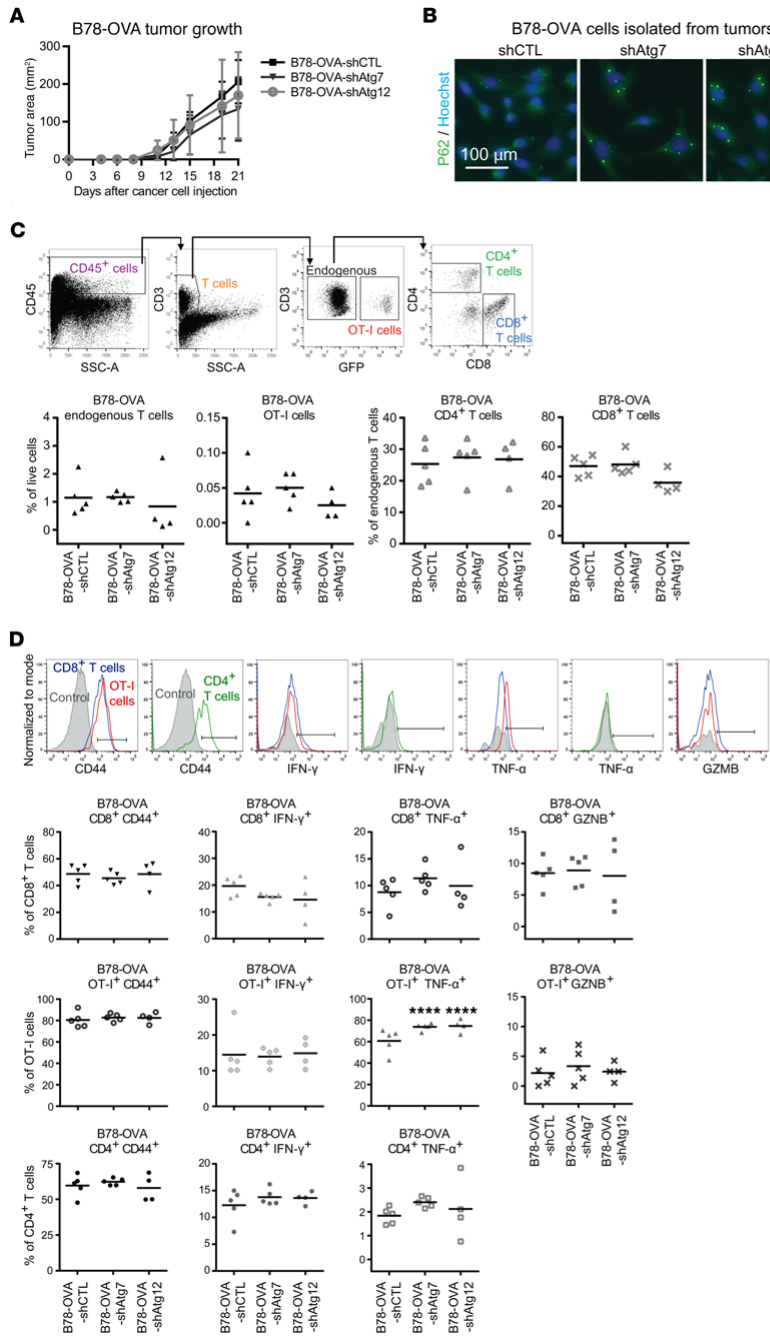


Figure 4. Transgenic OT-I cell activation is unchanged in autophagy-deficient OVA-expressing tumors. Freshly isolated transgenic OT-I CD8⁺ T cells expressing GFP were adoptively transferred by retro-orbital injection into mice bearing 2-week subcutaneous autophagy-competent and -deficient B78 melanomas expressing OVA. **(A)** Primary tumor growth of autophagy-competent and -deficient subcutaneous B78-OVA tumors in syngeneic host mice as assessed by caliper measurements of tumor area ($n = 5$ per cohort). **(B)** Autophagy deficiency was confirmed in B78-OVA cells isolated from digested tumors by immunofluorescence for P62. Accumulation of P62 aggregates was quantified per cell nucleus. Error bars represent SD; ** $P < 0.01$ using unpaired *t* test. **(C)** Total T cells were defined as the CD45⁺CD3⁺SSC-A^{lo} fraction of live cells and were further subdivided into OT-I (GFP⁺) and endogenous (GFP⁻) populations; the latter was analyzed for CD4 and CD8 surface expression. Endogenous and OT-I T cell populations were equivalent between autophagy-competent (shCTL) and -deficient (shAtg12) B78-OVA tumors. Error bars represent SD with 2-way ANOVA not significant. **(D)** Activation status was measured by surface CD44 and intracellular IFN-γ, TNF-α, and GZMB expression in endogenous and OT-I T cell populations from autophagy-competent and -deficient B78-OVA tumors. Representative histograms of functional marker staining of endogenous and OT-I T cell populations: solid gray plots represent unstained controls (for surface staining of CD44) and isotype controls (for intracellular stains of IFN-γ, TNF-α, GZMB). Positive staining is defined as that above the unstained or isotype control and is indicated by gates. In graphs, each data point represents a distinct tumor from an individual host mouse, and bars represent mean values. **** $P < 0.0001$ using 2-way ANOVA multiplicity-adjusted *P* values (Dunnett's correction).

cated in ICD (Figure 5A). Consistent with existing literature, we observed that Dox treatment induced ATP and HMGB1 secretion, which was attenuated in autophagy-deficient cells as compared with autophagy-competent controls. Interestingly, we noted that Dox treatment also led to a modest, albeit significant, reduction in the surface expression of the immunosuppressive protein programmed death-ligand 1 (PD-L1) in autophagy-deficient tumor cells (Figure 5A). Notably, B16-shAtg7 cells exhibited higher levels of death upon Dox treatment relative to B16-shCTL cells (Supplemental Figure 5A), indicating increased sensitivity to autophagy impairment; similarly, autophagy-deficient 4T1 cells showed reduced cellular viability following 24 hours of Dox treatment (Supplemental Figure 5B).

Because these *in vitro* findings suggested that autophagy status in B16 melanoma cells influenced their expression of several markers of ICD, we evaluated the effects of genetic autophagy inhibition on ICD *in vivo*. To assess whether autophagy-competent and -deficient B16 melanomas underwent equivalent levels of ICD *in vivo*, we used the prophylactic vaccination experimental design described previously by Michaud et al. (16). Based on dose-response curves to determine appropriate treatment regimens (Supplemental Figure 5A), we pretreated B16-shCTL and B16-shAtg7 with Dox *in vitro* and injected cocktails s.c. into mice in which 70% of cells were apoptotic; Matrigel was injected as a control "vaccination." One week later, healthy WT B16 cells were injected s.c. into contralateral flanks, and tumor incidence was measured by daily palpation. Tumor-free survival was unchanged between mice vaccinated with Matrigel, B16-shCTL, or B16-shAtg7 cells (Figure 5B). Thus, in spite of expressing classic ICD markers *in vitro*, Dox-treated B16 cells were unable to vaccinate mice against rechallenge irrespective of autophagy status. These results supported that ICD is a highly dynamic, context-dependent process (15), and further broached that autophagy inhibition does not universally perturb immunogenic responses following chemotherapy.

Based on these results, we sought to directly evaluate the effects of genetic autophagy inhibition on the immune response during *in vivo* Dox treatment. We generated autophagy-competent and -deficient B16 melanoma tumors in GREAT reporter mice; following the development of palpable tumors, mice were treated with Dox. There were no significant differences in tumor growth between cohorts, either by caliper measurements or tumor mass at resection (Figure 5C). Phosphorylated H2a histone family member X (γ H2AX) expression, a marker of DNA damage, was significantly elevated in Dox-treated tumors compared with untreated controls, but was unchanged between autophagy-competent and -deficient Dox-treated cohorts (Figure 5D). Thus, this dose regimen instigated DNA damage in B16 tumors, a prerequisite for cell death and immunogenic potential. We also confirmed autophagy deficiency in resected tumors by immunoblotting for LC3-II (Figure 5D).

Upon assessment of immune infiltration, we found that percentages of CD45⁺ cells, total T cells, and CD4⁺ and CD8⁺ subsets were equivalent between untreated and Dox-treated cohorts (Figure 5E). T cell activation phenotype was measured by flow cytometry using surface CD44 expression and endogenous eYFP fluorescence as a reporter for IFN- γ levels, while T cell immune checkpoint regulation was measured by surface PD-1 expression. However, no differences were observed in the

levels of any of these functional markers between control and ATG7 knockdown Dox-treated tumors (Figure 5E).

Importantly, we observed evidence of a chemotherapy-induced immune response in Dox-treated tumors compared with untreated controls. Most strikingly, CD44 expression was significantly elevated in both CD8⁺ and CD4⁺ T cell populations, in both Dox-treated B16-shCTL and B16-shAtg7 tumors, as compared with untreated counterparts (Figure 5E). Thus, Dox treatment of B16 tumor-bearing mice elicited immune responses within the tumor site, as evidenced by direct measurement of tumor-associated T cell activation. Because autophagy inhibition did not blunt this enhanced immune response during Dox treatment, our data suggest that autophagy inhibition and anthracycline chemotherapy can be safely combined in certain tumor types.

Antimalarial treatment of tumor-bearing mice does not alter the antitumor T cell response. Autophagy inhibition is currently accomplished in the clinical setting by systemic treatment with antimalarial drugs such as chloroquine and hydroxychloroquine (32). These drugs inhibit acidification of intracellular vesicular compartments such as the lysosome, thereby blocking the terminal stages of autophagic proteolysis. To ascertain the effects of systemic antimalarial treatment on the antitumor immune response, we evaluated the effects of chloroquine treatment on subcutaneous B16 melanomas in GREAT reporter mice. Mice bearing palpable tumors were treated with daily i.p. injections of 60 mg/kg chloroquine or vehicle control for 4–5 days before tumor resection. As with genetic autophagy inhibition, tumor growth kinetics was unchanged upon pharmacological autophagy inhibition (Figure 6A), which was confirmed by the accumulation of P62 aggregates in resected tumors (Figure 6B). T cell infiltration and activation, measured by CD44 and eYFP reporter activity, were unchanged in chloroquine-treated B16 melanomas compared with vehicle-treated controls (Figure 6C). In addition, chloroquine treatment did not change the levels of immune checkpoint regulator PD-1 (Figure 6C). To extend these results, we generated orthotopic 4T1 mammary tumors in BALB/c mice and evaluated the effects of chloroquine as well as quinacrine, another FDA-approved antimalarial demonstrated to inhibit autophagy in preclinical models (18, 33). Mice bearing palpable tumors were treated with daily i.p. injections of either 60 mg/kg chloroquine, 50 mg/kg quinacrine, or vehicle control. Tumor growth was not significantly different between the 3 cohorts (Figure 6A). Consistent with our results in B16 melanomas, T cell infiltration and activation were unchanged in both chloroquine- and quinacrine-treated 4T1 mammary tumors compared with vehicle-treated controls (Figure 6D). Overall, these data demonstrate that systemic pharmacological inhibition of autophagy using antimalarials does not adversely impact the antitumor T cell response.

Discussion

In this study, we demonstrate that the T cell immune response in preclinical models of melanoma and breast cancer is not dependent on autophagy activity of the tumor cell. This suggests the ability to safely combine autophagy inhibition with chemotherapy during cancer treatment, and opens the possibility of future combination with immunotherapy. While ongoing clinical trials are testing the efficacy of combining autophagy inhibition with chemotherapy in multiple cancer types, some recent studies have

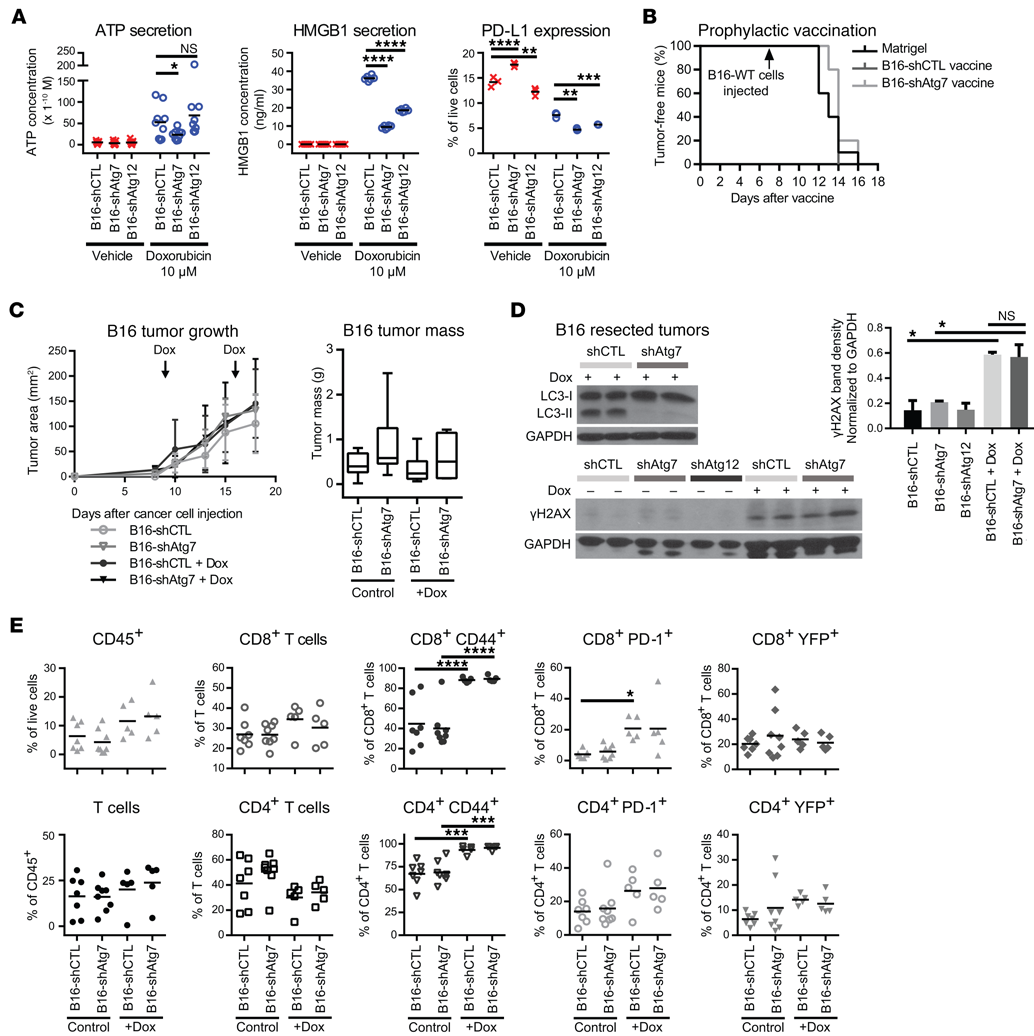


Figure 5. Dox-treated autophagy-deficient tumors elicit equivalent T cell responses despite altered secretion of immunomodulatory factors. (A) Autophagy-competent (shCTL) and -deficient (shAtg7 or shAtg12) B16 cells treated with 10 μM Dox or vehicle control. ATP and HMGB1 secretion measured in conditioned medium and surface PD-L1 measured by flow cytometry. Data points represent biological replicates; bars represent mean values. **P* < 0.05; ***P* < 0.01; ****P* < 0.001; *****P* < 0.0001; not significant (NS) using 2-way ANOVA multiplicity-adjusted *P* values (Dunnett's correction). **(B)** Autophagy-competent (shCTL) and -deficient (shAtg7) B16 cells were treated for 24 hours with 8.8 μM and 7.5 μM Dox, respectively, and subsequently injected into WT C57BL/6 mice (*n* = 5). Control mice were injected with Matrigel (*n* = 10). Mice were rechallenged with WT B16 cells 1 week later; tumor incidence was monitored daily. **(C)** Autophagy-competent and -deficient B16 cells were injected into GREAT reporter mice; mice were then treated with 5 mg/kg Dox weekly. Tumor growth curves: arrows indicate Dox treatment; error bars represent SD (B16-shCTL: *n* = 6; B16-shATG7: *n* = 7; B16-shCTL + Dox: *n* = 8; B16-shATG7 + Dox: *n* = 8). Untreated tumors are also included in Figure 1A. **(D)** Resected and digested tumors were immunoblotted for LC3 (autophagy deficiency) and γH2AX (DNA damage). Expression quantified normalized to GAPDH. Error bars represent SD. **P* < 0.05; NS, not significant, using unpaired *t* test. **(E)** T cell infiltration and functional status (CD44, PD-1, eYFP) in control and Dox-treated autophagy-competent and -deficient B16 tumors from 2 experimental cohorts. Each data point represents a distinct tumor from an individual host mouse. Bars represent mean values. **P* < 0.05; ****P* < 0.001; *****P* < 0.0001, using 2-way ANOVA multiplicity-adjusted *P* values (Tukey's correction). Measurements of untreated tumors are also included in Figures 2B and 3B.

argued against such combinations because of autophagic regulation of immunogenic mechanisms associated with chemotherapeutic efficacy (14, 16, 17). Because of the limited scope of those studies with regard to interrogating autophagy and T cell functional status, as well as the clinical importance of delineating the consequences of autophagy inhibition, we further addressed this critical issue in additional mouse models.

Our study design primarily included 2 tumor types: B16 melanoma in C57BL/6 mice and 4T1 mammary cancer in BALB/c mice (34, 35). These models have been extensively used in studies of the tumor microenvironment and immune response and provided us with the opportunity to interrogate the effects of autophagy inhibition in 2 distinct immune-competent genetic backgrounds. We found that the levels of autophagy within tumor cells did not affect either the quantities of infiltrating T cell populations or their functional status. As a further validation of our measurements of the functional analysis of T cells via antibody staining, we raised B16 melanomas in GREAT reporter mice and measured eYFP reporter activity. This model allowed us to use an entirely parallel technical approach to assessing T cell activity, and eliminated any technical caveats that could be introduced by the reliance on antibody reagents. Once again, we found equivalent tumor-associated T cell responses as measured by eYFP reporter expression between autophagy-competent and -deficient tumors. We also demonstrated that autophagy deficiency did not alter the quantity or quality of Tregs associated with B16 tumors, and did not alter the activation potential of restimulated CD8⁺ T cells isolated from 4T1 tumors.

Because of the ongoing efforts to repurpose antimalarials as autophagy inhibitors to treat cancer, we interrogated the effects of these agents on the antitumor T cell response. Similar to genetic autophagy inhibition in tumor cells, systemic treatment with the autophagy-inhibiting antimalarial agents chloroquine and quinacrine produced equivalent numbers of tumor-infiltrating T cells, which were functionally equivalent. Remarkably, antimalarials are used clinically in the treatment of autoimmune disorders, and it has been proposed these agents can act as immune suppressors by interfering with immune cell function (36, 37). However, in daily treatments of tumor-bearing mice for a short duration, we observed no evidence of a blunted T cell response. Thus, our results point to a therapeutic window in which antimalarials may be effectively combined with immunotherapies without antagonistic effects. Future preclinical and clinical studies will be necessary to define such combinatorial approaches.

In addition to assessing the endogenous, heterogeneous T cell response in B16 and 4T1 tumors, we used a more targeted approach to address whether autophagy-deficient cancer cells were less inherently immunogenic. It has been speculated that impaired autophagy leads to changes in antigen availability, processing, or presentation (38, 39), or to changes in immune-modulatory secreted proteins; such effects would potentially dampen cancer cell immunogenicity and subsequent T cell responses. Hence, we used the antigen-matched OT-I system (30), in which OVA-specific OT-I CD8⁺ T cells expressing a traceable fluorescent marker were adoptively transferred into mice bearing OVA-expressing B78 melanoma tumors, a derivative cell line of the B16 model. While the OT-I cells mounted a stronger antitumor

response than endogenous T cells, the overall T cell response was comparable between autophagy-competent and -deficient B78-OVA tumors. The majority of activation markers measured, most notably IFN- γ , were unchanged between tumor types, indicating that autophagy inhibition did not impair T cell function in this model of a highly active tumor antigen-specific T cell response. Taken together, the comparable antitumor responses of both endogenous and antigen-matched T cells indicate the autophagy independence of these programs.

Our results differ from previous work demonstrating that tumor cell autophagy promotes T cell infiltration and activation in response to anthracycline chemotherapy. These phenotypic differences may partly be due to the aggressive nature of the models used in our studies, which may diminish the immune modulatory effects of tumor cell autophagy following therapy. Importantly, autophagy promotes the *in vitro* secretion of key factors associated with ICD, including ATP and HMGB1 (15); consistent with those previous findings, we observe that ATP and HMGB1 secretion is impaired in Dox-treated autophagy-deficient B16 cells *in vitro*. However, in contrast to tumor models used previously to study ICD, the introduction of Dox-treated apoptotic B16 cells, either autophagy-competent or -deficient, is unable to vaccinate mice against rechallenge with healthy WT B16 cells, which is considered the benchmark assay for ICD (15). Accordingly, our results demonstrate that autophagy inhibition does not adversely impact immune cell function in the absence of a robust ICD response. Our results highlight the highly context-specific nature of ICD and suggest that more precise corroboration of this death pathway in individual patients may be needed to predict how autophagy inhibitors influence anticancer immunity in the clinical setting (15). Nevertheless, despite the absence of significant ICD, B16 tumor-bearing mice treated with Dox still exhibited significantly elevated immune activation compared with untreated tumor-bearing mice, which once again is unaffected by autophagy status. This raises the likely possibility that specific clinical contexts and therapeutic windows exist in which autophagy-dependent immune modulation will not compromise chemotherapeutic efficacy. We propose that autophagy inhibition can be safely combined with chemotherapy and still stimulate a productive antitumor T cell response in certain tumor types. Future studies analyzing patient-derived T cells from clinical trials of autophagy inhibitors will be crucial to determine whether this is truly the case. Finally, our studies raise the possibility that anticancer immunotherapies can be combined with autophagy inhibition; such a combination would be a dual-pronged treatment strategy that would unleash the power of the immune system upon tumor cells weakened by autophagy inhibition.

Methods

Antibodies. Commercial antibodies included the following: eFluor 450, Alexa 700, and APC-Cy7 anti-CD45 (clone 30-F11, 1:400); PE and APC anti-CD3 ϵ (clone 145-2C11, 1:400); PE-Cy7 anti-CD4 (clone RM4-5, 1:400); Percp-Cy5.5 anti-CD8 α (clone 53-6.7, 1:400); FITC and eFluor 450 anti-PD-1 (clone RMP1-30, 1:400); eFluor 660 anti-IFN- γ (clone XMGI.2, 1:400); FITC and eFluor 450 anti-TNF- α (clone MP6-XT22, 1:400); and eFluor 450 anti-Foxp3 (clone FJK-16s, 1:400) were obtained from eBioscience. APC-Cy7 anti-CD45 (clone 30-F11, 1:400); FITC anti-CD8 α (clone 53-6.7,

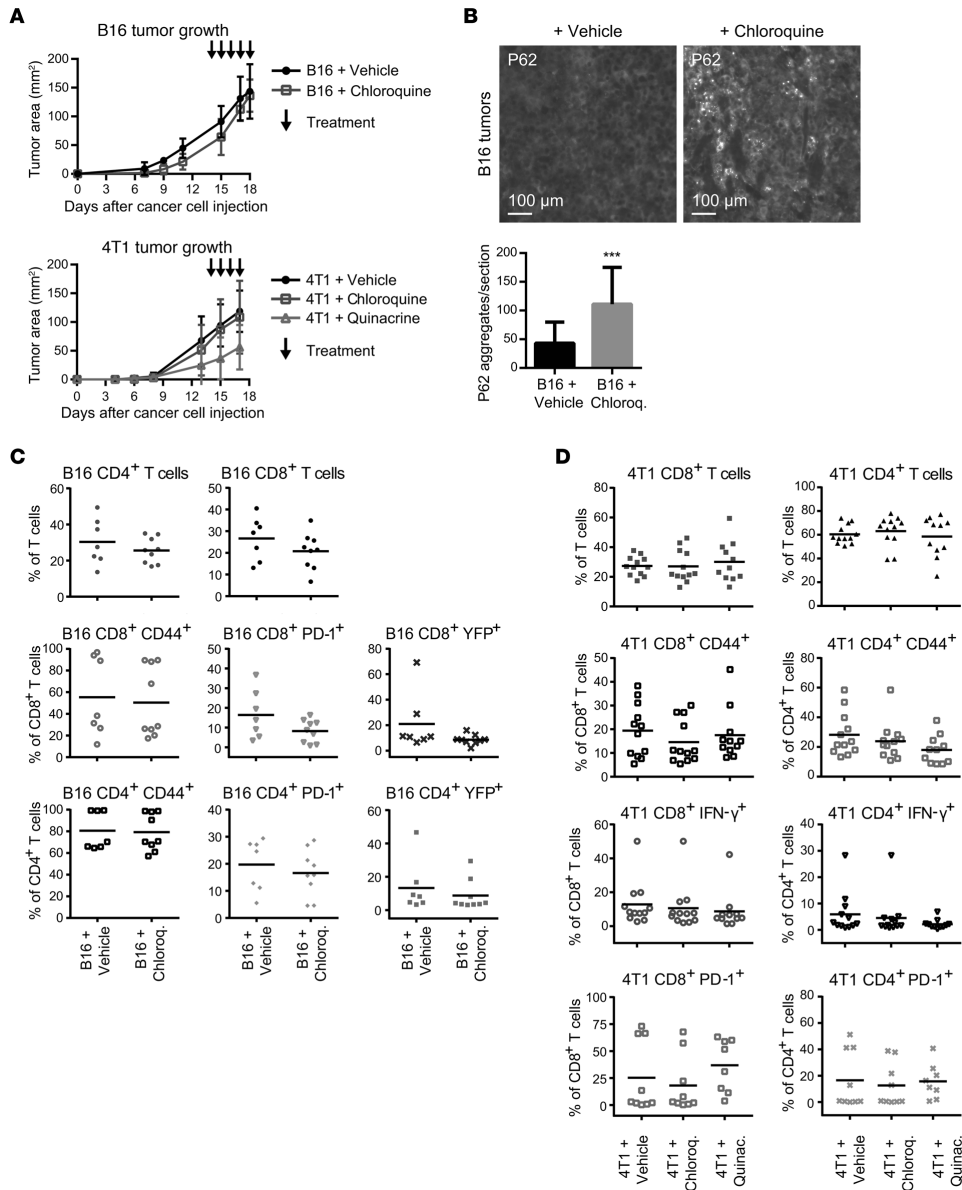


Figure 6. Antimalarial-treated tumors exhibit equivalent T cell responses. Subcutaneous B16 melanomas were raised in GREAT reporter mice and orthotopic 4T1 mammary tumors in WT BALB/c mice. Primary tumors were allowed to form for 7–10 days and were subsequently treated daily with chloroquine, quinacrine, or vehicle control by i.p. injection. **(A)** Primary tumor growth of B16 ($n = 5$ per cohort) and 4T1 tumors (Vehicle, $n = 9$; Chloroquine, $n = 9$; Quinacrine, $n = 8$) as assessed by caliper measurements of tumor area. Error bars represent SD, and arrows indicate treatment days. **(B)** Autophagy deficiency was confirmed in resected B16 tumors by immunofluorescence for P62, and accumulation of P62 aggregates was quantified. Error bars represent SD; *** $P < 0.001$ using unpaired t test. **(C)** Infiltration and functional phenotype of CD4⁺ and CD8⁺ T cell populations were measured by flow cytometry in vehicle- and chloroquine-treated B16 tumors. Data points represent distinct tumors from individual mice; bars represent mean values with 2-way ANOVA not significant. **(D)** Infiltration and activation of CD4⁺ and CD8⁺ T cell populations were measured by flow cytometry in vehicle-, chloroquine-, and quinacrine-treated 4T1 tumors. Data points represent distinct tumors from individual mice, and bars represent mean values with 2-way ANOVA not significant.

1:400); Brilliant Violet 785 anti-CD44 (clone IM7, 1:800); Pacific Blue anti-granzyme B (clone GB11, 1:400); and Brilliant Violet 421 anti-PD-L1 (clone 10F.9G2, 1:800) were obtained from BioLegend. Anti-ATG7 (2631, 1:500) was obtained from Cell Signaling Technology. Anti-ATG5 (NB110-53818, 1:2,000) was obtained from Novus Biologicals. Anti-P62 (GP62-C, 1:100 for immunofluorescence and 1:1,000 for immunoblotting) was obtained from Progen. Anti-phospho-histone H2A.X (clone JBW301, 1:1,000) and anti-GAPDH (AB2302, 1:5,000) were obtained from Millipore. A rabbit polyclonal anti-LC3 antibody was created using a conserved N-terminal peptide between human, rat, and mouse (40), which is also commercially available from Millipore (ABC232, 1:1,000).

Cell culture. Lewis Lanier (UCSF) provided B16 murine melanoma cells, 4T1 mammary carcinoma cells were purchased from the American Type Culture Collection, and Matthew Krummel (UCSF) provided B78-OVA murine melanoma cells, which express OVA via the mCherry-p2A-OVA sequence (41). All cells were cultured in D10 culture medium (DMEM, 10% FBS, penicillin/streptomycin), verified to be free of *Mycoplasma*, and authenticated via transplantation in the appropriate syngeneic host. For stable RNA interference, pLKO.1-puro (puromycin) lentiviral plasmids containing nontargeting shRNA (shCTL) or shRNA against mouse *Atg7* (NM_028835) and mouse *Atg12* (NM_026217) were purchased from Sigma-Aldrich. The target sequence for shRNA directed against mouse *Atg7* (TRCN0000092163) is CCAGCTCTGAACTCAATA-ATA, and directed against *Atg12* (TRCN0000257708) is TGGTAACTGGCTCCTGCATTA. Viral particles were produced using a third-generation lentiviral packaging system in HEK293T cells, and used to infect B16 murine melanoma, 4T1 mammary carcinoma, and B78-OVA murine melanoma cells. After infection and drug selection, early-passage stable pools of ATG knockdown cells were used for both in vitro and in vivo assays. To confirm autophagy deficiency following ATG knockdown, cells were cultured in full growth medium or starvation medium (HBSS), with or without bafilomycin A. Cell lysates were then assessed for autophagic flux by LC3-II turnover via immunoblot.

For analysis of secreted factors associated with ICD, cells were treated with 10 μ M Dox (Sigma-Aldrich, 44583) for 24 hours; conditioned medium was collected and analyzed for HMGB1 secretion by ELISA (GENTAUR, ST51011) or ATP secretion by Enliten ATP assay (Promega, FF2000). Viability of Dox-treated cells was assessed by crystal violet staining. Cultured cells were fixed with 4% paraformaldehyde (PFA) for 10 minutes at room temperature, incubated with 0.3% crystal violet for 20 minutes at room temperature, washed with deionized water, air-dried overnight, and resuspended in 45% methanol in deionized water for 30 minutes at room temperature before absorbance reading.

For T cell restimulation, tissue culture plates were incubated overnight with 1 μ g/ml purified CD3 antibody in PBS. Excess antibody was aspirated and plates were blocked with R10 medium (RPMI, 10% calf serum, penicillin/streptomycin) at 4°C. Tumor-associated CD8⁺ T cells were isolated by FACS and cultured overnight on CD3-coated plates with R10 medium and 0.5 μ g/ml purified CD28 antibody. Conditioned medium was collected and analyzed for IFN- γ secretion by ELISA (R&D Systems, MIF00). Experiments were also repeated in which untouched tumor-associated CD8⁺ T cells were isolated by negative bead selection kit (Miltenyi Biotec, 130-104-075).

Animals. Richard Locksley (UCSF, Howard Hughes Medical Institute, San Francisco, California, USA) provided the IFN- γ reporter (GREAT) mouse strain [Ifngtm3(EYFP)Lky], which carries a bicistronic IFN- γ -IRES-eYFP reporter allele under the control of the endogenous *Ifng* promoter/enhancer region. Murine cells expressing IFN- γ also express cytoplasmic eYFP, which can be detected by flow cytometry. Matthew Krummel (UCSF) provided OT-I mice specific for the OVA peptide SIINFEKL (SL8) in the context of H-2Kb. WT C57BL/6 and BALB/c mice were purchased from Jackson Laboratory.

For the generation of tumor-bearing mice, B16 and B78-OVA cells were injected s.c. (150,000 cells per injection in 50% growth factor-reduced Matrigel in PBS) into the back flanks of 6- to 7-week-old male and female WT C57BL/6 mice or GREAT reporter mice on the C57BL/6 background. For studies of intracellular cytokine staining, mice were injected by tail vein with 10 μ g/g body weight of brefeldin A (BFA; Sigma-Aldrich, B6542) at 6 hours before tumor resection. Tumors were resected, minced, and subjected to enzymatic digest with Collagenase IV (Sigma-Aldrich, C5138; 500 U/ml), Collagenase A (Worthington Biochemical, LS004197; 100 U/ml), and DNase (200 μ g/ml) in RPMI medium for 30 minutes at 37°C with shaking followed by passage through a 70- μ m cell strainer. BFA was also added to reagents to prevent ex vivo secretion during tissue processing.

Mice bearing 2-week B78-OVA tumors received an adoptive transfer of 2×10^6 freshly isolated OT-I T cells expressing CD2-GFP by retro-orbital injection. 4T1 cells were injected orthotopically into mammary fat pads of 6- to 7-week-old female WT BALB/c mice (100,000 cells per injection in 50% growth factor-reduced Matrigel in PBS). To confirm autophagy deficiency in resected B78-OVA tumors at endpoint, cancer cells were isolated by ex vivo culture from tumor digests in puromycin, plated on coverslips, and subjected to immunocytochemistry as described below to measure P62 accumulation.

For prophylactic vaccination, mice were injected s.c. with Matrigel or 10^6 B16 cells pretreated with Dox to achieve 70% dead and dying cells, as assessed by annexin V and DAPI staining. Interpolation from a dose-response curve indicated that 24 hours of treatment with 8.8 μ M or 7.5 μ M Dox yielded 70% dead and dying cells for B16-shCTL and -shAtg7 cells, respectively. One week after vaccination, mice were injected s.c. on the contralateral flank with 100,000 healthy WT B16 cells. Tumor incidence was assessed by daily palpation.

For chemotherapy, mice bearing palpable tumors were injected by tail vein with 5 mg/kg body weight of Dox (Sigma-Aldrich, 44583) once per 7 days for 2 weeks before tumor resection. For antimalarial treatment, mice bearing palpable tumors were injected i.p. with 60 mg/kg chloroquine, 50 mg/kg quinacrine, or vehicle control, daily for 4–6 days before tumor resection. B16-bearing mice were treated for either 4 or 5 consecutive days; 4T1-bearing mice were treated for 3 days on and 2 days off for 6 total injections. Only chloroquine treatment was used for the studies of B16 melanoma in GREAT mice because quinacrine is autofluorescent in a similar range to eYFP.

Flow cytometry and FACS. Red blood cell lysis was performed with 175 mM ammonium chloride on ice. Zombie NIR Fixable Viability kit (BioLegend, 423105) was applied to cells for 30 minutes on ice. Subsequent steps were performed in flow buffer (PBS, 2% calf serum, penicillin, streptomycin, glutamine, 2 mM EDTA, 0.01% sodium azide). Cells were incubated in flow buffer with FcR blocking reagent (Miltenyi Biotec, 130-092-575), 2% FBS, 2%

Armenian hamster serum (Innovative Research, IGHMA-SER), and antibodies against surface markers for 30 minutes on ice. Cells were then fixed with 2% PFA in flow buffer for 15 minutes at 25°C, permeabilized with 0.02% saponin in flow buffer for 10 minutes at 25°C, and incubated with 0.02% saponin and antibodies against intracellular markers in flow buffer for 30 minutes at 25°C. Fixation and permeabilization of cells for intracellular Foxp3 staining were performed using the Foxp3 transcription factor staining buffer set (eBioscience, 00-5523-00). All flow cytometry was performed on a BD LSR II flow cytometer. Flow cytometry data analysis was done with FlowJo software (version 10.1). Fluorescence-activated cell sorting (FACS) of tumor-associated CD8⁺ T cells was performed using a Beckman Coulter MoFlo XDP.

Immunoblotting. Cells were lysed in RIPA buffer with 10 mM NaF, 10 mM β -glycerophosphate, 1 mM Na₂VO₄, 10 nM calyculin A, 0.1 mM E64-D, 10 μ g/ml pepstatin A, and 20 nM bafilomycin A. Lysates were cleared by centrifugation for 15 minutes at 4°C, boiled in sample buffer, resolved by SDS-PAGE, and transferred to PVDF membrane. Membranes were blocked in 5% milk in PBS with 0.1% Tween-20 (PBS-T), incubated with primary antibodies overnight at 4°C in blocking buffer, incubated with HRP-conjugated secondary antibodies, and analyzed by chemiluminescence. Image analysis was performed on raw images, and image brightness was adjusted for publication. See complete unedited blots in the supplemental material.

Immunohistochemistry and immunofluorescence. For immunohistochemistry, tumors were resected and fixed in formalin overnight at 4°C, incubated in 30% sucrose for cryoprotection for 24 hours at 4°C, embedded in OCT, and stored at -80°C before and after tissue sectioning. Thawed tissue slides were incubated in 4% PFA for 5 minutes, washed with PBS-T, and incubated in 1X target retrieval solution (Dako, S1699) at 96°C for 20 minutes in a plastic Coplin jar submerged in a beaker of boiling water. Slides were cooled for 20 minutes at 25°C, washed with PBS-T, blocked with 10% goat serum in PBS-T, and incubated with primary antibody in blocking serum overnight at 4°C. Slides were washed with PBS-T and incubated with fluorescent secondary antibody for 1 hour at 25°C, washed with PBS-T, incubated with 10 mg/ml Hoechst 33342 nuclear stain (Thermo Fisher Scientific, H1399) for 5 minutes at 25°C, and washed with PBS-T and distilled water. Coverslips were mounted with Prolong Gold antifade mountant (Thermo Fisher Scientific, P36934) and sealed with nail polish.

For immunofluorescence, cells were cultured on fibronectin-coated coverslips for 24 hours. Cells were fixed with 4% PFA for 10 minutes at 25°C, incubated with 0.1 M glycine in PBS for 5 minutes at 25°C to quench PFA autofluorescence, permeabilized with 0.5% Triton X-100 for 5 minutes at 25°C, and blocked for 1 hour at 25°C with 10% goat serum in PBS. Primary antibody incubation was performed overnight at 4°C, and secondary antibody incubation for 1 hour at 25°C, and nuclei were stained with Hoechst 33342 nuclear stain (Thermo Fisher Scientific, H1399) for 10 minutes at 25°C. Coverslips were mounted with Prolong Gold

antifade mountant (Thermo Fisher Scientific, P36934) and sealed with nail polish. Washes were performed between each incubation with 1X immunofluorescence wash buffer (PBS, 0.1% BSA, 0.2% Triton X-100, 0.04% Tween-20).

Fluorescence imaging was performed using a Zeiss Axiovert 200 microscope equipped with a SPOT RT camera (Diagnostic Instruments) and mercury lamp; images were acquired and prepared using SPOT and ImageJ (NIH) software. Image analysis was performed on raw images, and brightness was adjusted for publication.

Statistics. Where representative images are shown, experiments were performed at least 3 times and no data were excluded from analysis. Statistical analysis was done using GraphPad Prism software (version 7.01). Error bars represent SD from at least triplicate experimental conditions. *P* values were determined by unpaired 2-tailed *t* test for comparisons of 2 groups or by 2-way ANOVA with Dunnett's or Tukey's correction for multiple comparisons as indicated. *P* values for all tests are indicated on graphs as **P* < 0.05, ***P* < 0.01, ****P* < 0.001, *****P* < 0.0001, and not significant (NS).

Study approval. All animal studies were performed in accordance with a protocol (AN107285) approved by the UCSF Institutional Animal Care and Use Committee.

Author contributions

HS and JD conceived the study and designed the experiments. HS performed the experiments and analyzed data. JY performed cell culture, tissue harvests, and tissue processing for experimental repeats. MB and KB performed B78-OVA experiments and assisted with flow cytometry. JG assisted with tissue harvests and performed cell culture assays for experimental repeats. TM and FR assisted with mouse experiments. MK assisted with design of experiments and provided materials. HS and JD wrote the manuscript, with input from the other authors. JD supervised the study.

Acknowledgments

We thank Zena Werb, Gabriele Bergers, and Dean Sheppard, as well as members of the Debnath laboratory and Timur Starobinets, for critical discussions. Grant support to JD includes the NIH (CA188404) and the Department of Defense Breast Cancer Research Program (W81XWH-11-1-013). HS was supported by a National Science Foundation Graduate Research Fellowship (DGE-1144247) and a UCSF Discovery Fellowship. Flow cytometry and FACS were performed in the UCSF Flow Cytometry Core Facility. Tissue sectioning was performed by Jennifer Bolen in the UCSF Mouse Pathology Core Facility.

Address correspondence to: Jayanta Debnath, UCSF Department of Pathology, 513 Parnassus Avenue, Box 0502, San Francisco, California 94143, USA. Phone: 415.476.1780; E-mail: Jayanta.Debnath@UCSF.edu.

1. Kaur J, Debnath J. Autophagy at the crossroads of catabolism and anabolism. *Nat Rev Mol Cell Biol.* 2015;16(8):461-472.
2. Kenific CM, Debnath J. Cellular and metabolic functions for autophagy in cancer cells. *Trends*

Cell Biol. 2015;25(1):37-45.

3. White E. The role for autophagy in cancer. *J Clin Invest.* 2015;125(1):42-46.
4. Rebecca VW, Amaravadi RK. Emerging strategies to effectively target autophagy in cancer. *Oncogene.* 2016;35(1):1-11.

gene. 2016;35(1):1-11.

5. Yang ZJ, Chee CE, Huang S, Sinicrope FA. The role of autophagy in cancer: therapeutic implications. *Mol Cancer Ther.* 2011;10(9):1533-1541.
6. Barnard RA, Wittenburg LA, Amaravadi RK,

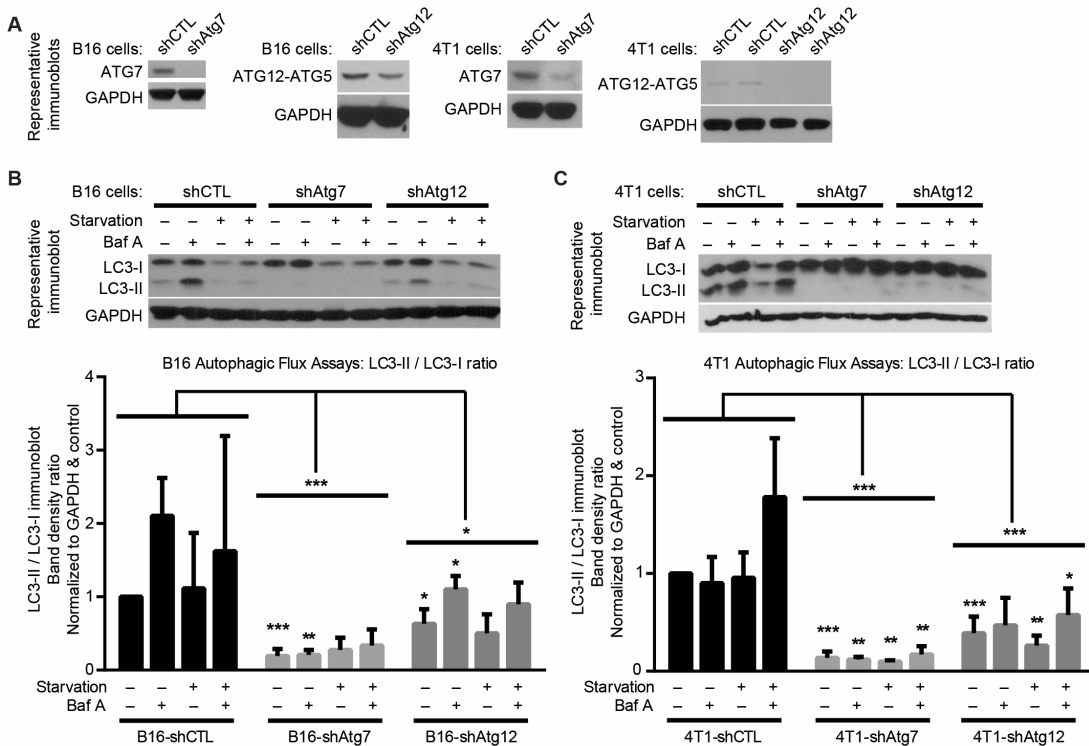
- Gustafson DL, Thorburn A, Thamm DH. Phase I clinical trial and pharmacodynamic evaluation of combination hydroxychloroquine and doxorubicin treatment in pet dogs treated for spontaneously occurring lymphoma. *Autophagy*. 2014;10(8):1415-1425.
7. Mahalingam D, et al. Combined autophagy and HDAC inhibition: a phase I safety, tolerability, pharmacokinetic, and pharmacodynamic analysis of hydroxychloroquine in combination with the HDAC inhibitor vorinostat in patients with advanced solid tumors. *Autophagy*. 2014;10(8):1403-1414.
8. Rangwala R, et al. Combined MTOR and autophagy inhibition: phase I trial of hydroxychloroquine and temsirolimus in patients with advanced solid tumors and melanoma. *Autophagy*. 2014;10(8):1391-1402.
9. Rangwala R, et al. Phase I trial of hydroxychloroquine with dose-intense temozolomide in patients with advanced solid tumors and melanoma. *Autophagy*. 2014;10(8):1369-1379.
10. Rosenfeld MR, et al. A phase I/II trial of hydroxychloroquine in conjunction with radiation therapy and concurrent and adjuvant temozolomide in patients with newly diagnosed glioblastoma multiforme. *Autophagy*. 2014;10(8):1359-1368.
11. Vogl DT, et al. Combined autophagy and proteasome inhibition: a phase I trial of hydroxychloroquine and bortezomib in patients with relapsed/refractory myeloma. *Autophagy*. 2014;10(8):1380-1390.
12. Wolpin BM, et al. Phase II and pharmacodynamic study of autophagy inhibition using hydroxychloroquine in patients with metastatic pancreatic adenocarcinoma. *Oncologist*. 2014;19(6):637-638.
13. Zitvogel L, Galluzzi L, Smyth MJ, Kroemer G. Mechanism of action of conventional and targeted anticancer therapies: reinstating immunosurveillance. *Immunity*. 2013;39(1):74-88.
14. Sistigu A, et al. Cancer cell-autonomous contribution of type I interferon signaling to the efficacy of chemotherapy. *Nat Med*. 2014;20(11):1301-1309.
15. Garg AD, Martin S, Golab J, Agostinis P. Danger signalling during cancer cell death: origins, plasticity and regulation. *Cell Death Differ*. 2014;21(1):26-38.
16. Michaud M, et al. Autophagy-dependent anticancer immune responses induced by chemotherapeutic agents in mice. *Science*. 2011;334(6062):1573-1577.
17. Michaud M, Xie X, Bravo-San Pedro JM, Zitvogel L, White E, Kroemer G. An autophagy-dependent anticancer immune response determines the efficacy of melanoma chemotherapy. *Onc Immunology*. 2014;3(7):e944047.
18. Gupta A, et al. Autophagy inhibition and antimicrobials promote cell death in gastrointestinal stromal tumor (GIST). *Proc Natl Acad Sci U S A*. 2010;107(32):14333-14338.
19. Leach DR, Krummel MF, Allison JP. Enhancement of antitumor immunity by CTLA-4 blockade. *Science*. 1996;271(5256):1734-1736.
20. Hodi FS, et al. Improved survival with ipilimumab in patients with metastatic melanoma. *N Engl J Med*. 2010;363(8):711-723.
21. Brahmer JR, et al. Phase I study of single-agent anti-programmed death-1 (MDX-1106) in refractory solid tumors: safety, clinical activity, pharmacodynamics, and immunologic correlates. *J Clin Oncol*. 2010;28(19):3167-3175.
22. Topalian SL, et al. Safety, activity, and immune correlates of anti-PD-1 antibody in cancer. *N Engl J Med*. 2012;366(26):2443-2454.
23. Pardoll DM. The blockade of immune checkpoints in cancer immunotherapy. *Nat Rev Cancer*. 2012;12(4):252-264.
24. Wolchok JD, et al. Nivolumab plus ipilimumab in advanced melanoma. *N Engl J Med*. 2013;369(2):122-133.
25. Schumacher TN, Schreiber RD. Neoantigens in cancer immunotherapy. *Science*. 2015;348(6230):69-74.
26. Blankenstein T, Coulie PG, Gilboa E, Jaffee EM. The determinants of tumour immunogenicity. *Nat Rev Cancer*. 2012;12(4):307-313.
27. Vanneman M, Dranoff G. Combining immunotherapy and targeted therapies in cancer treatment. *Nat Rev Cancer*. 2012;12(4):237-251.
28. Grivennikov SI, Greten FR, Karin M. Immunity, inflammation, and cancer. *Cell*. 2010;140(6):883-899.
29. Baaten BJ, Li CR, Deiro MF, Lin MM, Linton PJ, Bradley LM. CD44 regulates survival and memory development in Th1 cells. *Immunity*. 2010;32(1):104-115.
30. Hogquist KA, Jameson SC, Heath WR, Howard JL, Bevan MJ, Carbone FR. T cell receptor antagonist peptides induce positive selection. *Cell*. 1994;76(1):17-27.
31. Reinhardt RL, Liang HE, Locksley RM. Cytokine-secreting follicular T cells shape the antibody repertoire. *Nat Immunol*. 2009;10(4):385-393.
32. Manic G, Obrist F, Kroemer G, Vitale I, Galluzzi L. Chloroquine and hydroxychloroquine for cancer therapy. *Mol Cell Oncol*. 2014;1(1):e29911.
33. Salas E, Roy S, Marsh T, Rubin B, Debnath J. Oxidative pentose phosphate pathway inhibition is a key determinant of antimalarial induced cancer cell death. *Oncogene*. 2016;35(22):2913-2922.
34. Overwijk WW, Restifo NP. B16 as a mouse model for human melanoma. *Curr Protoc Immunol*. 2001;Chapter 20:Unit 20.1.
35. Pulaski BA, Ostrand-Rosenberg S. Mouse 4T1 breast tumor model. *Curr Protoc Immunol*. 2001;chapter 20: unit 20.2.
36. Salmeron G, Lipsky PE. Immunosuppressive potential of antimalarials. *Am J Med*. 1983;75(1A):19-24.
37. Fox RI. Mechanism of action of hydroxychloroquine as an antirheumatic drug. *Semin Arthritis Rheum*. 1993;23(2 suppl 1):82-91.
38. Vyas JM, Van der Veen AG, Ploegh HL. The known unknowns of antigen processing and presentation. *Nat Rev Immunol*. 2008;8(8):607-618.
39. Demachi-Okamura A, Torikai H, Akatsuka Y, Miyoshi H, Yoshimori T, Kuzushima K. Autophagy creates a CTL epitope that mimics tumor-associated antigens. *PLoS One*. 2012;7(10):e47126.
40. Fung C, Lock R, Gao S, Salas E, Debnath J. Induction of autophagy during extracellular matrix detachment promotes cell survival. *Mol Biol Cell*. 2008;19(3):797-806.
41. Engelhardt JJ, et al. Marginating dendritic cells of the tumor microenvironment cross-present tumor antigens and stably engage tumor-specific T cells. *Cancer Cell*. 2012;21(3):402-417.

SUPPLEMENTARY MATERIAL TO:

Intact Anti-Tumor Adaptive Immunity Following Autophagy Inhibition and Anti-Malarial Treatment

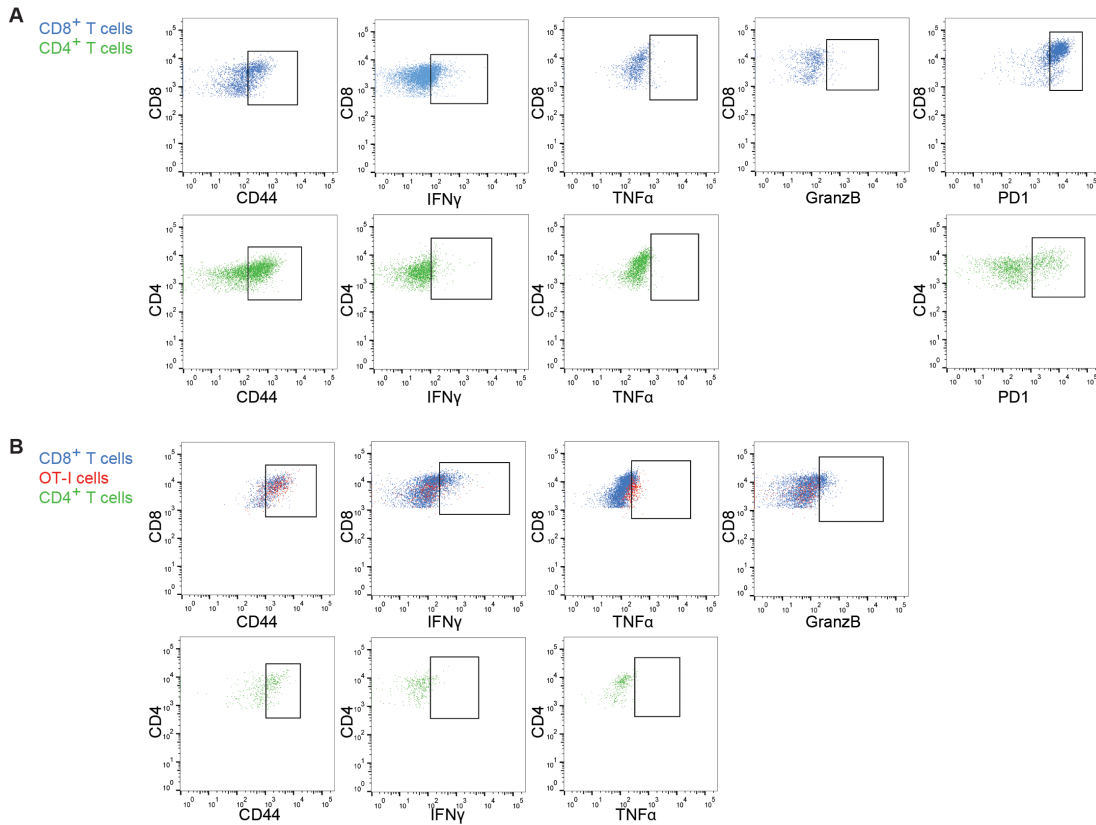
Hanna Starobinets¹, Jordan Ye¹, Miranda Broz¹, Kevin Barry¹, Juliet Goldsmith¹, Timothy Marsh¹, Fanya Rostker¹, Matthew Krummel¹, and Jayanta Debnath¹

Supplementary Figure 1



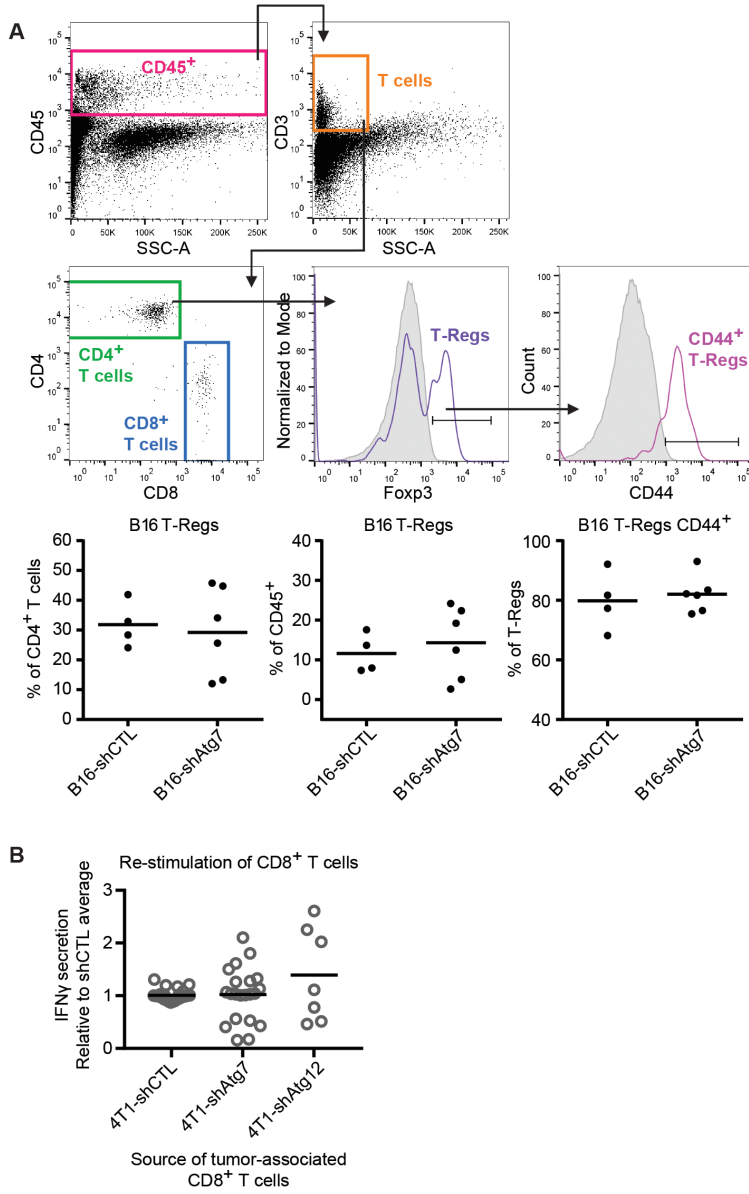
Supplementary Figure 1. Validation of autophagy deficiency in B16 melanoma and 4T1 mammary cancer cells. B16 mouse melanoma and 4T1 mouse mammary cancer cells were infected with lentivirus carrying either non-targeting (shCTL), ATG7 or ATG12 shRNA. (A) ATG7 and ATG12 knockdown was confirmed by immunoblotting. Autophagy flux assays were performed with full medium and starvation conditions, with or without Bafilomycin A (Baf A), with (B) B16 and (C) 4T1 cells. Band density was quantified from α -LC3 immunoblotting of cell lysates from three independent experiments and normalized to GAPDH and control cells grown in full medium without Baf A. Error bars represent standard deviation; * $p < 0.05$, ** $p < 0.01$, *** $p < 0.001$ using unpaired t test.

Supplementary Figure 2



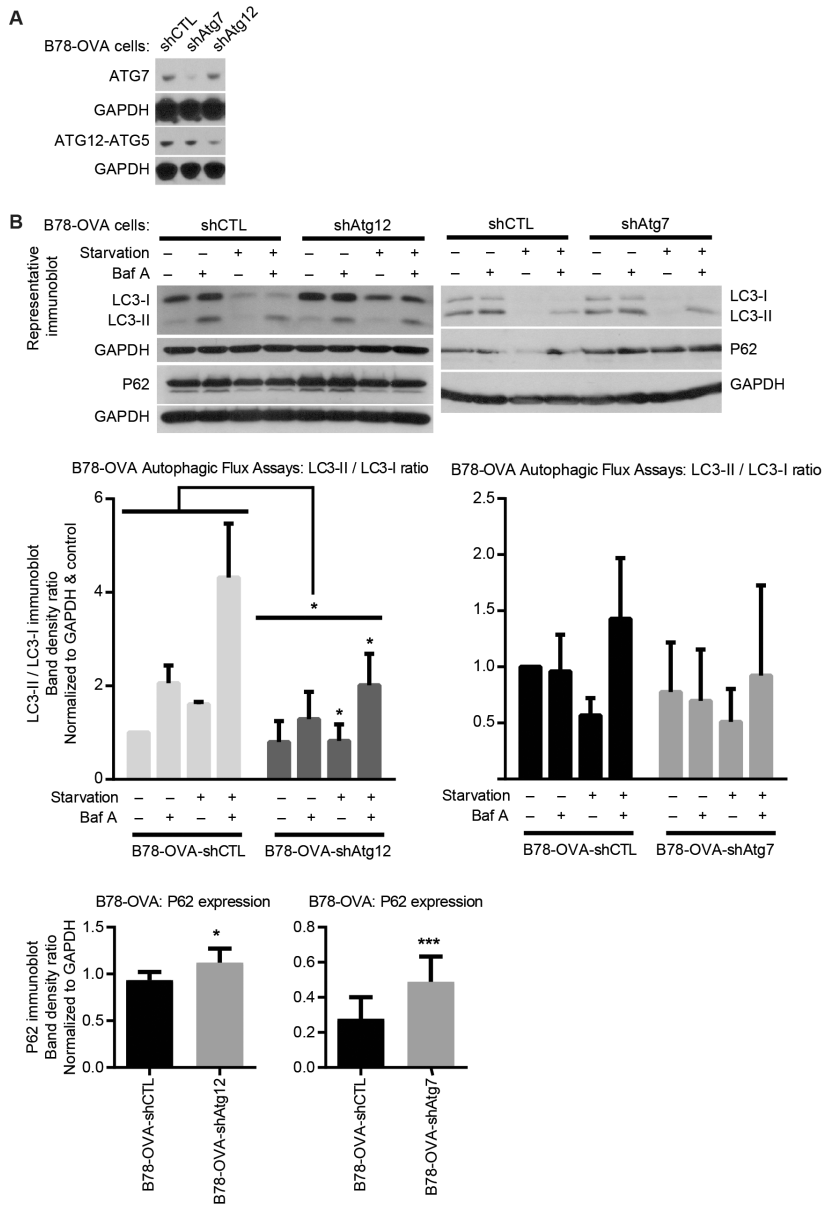
Supplementary Figure 2. Representative dot plots of T cell functional markers. (A) Dot plots corresponding to histograms in Figure 3A. Expression of T cell activation markers (CD44, IFN γ , TNF α , Granzyme B) and immune checkpoint marker PD1 were measured by flow cytometry in CD8⁺ (blue) and CD4⁺ (green) T cell populations. (B) Dot plots correspond to histograms in Figure 4D. Expression of T cell activation markers (CD44, IFN γ , TNF α , Granzyme B) were measured by flow cytometry in endogenous CD8⁺ T cells (blue), adoptively transferred OT-I cells (red), and endogenous CD4⁺ T cells (green).

Supplementary Figure 3



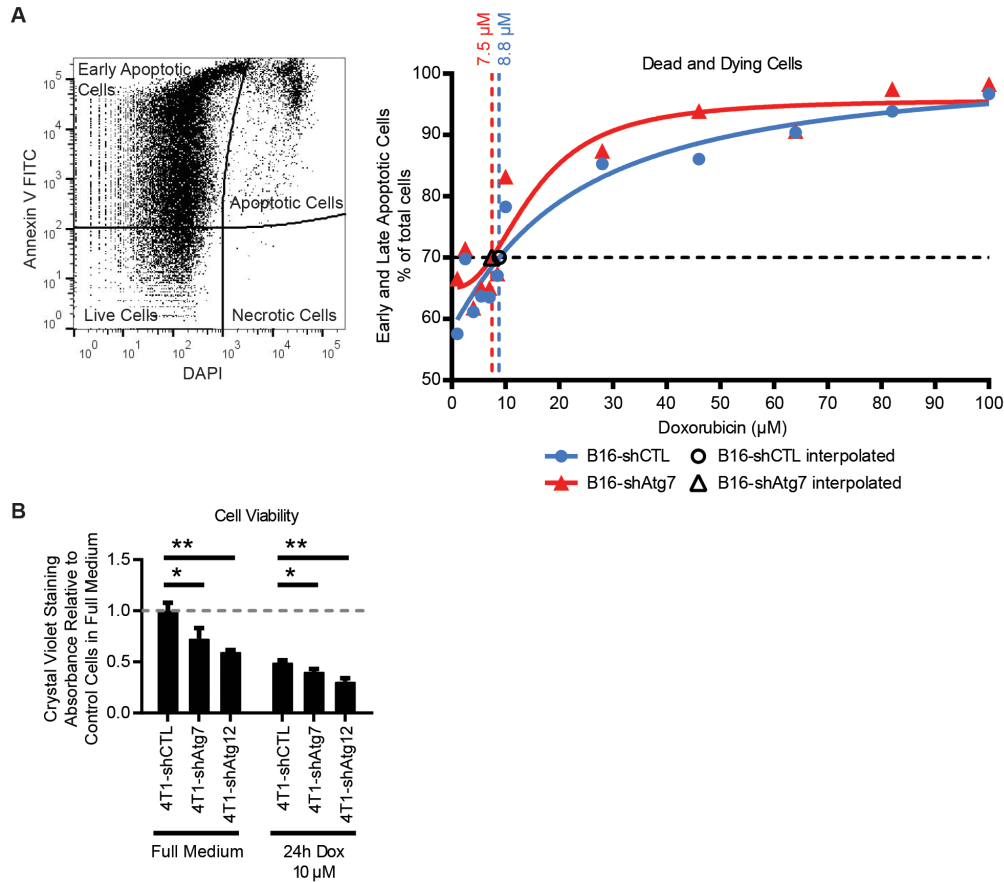
Supplementary Figure 3. T cell suppression and activation potential are unchanged in autophagy-deficient mouse tumors. Subcutaneous B16 tumors were allowed to form for 2 weeks. Tumors were resected and digested enzymatically, and regulatory T (TReg) cell infiltration and functional status were measured by flow cytometry. (A) Top: Representative flow cytometry gating strategy to define TReg cell populations. A live/dead marker was used to define live cells as a subset of singlets. CD45⁺ cells were defined from live cells and T cells were defined as the CD3⁺ SSC-A^{low} fraction of CD45⁺ cells. CD4⁺ and CD8⁺ single-positive T cell populations were subdivided from total T cells, and TRegs were defined as the Foxp3⁺ fraction of CD4⁺ cells. TReg activation was measured by surface CD44 expression. Solid gray plots represent isotype control (for stain of Foxp3) and unstained control (for stain of CD44). Positive staining indicated by gate and defined as that above the unstained or isotype control. Bottom: Each data point represents a distinct tumor from an individual host mouse. Bars represent mean values with two-way ANOVA not significant. (B) CD8⁺ T cells isolated from autophagy-competent and deficient 4T1 tumors are re-stimulated to equivalent activation levels. Orthotopic autophagy-competent (shCTL) and deficient (shAtg7 and Atg12) 4T1 tumors were allowed to form tumors for 2-3 weeks. Tumors were resected and digested enzymatically. CD8⁺ T cells were isolated by either FACS or negative bead selection, and re-stimulated in overnight culture with CD3 and CD28 antibodies. ELISA of conditioned medium from T cell cultures for IFN γ secretion. T cell isolation was performed 5 separate times; each data point represents a distinct conditioned medium sample and bars represent means; unpaired t test not significant.

Supplementary Figure 4



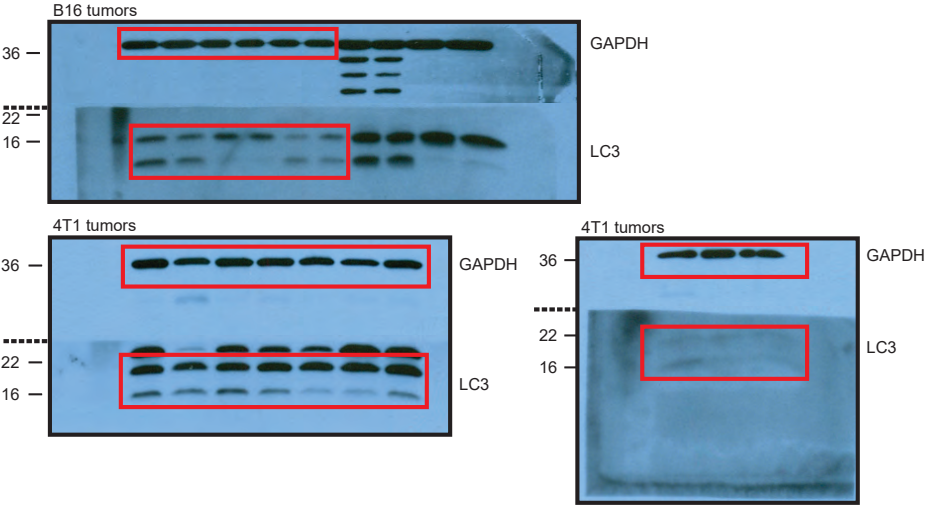
Supplementary Figure 4. Validation of autophagy deficiency in B78-OVA mouse melanoma cells. B78-OVA melanoma cells were infected with lentivirus carrying either non-targeting (shCTL), ATG7, or ATG12 shRNA. (A) ATG7 and ATG12 knockdown were confirmed by immunoblotting. (B) Autophagy flux assays were performed with full medium and starvation conditions, with or without Bafilomycin A (Baf A). Band density was quantified from α -LC3 immunoblotting of cell lysates from three independent experiments and normalized to GAPDH and control cells grown in full medium without Baf A. Error bars represent standard deviation; * $p < 0.05$ using unpaired t test. Band density quantified from P62 immunoblotting of cell lysates from 3 independent experiments and normalized to GAPDH. Error bars represent standard deviation; * $p < 0.05$; *** $p < 0.001$ using unpaired t-test.

Supplementary Figure 5

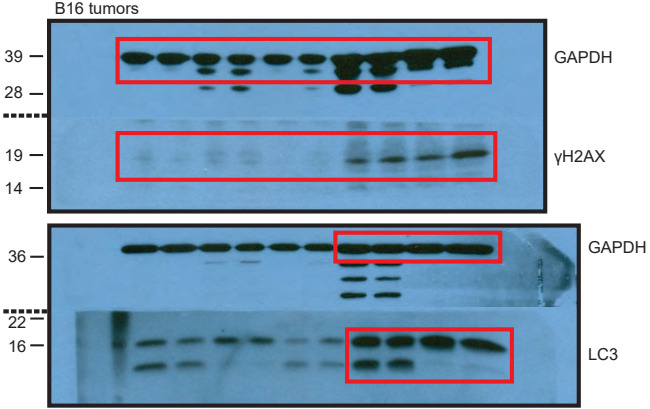


Supplementary Figure 5. Autophagy-deficient cells are more sensitive to doxorubicin treatment. (A) Autophagy-competent (shCTL) and deficient (shAtg7) B16 melanoma cells were cultured for 24 hours with indicated doses of doxorubicin. Floating and adherent cells were collected and stained with an Annexin V kit and DAPI. Representative dot plots of singlet cells analyzed by flow cytometry and divided into quartiles: live cells (Annexin V^{low} DAPI^{low}), early apoptotic cells (Annexin V^{high} DAPI^{low}), apoptotic cells (Annexin V^{high} DAPI^{high}), and necrotic cells (Annexin V^{low} DAPI^{high}). Dead and dying cells were defined as early and late apoptotic populations; dosages that achieved 70% of dead and dying cells were interpolated from the dose-response curve on the right. (B) Autophagy-competent (shCTL) and deficient (shAtg7 or shAtg12) 4T1 mammary carcinoma cells were cultured for 24 hours in full medium or 10 µM Doxorubicin. Cell viability was measured by crystal violet staining (N=3 for each cohort). Error bars represent standard deviation; * p<0.05; ** p<0.01 using unpaired t test.

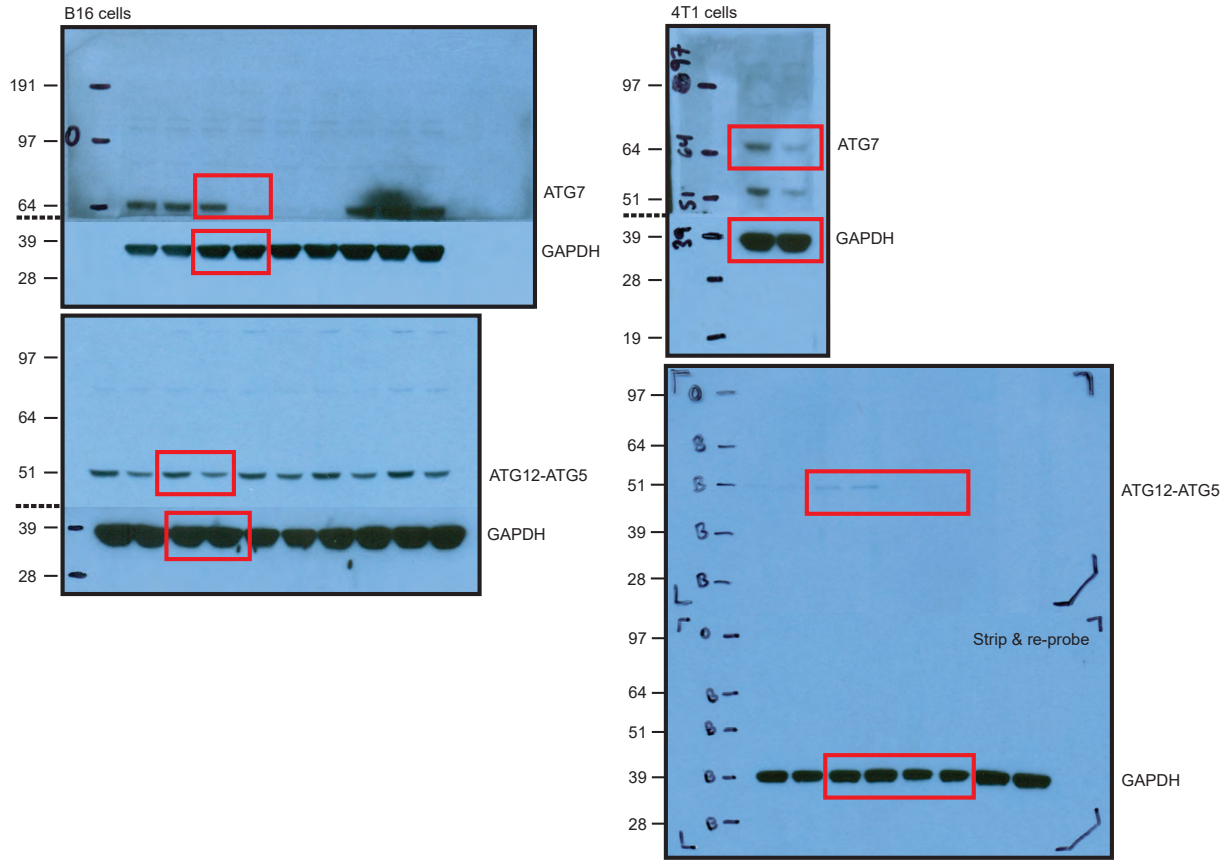
Full unedited gel for Figure 1B



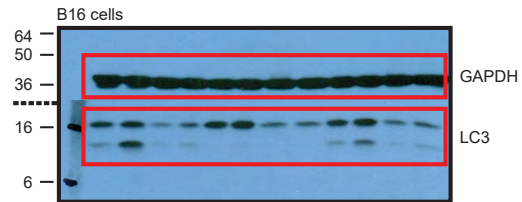
Full unedited gel for Figure 5D



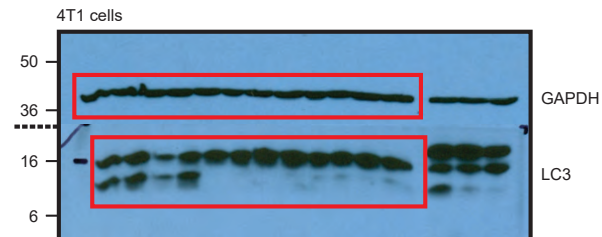
Full unedited gel for Supplementary Figure 1A



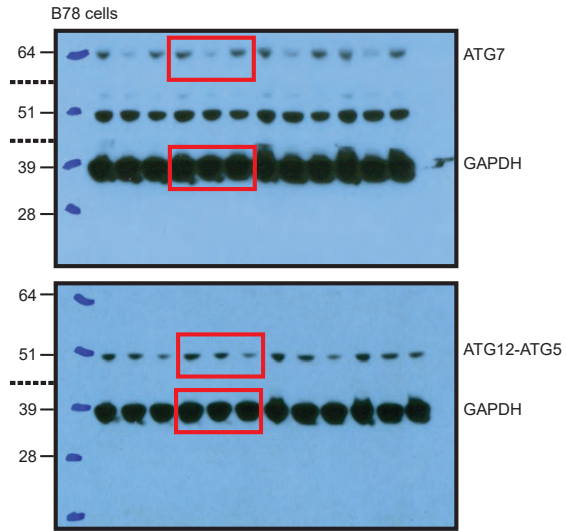
Full unedited gel for Supplementary Figure 1B



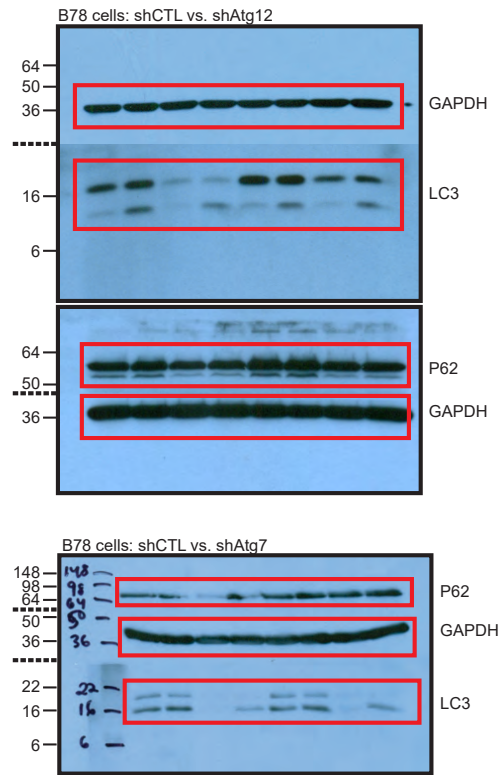
Full unedited gel for Supplementary Figure 1C



Full unedited gel for Supplementary Figure 4A



Full unedited gel for Supplementary Figure 4B



Publishing Agreement

It is the policy of the University to encourage the distribution of all theses, dissertations, and manuscripts. Copies of all UCSF theses, dissertations, and manuscripts will be routed to the library via the Graduate Division. The library will make all theses, dissertations, and manuscripts accessible to the public and will preserve these to the best of their abilities, in perpetuity.

Please sign the following statement:

I hereby grant permission to the Graduate Division of the University of California, San Francisco to release copies of my thesis, dissertation, or manuscript to the Campus Library to provide access and preservation, in whole or in part, in perpetuity.



Author Signature

10/19/2018
Date